Developing our understanding of the Transient Receptor Potential Melastatin 2 (TRPM2) channel

by

Sophie Janine Hesketh

Submitted in accordance with the requirements for the degree of

Doctor of Philosophy

The University of Leeds

School of Biomedical Sciences

Astbury Centre for Structural and Molecular Biology

May 2020

The candidate confirms that the work submitted is their own, except where work which has formed part of jointly authored publications has been included. The contribution of the candidate and the other authors to this work has been explicitly indicated below. The candidate confirms that appropriate credit has been given within the thesis where reference has been made to the work of others.

The work in Chapter 6 of this thesis has appeared in the following publication:

Publication (Journal Article):

Hesketh, S. J., Klebl, D. P., Higgins, A. J., Thomsen, M., Pickles, I. B., Sobott, F., Muench, S. P. (2020). Styrene maleic-acid lipid particles (SMALPs) into detergent or amphipols: An exchange protocol for membrane protein characterisation. *Biochimica Et Biophysica Acta (BBA) - Biomembranes*, 1862(5), 183192.

Contribution: Conceptualisation and design of experiments. Performed all preliminary experiments, wrote manuscript and created all figures using some results re-created by co-authors (credited in thesis and manuscript).

Acknowledgements

In my initial thesis submission, I wrote that this section could be a thesis in its' own right. For some reason, it also seemed the hardest to put into words.

Firstly, I would like to thank my supervisors, Prof. Asipu Sivaprasadarao and Dr. Stephen Muench – (a.k.a., Rao and Ste), for their endless patience, support and guidance throughout this PhD experience. You allowed me the freedom to be enthusiastic (by humouring my potentially ridiculous ideas), explore my own interests (allowing me to pursue those potentially ridiculous ideas), and making my own mistakes (sometimes realising that they may have, in fact, been ridiculous ideas all along…). It's been an absolute pleasure to work with you and alongside your lab groups, and in the kindest and funniest possible way, I hope you don't have another experience like it (I say this with a laugh and a smile).

I would additionally like to acknowledge my other (potentially unsuspecting), sort-of mentors who have influenced many of my decisions more than they may ever realise – Prof. Frank Sobott, Prof. Neil Ranson, Dr. Vas Ponnambalam, Dr. Albert Konijnenberg, Dr. Hervé-William Rémigy and Dr. Attieh Aminian. Especially to Frank for your enthusiasm and support in pursuing my own interests, and ultimately helping them become a reality. I would also like to thank the rest of the Sample Prep team at FEI/ThermoFisher Scientific for their support and encouragement during my pandeminternship, particularly Chris Budde for insightful discussions into the future. Despite the circumstances, it was a fantastic experience and I learned more than I could

have ever imagined. Thank all of the above for teaching me that it is possible to be both good people, positive influencers and great scientists.

To my fellow lab members (past and present), in the shared lab spaces of Astbury Level 6 and Garstang 6.45 (especially Ponnambalam *et al.*) – thank you for making every day an absolute joy (with added turmoil/challenge when trying to get you to the pub). There are far too many of you to list, but you know who you are and how much you mean to me. I'm aware a lot of people say this, but I also hope you know that it's true. If we've ever shared a crazy night out, laughed together, cried together, engaged in (sometimes also crazy) philosophical discussions (life or science), or adventured off into the unknown, *then you are on this list.*

However, I must make a few special mentions to the following for sharing in some of my most valued memories (in alphabetical order, of course): Amelia Leusik, Andreas Kiessling, Anthony Chan, Ben Lane, Dr. Craig Wilkinson, Dr. David Carrier, David Klebl, Dr. Eoin Leen, Dr. Faheem Shaik, Jannik Strauss, Joanna Mitchell, Dr. Julie Heggelund, Dr. Maren Thomson, Dr. Steven Harbourne, and finally, a dedication to Will's 'Western Blot' Face. You are all fantastic human beings. Especially to Anthony, who was one of the most (brutally) kind-hearted people I have ever had the honour of knowing. We were truly *et* and *al.* You will be sorely missed.

Unrelated to this project but very related to my PhD experience, I would also like to thank team Cryo-Cycle (also alphabetical); David Nicholson, Josh White, Laura Marr, Molly Gravett, Neil Ranson, Ollie Antoniak, Rebecca Thompson, Rodrigo Gallardo and Steve Thompson for sharing in one of the most challenging but sensational events

during this time to raise funds for a fantastic cause. It was a heart-warming experience, and I shan't forget it.

Special thanks to my cohort, particularly 'Da Ladiez' – Dr. Anna Stikane, Dr. Katherine Davies, Dr. Sian Irvine; and to whom I will refer to as 'Da Guyz' (for lack of a SFW name), Dr. Christian Nathan (Hamz), Dr. David Kealy and Dr. Jim Horne, for the amazing times we've shared over the past few years. I couldn't have asked to be surrounded by better human beings, and certainly couldn't have done it without you. We've been through a lot, and I am so proud of us all.

To those outside of lab groups, cohort and PI's, special mentions go to Dr. Arndt Rohwedder, the EM group and the university admin teams for their continuous support throughout this project. I would also like to acknowledge my students/tutees – Arran Pack, Rachel Cooper, David Klebl, Izzabelle Pickles, William Meddick-Dyson and Benjamin Lane* (*honorary tutee, I don't think I'll ever forget the milk incident…) for helping me explore different aspects of this project with new enthusiasm, and providing endless entertainment and laughter when 'something weird has happened'.

An extra special mention must also be had for Lucy Parker, Alan Berry and the FBS post-graduate administrative team - I think it's fair to say that no PhD student would make it out alive if not for you, especially me.

I would also like to thank Prof. Michelle Peckham, Dr. Joseph Cockburn and the Biotechnology and Biological Sciences Research Council (BBSRC) for making this all possible in the first place; as well as my examiners for reading this in the last place. I'm very grateful for the experience.

Of course, no thesis would be complete without extending thanks and gratitude to my family, particularly my mum, nan and brother for their continued support and encouragement throughout the years – I will always appreciate it.

Although we are currently in the middle of a pandemic and some type of global meltdown, and it's likely no one else will ever read or see this, I hope you all know how much you mean to me. I still have so many people to thank, even more to hug, and consider myself very lucky to have been surrounded by such wonderful people.

Thank you all for the journey, it's been one heck of a ride.

Now… to the science!

Abstract

Transient receptor potential (TRP) melastatin 2 (TRPM2) is a non-selective cation channel of the TRP channel superfamily. It plays key roles in mediating oxidative stress and immune responses and is endogenously activated at ~37 °C – human body temperature. Here, the styrene-maleic acid (SMA) *co*-polymer and a combination of detergents were used to biochemically, biophysically and structurally characterise the TRPM2 cation channel *in vitro*. Through these experiments, fascinating insights were gained into TRPM2 structure and function as a temperature sensor, as well as the role of native lipids in channel stabilisation.

The use of SMA was crucial to the success of these studies, but inherent issues with the polymer can render it unsuitable for use with some biophysical techniques – particularly mass spectrometry (MS) and electron microscopy (EM), and functional assays requiring divalent cations. In light of this, an 'SMA-exchange' was also developed, whereby the power of SMA as a solubilisation agent is utilised for extraction and purification, then exchanged for another solubilisation platform to enhance compatibility with downstream applications.

Overall, novel structural and functional mechanisms of the TRPM2 cation channel have been suggested, and when bottlenecks were met in TRPM2 characterisation, an exchange method was developed to circumvent the issues.

Table of Contents

List of Tables

List of Figures

List of Abbreviations

°C	Degrees Celsius
AA	Abscisic Acid
aa	Amino Acids
AcrB	Acridine Resistance Protein B
ADP	Adenosine Diphosphate
ADPR	Adenosine Diphosphate Ribose
ARD	Ankyrin Repeat Domain
A.U.	Absorbance Units
Ca^{2+}	Calcium Ion
CC	Coiled-coil
CB	Cerebrosides
CH	Cholesterol
Cryo-EM	Cryo-Electron Microscopy
dH2O	Distilled Water
ddH2O	De-ionised, Nuclease-Free Water
DDM	n-dodecyl-β-D-maltoside
DDM_TRPM2	DDM-purified TRPM2
DTT	Dithiothreitol
EM	Electron Microscopy
HRP	Horseradish Peroxidase
HV	High Voltage
Mg^{2+}	Magnesium Ion
MHR	TRPM Homology Region
MS	Mass Spectrometry
NaCl	Sodium Chloride
NaF	Sodium Fluoride
NaP	Sodium Phosphate
NUDIX	Nucleotide Diphosphate linked to X Moiety
NUDT9	Nudix-type motif 9
NUDT9H	Nudix-type motif 9 homology domain

PBS	Phosphate Buffered Saline
PBST	Phosphate Buffered Saline/Tween20
PA	Phosphatidic Acid
PC	Phosphatidylcholine
PE	Phosphatidylethanolamine
PI	phosphatidylinositol
PIP_2	Phosphatidylinositol 4,5-bisphosphate
PPI	Protein-Protein Interactions
ROS	Reactive Oxygen Species
RNS	Reactive Nitrogen Species
RT	Room Temperature
SANS	Small-Angle Neutron Scattering
SAXS	Small-Angle X-ray Scattering
SDS	Sodium Dodecyl Sulphate
SMA	Styrene-Maleic Acid
SMALP	Styrene-Maleic Acid Lipid Particle
SMA_TRPM2	SMA-purified TRPM2
SPA	Single Particle Analysis
TM	Transmembrane
TRP	Transient Receptor Potential
TRPA	Transient Receptor Potential Ankyrin
TRPC	Transient Receptor Potential Canonical
TRPM	Transient Receptor Potential Melastatin
TRPM1	Transient Receptor Potential Melastatin 1
TRPM2	Transient Receptor Potential Melastatin 2
TRPML	Transient Receptor Potential Mucolipin
TRPN	Transient Receptor Potential NOMPC
TRPP	Transient Receptor Potential Polycystin
TRPV1	Transient Receptor Potential Vanilloid 1
TRPY	Transient Receptor Potential Yeast
UV	Ultraviolet
VSLD	Voltage Sensor-Like Domain
WB	Western Blot

Chapter 1:

Introduction to TRP Channels and Membrane Protein Characterisation

1.1 Preface

Membrane proteins comprise over ~30 % of all cellular proteins and play significant roles in a plethora of cellular functions (Wallin, Gunnar and Heijne, 1998). Despite their physiological importance, our structural, biochemical and biophysical understanding of membrane proteins *in vivo* is limited. Fundamental to developing our understanding of their direct mechanisms *in vivo*, is their analysis *in vitro*.

To study membrane proteins *in vitro*, they are commonly overexpressed in a suitable system that facilitates their correct folding and reconstitution into native lipid bilayers. The membrane fraction is then isolated and solubilised with amphipathic surfactants, usually detergents, which strip away the native membrane and suspend the membrane protein of interest in solution (Figure 1A; (Le Maire, Champeil and Møller, 2000)). Keeping the membrane protein in a stable, unperturbed and active state in aqueous solutions remains one of the biggest challenges in the field of membrane protein characterisation (Carpenter *et al.*, 2008; Zorman *et al.*, 2015; Hardy *et al.*, 2016).

When choosing a specific extraction method, the pH, ionic strength, additives and usability in downstream applications must be considered, as all are factors in solubilisation success (Le Maire, Champeil and Møller, 2000). Currently, there are two extraction methods that consistently facilitate direct membrane protein extraction through to subsequent biochemical or biophysical characterisation – either using detergents (Seddon, Curnow and Booth, 2004), or polymers such as the styrene-maleic acid (SMA) *co*-polymer (Postis *et al.*, 2015a)(Figure 1.1B and 1.1C). Other solubilisation vehicles exist but require detergents for the initial solubilisation step.

This introduction will provide a succinct explanation of each process, before moving onto their application in TRP channels.

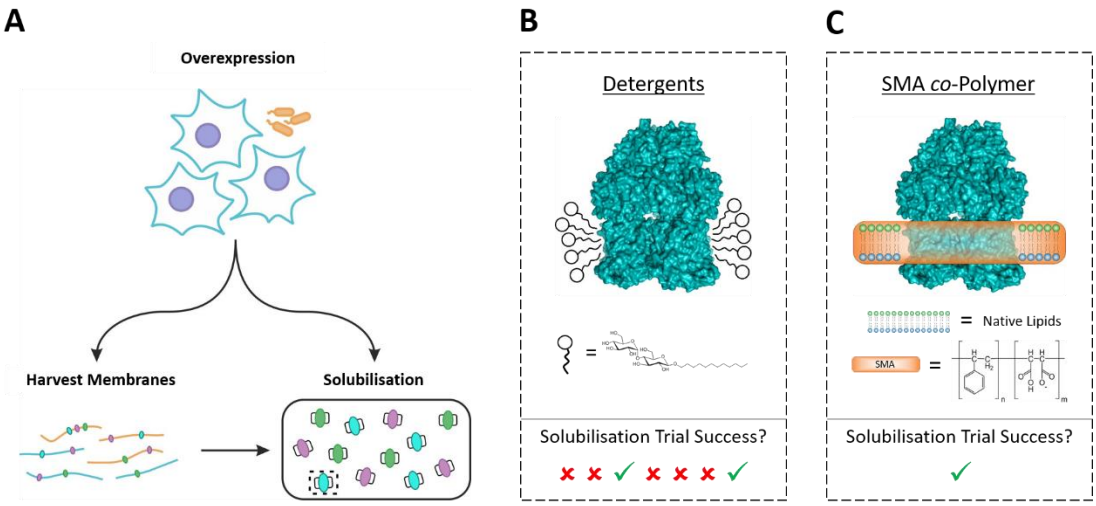

Figure 1.1: Membrane protein expression and solubilisation procedure.

A)Membrane proteins are overexpressed in either eukaryotic or prokaryotic host cells. From here, the membrane protein can either be directly solubilised from whole cells, or the membrane fractions can be isolated and kept for storage for later solubilisation, either with detergents (B) or the SMA *co*-polymer (C). B) Detergent monomers are depicted in 'head and tail' diagrams, with the structure of n-dodecyl-β-D-maltoside (DDM) as an example, surrounding a membrane protein (blue). Numerous detergents are screened for solubilisation efficiency and stability, with relative success or failure signified by the ticks and crosses. C) The styrene-maleic acid (SMA) *co*-polymer (orange) solubilises membrane proteins (blue) directly from the native bilayer, retaining its native lipid annulus. SMA solubilisation requires no other screening and is frequently successful, signified by a green tick.

1.2 Membrane Proteins and the Native Membrane Environment

Membrane proteins are situated within the lipid bilayer of a cell or organelle. This is a 'greasy mixture' comprising lipids, proteins and signalling molecules. The bilayer consists of a hydrophobic, fatty acid core sandwiched between a polar layer of phospholipid head groups. These self-assemble as a barrier for selective trafficking of a variety of molecules. This selectivity can be a function of the lipid bilayer itself, or the membrane proteins embedded or associated within them (Alberts *et al.*, 2002).

The lipid bilayer is ~30 Å wide and while fluid, can also be segmented in the form of nano-domains, macro-domains and lipid rafts (Nicolson, 2014; Ogiso, Taniguchi and Okazaki, 2015). Each domain will have a different lipid composition, different physical dimensions and physical tension properties. Membrane proteins can be randomly distributed and diffuse in the bilayer, but the more recent view is that they are sequestered to these domains either by intracellular anchors, or their direct interaction with the lipid bilayer around them. In fact, some membrane proteins rely on the rigidity of the bilayer to function, and its fluidity can directly affect oligomerisation, activation and inhibition (Nicolson, 2014).

1.3 Membrane Protein Overexpression

All *in vitro* reconstitution methods start with protein overexpression, and for membrane proteins, the choice of overexpression system can be pivotal. There are several essential criteria to consider when selecting an overexpression system for any given membrane protein, such as the expression mechanism, construct/tag system, required folding machinery and host cell membrane lipid composition (Andréll and Tate, 2013; Hardy *et al.*, 2016). However, the type of expression system selected

ultimately depends upon the way the protein product will be used and analysed. Despite these considerations, the effect an overexpressed protein will have on the host cell, and inversely, the host-cell's effect on it is seemingly impossible to predict (Markossian and Kurganov, 2004; Le Bon *et al.*, 2018). This is particularly the case for membrane proteins, for which expression levels are frequently very low, making any downstream experimentation even more difficult (Goehring *et al.*, 2014; Hardy *et al.*, 2016).

1.3.1 Overexpression of Escherichia coli membrane proteins

For decades, *Escherichia coli* (*E. coli*) have been the 'workhorse' behind recombinant protein expression. Since the proposition of operon theory (Jacob and Monod, 1961), *E. coli* expression strains, plasmids and culture conditions have evolved substantially to facilitate recombinant expression of a variety of soluble and membranous proteins (reviewed in Rosano and Ceccarelli, 2014). Their success as a host system is attributed to their relative ease of genetic manipulation and scalability, which has allowed the repertoire of possible expression targets to expand to unprecedented levels. However, the *E. coli* expression system remains primitive in its folding machinery and cellular complexity, and as more complex proteins are studied, more advanced expression systems are required.

1.3.2 Overexpression of mammalian membrane proteins

Mammalian membrane proteins comprise some of the most difficult targets to express and purify for biochemical and biophysical characterisation (Tate, 2001; Andréll and Tate, 2013). They often form highly integrated membrane structures, with even more

complex lipid dynamics/influences and environments. Often yeast, insect and mammalian cell cultures are required to produce a native product, as they provide folding machinery and/or post-translational modification pathways are required to produce a representative final protein product. Advances in construct design (Goehring *et al.*, 2014), inducible expression systems (Yao *et al.*, 1998), and screening methods (Hattori, Hibbs and Gouaux, 2012; Goehring *et al.*, 2014), culture methods (Portolano *et al.*, 2014) in mammalian cells have led to the successful expression of complex multi-domain structures for biochemical and structural characterisation (Tate, 2001; Goehring *et al.*, 2014). However, excessive expression of any protein can lead to host cell toxicity either through disruption of trafficking pathways or abhorrent aggregation/accumulation in the ER or cytoplasm (Jones *et al.*, 2005). Once an optimum expression system has been established, which is no trivial task, solubilisation trials can commence.

1.4 Membrane Protein Solubilisation

Surfactant efficiency and success is a function of its operating conditions, and each will have unique susceptibilities to pH, temperature, additives and ionic strength (Le Maire, Champeil and Møller, 2000). They become bio-active surfactants when they interact with biological membranes, and form lipid-surfactant mixtures in solution – encapsulating the membrane proteins within them (Seddon, Curnow and Booth, 2004). Surfactants, particularly a sub-set of surfactant known as detergents, have been successfully implemented for membrane protein solubilisation since the introduction of alkyl glycosides (Rosevear *et al.*, 1980), but recently, other polymeric amphiphiles, such as amphipols (Tribet, Audebert and Popot, 1996), and the styrene-maleic acid *co*-

polymer (Knowles, Finka, Smith, Y.-P. Lin, *et al.*, 2009), have been developed in response to detergent-associated issues (Seddon, Curnow and Booth, 2004; Dörr *et al.*, 2016; Hardy *et al.*, 2016). Solubilisation success can also be influenced by the membrane itself, and detergent-resistant membranes with more compact dimensions are even more challenging to dissolve (Schuck *et al.*, 2003).

1.4.1 Detergent Solubilisation

1.4.1.1. Detergents

Detergents are amphipathic molecules that come in a variety of shapes and sizes, but are broadly categorised into four groups according to their chemical structure: ionic, non-ionic, zwitterionic and bile acid salts (Seddon, Curnow and Booth, 2004). Conventional detergents consist of a polar, hydrophilic 'head' group, a nonpolar hydrophobic 'tail', and form spherical detergent micelles in aqueous solutions (Figure 1.2A). Their variable shape, size and charge directly contribute to their solubilisation efficiency, micellar formation and stabilising influence on the membrane protein of interest (Figure 1.2A and 1.2B). Micellar formation and structure can be a considerable factor for structure determination, particularly for X-ray crystallography and electron microscopy (Gewering *et al.*, 2018). Spherical, homogeneous micelle:MP complexes with low critical micellar concentrations (CMC) are preferred for electron microscopy, whereas cylindrical micelles/lipid cubic phases are preferred for X-ray crystallography (Privé, 2007).

The packing parameter of the detergent monomer is a key determinant of micelle formation (Figure 1.2; (Salim *et al.*, 2014). The length and degree of saturation of the

hydrophilic alkyl chains and the type of hydrophilic moiety can also highly influence the properties the detergent exhibits in aqueous solution, whereby longer alkyl chains

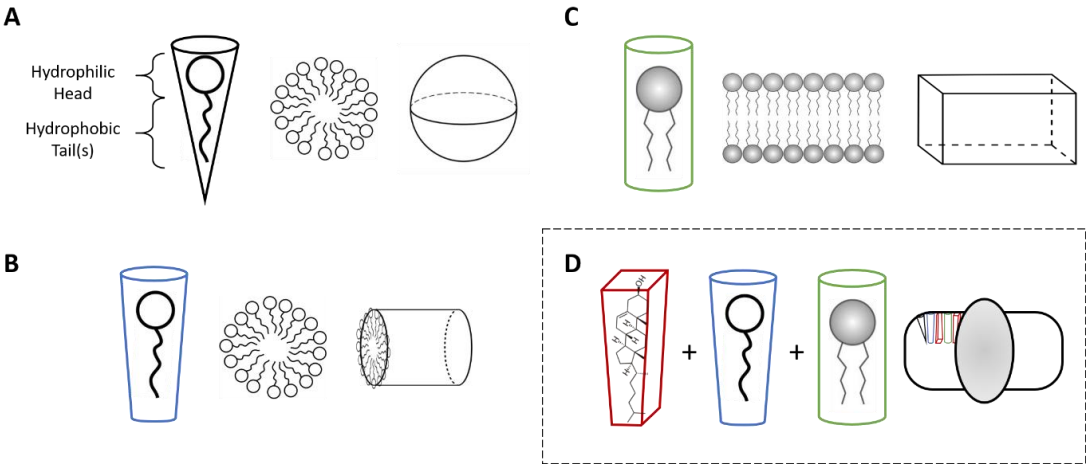

contribute to a lower CMC but are more likely to self-aggregate; shorter chains tend to contribute to a higher CMC, but negatively influence protein stability, oligomerisation and function (Seddon, Curnow and Booth, 2004; Privé, 2007). The charge of the polar head group can be positive (cationic), negative (anionic), zwitterionic (both positive and negative charges) or neutral (non-ionic), and the CMC is influenced by the presence of counter ions (Seddon, Curnow and Booth, 2004).

Figure 1.2: Detergents and their micellar formations.

A) Example of a conical detergent monomer and the types of micelle pore and spherical structure it forms, highlighting the hydrophilic head and hydrophobic tail moieties. B) Example of a detergent with wider dimensions in the tail domain, alongside depictions of the micelle pore and cylindrical structures that they form. C) Example of detergent or lipid with cylindrical structure, depicting the bilayer and cubic/planar bilayer phases that they form. D) A combination of the aforementioned detergents and lipids can be used to stabilise the membrane protein (grey) in solution with a mixed-micelle annulus. Cholesterol has been depicted as a block lipid to exemplify its structural rigidity. Redrawn with modifications from Le Maire et al., 2000 and Salim et al., 2014.

The most popular membrane protein detergent, *n*-dodecyl-β-D-maltopyranoside (DDM), is a non-ionic detergent that is conical in shape and forms spherical micelles at a CMC of 0.0087 % (~170 μM) (Figure 1.2A; Rosevear et al., 1980). In contrast, the increasingly popular neopentyl derivative of DDM, lauryl maltose neopentyl glycol (LMNG), preferentially forms tubular micelles and has a CMC of 0.001 % (~10 μM) (Figure 1.2B; Chae et al., 2010). Native phospholipids in solution tend to form clustered sheets that mimic the bilayer structure (Figure 1.2C; Balazs and Godbey, 2011), and are frequently required alongside detergents to retain membrane protein function. Cholesterol is a steroid-based lipid which can be added to form more rigid, planar micellar systems to support/sustain a more native-like membrane protein annulus (O'Malley *et al.*, 2011; Cuevas Arenas *et al.*, 2016; Lyons *et al.*, 2016). A combination of detergents, lipids and other structural lipids such as cholesterol, can alter the properties of micelles and positively influence the associated membrane protein (Figure 1.2D; (Stuart and Boekema, 2007; O'Malley *et al.*, 2011). The Krafft point, hydrophobic-lipophilic balance and cloud points are other factors that affect micelle formation, but can more broadly be governed by environmental conditions, such as pH, temperature and salt concentration (Le Maire, Champeil and Møller, 2000; Seddon, Curnow and Booth, 2004).

1.4.2 Detergent Exchange

Despite their success in membrane protein characterisation by biochemical and structural methods, detergents are poor bilayer mimetics, and membrane protein stability and activity in detergent micelles remains an issue (Le Maire, Champeil and Møller, 2000). Delipidation can also occur as a result of harsh extraction and

solubilisation, removing essential functional or structurally integral lipids which can have a knock-on effect on oligomerisation and folding (Bowie, 2001; Seddon, Curnow and Booth, 2004; Reading, Walton, *et al.*, 2015; Hardy *et al.*, 2016; Gupta *et al.*, 2018; Pyle *et al.*, 2018). Additionally, and perhaps the most critical, is the interference of excess detergent micelles on biochemical, biophysical and structural studies, particularly electron microscopy (Le Maire, Champeil and Møller, 2000; Gewering *et al.*, 2018).

For this reason, a number of subsequent reconstitution platforms have been developed to combat detergent-associated issues, such as membrane scaffold protein (MSP) nanodiscs (Civjan *et al.*, 2003; Nath, Atkins and Sligar, 2007; Ritchie *et al.*, 2009), amphipols (Tribet, Audebert and Popot, 1996; Zoonens and Popot, 2014), peptidergents or peptidiscs (Schafmeister, Miercke and Stroud, 1993; Carlson *et al.*, 2018), bicelles (Dürr, Gildenberg and Ramamoorthy, 2012), lipid cubic phases for crystallisation (Cherezov, 2009) and liposomes (Rigaud, Pitard and Levy, 1995) (Figure 1.3).

The most commonly used are lipid bilayer-based reconstitution systems, such as liposomes (Rigaud, Pitard and Levy, 1995), bicelles (Dürr, Gildenberg and Ramamoorthy, 2012) or nanodiscs (Nath, Atkins and Sligar, 2007; Borch and Hamann, 2009). Lipid nanodiscs can be of defined size and lipid composition, offering advantages for accurate mass calculations (Michael T Marty, Hoi and Robinson, 2016), functional assays (Nath, Atkins and Sligar, 2007; Borch and Hamann, 2009) and structural studies (Denisov and Sligar, 2017). Liposomes are widely regarded as the best method of reconstitution for functional assays (Rigaud, Pitard and Levy, 1995), but are less amenable to structure analysis (Wang and Sigworth, 2009; Guo and

MacKinnon, 2017). Peptidergents or peptidiscs are short amphipathic peptides that form helix-like structures in solution, and bind directly to the transmembrane region of membrane proteins, but can negatively alter their activity (Schafmeister, Miercke and Stroud, 1993; Bavec *et al.*, 1999; Carlson *et al.*, 2018).

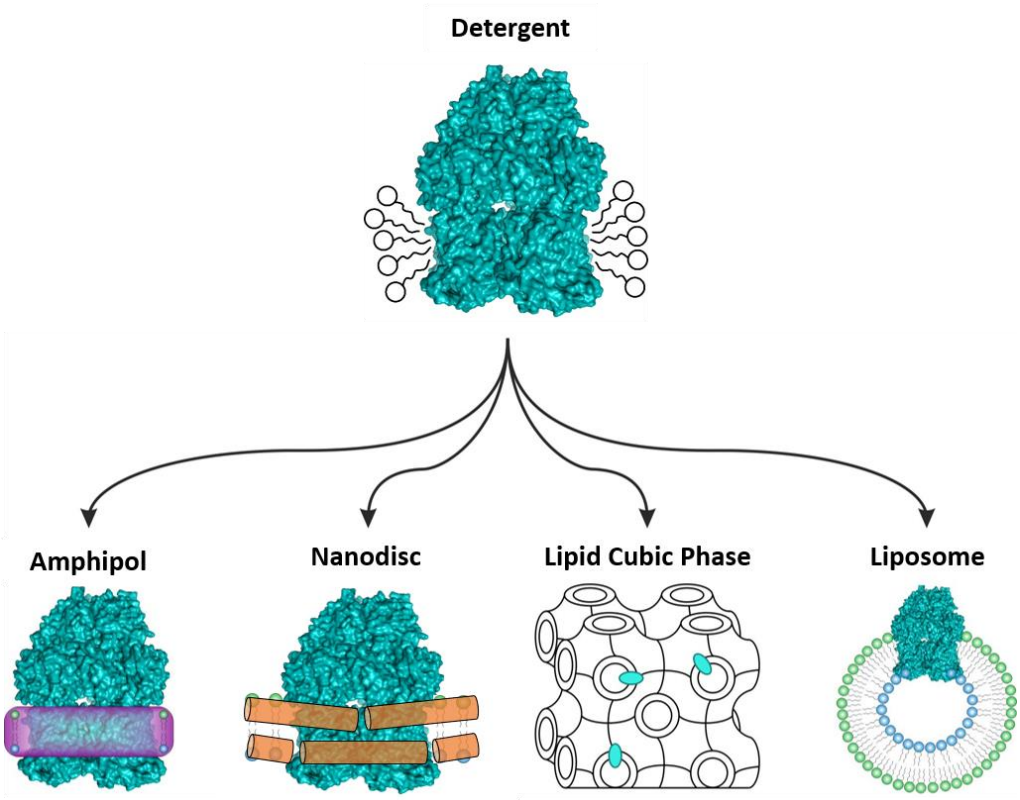

Figure 1.3: Exchanging detergents for more versatile solubilisation platforms.

Once solubilised in detergent, membrane proteins (blue) can be exchanged into amphipols, nanodiscs, lipid-cubic phases and liposomes to enhance stability. The organisation of the membrane protein within each system is shown.

Of the available reconstitution tools, amphipols are the most characterised and have been widely cited for use with structural methods such as mass spectrometry (Leney *et al.*, 2012) and electron microscopy (Althoff *et al.*, 2011; Huynh, Cohen and

Moiseenkova-Bell, 2014). While originally designed in hope of providing an alternative solubilisation platform entirely, they were found to have low extraction efficiency on native membranes (Tribet, Audebert and Popot, 1996). However, when mixed with detergent-extracted proteins in solution, they can exhibit significantly enhanced stabilisation properties (Popot *et al.*, 2011).

1.4.3 Amphipols as membrane protein stabilisers

Amphipathic polymers or 'amphipols' were introduced by Tribet *et al.* in 1996 as a novel tool for enhancing MP longevity in aqueous solutions. Amphipols are created from a polyacrylate backbone with repeating hydrophilic and hydrophobic side groups. Like detergents, they come in a variety of shapes and sizes depending on their intended use, and their nomenclature reflects their unit composition. The first amphipol, A8-35 is so-named after its composition, designated 'A' for anionic, '8' signifies the molecular weight, and '35' is the percentage of ungrafted carboxylates backbone moieties in each polymer (Tribet, Audebert and Popot, 1996). Its ability to solubilise membranes is attributed to the ~75-80 octyl chains spaced at a specified ~1 nm from each other along the polymer length (Tribet, Audebert and Popot, 1996). The side chain of A8-35 mimics the bilayer, where the carboxylate chains integrate within the hydrophobic domains of the transmembrane region and confer solubility (Popot *et al.*, 2011). Long chain amphipathic polymers were also tested for MP solubilisation, but the short-chain polymers were found to exhibit more detergent-like properties in solution (Tribet, Audebert and Popot, 1996).

Amphipols bind tightly with high affinity, forming a tight 1.5-2 nm annulus around the transmembrane domain (Tribet, Audebert and Popot, 1996). This comes with a 20-

fold reduction in bulk surrounding the lipid annulus compared to detergents (Gohon and Popot, 2003). A8-35 forms micellar-like aggregates of ~ 40 kDa in solution when its' concentration exceeds its' critical aggregation concentration (CAC – 0.002g/L for A8-35) (Zoonens *et al.*, 2007a). Normally, a ratio of 0.3 g of amphipol to 0.1 g of protein is quoted (3:1), but optimal ratios vary depending on sample (Popot *et al.*, 2011). Additionally, too much A8-35 can create a hydrophobic sink and can be detrimental, whereas too little can cause the protein to precipitate (Popot *et al.*, 2011). Some excess amphipols are required to maintain solubility of the membrane protein, but these are often in much lower abundance and interfere less than detergent micelles (Tribet, Audebert and Popot, 1997).

However, as with detergent solubilisation, stability of the amphipol:MP complex increases when amphipols are trapped in the presence of lipids (Tribet, Audebert and Popot, 1996). Additionally, the functional groups of the polymer that facilitate solubilisation also make A8-35 sensitive to calcium ions, pH below 7 and salt concentrations above 200-300 mM (Popot *et al.*, 2011). Other amphipols were created to combat these issues, with greater stability (Zoonens and Popot, 2014).

1.5 The Styrene-maleic acid (SMA) co-polymer

1.5.1 Introduction

As mentioned in section 1.3.1.2, several alternative reconstitution platforms have been developed to combat detergent-associated issues, but all require an initial detergent extraction step. As detergents can cause structural perturbations, dilapidation and inactivation of the membrane protein of interest (Seddon, Curnow and Booth, 2004;

Dörr *et al.*, 2014; Jamshad, Charlton, *et al.*, 2015; Reading, Walton, *et al.*, 2015; Gupta *et al.*, 2017), they may never truly be representative of the native membrane environment. To overcome some of the issues associated with membrane protein characterisation in detergent, the styrene maleic acid *co*-polymer (SMA) was developed as a unique solution for membrane protein extraction and solubilisation (Knowles, Finka, Smith, Y. P. Lin, *et al.*, 2009). They have since found broad applications in a number of 'omics' applications (Overduin and Esmaili, 2019), and medical diagnostics (Smith *et al.*, 2019).

Membrane active polymers were shown to dissociate lipid vesicles in the 1980's (Seki and Tirrell, 1984). Since then, they were adapted for use as lipid-carriers for cosmetics and pharmaceuticals (Tonge and Tighe, 2001; Tonge, 2006), before finding their application in membrane protein extraction and solubilisation in 2009 (Knowles et al., 2009).

The SMA *co*-polymer has since been futher characterised as a platform for the direct solubilisation of membrane proteins from their native membrane environment, while retaining their native lipid annulus (known as SMA lipid particles, or SMALPs; Figure 1.4) (Knowles et al., 2009; Jamshad, Grimard, et al., 2015; Scheidelaar, Martijn C Koorengevel, et al., 2015; Lee et al., 2016; Dörr et al., 2016). Once extracted, the SMALP:membrane protein complexes remain intact without extra addition of the SMA polymer throughout the purification process, and later during storage (Jamshad, Charlton, *et al.*, 2015).

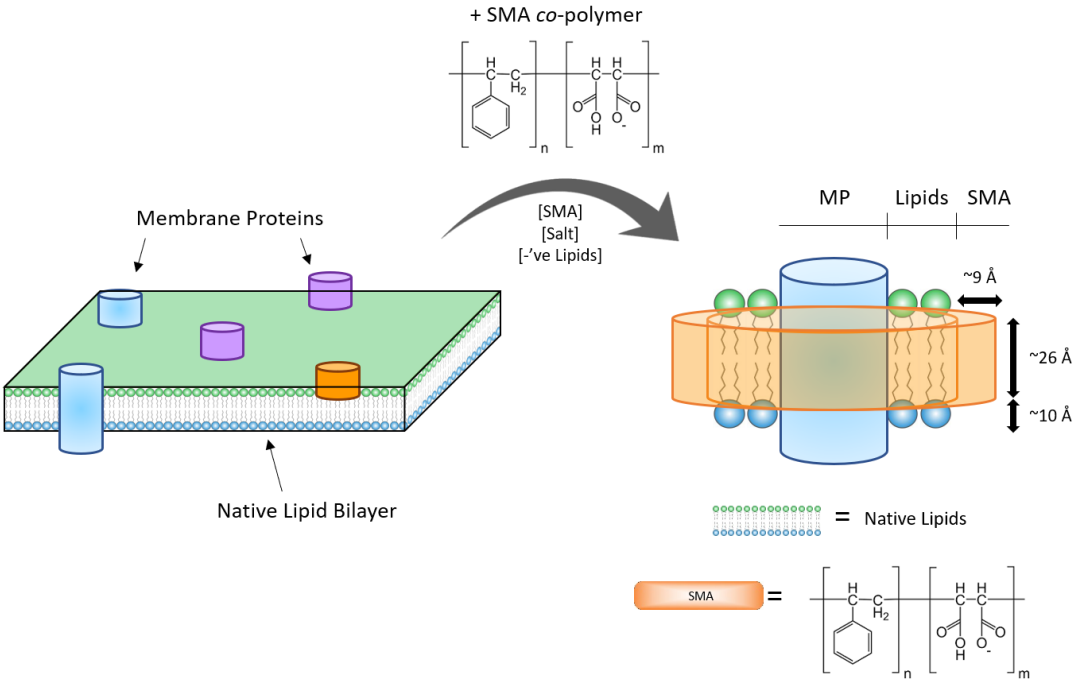

Figure 1.4: Membrane protein solubilisation by the styrene maleic acid (SMA) *co*-polymer.

Addition of the styrene maleic acid (SMA) *co*-polymer to native lipid bilayers facilitates extraction and stabilisation of membrane proteins. The membrane proteins are suspended in solution in SMA lipid particles (SMALPs), which comprise the membrane protein, its native lipid annulus, and the polymer (orange). The polymer spans the transmembrane region at a height of ~ 26 Å, and adds 9 Å of bulk to the complex (Knowles et al., 2009). There is a ~ 10 Å distance between the surface of the polymer and the top of the lipid heads demonstrating binding to the hydrophobic regions.

1.5.2 SMALP Structure and Properties

The anhydrous SMA precursor, SMAnh, is formed of repeating styrene and maleic anhydride units that can be polymerised in pre-defined ratios (most commonly 2:1 or 3:1 for membrane protein extraction) according to the percentage of monomers in the feed (Dörr *et al.*, 2016); although, this is not a precisely controlled process (Craig *et al.*, 2016). The SMA 2:1 *co*-polymers are quite heterogeneous, and have a polydispersity index of ~2.0-2.6 with an average molecular weight distribution between 7.5-10 kDa (Dörr *et al.*, 2016). The most widely reported styrene:maleic acid ratios are of 2:1 and 3:1 (Orwick-Rydmark *et al.*, 2012b; Swainsbury *et al.*, 2017). The 2:1 polymer appears to be more efficient at solubilising and stabilising membrane proteins, whereas 3:1 has been shown to remain on the surface of membranes and extract lipids in patches (Orekhov et al., 2019).

The 2:1 polymer's success in membrane protein characterisation is attributed to its inherent structural properties. The alternating styrene and maleic acid groups allow it to intercalate with the lipid acyl chains while protecting the hydrophobic core with external-facing hydrophilic maleic acid groups (Orwick *et al.*, 2012; Jamshad, Grimard, *et al.*, 2015). However, solubilisation efficiency is a function of solubilisation conditions, which require optimised salt concentrations, and a pH > 6.5 (Scheidelaar, Martijn C. Koorengevel, *et al.*, 2015). Additionally, the fluidity and packing of the bilayer can affect the efficiency of SMA to solubilise the protein (Dörr *et al.*, 2016). In the presence of lipids, SMA 2:1 *co*-polymers consistently form discs of ~10 nm in diameter (Knowles, Finka, Smith, Y. P. Lin, *et al.*, 2009; Jamshad, Grimard, *et al.*, 2015; Scheidelaar, Martijn C. Koorengevel, *et al.*, 2015), but can adapt to much larger

structures, such as the 36-transmembrane protein AcrB (Postis *et al.*, 2015b). They have also been demonstrated to exhibit no bias towards a certain lipid subset upon membrane protein extraction (Teo *et al.*, 2019).

SMALPs have since been utilised successfully with a number of biochemical and biophysical techniques for the characterisation of membrane proteins, including cryo-EM (Postis *et al.*, 2015b; Sun *et al.*, 2018), X-ray crystallography (Broecker, Eger and Ernst, 2017), circular dichroism (Knowles, Finka, Smith, Y.-P. Lin, *et al.*, 2009), SAXs (Brady, Qian and Bruce, 2019) and SANS, differential scanning calorimetry and nuclear magnetic resonance spectroscopy (Jamshad, Grimard, *et al.*, 2015). More recently, exciting advances in lipidomic assessment of isolated SMALP:membrane protein complexes have shown great promise for their membrane protein:lipid characterisation (Teo *et al.*, 2019).

However, the SMALP system is not without limitations, as they are particularly susceptible to changes in pH (<6.5), and the presence of divalent cations (> 5 mM) (Cuevas Arenas *et al.*, 2016)(Dörr *et al.*, 2016; Lee *et al.*, 2016; Fiori *et al.*, 2017). These properties limit their application in a number of downstream applications, for example, those which have particular constraints in buffer composition, functional assays and structural techniques including mass spectrometry and electron microscopy (Hernández and Robinson, 2007; Thompson et al., 2016). Derivatives of SMA and alternative co-polymers have been designed to overcome issues with sample heterogeneity (Domínguez Pardo et al., 2018), and susceptibility to pH and divalent cations (Oluwole et al., 2017; Fiori et al., 2017; Stephen C.L. Hall et al., 2018), but as of yet no one-size-fits-all solution has been established. TRP Channels

1.6 TRP Channels

1.6.1 TRP Channel Superfamily

Transient receptor potential (TRP) channels were discovered by Cosens and Manning (1969) from a mutant strain of *Drosophila melanogaster* which behaved as though temporarily blind in response to continuous light. When an electroretinogram was taken of a compound eye under conditions of continuous illumination, the mutant strain elicited a transient receptor potential response, dissimilar to the continuous response observed from wild-type flies. The source of this mutation was mapped to what became known as the *trp* locus the third chromosome of the Drosophila genome (Levy *et al.*, 1982), and later narrowed down to a single *trp* gene of this superfamily of cation channels (Montell *et al.*, 1985). Montell and Rubin (1989) went on to characterise the molecular nature of the gene, which they determined to encode an 8-transmembrane protein receptor with a characteristic C-terminal domain of an 9 x 8 amino-acid tandem repeats. They concluded that this channel was unlike the voltage-gated or ligand gated receptors previously described.

Work continued to characterise the photoceptor response in Drosophila, which led to the discovery of a second TRP channel, TRPL (Phillips, Bull and Kelly, 1992). Since then, three mammalian TRP channel family members were identified in quick succession: TRP (TRPC1; Wes et al., 1995), vanilloid receptor 1 (VR1) (Caterina *et al.*, 1997) and the melastatin receptor (melastatin) (Hunter *et al.*, 1998). These and other TRP channel homologues from a variety of organisms were described according to sequence homology of a core region comprising six transmembrane segments (Harteneck, Plant and Schultz, 2000). As the number of homologues grew, a unified

nomenclature system was introduced to appropriately categorise newly identified members into a TRP channel superfamily (Montell *et al.*, 2002a), rebranding the aforementioned mammalian TRPs to TRPC1, TRPV1 and TRPM1, respectively.

Further classification of TRP channels is performed according to sequence homology of their N- and C-terminal regions, with eight subfamilies defined to date: canonical (TRPC), vanilloid (TRPV), melastatin (TRPM), polycystin (TRPP), mucolipin (TRPML), ankyrin (TRPA), NOMPC (TRPN) and yeast (TRPY). TRPN and TRPY are often excluded from family trees, as they have not been identified in mammals (Montell, 2005; Venkatachalam and Montell, 2007). TRPY channels were the first insight into the evolutionary history of TRP channels, which predate the emergence of metazoans; but another ancient *trp* homologue was recently identified in the unicellular protist dinoflagellate *Lingulodinium polyedra*, giving further insight into the evolutionary role of TRP channels and somatosensory transducers (Lindström, Pierce and Latz, 2017).

1.6.2 Mammalian TRPs

In mammals, the remaining six TRP channel subfamilies are found to take up significant roles in cation signalling (Minke and Cook, 2002; Montell, 2005; Minke, 2006; Venkatachalam and Montell, 2007). Most TRP channels are non-selective cation channels, but a few exhibit exclusive and high selectivity for magnesium and sodium ions (Owsianik *et al.*, 2006). Their involvement in number of seemingly disparate signalling mechanisms have also made them extremely interesting to study biologically, and their roles in pathophysiological diseases such as diabetes,

tumorigenesis and neurodegeneration have made them attractive drug targets (Montell, 2001; Jiang, Gamper and Beech, 2011; Nilius and Szallasi, 2014).

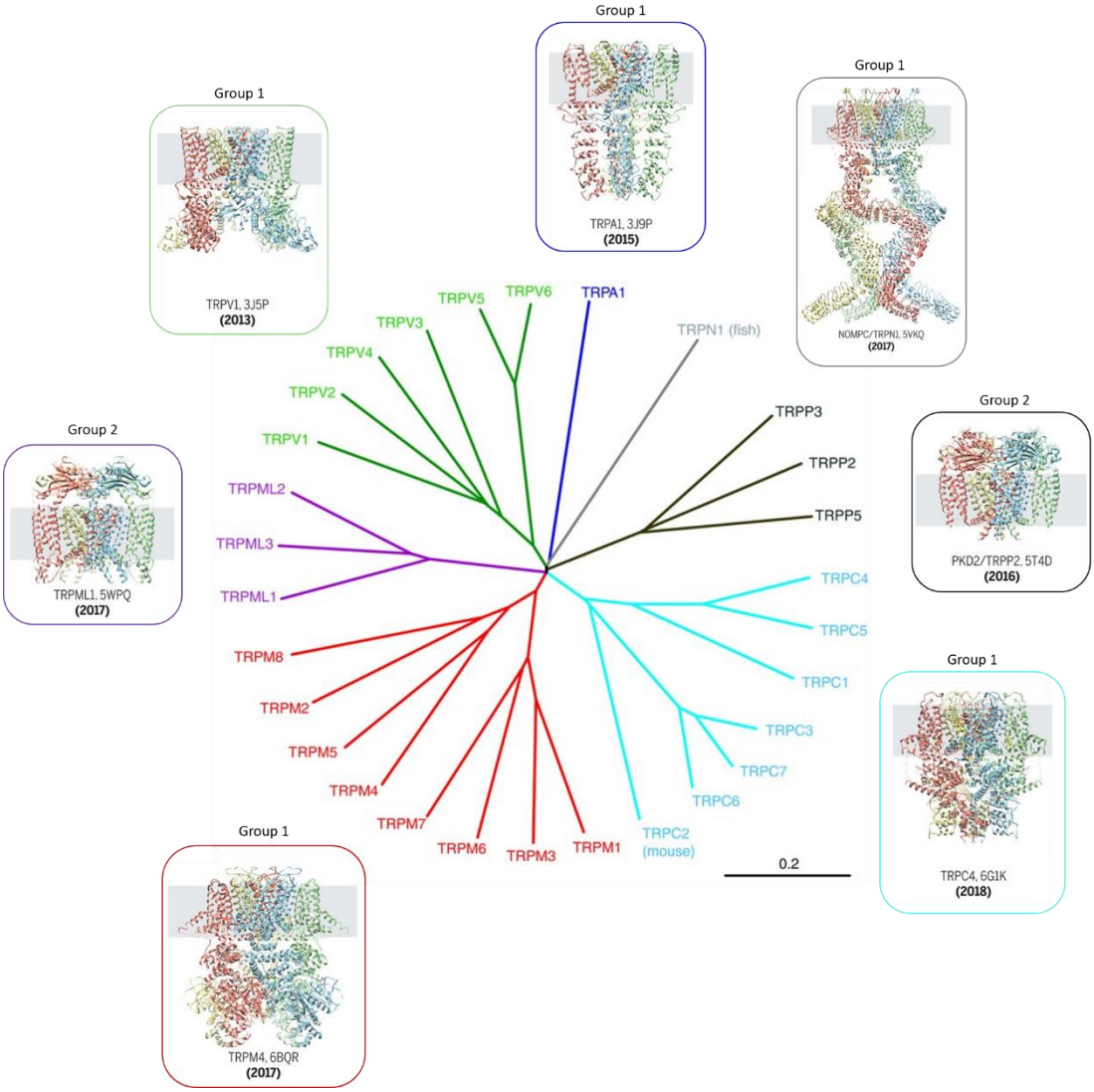

Figure 1.5: Phylogenetic tree showing distance between each TRP channel family member from within its own clade and adjacent clades, alongside representative structures of each subfamily.

The mammalian TRPs can be separated into 7 subfamilies according to sequence homology, two groups based on topology and subcellular localisation. Group 1 comprises the TRP channels with ankyrin-repeat domains, and group 2 comprises

TRPP and TRPML, which have large loop insertions between transmembrane segments 1 and 2. Group 1 TRPs are predominantly localised to the plasma membrane and mediate signals from extracellular ligands, whereas TRPP and TRPML are localised to lysosomes and sub-cellular organelles. High resolution cryo-EM structures have been solved of at least one member from every family, highlighting the structural differences between clades. Scale bar represents 0.2 substitutions. Figure adapted and modified from Nilius and Owsianik, 2011 and Cheng, 2018.

1.6.3 Overview of TRPM Subfamily

Of the identified TRP channel subfamilies to date, TRPM channels exhibit low sequence homology to one another and make up the some of the largest and most diverse of them all (Fleig and Penner, 2004a). TRPM channels were initially grouped by the length of the translated protein as 'long-TRPCs' and by their homologous N-terminal region ('TRPM homology region'; MHR), which was predicted to have no ankyrin repeat domains, unlike all other TRP channel family members identified at the time (Harteneck, Plant and Schultz, 2000). TRPM C-terminal domains (CTDs) also vary considerably, and overall sequence homology between members further divides them into four sub-groups: TRPM1/3, TRPM4 /5, TRPM6/7, and TRPM2/8 (Venkatachalam and Montell, 2007). However, while TRPM2 and TRPM8 are grouped according to their sequence similarity, it's more a lack of similarity to the other family members that defines them into this group, as they differ considerably between each other in their structure, ion selectivity and activation mechanisms (Kühn *et al.*, 2010).

The recent technological advances in direct-electron detectors and image processing software for cryo-EM has led to astonishing advances in the TRP channel field. Prior to this, TRP channels evaded structural characterisation due to their low-level expression, instability outside of their native bilayer, and inaccessibility to high resolution structural techniques such as X-ray crystallography and NMR due to their dynamic flexibility.

Since 2018, four different TRPM family member structures have been solved: TRPM2, TRPM4, TRPM7 and TRPM8. Of these, only TRPM2 and TRPM4 are of human origin (Winkler *et al.*, 2017; Wang *et al.*, 2018; Z. Zhang *et al.*, 2018a), but all structures give individual insights into the overall mechanisms of the TRPM family. Each channel is seen to form a three or four-tiered structure, where the core three tiers are made up of the homologous transmembrane domain, MHR 1/2 and MHR 3/4 (see Figure 1.7). For TRPM1/2/3/6/7, a fourth-tier accounts for their unique C-terminal domains

1.7 hsTRPM2

1.7.1 hsTRPM2 Physiology

TRPM2, previously known as KPN3, TRPC7 and LTRPC2 (Nagamine *et al.*, 1998; Harteneck, Plant and Schultz, 2000), was first cloned for an exon trapping experiment which aimed to identify novel genes associated with autoimmune polyglandular disease type I (Kudoh *et al.*, 1997). The gene responsible for this disorder was later identified as *AIRE* (Nagamine *et al.*, 1997), but during their search, the authors identified a 6.5 kbp transcript highly expressed in the human brain, which showed significant sequence homology with calcium channels in *Caenorhabditis elegans*, as

well as the *Drosophila* and human TRP proteins (Nagamine *et al.*, 1998). The authors went on to describe its expression in various human tissues, and this information coupled with recent transcriptomics and proteomics data found it to be highly expressed in the brain, bone marrow, endothelium, lymphatic and endocrine tissues (Nagamine *et al.*, 1998; Uhlén *et al.*, 2015). Nagamine et al. then went on to characterise the transcript of this gene as a 7-pass transmembrane protein, later recharacterized as the 6-pass transmembrane protein TRPM2, as part of the novel TRP channel superfamily (Nagamine *et al.*, 1998; Harteneck, Plant and Schultz, 2000).

TRPM2 is a non-selective cation channel (PCa/PNa = ~0.5-5) (Owsianik *et al.*, 2006), of 1503 amino acids (~171 kDa) (Nagamine *et al.*, 1998). Until recently, its structure was unknown (later described), and its domain topology was described as that of other TRPM channels – comprising a TRPM homology region (MHR), a core six-segment transmembrane domain (S1-S6), and the C-terminal domain appended with a putative NUDIX pyrophosphatase, NUDT9H (Perraud *et al.*, 2001). TRPM2 has since been linked to several pathophysiological processes, such as oxidative stress, neurodegeneration, ischemia reperfusion injury, apoptosis, cancer, immunity and diabetes (Massullo *et al.*, 2006; Cheung and Miller, 2017; Li *et al.*, 2017; Belrose and Jackson, 2018; Hantute-Ghesquier *et al.*, 2018). In addition to its role in disease, it has also been identified as a key regulator non-noxious temperature sensation at ~37 °C (summarised in Voets, 2016). Its physiological role is broadly a result of its activation and modulation by three signalling pathways: through reactive oxygen species (ROS), calcium signalling and/or adenosine diphosphate ribose (ADPR; Figure 1.6). However, a large variety of intra- and extracellular events can result in a Ca^{2+} influx, so this signalling pathway will not be discussed in detail.

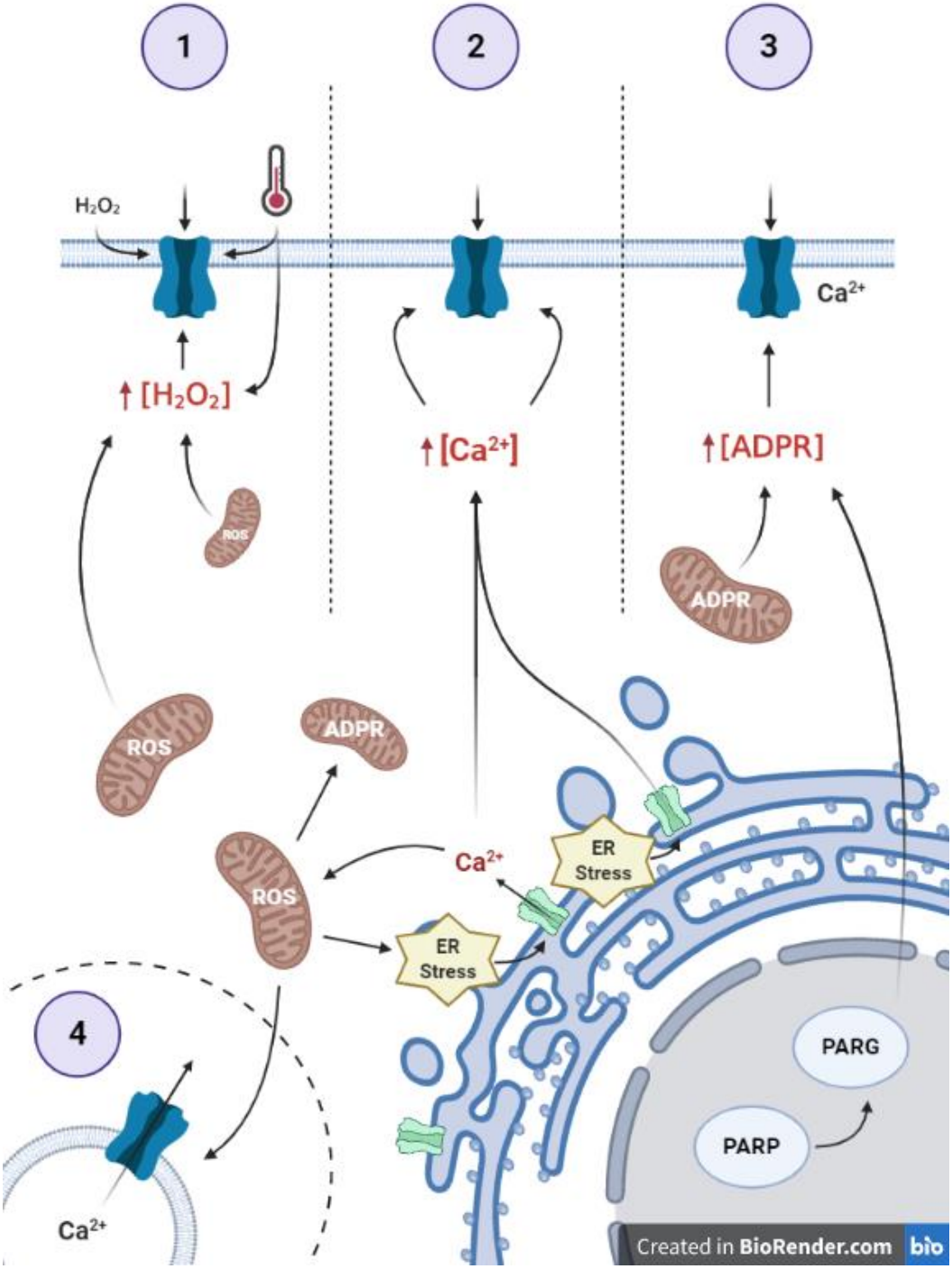

Figure 1.6: Overview of TRPM2 activation and signalling mechanism within a single cell.

Intracellular signalling mechanisms that govern TRPM2 activation can be split into 4 broad mechanisms. 1 = activation by increased H_2O_2 or reactive oxygen species (ROS) as a result of oxidative stress. ROS can be released from mitochondria as a result of increased intracellular

calcium concentrations, which can also come from ER-mediated stress responses. TRPM2 is also activated by temperature, but this can potentially be interlinked with ROS activation. 2 = Raised intracellular calcium concentrations can activate TRPM2 via a number of pathways, and this is the broadest signalling pathway influenced by many factors. 3 = TRPM2 activation by adenosine diphosphate ribose (ADPR) when already bound by Ca^{2+}. ADPR can be released as a result of cell stress by the PARP-PARG pathway (Buelow, Song and Scharenberg, 2008), or released from mitochondria under conditions of calcium stress (Perraud *et al.*, 2005). These mechanisms work in concert to activate and regulate TRPM2 channel function and gating. There is a fourth mechanism by where TRPM2 sequestered in lysozymes may play a role in release of this calcium store, but this is not discussed here. Figure created at BioRender.com.

1.7.1.1 Activation by cADPR/ADPR

ADPR is considered a primary regulator of TRPM2 activity, and binds to TRPM2 with reportedly variable EC_{50} values of 1-90 μM (Sumoza-Toledo and Penner, 2011). In the cell, ADPR can be released from mitochondria under conditions of cell stress, or as product of nicotinamide adenine dinucleotide (NAD^+) hydrolysis, such as via the poly-ADPR polymerase (PARP) – polyADPR glycohydrolase (PARG) pathway (Perraud *et al.*, 2005). Many studies have attempted to discern the mechanism of ADPR action on TRPM2, but the ways in which ADPR influence channel activity is somewhat in dispute.

It was initially presumed that ADPR would bind the NUDT9H domain to facilitate channel gating (Perraud *et al.*, 2001). The ADPR binding pocket in NUDT9H domain was characterised further using structural homologues and chimeras of isolated NUDT9H (Shen *et al.*, 2003), but later experiments demonstrated that the this NUDIX

domain was not an active enzyme in humans and could be removed without channel inactivation in orthologues (Iordanov *et al.*, 2016a).

Irrespective of how ADPR binds to the channel, there is strong evidence that ADPR activation is reliant on cooperative binding of Ca^{2+} ions in the transmembrane domain; as without Ca^{2+} binding, TRPM2 is inactive (McHugh *et al.*, 2003a; Heiner *et al.*, 2006). There is also evidence that TRPM2 can be activated in response to elevated cADPR (Kolisek *et al.*, 2005; Togashi *et al.*, 2006). However, in the absence of a structure, the mechanism of activation by ADPR or cADPR was unknown.

1.7.1.2 Activation by Reactive Oxygen Species and Temperature

Superoxide ($O_2^{\cdot-}$), hydroxyl radicals ($OH^{\cdot-}$) and hydrogen peroxide (H_2O_2) – collectively known as reactive oxygen species (ROS) – are natural metabolites of mitochondria respiration, nicotinamide adenine dinucleotide phosphate (NADPH) oxidation and protein folding (Finkel and Holbrook, 2000). These, along with reactive nitrogen species such as nitric oxide ($NO^{\cdot}$), play important roles in intra- and extra-cellular signalling, cell proliferation, migration, differentiation, protection and apoptosis (Zhu and Javid, 2015). However, excessive production or mis-regulation of ROS concentration results in 'oxidative stress', which is a predominant feature in numerous disease pathologies, including cancer, aging, autoimmunity, neurodegeneration and diabetes (Finkel and Holbrook, 2000).

TRPM2 can be both directly and indirectly activated by exogenous or endogenous ROS, specifically H_2O_2 (Hara *et al.*, 2002; Wehage *et al.*, 2002). Wehage et al. tested TRPM2 activation as a result of elevated H_2O_2 on wild-type TRPM2 versus a C-terminal splice variant ADPR binding – lacking residues 1292-1325 in the NUDT9H

domain; they reported that in the absence of the C-terminal region the channel could still be activated by H_2O_2, but not ADPR. Hara et al. identified a 'MutT' nucleotide binding sequence - later described as the NUDT9H domain (Perraud *et al.*, 2001) - and found that mutating residue methionine 1397 with isoleucine (M1397I), channel activity was slightly reduced (Hara *et al.*, 2002).

Hara and colleagues also reported a novel arachidonic acid (AA) response sequence in the N-terminal domain between residues 307-316, which when mutated, completely abrogated channel responses to H_2O_2 and AA (Hara *et al.*, 2002). This was followed by another study that identified M214 in the N-terminal domain as critical for TRPM2 activation by H_2O_2, and was also directly involved in TRPM2 channel sensitisation to temperature in pancreatic islet cells, altering function in insulin secretion (Kashio *et al.*, 2012).

1.7.1.3 Temperature Activation

TRPM2 is activated in response to non-noxious heat (>35 °C) and is part of the ThermoTRP group of the TRP channel family members. Heat sensitivity was first reported as part of an insulin secretion pathway, whereby Ca^{2+} currents in response to heat stimulation were abolished with TRPM2-specific siRNA (Togashi *et al.*, 2006). It was later found to play a role in macrophage redox signalling, leading to cytokine release and fever-enhanced phagocytic activity (Kashio *et al.*, 2012). In 2016, TRPM2 was identified *in vivo* as the primary driver of hypothalamic non-noxious heat sensation in mouse models (Song, Wang, Gretel B Kamm, *et al.*, 2016; Tan and McNaughton, 2016). Whether temperature sensitivity is an inherent property of the channel or if it is mediated via a ROS-dependent pathway remains to be shown.

Over the years, conflicting results from biochemical and physiological studies have raised many questions regarding the mechanism of TRPM2. In the absence of any TRPM2 or TRPM family structure, these have been even more difficult to discern. An example of this is the domain topology and fold of the MHR domain. While common to all TRPM family members and implicated in a number of TRPM2 activation mechanisms, its domain topology and mode of action is unclear. Recently, several structures of TRPM2 have been published at high resolution, providing some long-awaited answers to these questions.

1.7.1.4 Other activators and inhibitors

In addition to direct binding of calcium, a calmodulin-binding IQ-motif was identified between N-terminal residues 404-416 and found to add another level of calcium-mediated regulation to channel function (Tong *et al.*, 2006). The native membrane lipid PIP_2 has also been shown to have a direct role in channel gating, and patch-clamp experiments have suggested that there is a high-affinity PIP_2 binding site in the voltage-sensor-like domain (VSLD) of TRPM2 that upon binding, creates a non-inactivating channel (Tóth and Csanády, 2012). 8-Br-cADPR is a non-specific inhibitor of cADPR-mediated calcium signalling, and has also been shown to directly antagonise TRPM2 activity (Kolisek *et al.*, 2005).

1.7.2 TRPM2 Structure and Function

1.7.2.1 Overall Architecture

TRPM2 follows a similar domain topology to other TRPM channels. The N-terminal domain comprises four MHRs and a calmodulin binding site (Tong *et al.*, 2006), and the C-terminal domain contains the evolutionary conserved TRP-box, a coiled-coil domain and a nudix type-motif 9 (NUDT9) homology domain (NUDT9H) (Perraud *et al.*, 2001; Hara *et al.*, 2002). Each of these C-terminal domains contributes to a specific role in channel function. The C-terminal coiled-coil is involved in homotetramerization of the channel, the TRP box is implicated in channel regulation gating near the pore, and the NUDT9H domain binds ADP-ribose (ADPR). Initially, TRPM2 was thought to hydrolyse ADPR in a similar fashion to its' soluble mitochondrial equivalent, NUDT9 (Perraud *et al.*, 2001, 2003), but this was later disproven, and instead the NUDT9H domain was re-branded as an ADPR sensor (Iordanov *et al.*, 2016a). The domain boundaries of NUDT9H and transmembrane domains in the primary sequence is consistent, but segmentation of the N-terminal MHR into more defined regions varies between family members.

The first insights into the full length TRPM2 structure, or any TRPM family member, came from a 2.8 nm negative stain reconstruction of TRPM2. This provided the first insight into domain organisation/topology within the structure, and revealed an overall bell or umbrella shaped architecture of dimensions ~170 Å in width by ~250 Å in height (Maruyama *et al.*, 2007). The first TRP structure published, TRPV, was of 100 Å by 100 Å (Cao *et al.*, 2013), demonstrating the increased volume of TRPM2 from the extensive intracellular domains versus the smaller TRPV channels. Prior to this,

high resolution crystal structures of the TRPM7 C-terminal coiled-coil domain (Fujiwara and Minor, 2008), and the mitochondrial NUDT9 (Shen *et al.*, 2003) were available, and their location within the density could be broadly suggested.

Since then, several high-resolution structures have been solved from *Nematostella vectensis* (*nv*), *Danio rerio* (*dr*) and *Homo sapiens* (*hs*) TRPM2 channels in apo- and ligand-bound conformations (Huang *et al.*, 2018, 2019; Wang *et al.*, 2018; Z. Zhang *et al.*, 2018a; Yin, Wu, *et al.*, 2019), summarised in Table 1. The domain organisation within the overall sequence and structure became more refined (Figure 1.7A), designating a three-segmented N-terminal MHR instead of the previously assumed four-segment MHR (Figure 1.7A and 1.7B). All structures revealed an overall three-tiered architecture as with previously published TRPM channels, that can be split into a four-tiers according to each topological domain (Figure 1.8B).

Between them, three ligand binding sites were identified; A Ca^{2+} binding in the S1-4 VSLD above the TRP helix (Figure 1.7C), an ADPR/8-Br-cADPR binding site in MHR1/2 (Figure 1.7D), and a second ADPR binding site in the NUDT9H domain (Figure 1.7E).

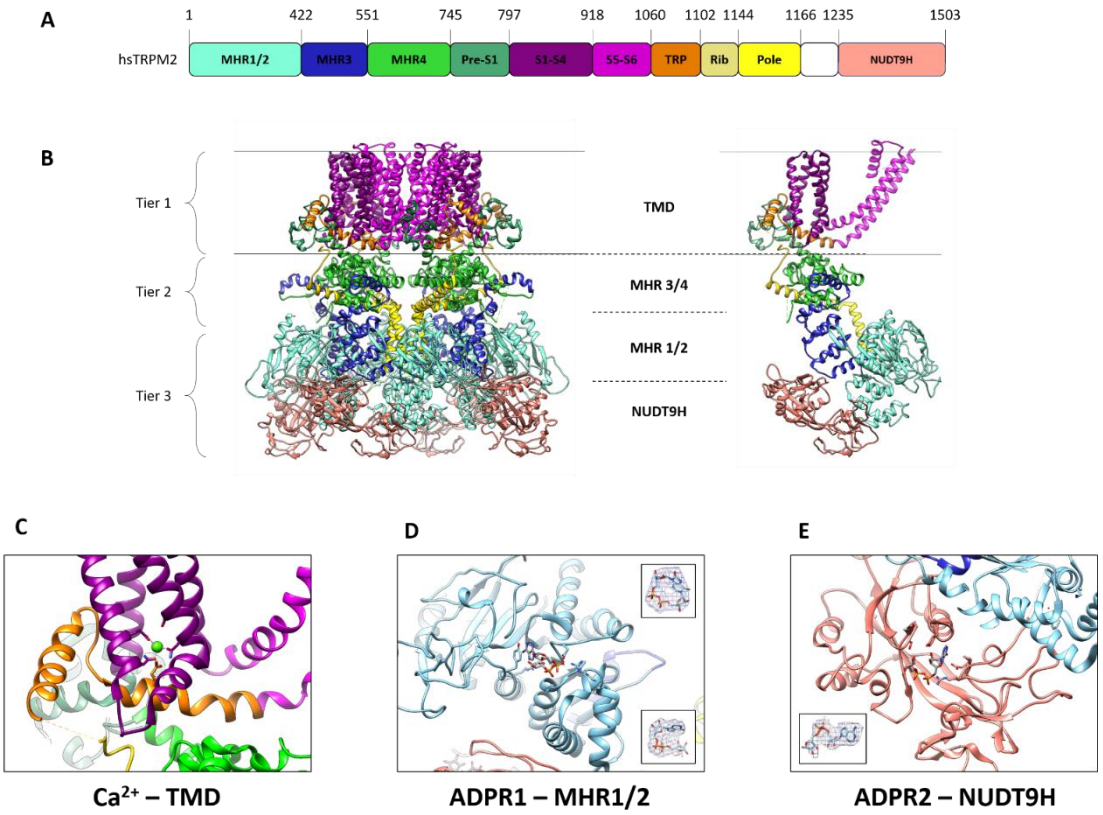

Figure 1.7: Overall architecture and structure of TRPM2.

A) Domain organisation of *hs*TRPM2 primary sequence. B) The apo structure of hsTRPM2 in its tetrameric and monomeric assembly as published by Huang et al. 2019 (PDB ID: 6PUO), coloured according to domain assignments in A. TRPM2 shows a three-tiered organisation, that can be further segregated by topological domains: the transmembrane domain (TMD), TRPM homology regions (MHR) 3/4, MHR1/2 and the NUDT9H domain. C) Close up of the calcium binding site in the VSLD coordinated between S1-S4 and the TRP helix. Residues involved in Ca^{2+} binding are shown as sticks. D) The first ADPR binding site (ADPR1) in the MHR1/2 domain. Electron density for 8-Br-cADPR (PDB ID: 6PUU; upper box) and U-shaped ADPR (PDB ID: 6PUR, lower box) shown, adapted from Huang et al. 2019. E) The second ADPR (ADPR2) binding site in the NUDT9H domain. The electron density for the

elongated ADPR ligand is shown in the lower box (PDB ID: 6PUR), adapted from Huang et al. 2019.

Table 1: Cryo-EM structures of TRPM2 and their associated ligands.

Species	Ligand	Functional State	Resolution (Å)	Reference
Nematostella vectensis	Ca^{2+}	Closed	3.0	Zhang et al., 2018
Danio rerio	Apo	Closed	3.8	Huang et al., 2018
	ADPR/Ca^{2+}	Open	3.3	
	Apo, C4	Closed	4.3	Yin et al., 2019
	Apo, C2	Closed	4.5	
	Ca^{2+}	Closed	3.8	
	ADPR/Ca^{2+}	Intermediate	4.2	
Homo sapiens	Apo	Closed	3.6	Wang et al., 2018
	ADPR	Closed	6.1	
	ADPR/Ca^{2+}	Closed	6.4	
	Apo	Closed	3.3.	Huang et al., 2019
	ADPR	Closed	4.4	
	ADPR/Ca^{2+}	Pre-open/ Closed	3.7	
	8-BR-cADPR/ Ca^{2+}	Closed	3.7	

1.7.2.2 Ligand Binding and Activation Mechanism

Each apo structure of TRPM2, with the exception of *nv*TRPM2 by Zhang et al., 2018, was published alongside a ligand-bound form for direct comparison. Despite a lack of comparison structure, *nv*TRPM2 was able to reveal clear density for both Ca^{2+} and surprisingly, an adjacent phospholipid binding site within the VSLD of S1-S4. The phospholipid was mapped as phosphatidic acid (PA) in the structure, but it is suggested that this is the binding site of PIP_2. This binding site was also later mapped in the

structure of *Ficedula albicollis* TRPM8, and caused structural rearrangements in the VSLD to convey activity (Yin, Le, *et al.*, 2019).

Zhang et al. (2018) also explored the functional role of mutations in the pore domain, revealing that mutation of essential pore-forming residues 984-986 (GY-) in *hs*TRPM2 to 1040-1043 (LDE) found in *nv*TRPM2, *hs*TRPM2 currents were continuously activated in response to ADPR and Ca^{2+}, whereas in native *hs*TRPM2 they immediately decline. While the NUDT9H domain of *nv*TRPM2 is missing in the density, it is required for *nv*TRPM2 activation. In contrast, the NUDT9H domain of *hs*TRPM2 is inactive. A later study suggested that the channel pore and NUDT9H domain of TRPM2 may have simultaneously mutated during the evolution of vertebrates, uncoupling NUDT9H activity from channel activity, as an explanation for this disparity in function (Iordanov *et al.*, 2019).

The remainder of this introduction will draw on conclusions made from the remaining TRPM2 structures and how this relates to activation and channel gating.

Calcium ions were found to bind within the VSLD S1-S4 region in all structures containing Ca^{2+}, causing rearrangements of the S3 domain and TRP helix. This binding site is conserved within the TRPM channel family, and for TRPM2, the channel remains closed without it (McHugh *et al.*, 2003b; Csanady and Torocsik, 2009). This puts the structure in a primed state, where it can be fully activated when co-operatively bound by ADPR.

The most surprising discovery was the existence of two ADPR binding sites – one in the MHR1/2, and one in the NUDT9H domain. Binding of ADPR to the NUDT9H domain was expected and has been linked to channel function. However, a few studies

removal of the NUDT9H domain in *nv*TRPM2 still induced activation currents (Kühn, Kühn and Lückhoff, 2017). A recent study has also concluded that *hs*TRPM2 is able to bind ADPR and cADPR in the absence of the NUTD9H domain, indicating that the MHR1/2 is a primary recognition site for ADPR by TRPM2 (Yu *et al.*, 2019). This is further evidenced from the structure, which shows that ADPR and 8-Br-cADPR can bind in the same cleft in a U-shape conformation in MHR 1/2 (Huang *et al.*, 2019). While other structures by Wang et al (2018) claim that TRPM2 is bound to ADPR in their ADPR-condition structure, there is no evidence for this in the cryo-EM density maps.

The structures together suggest an overall cooperative gating mechanism by Ca^{2+} and ADPR, and the sequence can be described by a 'twisting and lifting' mechanism as described in figure 1.8. However, all TRPM2 structures are missing the crucial linker region between the pole helix and NUDT9H domain, which likely have a significant role in channel function. Additionally, activation by ROS has not been covered in any of the suggested mechanisms. For ROS activation, mapping the crucial M214 residue in the structure reveals its position adjacent to the ADPR binding domain in MHR1/2. It would therefore perhaps not be surprising that ROS modification of this residue interferes with ADPR activation but may disrupt domain interactions between its own and adjacent NUDT9H and MHR1/2 regions.

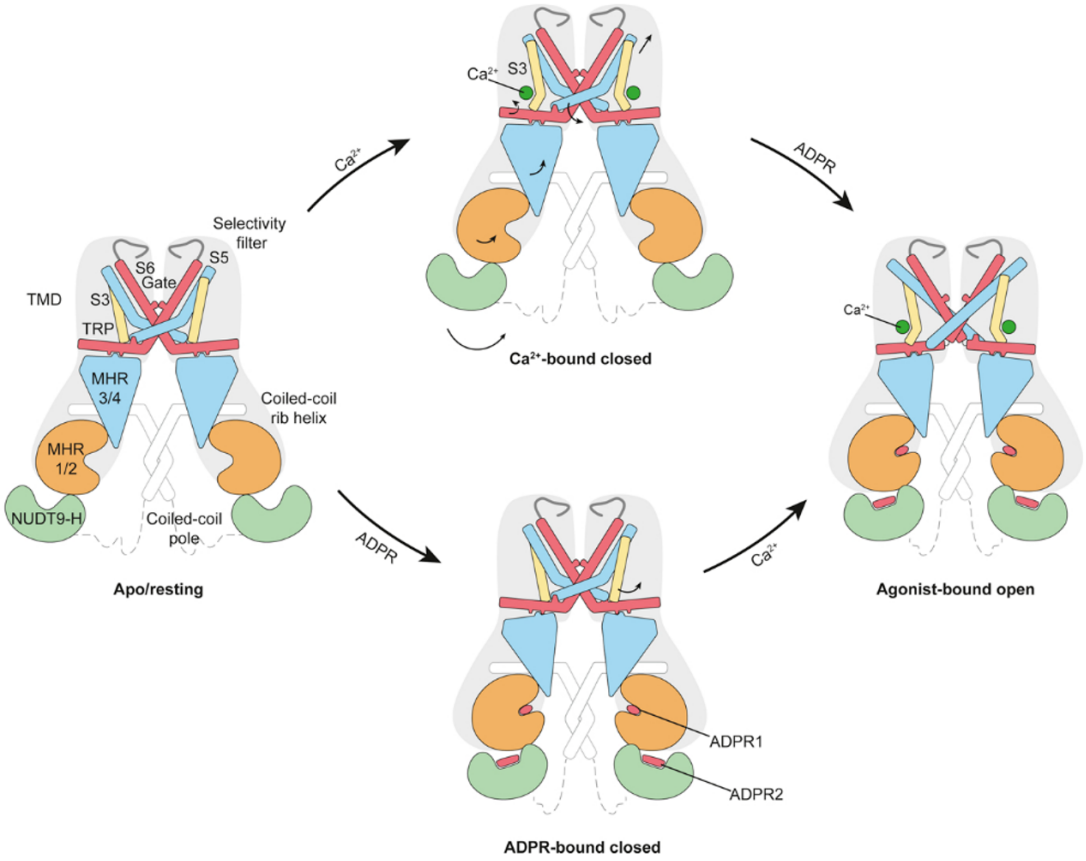

Figure 1.8: Mechanism of TRPM2 activation by Ca^{2+} and ADPR.

Ca^{2+} binds independently in the VSLD between S1-S4, directly inducing small motions primarily between the S3 and TRP helix, to free space around the S4-S5 linker for further activation by ADPR. Binding by ADPR to the MHR1/2 and NUDT9H domains brings the lower cytosolic domains together, causing the rearrangement of the central pole helix and S3. When Ca^{2+} is bound, these structural rearrangements in the cytosolic domain propagate up to the TMD, allowing the S4-S5 linker region to unfold and 'flip' to the other side of the TRP helix in the free space created from Ca^{2+} binding, which then tilts S6 outwards to facilitate channel opening. Figure adopted from Huang et al., 2020.

1.8 Aims and Objectives

The overall aim of this project is to understand the molecular mechanisms behind TRPM2's ability to sense and respond to a range of stimuli, focusing predominantly on the effects of the native lipid bilayer and transmembrane annulus. To achieve this, robust solubilisation extraction and purification procedures will be established, and the purified TRPM2 channel will be used for subsequent biochemical, biophysical and structural characterisation. Circular dichroism, negative stain and single particle cryo-electron microscopy (cryo-EM) will be the primary techniques used to characterise the purified TRPM2 complex, with the aim of elucidating a potential structure-function relationship. Stability and homogeneity of the complex will be important for success in cryo-EM, and steps will be taken to determine optimal stabilising conditions for the solubilised protein, and to reduce the conformational flexibility of the tetramer with the addition of ligands and co-factors.

The influence of the lipid environment surrounding the TRPM2 transmembrane domain upon extraction in different scaffolds will also be explored using a combination of thermostability assays, circular dichroism and thin layer chromatography for lipidomic analysis. Together, biochemical and biophysical characterisation of the isolated protein product gave significant and novel insights into the mechanism of TRPM2 *in vitro* and *in vivo*.

In addition, the relationship of different solubilisation scaffolds, namely detergents and amphipathic polymers, and their influence on the membrane protein structure and analysis will be explored, ultimately generating a novel method of scaffold exchange that can be applied to a variety of membrane proteins in the future.

Chapter 2:

Materials and Methods

2.1 Materials

2.1.1 Purification Buffers

Buffers used during TRPM2 purifications are described in table 2.1, and buffers used for AcrB purifications are in 2.2. All reagents were dissolved in distilled H_2O before being filter sterilised to 0.22 µM. Buffers used in size exclusion chromatography were thoroughly degassed beforehand.

2.1.1.1 AcrB Purification

Table 2.1: Buffers used in AcrB purification in SMA and DDM.

Solubilisation Agent	**Buffer**	**Composition**
Styrene-Maleic Acid (SMA)	Binding Buffer (BB)	500 mM NaCl, 50 mM Tris.HCl, 10 % w/v Glycerol, pH 8.0
	Elution Buffer (EB)	500 mM NaCl, 20 mM Tris.HCl, pH 8.0
Dodecyl-β-D-Maltoside (DDM)	DDM Binding Buffer (DBB)	1% DDM, 10 % w/v Glycerol, 150 mM NaCl, 20 mM Tris.HCl, pH 8.0
	DDM Elution Buffer (DEB)	0.025 % DDM, 300 mM NaCl, 20 mM Tris.HCl, pH 8.0

2.1.1.2 TRPM2 Purification

Table 2.2: Buffers used for TRPM2 purifications in SMA, DDM and LMNG.

Solubilisation Agent	**Buffer**	**Composition**
Styrene-Maleic Acid (SMA)	Binding Buffer (BB)	150 mM NaCl, 20 mM Tris.HCl, 10 % w/v Glycerol, pH 7.5
	Elution Buffer (EB)	300 mM NaCl, 20 mM Tris.HCl, pH 7.5

	CD Binding Buffer (CDBB)	10 % w/v Glycerol, 200 mM NaF, 20 mM NaP, pH 7.5
	CD Elution Buffer (CDEB)	200 mM NaF, 20 mM NaP, pH 7.5
Dodecyl-ß-D-Maltoside (DDM)	DDM Binding Buffer (DBB)	1% DDM, 10 % w/v Glycerol, 150 mM NaCl, 20 mM Tris.HCl, pH 7.5
	DDM Elution Buffer (DEB)	0.025 % DDM, 300 mM NaCl, 20 mM Tris.HCl, pH 7.5
	DDM CD Binding Buffer (DCDBB)	10 % Glycerol, 200 mM NaF, 20 mM NaP, pH 7.5
	DDM CD Elution Buffer (DCDEB)	200 mM NaF, 20 mM NaP, pH 7.5
DDM + Cholesterol Hemisuccinate (DDM:CHS)	DDM:CHS Binding Buffer (DDM:CHSBB)	1 % DDM, 0.2 % CHS, 10 % Glycerol, 150 mM NaCl, 20 mM Tris.HCl, pH 7.5
	DDM:CHS Elution Buffer (DDM:CHSEB)	0.025 % DDM, 0.005 % CHS, 300 mM NaCl, 20 mM Tris.HCl, pH 7.5
Lauryl Maltose Neopentyl Glycol (LMNG) + CHS	LMNG Binding Buffer (LBB)	0.2 % CHS, 10 % Glycerol, 150 mM NaCl, 20 mM Tris.HCl, pH 7.5
	LMNG Elution Buffer (LEB)	0.005 % CHS, 300 mM NaCl, 20 mM Tris.HCl, pH 7.5

2.1.2 Bacterial Culture

2.1.2.1 Culture Media

All media was made up to the required volume with distilled H_2O and autoclaved for sterilisation before use.

Table 2.3: Composition of medias used for bacterial cultures.

Broth Type	**Tryptone (%)**	**Yeast Extract (%)**	**NaCl (%)**	**pH (+NaOH)**
Lysogeny Broth (LB)	1.0	0.5	1.0	7.4
Super Broth (SB)	3.2	2.0	1.0*	7.4

**NaCl was omitted for auto-induction media.*

2.1.2.2 LB Agar

1.0 % Tryptone, 0.5 % Yeast Extract, 1.0 % NaCl, 1.5 % Agar, made up to volume with H_20 and adjusted to pH 7.0 with 1 M NaOH, before autoclaving for sterilisation.

2.1.2.3 Bacterial Antibiotics

All antibiotics were made up at stock concentrations shown in table 2.4 and stored at -20 °C. When required, stocked were diluted 1000X into the appropriate medium.

Table 2.4: Antibiotic stocks for bacterial culture.

Antibiotic	**Stock Concentration (mg/ml)**	**Solvent**
Carbenicillin	100	H_2O
Chloramphenicol	30	C_2H_5OH
Kanamycin	50	H_2O

2.1.2.4 Auto-induction supplement stocks.

Stocks were made up as described in Table X and were either filter sterilised at 0.22 μM ($MgSO_4$ and 5,052) or autoclaved (Nitrogen, Sulphur and Phosphorous Solution: NSPC) before use.

Table 2.5: Auto-induction stock concentrations for bacterial culture.

Additive	**Stock Components**	**Stock Concentration**	**Working Concentration**
1 M $MgSO_4$	$MgSO_4$	1 M	1 mM
5,052	Glycerol	25 % (w/v)	0.5 %
	Glucose	2.5 % (w/v)	0.05 %

	α-Lactose monohydrate	10 % (w/v)	0.2 %
NSPC	Na_2HPO_4	0.5 M	50 mM
	KH_2PO_4	0.5 M	50 mM
	Na_2SO_4	0.1 M	5 mM
	NH_4Cl	1 M	25 mM

2.1.3 Mammalian Culture

2.1.3.1 Complete Media

All products were purchased from ThermoFisher Scientific, UK, unless otherwise specified. Complete media is defined as Dulbecco's Modified Eagle Medium (DMEM) + GlutaMAXTM-1, [+] 4.5 g/L D-Glucose, [+] 110 mg/L sodium pyruvate (Product ID: 31966201), supplemented in-house with 10 % gold standard foetal bovine serum (Sigma-Aldrich, UK ca. 2016-2018, PAA, UK ca. 2018-2019), 100 units/ml Penicillin and 100 μg/ml Streptomycin (Product ID: 15140122).

2.1.3.2 TC Phosphate Buffered Saline (DPBS)

Magnesium and Calcium-free Dulbecco's PBS (DPBS) was purchased from Sigma-Aldrich, UK (Product ID: D8537).

2.1.3.3 Trypsin

Gibco® 0.05 % Trypsin-EDTA was purchased from ThermoFisher Scientific, UK.

2.1.3.4 Plasticware

Nunc plasticware cannot be used with the HEK293-TRPM2tet cell line.

2.2 Methods

2.2.1 General Microbiology Techniques

2.2.1.1 Heat Shock Transformation

Communal *E. coli* competent cells are stored in 30 µl aliquots at -80 °C. Desired plasmid DNA and *E. coli* strain were thawed immediately prior to use. When thawed, 1 µl of plasmid DNA (~100 ng/µl) was added to the *E. coli* tube and the mixture was left to incubate on ice for 30 minutes. The transformation mixture was then heat-shocked at 42 °C for 45 seconds, before placing back on ice for no longer than 5 minutes. At this point, 200 µl of LB media was added to the tube, before incubating in an orbital shaker at 37 °C, 220 rpm, for 1 hour. Samples were then spread onto pre-warmed LB agar plates supplemented with the required selection antibiotic and left to incubate overnight at 37 °C.

2.2.1.2 Small-Scale Starter Cultures

2.2.1.2.1 Plasmid Propagation and Expression Trial Starter Cultures

For plasmid propagation or small-scale expression trials, 5 ml of LB media supplemented with the required selection antibiotic was inoculated with a single colony from a successful transformation plate. Inoculated cultures were left to incubate in an orbital shaker overnight at 37 °C, 220 rpm.

2.2.1.2.2 Pre-expression Cultures

For small scale pre-expression cultures, a single successful colony was inoculated into a 20 ml volume of LB media supplemented with the required selection antibiotic. Inoculated cultures were left to incubate in an orbital shaker overnight at 37 °C, 220 rpm.

2.2.1.3 Small-Scale Over-Expression Cultures

A successful 5 ml starter culture was inoculated into 45 ml of LB media supplemented with the appropriate selection antibiotic. Cultures incubated in an orbital shaker at 37 °C, 220 rpm, and the OD_{600} was monitored and small samples were taken for subsequent analysis. Cultures were induced with 0.2-0.5 mM Isopropyl-β-D-thiogalactoside when the OD_{600} reached 0.6 and incubated in an orbital shaker overnight at 37 °C, 220 rpm.

2.2.2 Harvesting Small-Scale Cultures

All small-scale bacterial culture preparations were harvested by centrifugation at 4000 rpm for 20 minutes in a benchtop centrifuge, and pellets were stored at -80 °C.

2.2.3 Large-Scale Auto-Induction Over-Expression Cultures

LB or SB media was prepared as described in Table 2.3. When cool, 371 ml was measured into a 2 L baffelled flask. Auto-induction supplements from Table 2.4 were added in the following quantities: 1 ml $MgSO_4$, 8 ml 5,052 and 20 ml NSPC, to give a final culture volume of 400 ml. Small -scale starter cultures were inoculated at a volume normalised to give a theoretical OD_{600} of 0.05 in the final culture.

2.2.4 Polyacrylamide Gel Electrophoresis (PAGE)

2.2.4.1 Native-PAGE

Samples were mixed 1:1 with native loading dye (1 mg/ml bromophenol blue, 50 % glycerol, 25 mM Tris, pH 8.0) and loaded into 4-20 % Mini-TGX non-denaturing gels (Bio-Rad, U.K.). Gels were run with home-made Tris/glycine running buffer (192 mM glycine, 25 mM Tris, pH 8.8), and run at 4 °C, 150 V for 3 or 5 hours.

2.2.4.2 Sodium-dodecyl Sulphate (SDS)-PAGE

2.2.4.3 Denatured Sample Preparation

Prior to loading, 10 µl of sample was routinely mixed with 4X LDS loading dye (Invitrogen, U.K.), DTT and made up to a final volume of 20 µl with H_2O. Once mixed, samples were either incubated at or at 95 °C for 5 minutes before loading.

2.2.4.4 Sample Separation and Visualisation

SDS-PAGE was either performed using Bolt™ 4-12 % Bis-Tris Plus precast gels (Invitrogen, U.K.) or handmade Bis-Tris gels (recipes in table 2.9). Precast gels were secured in a Bolt™ mini-gel tank and run with Bolt™ MES Running buffer (Invitrogen, U.K.) at 160 V for 50 minutes at . Handmade gels were poured into 0.75 mm glass casts (Bio-Rad, U.K.), and also run at 160 V for 50 minutes at 200 V. 10 µl of denatured sample was loaded into the wells alongside either 3 µl or 5 µl of PageRuler™ Plus Prestained Protein Ladder (Thermo Scientific, U.K.), unless otherwise specified, for staining or western blot respectively. Bands were stained with

Quick Coomassie (Generon, U.K.) or InstantBlue Protein Stain (Expedeon, U.K.) and imaged with the SynGene G:BOX Chemi XX6 system.

Table 2.9: Composition for 7 %, 10 % and 4 % SDS-PAGE gels.

	Resolving		**Stacking**
	7 %	**10 %**	**4 %**
dH_20	4.97 ml	4.00 ml	2.73 ml
Bis/Acrylamide (30 %)	2.33 ml	3.33 ml	680 µl
1.5 M Tris.HCl (pH 8.8)	2.50 ml	2.50 ml	-
1.0 M Tris.HCl (pH 6.8)	-	-	500
APS (10%)	100 µl	100 µl	40 µl
SDS (10%)	100 µl	100 µl	40 µl
TEMED	10 µl	10 µl	4 µl

2.2.5 Western Blotting (WB)

2.2.5.1 Buffers

2.2.5.2 10 X Phosphate Buffered Saline (PBS), pH 7.4

137 mM NaCl, 2.7 mM KCl, 10 mM $Na_2HPO_4.7H_2O$ and 1.8 mM KH_2PO_4.

2.2.5.3 PBS/Tween20 (PBST)

PBS was diluted 1/10 and 0.05 % Tween20 was added.

2.2.5.4 Transfer Buffer

192 mM glycine, 25 mM Tris pH 8.0, 0.1 % SDS and 20 % methanol, pH 8.3.

2.2.5.5 Semi-Dry WB Transfer Conditions

Samples were initially subject to SDS-PAGE using either precast or hand-poured gels. Gels, nitrocellulose blotting paper (0.45 μM) and card pieces were soaked in ice-cold transfer buffer for no longer than 15 minutes. The transfer stack was assembled before electroblotting for either 90 minutes at 60 mA using the Bio-Rad Trans-Blot® SD Semi-Dry Transfer Cell, or 10 minutes at 1.3 A, 25 V, using the Bio-Rad Trans-Blot ® Turbo™. Native-PAGE samples were transferred using the Bio-Rad Trans-Blot ® Turbo™ at 1.3 A, 25 V, but the transfer time was extended to 30 minutes.

2.2.5.6 Dot Blot

Samples were incubated for 5 minutes with varying quantities of SDS and DTT to optimise denaturing conditions. Once established, 0.1 % SDS with 0.25 mM DTT was added to samples in a 1:1 v/v ratio and incubated for a minimum of 5 minutes before 2 μl was pipetted directly onto nitrocellulose blotting paper (0.45 μM). When dry, the blotting paper was treated as described in subsequent sections.

2.2.5.7 Antibody Labelling

2.2.5.7.1 Anti-His Detection of AcrB

Blots were blocked with 5 % milk:PBST solution for either 1 hour at RT or overnight at 4 °C. Membranes were rinsed twice in PBST for 5 minutes, before submerging in 2 % milk:PBST supplemented with 1:4000 diluted HRP-conjugated monoclonal mouse α-HIS antibody (R&D Systems, U.K). Blots were incubated with antibody at room

temperature for 1 hour, or overnight at 4 °C, then washed 3-4 times in PBST over 1 hour before developing and imaging.

2.2.5.7.2 Anti-FLAG Detection of TRPM2

Blots were placed in 5 % milk:PBST overnight at 4 °C. After rinsing twice with PBST for 5 minutes, blots were submerged in 2 % milk:PBST supplemented with 1:500 diluted monoclonal mouse M2-α-FLAG antibody (Sigma-Aldrich, U.K.) and incubated for 4 hours at room temperature. The membrane was then washed 3-4 times with PBST over 1 hour, before incubating in 2 % milk:PBST supplemented with HRP-conjugated goat α-M2 antibody diluted 1:5000 for 1 hour at RT. The membrane was finally washed 3-4 times in PBST over 1 hour before developing and imaging.

2.2.5.8 Chemiluminescent Blot Development

Lumi-Phos HRP (PS-atto) (Lumigen, U.S.A.) solutions A and B were mixed in a 1:1 ratio and incubated in the dark for 2 minutes. The membrane was transferred onto a transparent plastic sheet – transfer-side up – before the PS-atto mixture was applied. Another plastic sheet was placed on top to compress the membrane and evenly distribute the mixture before it was left in the dark for 2 minutes. Chemiluminescence was then captured with the SynGene G:BOX Chemi XX6 system.

2.2.5.9 Membrane Stripping for Re-probing

Membranes were incubated in mild stripping buffer (200 mM glycine pH 2.2, 3.5 mM SDS, 1 % Tween20) at room temperature for 5-10 minutes. The buffer was exchanged for fresh stripping buffer and the membrane was incubated at room temperature for a

further 5-10 minutes. The buffer was discarded once again, and the membrane was washed twice in PBS for 10 minutes per turn; then twice with PBST for 5 minutes per turn. After washing membranes were ready for antibody labelling.

2.3 Styrene-Maleic Acid co-polymer (SMA) synthesis

SMA was prepared from precursor styrene maleic anhydride *co*-polymer as described in Lee *et al.* 2016, albeit with a few modifications. Firstly, anti-bumping granules were omitted in favour of a non-reactive plastic stirrer bar. Secondly, step 4 was carried out overnight at 4 °C. Lastly, the polymer was freeze-dried with liquid nitrogen instead of at -20 °C.

2.4 TRPM2 Structural Bioinformatics

2.4.1 3D Model Generation

Residues from the human TRPM2 protein sequence (Uniprot ID: O94759), were used as input for *in silico* modelling by three independent structure prediction servers; SWISS-MODEL, Phyre2 and I-TASSER. All modelling programmes are based on the hidden Markov model (HMM) target-template alignments. Results were visualised and interpreted using PyMOL (The PyMOL Molecular Graphics System, Version 2.0 Schrödinger, LLC.).

2.4.2 SWISS-MODEL

Residues 1-554 were submitted to the SWISS-MODEL server (last updated on 08-02-2017; alongside PDB release 02-02-2017). A template search and selection is

performed using the SWISS-MODEL Template Library (SMTL), and subsequent templates are indexed by database search programmes BLAST and HHBlits, before models are generated using ProMod-II and scored based on QMEAN potential (Biasini *et al.*, 2014).

2.4.3 Phyre2

Residues 1-752 were submitted to the Phyre2 server and run in 'normal' mode. Phyre2 searches for homologous sequences using a similar initial sequence alignment and secondary structure prediction as SWISS-MODEL (1.1.2), without the SMTL, and uses this to build a final 3D model. Phyre2 was accessed in 2016 at http://www.sbg.bio.ic.ac.uk/phyre2/html/page.cgi?id=index.

2.4.4 I-TASSER

Residues 1-554 were submitted to the I-TASSER server to generate an initial model that was subsequently used as a template in a second round of modelling in intensive mode for full length TRPM2. I-TASSER was accessed in 2016 at https://zhanglab.ccmb.med.umich.edu/I-TASSER/.

2.4.5 Coiled-Coil Prediction

PCOILS V1.0.1 was used to predict the location of potential coiled-coil regions within the TRPM2 primary protein sequence (Uniprot ID: O94759). PCOILS was accessed initially in 2016, and later in 2019 at https://toolkit.tuebingen.mpg.de/tools/pcoils. The date accessed is significant for results interpretation, as there has been an algorithm update since the first search attempt.

2.4.6 Calmodulin Binding Site Prediction

The Calmodulin Target Database was used to determine potential Calmodulin binding sites on the TRPM2 primary protein sequence. This resource was access in 2016 at http://calcium.uhnres.utoronto.ca/ctdb/ctdb/sequence.html.

2.5 TRPM2 Expression and Purification

The HEK293 *hs*TRPM2 expression cell line was kindly donated by Dr. A.M. Scharenberg (Washington University, U.S.A.). As described in Perraud et al. 2001(Perraud *et al.*, 2001), the TRPM2-FLAG construct was cloned into a modified pcDNA™4/TO (*Zeocin*$^{-}$) mammalian expression vector and *co*-transfected into a naïve HEK293 cells alongside the pcDNA™6/TR (*Ampicillin*$^{-}$, *Blasticidin*$^{-}$) vector. Both pcDNA™4/TO and pcDNA™6/TR work in synergy to control TRPM2 expression under the Tetracycline-Regulated Expression system (T-REx™).

2.5.1 Regeneration and Maintenance

Complete media and trypsin were pre-warmed to 37 °C prior to use.

Stable cells were cultured in complete media in a humidified incubator with 5 % CO_2 at 37 °C. Shortly after revival, cells were challenged with 200 µg/ml Zeocin and 0.4 µg/ml Blasticidin to preserve the TRPM2-FLAG insert, and then regularly passaged at ~70 % confluency to maintain stable monolayer growth. To passage, cells were washed with Dulbecco's PBS, then a minimal volume of trypsin was added before incubating at 37 °C for no longer than 5 minutes, or until the cells had detached.

2.5.2 Freezing Cells

For long term storage, a confluent T175 flask of cells were resuspended as described for passaging, then centrifuged at 1000 rpm for 5 minutes. The supernatant was gently removed, and the cell pellet was resuspended in 10 ml of DMEM + GlutaMAXTM-1, [+] 4.5 g/L D-Glucose, [+] 110 mg/L sodium pyruvate media with 20 % foetal bovine serum and 10 % DMSO. Resuspended cells were aliquoted into cryogenic vials and placed in isopropanol containers for gradual freezing overnight at -80 °C. Cells were either kept at -80 °C or transferred to a liquid nitrogen storage tank.

2.5.3 Overexpression of TRPM2

For large scale expression, cells were split into Sarstedt 175 cm^2 culture flasks. At 50-60 % confluency, the media was changed and 1 µM tetracycline was added to induce expression. Cells were then left to incubate at either 33 °C or 37 °C, 5 % CO_2 for 48 hours. When fully confluent, cells were harvested by first suspending in ice-cold phosphate-buffered saline (PBS: 137 mM NaCl, 2.7 mM KCl, 10 mM Na_2HPO_4, KH_2PO_4, pH 7.4) then pelleted by centrifugation at 500 xg, 4 °C for 5 minutes. Pellets were washed three times with PBS before proceeding to further experiments or storing at -20 °C.

2.5.4 TRPM2 Purification

Reconstituted HEK293 cells were harvested 48 hours after tetracycline treatment. Cells were pooled according to the desired scale-up quantity (4-8 g) and sonicated (5 seconds on, 30 seconds off) in the presence of the relevant TRPM2 binding buffer

(BB), 0.2 g of SMA, 1 mM PMSF and Roche cOmplete EDTA-free protease inhibitors. 100 U (10 µl) Benzonase (Sigma) was added to the lysate and incubated at RT for 10 minutes, before a 2-hour incubation at 4 °C with mechanical inversion. The lysate was then centrifuged for 1 hour at 100000 xg, 4 °C, and the soluble fraction was added to 500 µl M2-anti-FLAG resin (Sigma) and incubated overnight at 4 °C while mixing end-over-end. The overnight SMA-TRPM2-Resin sample was added to a column and allowed to flow through completely. The resin was then washed with 4 ml of BB, before equilibrating in 4 ml of elution buffer (EB) collected in 1 ml fractions. Samples were then eluted from the column across an increasing FLAGX3 peptide gradient (20-150 ng/µl in EB), in volumes of 250 µl.

2.6 AcrB Expression and Purification

The pTTQ18-*carb*$^{-}$ based vector (named pBPT0480-CHH) encoding the *Escherichia coli* (*E.coli*) acridine resistance protein B (AcrB) gene alongside a C-terminal octa-histidine tag (AcrB(His)$_8$) was kindly donated by Dr. Vincent Postis (Leeds Beckett University, U.K.).

2.6.1 Transformation

Heat-shock at 42 °C was used to transform ~100 µg of plasmid DNA into chemically competent C43 (DE3) Δ(*acrB*) *E. coli* cells harbouring an additional pRARE2-*chlo*$^{-}$ plasmid. Transformed cells were then plated onto agar supplemented with 30 µg/ml chloramphenicol and 100 µg/ml carbenicillin, and left to incubate overnight at 37 °C.

2.6.2 Starter Cultures and Scale Up

Single colonies were inoculated into 20 ml of LB supplemented with 30 µg/ml chloramphenicol and 100 µg/ml carbenicillin, and left to grow overnight at 37 °C, with shaking at 220 rpm. The next day, the OD_{600nm} of each starter culture was measured and normalised to give an OD_{600nm} of 0.05 in 400 ml of complete auto-induction media in a 2 L baffled flask. Cells were then left to incubate for 24 hours at 37 °C, 220 rpm.

2.6.3 Harvesting Bacterial Cells

Cultured cells were harvested by centrifugation at 9,000 xg for 40 minutes at 4 °C. Pellets were placed in a new container and weighed, before either being stored at -80 °C, or re-suspended in ice-cold PBS plus EDTA-free cOmplete protease inhibitors (6 ml/1 g cells) for immediate use.

2.6.4 Bacterial Membrane Preparation and Storage

Unless otherwise specified, samples were kept on ice at all stages.

Cell pellets were thawed and re-suspended in 0.5mM EDTA, cOmplete protease inhibitors (Roche) 20 mM Tris, pH 7.5 at a 4 ml/1 g ratio by dounce homogenisation at 4 °C. The homogenate was then passed twice through a cell disruptor operating at 30 KPsi, 4 °C. Remaining cell debris was pelleted by centrifugation at 12,000 xg for 45 minutes at 4 °C. The supernatant was then transferred to a new tube and centrifuged at 43,000 rpm (Beckman Coulter; Type Ti 45 Rotor) for 2 hours at 4 °C. The membrane pellet was then washed by first re-suspending in 40 ml of 20 mM Tris, pH 7.5, and centrifuging again at 43,000 rpm (Beckman Coulter; Type Ti 45 Rotor) for 2 hours at

4 °C. This was repeated for a third wash, before finally re-suspending the membrane pellet in a minimal volume of 20 mM Tris, pH 7.5. A bicinchoninic acid (BCA) assay was performed on the suspension to determine total protein concentration before drop-freezing in liquid nitrogen and storing at -80 °C.

2.6.5 AcrB Purification

For solubilisation, membranes were weighed to give a total protein content of ~45 mg, then resuspended in BB to an equivalent protein concentration of 1 mg/ml. SMA powder was added to a final concentration of 2.5 % (w/v), and the mixture was incubated for 2 hours at RT with gentle agitation. Insoluble material was pelleted by centrifugation at 100,000 xg_{av}, 4 °C, and the soluble fraction was left to incubate with pre-equilibrated cobalt resin overnight at 4 °C. To purify, the resin was first washed with 10 column volumes (CV) of BB, before eluting with EB (BB plus 300 mM Imidazole). After IMAC purification the sample was dialysed into BB to remove remaining imidazole, then concentrated before being used immediately or snap-frozen in liquid nitrogen for storage at -80 °C.

2.7 Thermostability Assay

2.7.1 Sample preparation

N-[4-(7-diethylamino-4-methyl-3-coumarinyl)phenyl] maleimide (CPM) dye was diluted 50-fold from a 5 mg/ml to give a 0.1 mg/ml solution, with a final volume of 100 µl, and left in darkness to equilibrate to for 10 minutes. Samples were diluted to 0.1 mg/ml in a 90 µl, then serially diluted to give final reaction volumes of 45 µl at the

following concentrations (mg/ml): 0.1, 0.05, 0.025, 0.0125, 0.00625 and 0.003126. After equilibration, 5 µl of the CPM dye was added to each sample and vortexed briefly, before being left to incubate for a further 10 minutes. The Agilent Mx3005P q-PCR machine was used to read out fluorescence during a temperature ramp from 25-90 °C.

2.7.2 Data Processing

Thermostability data was interpreted and visualised using Origin2020) and the online JTSA server (http://paulsbond.co.uk/jtsa). For manual data analysis, raw data were first plotted to examine the quality of the data. The data were then smoothed and the first derivative was calculated to generate polynomial melting curves. The approximate melting temperature was taken as the peak of the polynomial function which indicated the (Tm) of the sample. For data analysed on either the JTSA server or manually, thermostability was assessed according to a shift in the Tm.

2.8 Circular Dichroism

Samples were routinely analysed by circular dichroism using a Chirascan Plus (Applied Photophysics), equipped with xenon lamp source, peltier temperature control and automated temperature ramping capabilities. Data was collected in absorbance mode using standard parameters as follows: Protein concentration = 0.2 mg/ml, path length = 0.1 cm, bandwidth = 2.5 nm, λ = 190-260 nm, increment = 1 nm, time-per-point = 1.0 seconds, repeats = 2. Deviations for protein concentration and increments for each experiment are specified within the text.

2.9 Size Exclusion Chromatography with Multi-Angle Laser Light Scattering (SEC-MALLS)

All SEC-MALLS data were collected on a DAWN 8+ multi-angle light scattering (LS) detector, an Optilab T-rEX differential refractive index (dRI) detector and UV-absorbance (UV) detector (Wyatt Technology), running at a flow rate of 0.2 ml/minute.

2.9.1 SEC-MALLS of TRPM2 in SMA

SEC-MALLS of TRPM2 in SMA was performed using a Superose 6 5/150 column pre-equilibrated with SEC.B (300 mM NaCl, 50 mM Tris.HCl, pH 8).

2.9.1.1 SEC-MALLS of AcrB in SMA and DDM

SEC-MALLS was performed using either a Superose 6 5/150 or Superdex 200 10/300 column pre-equilibrated with SEC.B (300 mM NaCl, 50 mM Tris.HCl, pH 8) for SMA purified and amphipol-exchanged samples, or DDM-SECB (SEC.B plus 10 % Glycerol and 0.025 % DDM) for DDM purified and DDM exchanged samples. Where molar masses could be determined for the samples in DDM, an extinction coefficient of 0.7890 mL/g was used for the full length AcrB construct including octahistidine tag, and dn/dc modifiers of 0.185 and 0.143 were used for protein and DDM modifier, respectively. Molar masses could not be accurately determined for SMA and A8-35 exchanged (A8-35_Ex) samples, but modifiers of 0.2 and 0.15 were used with SMA and A8-35_Ex samples respectively.

2.10 Electron Microscopy

2.10.1 Negative Stain Electron Microscopy

2.10.1.1 Conventional Grid Preparation

In-house carbon-coated copper grids (prepared as previously described using the carbon sheet method (Thompson *et al.*, 2016), were glow-discharged for 30 seconds in negative mode under 0.39 atmospheric pressure using the PELCO easiGlow™ (Ted Pella Inc., U.S.A.) discharge system. Samples were applied to charged grids at concentrations of ~20 μg/ml (~0.5 μM for TRPM2, ~0.7 μM for AcrB) in 3 μl volumes and left to incubate for 30 seconds in a humidity-controlled environment. The sample was then wicked away, leaving a minimum meniscus, before 3 μl of 1 % or 2% uranyl acetate (UA) was added and incubated for 60 seconds. UA was then wicked and re-applied for a further 60 seconds, before finally blotting and drying under a pre-heated lamp.

2.10.1.2 Data Collection

Micrographs were collected on either the FEI Tecnai G^2-Spirit (T12) or F20 (FEI) electron microscopes at the Astbury Biostructure Laboratory, University of Leeds. At the time of data collection, the T12 microscope was equipped with a Gatan Ultra Scan 4000 CCD camera and either a LaB_6 or Tungsten filament, operating at 120 kV. The F20 was equipped with a FEI Ceta CMOS detector and a field emission gun (FEG) electron source operating at 200 kV. The spherical aberration (Cs) for the T12 and F20 were 6.3 mm and 2.0 mm, respectively. Nominal magnifications for each sample are

specified in the text, but camera and calibrated pixel size details relevant for image analysis and data processing in this thesis are highlighted in table 2.10 below.

Table 3.10: Magnification references for the T12 and F20 microscopes.

T12		***F20***	
Nominal mag. (KX)	**Pixel Size (nm)**	**Nominal Mag. (kx)**	**Pixel Size (nm)**
23	0.48	25	0.418
30	0.37	29	0.351
49	0.23	50	0.200

2.10.1.3 Data Processing

Three TRPM2 negative stain datasets are described in this thesis: Dataset 1 = Apo-TRPM2, Dataset 2 = XLCaM-TRPM2 and Dataset 3 = A second attempt at Apo-TRPM2. Dataset 1 was collected on the T12 microscope at 30 kx magnification and initial particles were picked and processed in the Eman2.0 software suite, before final 2D classifications were generated using iMagic. Dataset 2 was collected on the F20 microscope at 25 kx magnification, and all particles were picked and processed to generate a final 3D reconstruction in Relion 2.1. Dataset 3 was also collected on the F20 microscope, but at a nominal magnification of 29 kx and processed with Relion 3.0. Specific data processing parameters are discussed in the text.

2.10.2 Cryo-Electron Microscopy (Cryo-EM)

All samples and data were prepared, imaged and processed at the Astbury Biostructure Laboratory, University of Leeds.

2.10.2.1 Conventional grid preparation

A number of grid types were used for initial screening. All grids were first glow-discharged for 30 seconds in negative mode under 0.39 atmospheric pressure using the PELCO easiGlow™ (Ted Pella Inc., U.S.A.) discharge system. Grids were then prepared using a FEI Vitrobot Mark IV at pre-equilibrated conditions of 100 % humidity, 10 °C. For the primary dataset in this thesis, 3 µl of purified TRPM2 (0.34 mg/ml) was applied to a Cu Quantafoil R1.2/1.3, 300 mesh holey grid (or other grid choice, described in the text) and incubated for 30 seconds, before blotting at a force of 6 for 5 seconds and plunge freezing in liquid ethane.

2.10.3 Data Collection

2.10.3.1 Apo-TRPM2 Dataset 1

The Apo-TRPM2 cryo-EM dataset was collected on the FEI Titan Krios 1 microscope operating at 300 kV in integrating mode. At the time of collection, Krios 1 was equipped with a Falcon II direct electron detector. Data was collected over a 12-hour period at a magnification of 75,000 x, with an applied defocus range of -2.0 to -4.0 µm with 0.5 µm increments. At this magnification, the calibrated pixel size is 1.065 Å/pixel. 1,018 movies were collected over 2 second exposures, with a total dose of 71 $e^-/Å^2$, split over 40 frames (1.8 $e^-/Å^2$ per frame).

2.10.3.1.1 Cross-linked TRPM2:CaM

The on-grid cross-linked TRPM2:CaM complex dataset was collected on the FEI Titan Krios 1 microscope operating at 300 kV in integrating mode. At the time of collection,

Krios 1 was equipped with a Falcon II direct electron detector. Data was collected over a 48-hour period at a magnification of 75,000 x, with an applied defocus range of -2.0 to -3.0 μm with 0.5 μm increments. At this magnification, the calibrated pixel size is 1.065 Å/pixel. 5,054 movies were collected (only 3179 could be used) over 2 second exposures, with a total dose of 71 $e^-/Å^2$, split over 40 frames (2.015 $e^-/Å^2$ per frame).

2.10.3.2 Data Processing

Data was processed in the Relion 2.1 software suite (Scheres, 2012). Movies were motion-corrected using MotionCorr2 , and CTF estimation was performed using Gctf. Particle picking, extraction and 2D classification were all performed within the Relion 2.1 suite and are described in the text. Briefly, 2652 particles were manually extracted to generate an initial 2D reference set. These were used to set up auto-picking parameters, from which 122,984 particles were identified. Particles were extracted from CTF corrected micrographs using a particle box size of 320 pixels, and subject to another round of 2D classification with a mask of 270 Å. Data could not be processed further.

2.10.4On-grid cross-linking.

In the droplet order described in table 2.11, 40 μl of each buffer was dotted on to a strip of parafilm. Grids were glow-discharged and 3 μl of sample was applied for 30 seconds, before floated sample-side down on top of droplet 1. The grid was suspended on the droplet 2 minutes, before transferring to droplet 2, and proceeding through each droplet number as described in table 2.11. The grid was not blotted at any point during

this process, but after droplet 8, grids were processed as normal for negative stain or cryo-EM.

Table 2.11: On-grid cross-linking procedure.

Droplet No.	Buffer Type	Time (minutes)
1	Sample Buffer	2
2	Sample Buffer	2
3	0.5 % Gluteraldehyde	5
4	100 mM Ammonium Acetate	0.5
5	50 mM Ammonium Acetate	2
6	10 mM Ammonium Acetate	2
7	New Buffer	2

2.11 Thin Layer Chromatography (TLC)

All procedures were performed at room temperature, under air, unless otherwise specified.

2.11.1.1 Materials

TLC was performed using LiChrospher® HPTLC Silica gel 60 F_{254}s plates and phospholipid standards of undefined chain compositions as well as cholesterol were kindly donated from Dr. Arndt Rohwedder, originally purchased as part of the Natural Phospholipids Kit from Larodan, UK (Product ID: 37-0000) and Fluorochem, UK (Product ID: 57-88-5), respectively. All phospholipids standards were solubilised in a 1:1 Methanol:Chloroform solution.

2.11.1.2 Lipid Extraction from SMA Samples for TLC

A modified Folch method (Folch *et al.* 1957) was used to extract lipids from SMA-purified proteins. In a 2 ml microfuge tube, 170 µl of sample was added to 750 µl of extraction solution (2:1 methanol/chloroform with 31.25 mM HCl), and vortexed vigorously, and left to incubate at RT for 5 minutes. An additional 725 µl of chloroform and 170 µl of 1M HCl was added before centrifuging at 1500 xg for 5 minutes. The organic (lower) phase was transferred to a new vial, and 708 µl of wash solution (2:1 chloroform/methanol with 2 µM of HCl) was added and vortexed again. The 5-minute incubation and 5-minute centrifugation step were repeated, and the lower phase, representing the final lipid sample, was transferred to a new vial.

2.11.1.3 High-performance TLC (HPTLC) Separation of Lipids

HPTLC plates were developed in two sequential runs for initial separation of neutral lipids and sterols, then phospholipids according to Churchward et al., 2008. HPTLC plates were washed with methanol/acetate (6:4, v/v) and activated at 110 °C for 30 minutes, before lipid standards (see 2.13.1) were loaded ~1 cm from the base of the plate in a fashion to form a line instead of a dot. Samples were then added alongside in a similar linear manner. First, for separation of sterols and neutral lipids, a mobile phase of methylene chloride/ethyl acetate/acetone (80:16:4, v/v/v) was added to the glass TLC chamber to cover a distance of ~1 cm high from the base of the chamber, and left to equilibrate. The plate was then inserted into the chamber and developed to as close to the top of the plate as possible. The plate was then removed and left to dry in a fume hood for ~6 minutes, meanwhile the chamber buffer was replaced with chloroform/ethyl acetate/acetone/isopropanol/ethanol/methanol/water/acetic acid

(30:6:6:6:16:28:6:2, by volume) to the same ~1 cm height, and left to equilibrate. When the plate was dry, it was re-inserted to the chamber and developed to ~1 cm from the top of the plate to separate phospholipids.

2.11.1.4 TLC Plate Staining and Fluorescence Detection

Chromatogram plates were stained and visualised according to (Churchward *et al.*, 2008). The TLC plate was sprayed uniformly with a solution of 10 % $CuSO_4$, 8 % aqueous phosphoric acid and allowed to dry for 10 minutes, before being charred at 145 °C for 10 minutes. Plates were then imaged with UV light using the SynGene G:BOX Chemi XX6 system

2.12 Mass Spectrometry (MS)

All data were analysed with MassLynx software (Waters).

2.12.1 Preparation of glass capillaries

Filament capillaries were pulled to form a fine aperture using a pre-defined setting on a Flaming/Brown Micropipette Puller. Pulled pipettes were then sputter-coated with gold and palladium for 75 seconds using an Emitech Sputter Coater, operating at 2-4 $x10^{-2}$ mbar, 25-30 mA, under argon. This was repeated a second time to produce an even coating.

2.12.2 Native MS

Samples of varying concentrations were exchanged into an MS appropriate buffer (200 mM ammonium acetate pH 7.4 or 200 mM ammonium bicarbonate pH 8.0), by three

rounds of dilution and concentration with an Amicon Ultra 0.5 mL (100 kDa MWCO) concentrator. After buffer exchange, samples were immediately analysed by nano-electrospray ionisation (nESI)-MS using in-house coated gold/palladium nanospray capillaries and a quadrupole time-of-flight MS (Synapt G1 HDMS, Waters) with ion mobility capabilities operating in negative mode. For both native and denaturing MS, the instrument was operated in TOF mode using a source temperature of 80 °C. For native MS, the parameters were as follows: Capillary voltage = 2.0 kV; sampling cone = 180 V; extraction cone = 4 V; backing pressure = 6 mbar; trap collision energy (CE) = 220 V; transfer CE = 200 V and trap DC bias = 4.

2.12.3 Denaturing MS and Lipidomics

2.12.3.1 Lipid Extraction for MS

All steps of lipid extraction were performed on ice or at 4 °C. To 40 µl A8-35_Ex (1 volume; [AcrB] ~1.5 mg/mL), 1 volume of chloroform and 2 volumes of methanol were added. After mixing the sample, another volume of chloroform was added. After mixing again, 1 volume of water was added. The sample was centrifuged (7 min, 17,000 xg), before the organic (lower) phase was washed three times with 2 volumes of cold water. The organic phase was then directly injected into the Synapt G1 HDMS (Waters).

2.12.3.2 MS/MS

For MS of lipid extracts, the Synapt was also operated in TOF mode with the following parameters: Capillary voltage = 1.2 kV, sampling cone = 80 V; extraction cone = 4 V;

backing pressure = 2 mbar; trap CE = 20 V; trap flow rate = 2 mL/min, transfer CE = 10 V and trap DC bias = 4. The most intense signal (719 m/z) was selected and fragmented by MS/MS under the same conditions, except with trap collision energy = 50 V.

Chapter 3:

Expression and

Purification of TRPM2

3.1 Introduction

The *hs*TRPM2-FLAG stable HEK293 cell line was previously established and characterised in the laboratory of A. M. Scharenberg to examine the putative ADPR pyrophosphatase activity of the TRPM2 C–terminal NUDT9H domain. The full length TRPM2 cDNA was N-terminally fused to a FLAG tag epitope and cloned into a pCDNA4/O vector as part of a tetracycline-controlled expression system. Prior to joining the lab, this cell line had been maintained and used extensively for *in vitro* functional assays such as calcium imaging, single-cell electrophysiology and high resolution fluorescence microscopy (Perraud *et al.*, 2001). It was therefore the aim of this project to express, purify and characterise TRPM2 for biochemical and biophysical characterisation, particularly with cryo-electron microscopy. This chapter will focus on optimisation of purification conditions to yield the most stable, homogeneous sample for use in cryo-electron microscopy.

3.1.1 Project progress prior to this PhD

The tetracycline-inducible HEK293-TRPM2 cell line was already established in the lab. As the aim of this project was to biochemically and biophysically characterise the TRPM2 receptor *in vitro*, with the ultimate goal of producing a high resolution TRPM2 structure by cryo-EM, a reproducible purification protocol needed to be established. Preliminary experiments performed by Wellcome Trust Rotation Students (Matthias Ganther and Rachel Johnson) confirmed that the tetracycline-induced HEK293-TRPM2-FLAG system was suitable for structural studies, by demonstrating that both tetracycline-controlled expression (Figure 3.1A) and receptor function (Figure 3.1B)

was maintained at low and high passage numbers which were required to continuously generate cell mass for purifications. Rachel J. then performed small-scale purification experiments of TRPM2, solubilised with detergent (*n*-dodecyl-β-D-maltoside; DDM) or the styrene-maleic acid *co*-polymer (SMA), to test the viability of using M2 anti-FLAG resin for affinity purification of the FLAG-tagged channel (Figure 3.1C). Purifications performed with SMA appeared to give superior results for both purity and yield. However, salt concentration affects SMA solubilisation efficiency and aggregation propensity, and this was increased from the manufacturer's recommended concentration of 150 mM NaCl to 300 mM NaCl.

Negative stain analysis of samples eluted with 300 mM NaCl demonstrated that the protein was visible and less aggregated than previously seen but formed 'daisy-chain' aggregates (Figure 3.1D). A large-scale purification using cell pellets derived from 12 x T175 flasks was also trialled and gave very promising results (Figure 3.1E). The later fractions from this purification were pooled and concentrated, before the resulting protein was qualitatively assessed by electron microscopy (Figure 3.1F). While it was clear that particles of the estimated size and shape of TRPM2 were visible in the sample (based on the size and shape of the published TRPV1 and TRPA1 structures (Cao *et al.*, 2013; Paulsen *et al.*, 2015). The sample concentration and homogeneity were insufficient for further experimentation at that time. These preliminary results showed promise and formed the basis for this project. However, it was clear that further optimisation of purification conditions was required, and thus is the focus of this chapter.

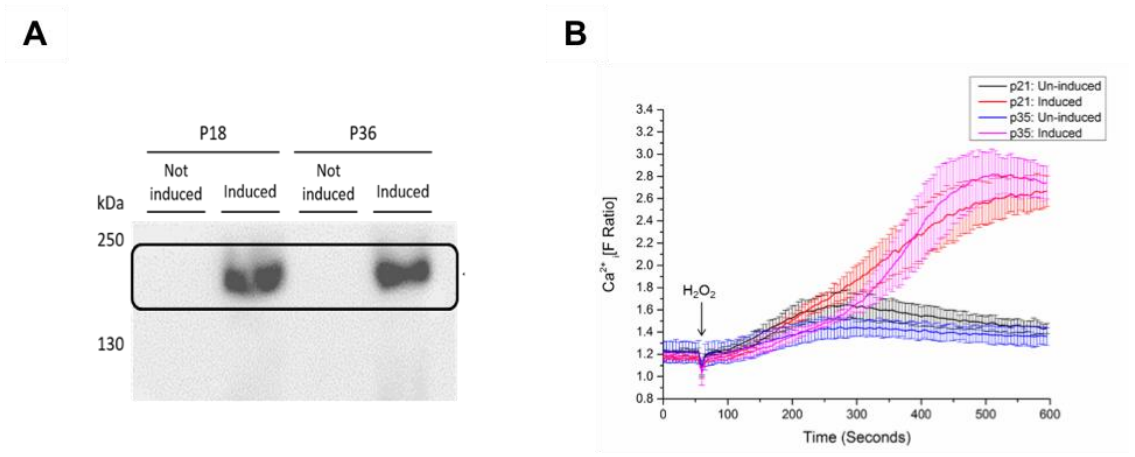
A
P18
P36
Not induced
Induced
Not induced
Induced
kDa
250
130
B
p21: Un-induced
p21: Induced
p35: Un-induced
p35: Induced
Ca^{2+}_i [F Ratio]
H_2O_2
Time (Seconds)

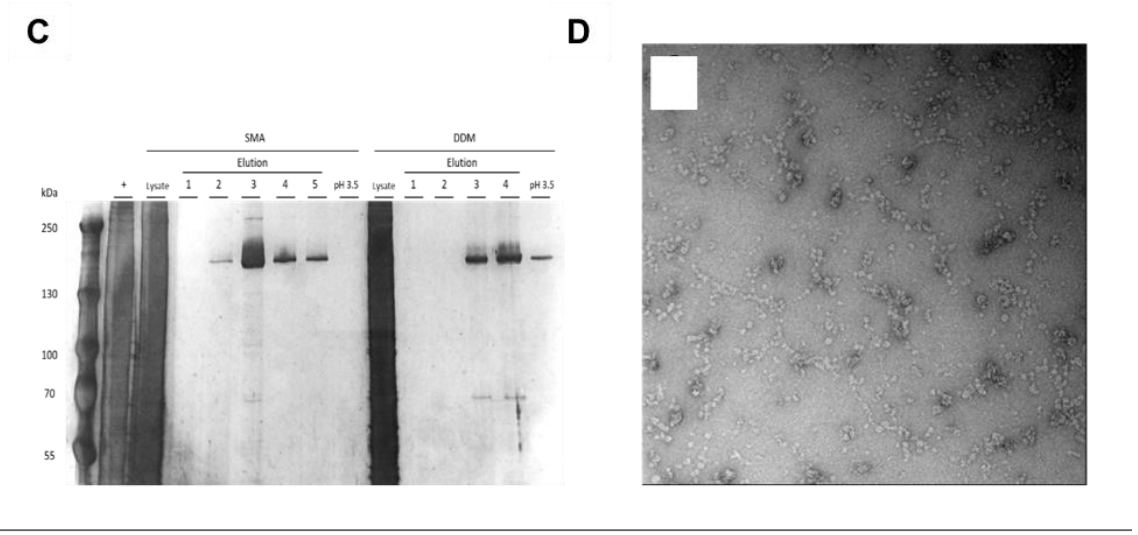
C
SMA
DDM
Elution
Elution
kDa
+
Lysate
1
2
3
4
5
pH 3.5
Lysate
1
2
3
4
pH 3.5
250
130
100
70
55
D

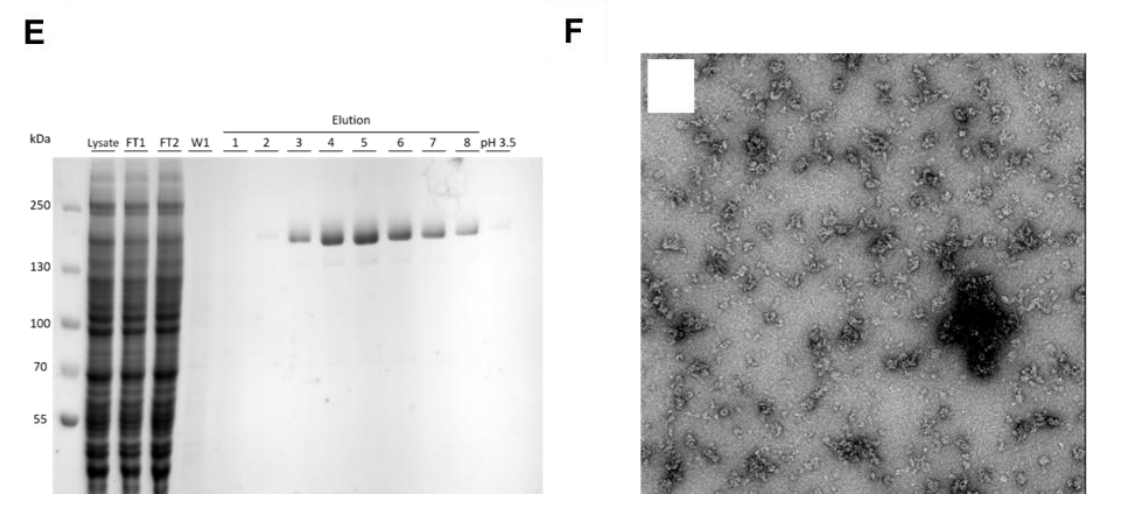
E
Elution
kDa
Lysate
FT1
FT2
W1
1
2
3
4
5
6
7
8
pH 3.5
250
130
100
70
55
F

Figure 3.1: Results from preliminary functional assays and purification experiments performed prior to the start of this project.

A) Western blot showing tetracycline-induced expression of TRPM2 in HEK293 cell lines as low passage (P18) and high passage (P36) numbers. Numbers to the right indicate the location of MW markers in kDa. B) Results from Fura-2 calcium imaging assay demonstrating significant increase in intracellular Ca^{2+} concentration upon H_2O_2 treatment, indicative of TRPM2 overexpression and activation, irrespective of passage number (p21 vs p35). C) Preliminary small-scale anti-FLAG affinity purification of TRPM2 solubilised with either SMA or DDM, and eluted with FLAG-peptide. The samples were run alongside whole cell lysates from each batch of cell pellet, and the resin was washed with 0.2 M glycine (pH 3.5) after the final elution to determine levels of residually bound protein. Individual fractions were run alongside MW markers on a 7 % gel and protein bands were visualised by silver staining. D) Negative-stain micrograph of sample taken from a small-scale purification of TRPM2 in SMA, taken on the T12 at 30, 000x magnification. No scale bar was available for this micrograph, and the white box covers a previous label. E) Coomassie-stained SDS-PAGE results from the first large-scale purification of TRPM2 in SMA showing elution fractions 1-8 alongside samples from whole cell lysate, flow-through's 1 and 2 (FT1 and FT2), and a low pH glycine wash (as described for C). Samples were run alongside a standard MW marker (kDa). F) Negative-stain micrograph of the pooled fractions shown in E. No scale bar was available for this micrograph, and the white box covers a previous label.

3.2 Results and Discussion

3.2.1 Assessing the condition and behaviour of SMA_TRPM2

While initial results looked promising, there were obvious areas for improvement in sample homogeneity, purity and concentration in order to progress to structural studies with cryo-EM. Firstly, to examine the purification process and protein behaviour further, TRPM2 was purified in SMA as previously described using 100 µg/ml of FLAGx3 peptide to elute bound sample from the M2 affinity gel in 100 µl fractions. Frozen cell pellets and freshly made cell pellets were compared to analyse the degradation of the protein and suitability for purification. These were analysed by SDS-PAGE, and clearly demonstrated the advantages of using fresh cell pellets vs stored cell pellets. Purification fractions from stored cell pellets appeared to contain more degradation products (Figure 3.2A), and these were not seen with freshly harvested cells (Figure 3.2B). This has been noted previously with this cell line, and could be related to slow freezing, or other freeze-thaw cycles.

The fractions from the purification shown in Figure 3.2B were of sufficient purity to be taken to further assess the protein content. Conventionally, protein fractions are pooled according to their perceived purity by SDS-PAGE, and in previous results from TRPM2 purifications, later fractions were perceived as being of higher quality. However, it was clear that in purification by this method eluted TRPM2 in two batches – whereby the protein concentration appears to peak in fractions 3-5, and then again in fractions 7-9. The only difference between the first 'peak' and second 'peak' was the continual addition of 100 µg/ml of FLAGx3 peptide, and consequently the increased incubation time of the resin with the FLAGx3 peptide. For this reason, fractions were

analysed by circular dichroism and negative stain microscopy both individually and according to these peaks. However, precise protein concentrations are required to properly analyse results from circular dichroism, and excess SMA polymer is known to interfere with absorbance measurements.

To calculate the relative amount of protein in each fraction, samples were analysed by SDS-PAGE alongside bovine serum albumin (BSA) standards of known concentration (Figure 3.2C). For this experiment, fractions 4 and 5 individually, and pooled fractions 7-10 were concentrated in vivaspin 100 kDa MWCO concentrators. According to the gel, the fractions examined contained ~100-250 ng of protein from 5 µl samples, equating to a maximum of concentration of 20-50 ng/µl (or 0.02-0.05 mg/ml). Since an approximate protein concentration had been determined from the purification shown in figure 3.2B, pooled fractions 7-10 were concentrated to ~0.2 mg/ml in new buffer containing 150 mM NaF to replace NaCl, for examining the effect of freeze-thawing the purified protein by circular dichroism (CD). Chloride ions absorb at ~195 nm and can strongly conceal true signals in this region of the spectra (Miles *et al.*, 2016). In contrast, NaF does not absorb above 170 nm in circularly polarised light (Miles *et al.*, 2016). Tris is also known to absorb at 200 nm, but only at 0.13 AU which was acceptable for examining alpha helical content.

In addition to E7-10, fractions 4-5 were also pooled and concentrated to ~0.2 mg/ml in 150 mM NaF buffer. However, the sample volume at this concentration was insufficient for CD (~40 µl for 4-5 and ~80 µl for 7-10), so was re-diluted to 200 µl for this particular experiment. The final protein concentrations measured before CD were ~0.02 mg/ml for pooled fractions 4-5, and ~0.06 mg/ml for E7-10 in ~200 µl. This apparent protein loss is noteworthy and is addressed later in this chapter. A standard

CD spectrum was obtained for the pooled fractions and showed that there was folded protein in both (Figure 3.3A and B, 'Before'). The samples were then snap-frozen in liquid nitrogen, thawed and their CD spectral properties were examined again (Figure 3.3A and B, 'After').

Despite some sample loss, it was clear from the spectra and significant drop in protein concentration that the freeze-thaw process was detrimental to both the protein recovery and secondary structure. Fraction E5 was also examined individually by negative stain microscopy and showed that this fraction alone contained the most homogeneous sample seen to date, at a reasonable concentration that could be optimised further for cryo-EM (Figure 3.3C and D). These, together with results from preliminary data described in 3.1.2, suggest that both pooling and concentrating fractions from this FLAG affinity chromatography step was detrimental to sample quality in that pooling fractions introduces heterogeneity in the form of contaminants/aggregates, and concentrating amplifies aggregation and results in significant protein loss. From this, it was taken that freshly purified protein should be used if the best possible cryo-EM structure is to be obtained, and alternative methods of concentrating should be employed/tested.

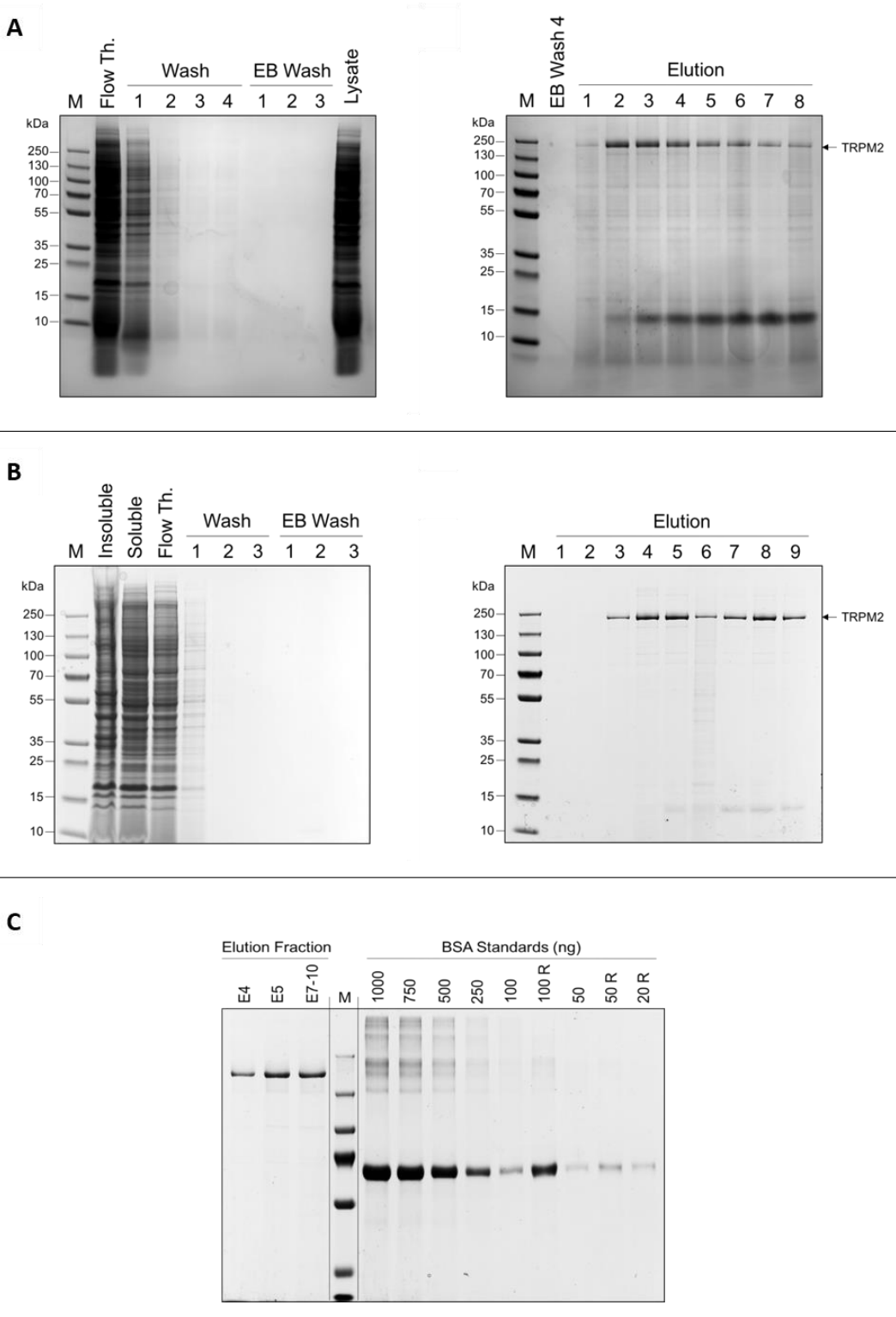
A
M
Flow Th.
Wash
1 2 3 4
EB Wash
1 2 3
Lysate
kDa
250
130
100
70
55
35
25
15
10
EB Wash 4
Elution
1 2 3 4 5 6 7 8
TRPM2
B
Insoluble
Soluble
Flow Th.
Wash
1 2 3
EB Wash
1 2 3
Elution
1 2 3 4 5 6 7 8 9
TRPM2
C
Elution Fraction
E4
E5
E7-10
BSA Standards (ng)
1000
750
500
250
100
100 R
50
50 R
20 R

Figure 3.2: SDS-PAGE analysis of fractions eluted from TRPM2 purifications in SMA.

(Previous page): Two replicate affinity purifications were performed: A) and B). Washes with binding buffer and elution buffer (EB), flow through (Flow. Th.), lysates, insoluble and soluble fractions were analysed on a separate SDS-PAGE gel to the FLAGX3 peptide elution fractions 1-8 for both purifications, alongside the same molecular weight marker (M). The band representing TRPM2 is indicated by the arrow in A and B. C) Individual and pooled eluent fractions (E4, E5, E7-10) from B were qualitatively quantified by comparison with varying nanogram (ng) concentrations of BSA alongside the same marker used in A and B. BSA concentrations followed by 'R' were samples taken from an old BSA aliquot and were discounted from the analysis.

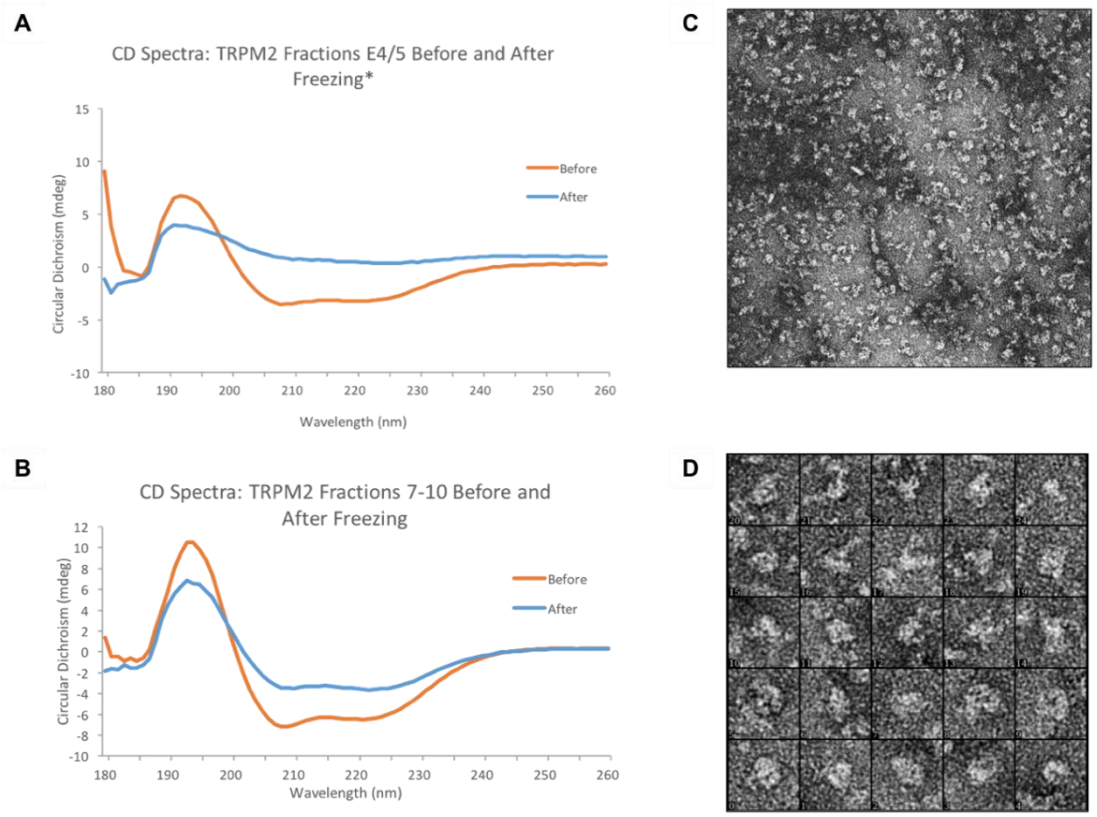

Figure 3.3: Analysis of protein secondary structure, heterogeneity and quality from fractions eluted using the original FLAGx3 protocol.

Circular Dichroism (mDegθ) spectra of TRPM2 fractions E4/5 (A) and E7-10 (B) taken before (orange) and after (blue) one freeze-thaw cycle in liquid nitrogen. C) Negative stain micrograph of fraction E5 prior to mixing with E4. D) Selected particles from E5 shows promising TRPM2-like structures and highlights some other aggregates or degradation products.

3.2.2 Optimisation of TRPM2 Purification in SMA

While the initial FLAG purification attempts gave promising results, small contaminants were visible in the micrographs alongside the larger TRPM2 homotetramer and protein aggregates. In cryo-EM, this heterogeneity would be amplified, and the sample would not be suitable for data collection. As a first attempt to combat this heterogeneity and enhance the overall quality of the protein in each fraction, a FLAG peptide gradient was introduced. The elution fractions already appeared to be of high purity, but introduction of a gradient might allow individual TRPM2 tetramers to elute separately from the aggregates.

3.2.2.1 Introduction of a FLAG peptide gradient

Maximum optimisation of the FLAG purification protocol at this stage would eliminate the need for further chromatographic separation, reducing the potential for further sample loss. Additionally, it could be seen from the initial purifications that the protein appeared to elute in a first and secondary peak, whereby a large amount of protein could be seen in elution fraction 4 and then again in 8. This different affinity

of this particular type of protein to the affinity resin suggests that there may be differences in aggregation levels between this fraction, whereby the first elution peak may be more loosely bound monomers and the second may be tightly bound aggregates.

To introduce this manual step gradient, 20, 50, 100 and 150 μg/ml concentrations of FLAGx3 peptide were prepared in EB. Different elution volumes were also trialled in order to maximise sample concentration while maintaining an appropriate volume for downstream experimentation, particularly circular dichroism, which required 200 μl in our home set up to get data of sufficient signal to noise ratios.

For an initial attempt to elute TRPM2 over a FLAG peptide gradient, the volume of eluent was increased from 100 μl to 500 μl to allow for repeat circular dichroism scans to be performed on the final samples, as well as providing enough sample for EM. The FLAG peptide concentration gradient was introduced as follows: fractions 1-2 were eluted with 20 μg/ml, 3-4 with 50 μg/ml, 5-6 with 100 μg/ml and 7-8 with 150 μg/ml FLAG peptide.

This gradient elution led to TRPM2 elution in fractions 2-8 (Figure 3.4A), which was not dissimilar to the original purification with 100 μg/ml FLAGx3 peptide (Figure 3.2A). However, there was no obvious first and second 'peak' as seen previously. Instead it appeared that the protein eluted over a broad range, with a primary peak in fraction 4 containing the highest concentration of TRPM2. It is also noteworthy that no TRPM2 protein was found in the wash fractions or the first elution fraction.

Fractions from this purification were individually examined by negative stain EM, and as suspected, the protein content, quality and conformation differed drastically

between each fraction (representative micrographs shown in figure 3.4C). Analysis of these micrographs revealed that, contrary to previous assumptions, the protein eluted in later fractions were more aggregated than the protein seen in earlier fractions. In fact, the fractions 3-4 were significantly more homogeneous and monodisperse on the grid than fractions 5 and 7 (elution fractions 3-4, figure 3.4C), and suggested that the sample preparation including only these fractions might be almost of sufficient quality for cryo-EM. Very few individual TRPM2 particles were observed from fraction 7, and it was found that this may be because much of the protein was aggregated on the grid.

3.2.2.2 TRPM2 analysis with Circular Dichroism

The remaining samples from fractions in figure 3.4A were prepared for analysis with CD by concentration and resuspension in a vivaspin concentrator, with 100 kDa MWCO, to exchange the NaCl for NaF. The samples were made up to 2 ml with NaF buffer and concentrated, then resuspended twice with fresh NaF buffer to complete exchange. At ~30 µl, the concentration of each fraction was measured by spectrophotometry and gave no absorbance at 280 nm (A_{280nm}). The flow through also gave no obvious A_{280nm} signal. From this, it was apparent that the protein had been lost to the membrane. Membrane proteins are sensitive to certain concentrator membranes due to their hydrophobicity and sample loss at this stage is not an uncommon occurrence in membrane protein purification. This was evidenced in figure 3.5B, where the protein is no longer visible in the concentrated fraction, but later re-appears after the membrane was washed extensively with high salt (1 M NaCl). It may be that the strength of a negative chloride ion was needed to keep TRPM2 in solution during

this process and prevent aggregation or sticking to the Vivaspin membrane. Therefore, this method of buffer exchange, specifically with the Vivaspin brand of centrifugal concentrators was not suitable for use with TRPM2, and future samples would have to be exchanged by other means.

A second purification was performed, but with 250 µl fraction volumes instead of 500 µl and gave a very similar elution profile to that observed in Figure 3.4A, whereby the most protein eluted after the addition of ~50 µg/ml of FLAGx3 peptide. The introduction of this gradient had already seemed to increase the reproducibility of the purification at this point. To examine the secondary structure content of the purified protein without concentration, each fraction was analysed by CD (Figure 3.5A).

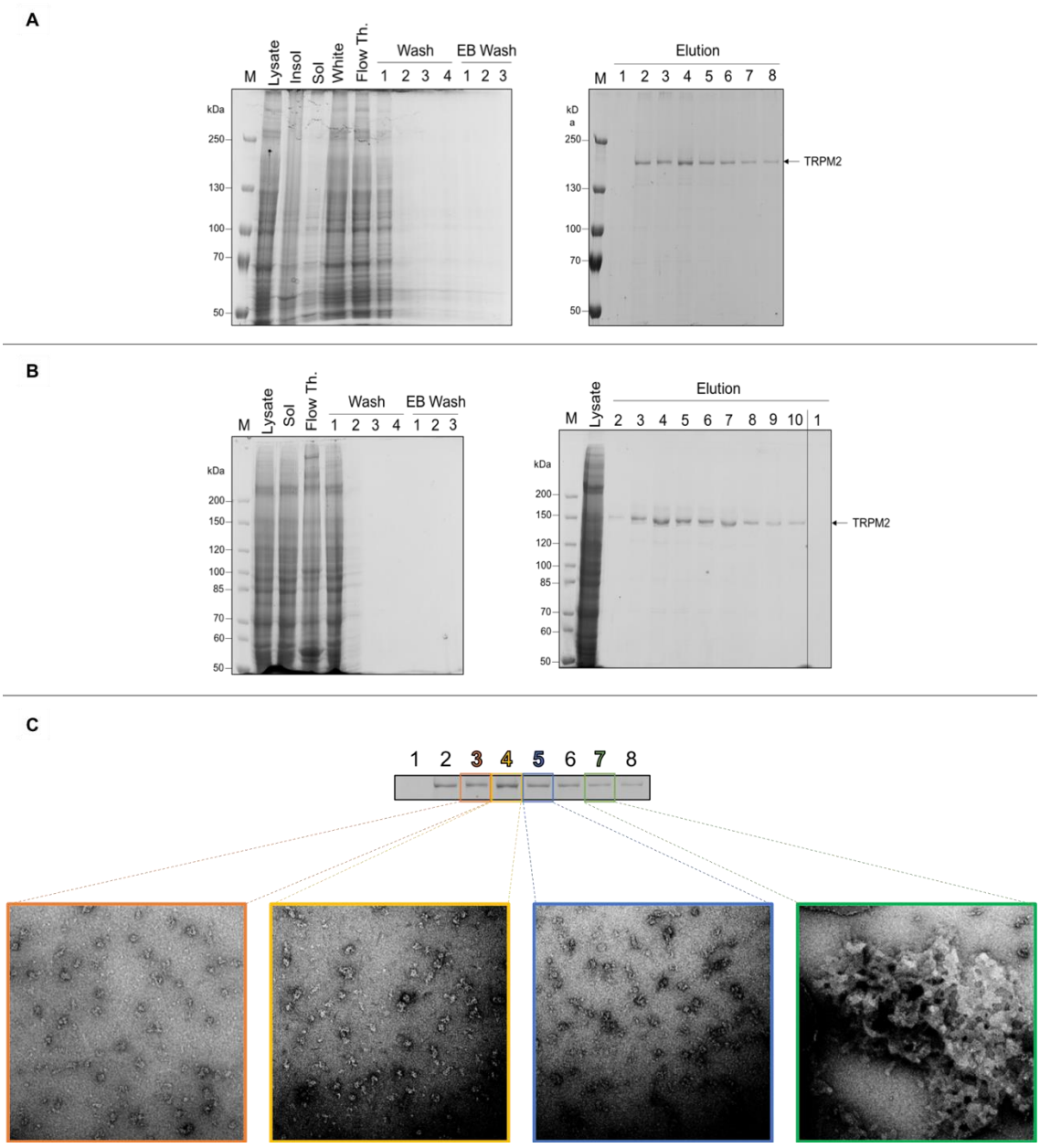

Figure 3.4: Introduction of FLAG peptide gradients to TRPM2-FLAG purification.

Gels are displayed as described in Figure 1, whereby samples taken throughout the purification process were analysed on a separate gel to the final elution fractions (labelled 1-8 (A) or 1-10 (B)). All samples were analysed alongside a molecular weight marker (M). The band representing TRPM2 is again indicated by the arrow in A and B. C) Negative stain micrographs of fractions 3, 4, 5 and 7 from B diluted 10x. Micrographs were taken at 30,000x magnification.

A

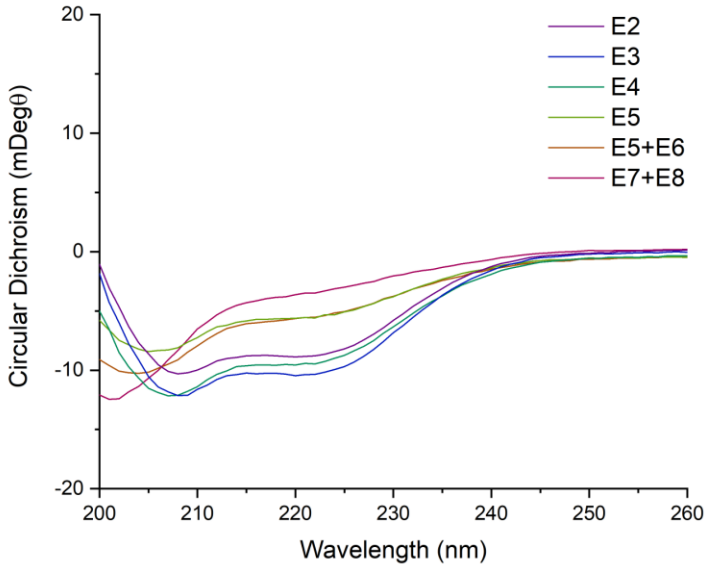

B

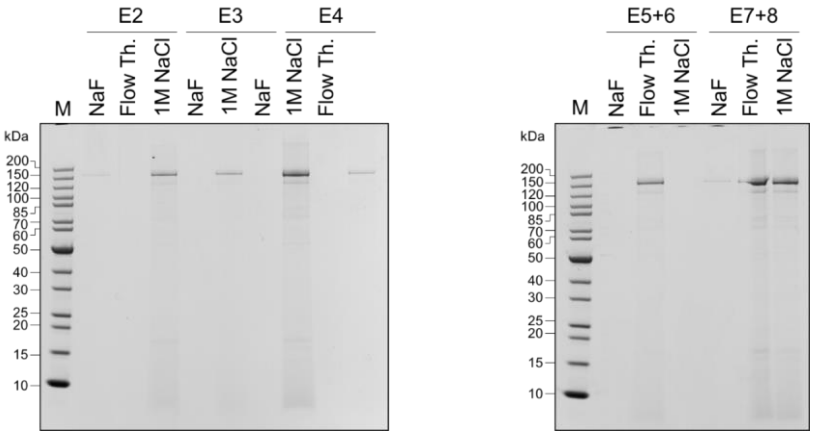

Figure 3.5: Circular Dichroism spectra of each fraction from a TRPM2 standard purification.

A) Circular Dichroism spectra of individual and pooled fractions shown in Figure 3.4B. Pooled fractions are indicated by '+'. B) High salt wash of vivaspin membranes elutes bound protein.

CD revealed that the protein component in each fraction was indeed different. Conventionally, a protein with a predominantly alpha helical content will absorb more right-handed circularly polarised light, giving a characteristic negative 'W' spectrum with maximum absorbance at 208 nm and 222 nm (Kelly, Jess and Price, 2005a; Greenfield, 2006b). Measurements beyond 200 nm in these samples were unreliable due to the presence of chloride and Tris in the buffer solution. To eliminate the possible contribution to the increasing FLAG concentration perhaps inducing a more unstructured spectra, FLAG peptide spectra were also measured. While there was some CD signal, it was not enough to justifiably dampen the signal obtained from TRPM2 purification fractions to the degree observed between fractions.

3.2.2.3 Examining SMA_TRPM2 aggregation with Size Exclusion Chromatography

Similar to negative stain, and in contrast to what was originally thought, the samples eluting later from the column appear to form aggregates more easily than the samples eluting earlier from the column. Without the complementary EM micrographs of each fraction, it might be assumed that the higher FLAG peptide concentration is contributing more to the unstructured signal observed for fractions 7-8. However, this is shown to not be the case, as the protein observed in these fractions is consistently aggregated when observed by EM. Interestingly, a contaminant at ~ 15 kDa is repeatedly observed as increasing in each fraction with increasing FLAG concentration. This can potentially be attributed to the SMA *co*-polymer itself.

While a standard purification protocol with FLAG peptide gradient had been established, the CD and negative stain EM micrographs suggested that there was

significant heterogeneity between TRPM2 elution fractions. Another purification was performed using the new gradient protocol and fractions E4 and E6 were subject to analytical size-exclusion chromatography (Figure 3.6A) to see any possible differences in sample composition that may give hints as to why we see such heterogeneity in negative stain. No absorbance was observed in the void volume (~5 minutes) for either sample, indicating the possible absence of such large aggregates as seen in negative stain.

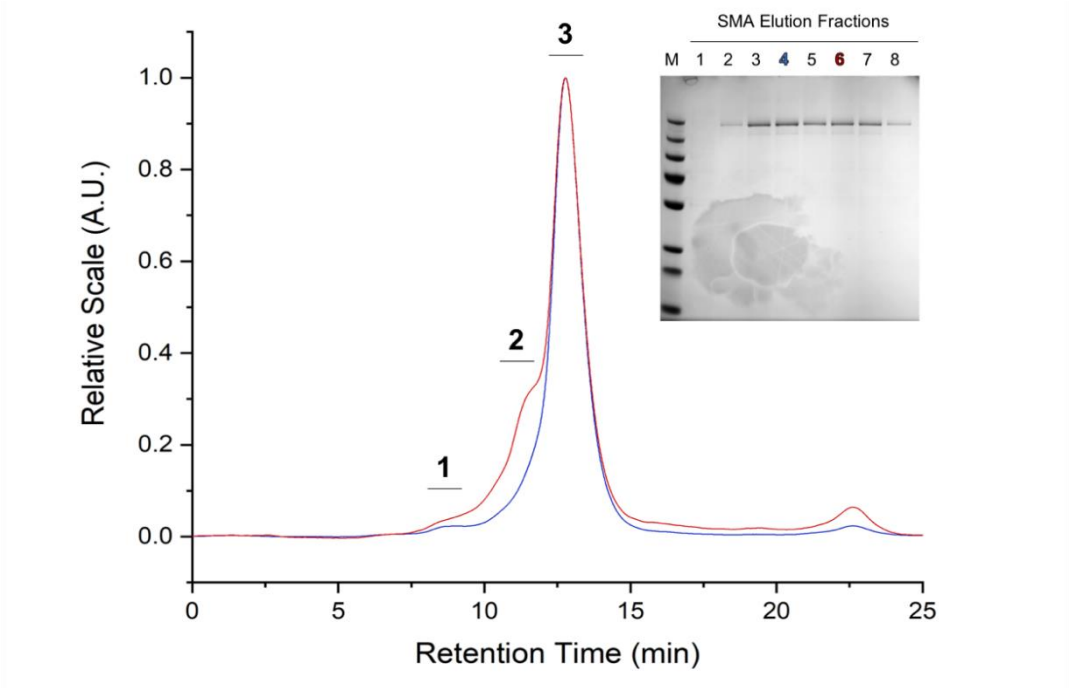

Figure 3.6: Size exclusion chromatography of TRPM2.

Fractions E4 (blue) and E6 (red) show TRPM2 eluting in three distinct peaks.

The protein concentrations were also too little to give any significant light scattering (LS) signal, but absorbance peaks can be observed at ~8.5 minutes, ~11.5 minutes and

~13 minutes (peaks 1, 2 and 3 in figure 3.6A, respectively). These were samples taken directly from the FLAG-elution, so the largest observable peak at ~13 minutes could be the absorbance from interfering FLAG peptide, and the TRPM2 peaks may be hidden in either shoulder peak 1 or shoulder peak 2. Based on molecular weights of standards ADH and comparison to SEC-MALLS of AcrB (Chapter 5), peak 1 is assigned as TRPM2. Despite the capabilities of SEC-MALLS as a technique for determining accurate mass measurements of proteins, no molar mass could be determined due to the lack of agreed refractive index modifier value (dn/dc) of SMA, relating to the polymer's high polydispersity index.

3.2.3 Optimisation of TRPM2 Purification in Detergents

3.2.3.1 TRPM2 in DDM

Prior TRPM2 purifications have been performed using SMA with success. However, when it comes to downstream biochemical assays, the polymer quickly reveals its limitations. Additionally, the polymer:protein complex appears to be unstable in cryo-electron microscopy (discussed later in this chapter). While there have been a number of attempts to rectify the apparent dissociation of the polymer in cryo-EM by altering grid types and vitrification conditions, none have proven resoundingly successful. This led to the development of an SMA-amphipol exchange method, described in chapter 5, but as the priority of this project is to determine the structure of TRPM2, large scale detergent purifications were performed as they are a tried and tested solution for structure elucidation by cryo-EM.

There are a number of issues arising from the continuous use of the SMA polymer for TRPM2 characterisation. Firstly, the polymer's inherent properties prevent the inclusion of divalent cations at any stage of the protein's lifetime, which eliminates the possibility of performing functional assays which require calcium ions. Secondly, the heterogeneity introduced by the polymer makes it unsuitable for structural averaging techniques such as single particle cryo-EM. It would therefore be beneficial to purify TRPM2 in a detergent that forms more homogeneous micelles and is more compatible with biochemical and functional assays. Anti-FLAG purification experiments have previously demonstrated that DDM solubilised TRPM2 (DDM-TRPM2) is able to bind the anti-FLAG affinity gel and can be eluted upon FLAGx3 peptide addition (Figure 3.8A).

A large-scale purification using 1 % DDM as a solubilisation agent was first performed on whole cell extracts and characterised analogously to SMA-TRPM2. This would allow for direct comparison with results from the SMA-TRPM2 purification. The purification was performed as standard using the gradient FLAGx3 elution protocol, albeit with decreasing concentrations of DDM in the wash (0.1 %) and elution (0.05 %) buffers. High concentrations of detergent micelles can severely interfere with downstream experiments, and it is conventionally better to decrease the detergent concentration in the eluent than to later attempt to remove it by dialysis or concentration, as micelles may remain. The results of the DDM purification are comparable to SMA purification of TRPM2 (Figure 3.7A and B).

A number of strong contaminating bands were observed by SDS-PAGE. The most prominent of these were analysed by peptide mass spectrometry, but no peptides were mapped to TRPM2.

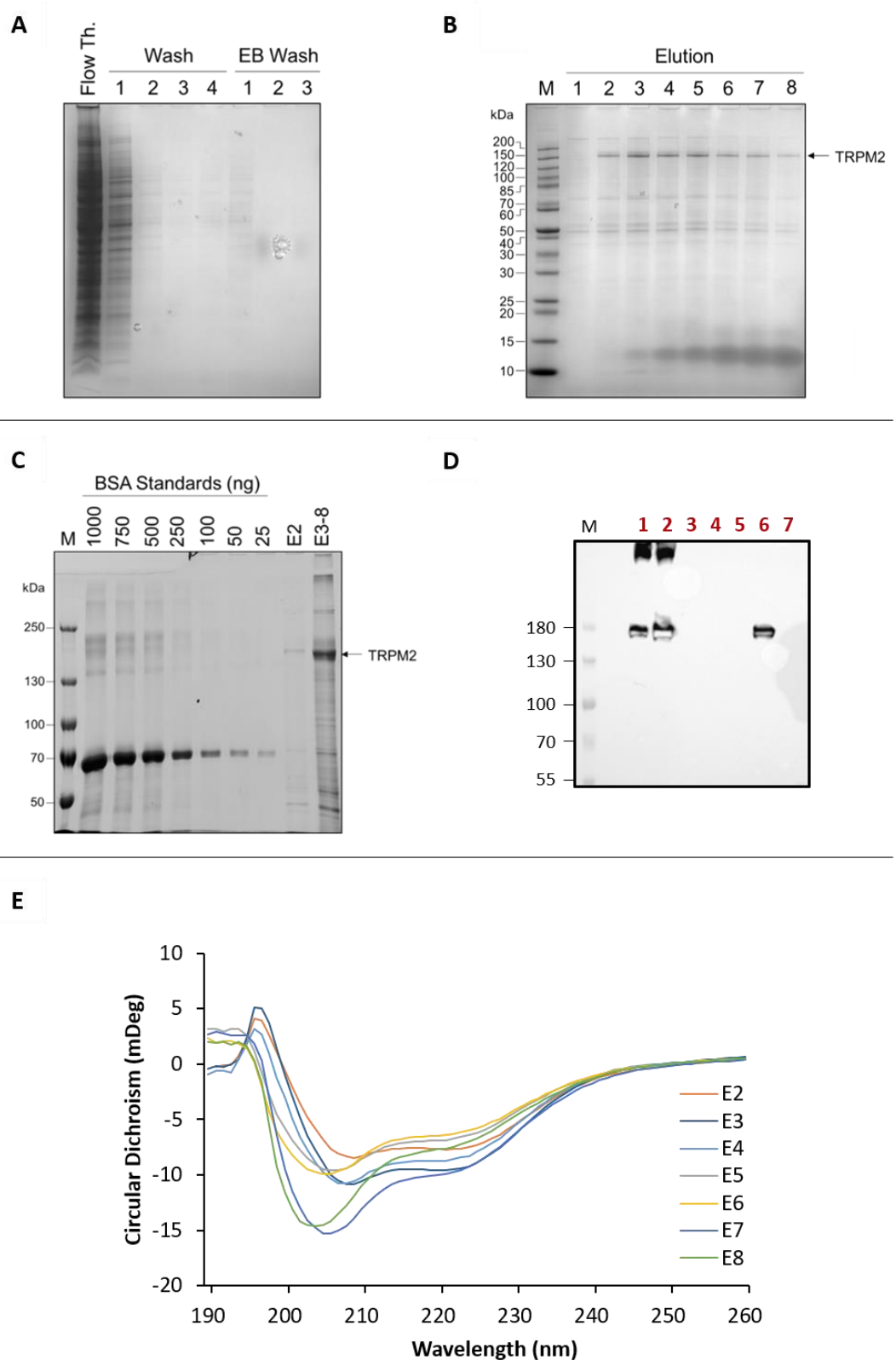
A
Flow Th.
Wash
EB Wash
1 2 3 4 1 2 3
B
Elution
M 1 2 3 4 5 6 7 8
kDa
200
150
120
100
85
70
60
50
40
30
30
25
20
15
10
TRPM2
C
BSA Standards (ng)
M 1000 750 500 250 100 50 25 E2 E3-8
kDa
250
130
100
70
50
TRPM2
D
M 1 2 3 4 5 6 7
180
130
100
70
55
E
Circular Dichroism (mDeg)
10
5
0
-5
-10
-15
-20
190 200 210 220 230 240 250 260
Wavelength (nm)
E2
E3
E4
E5
E6
E7
E8

Figure 3.7: SDS-PAGE, western blot and circular dichroism analysis of fractions from large scale purification of TRPM2 in DDM.

A) Wash and flow through fractions analysed by SDS-PAGE, displayed as described in figure 3.2 for SMA_TRPM2. The DDM concentration was decreased over this elution patter, with 1 % DDM represented in the flow through, 0.1 % DDM in the standard wash fractions and 0.05 % DDM in the EB wash fractions. B) SDS-PAGE of FLAGX3 peptide elution fractions 1-8, alongside a molecular weight marker (M). The band representing TRPM2 is highlighted by the arrow. C) Pooled eluent fractions (E3-8) from B were qualitatively quantified by comparison with varying nanogram (ng) concentrations of BSA alongside a molecular weight marker (M). D) Western blot of supernatant's taken at each stage of membrane solubilisation for troubleshooting TRPM2 detergent purification. Samples 1 and 2 are of DDM_TRPM2 and SMA_TRPM2 solubilised from whole cells. Samples 3 and 4 are from the pellet and supernatant of a 2000 xg centrifugation step after lysis. Sample 5 is the supernatant after centrifugation of the whole cell lysate. The membrane fraction was solubilised in DDM, and a final centrifugation step revealed TRPM2 in the supernatant shown in sample 6, with no detectable TRPM2 in the insoluble pellet (sample 7). E) Circular dichroism (CD) spectra of individual elution fractions (E) 2-8 in millidegrees (mDegθ).

In most cases repeats of this experiment on a large scale proved challenging, as TRPM2 remains in a soluble state only for a short period of time before it starts to become unstable and insoluble. Initially, it was the hope that TRPM2 would form more homogenous particles in solution when purified in DDM due to the nature of the

detergent micelle. It was also the hope that if TRPM2 could be purified in DDM, it would better tolerate centrifugal concentration with a spin concentrator, as SMA was found to aggregate and stick to the membrane in this process (Figure 3.5). Fractions E3-8 from the purification were pooled and concentrated using a Vivaspin 50 kDa MWCO concentrator, and the resulting protein solution was analysed by SDS-PAGE, alongside BSA standards (Figure 3.2C). there were consistently more contaminants in the DDM preparations that may interfere when calculating the true DDM-TRPM2 protein concentration.

The concentration of the final sample was measured by spectrophotometry and by comparison to a series of BSA standards. The concentration was determined to be ~0.8 mg/ml in ~100 µl by spectrophotometry. However, as can be seen from the BSA gel in Figure 3.2C, the final TRPM2 concentration appears to be closer to 0.25 mg/ml (250 µg/ml). While TRPM2 at this concentration may have been suitable for cryo-EM, the protein was obviously unstable in this detergent, and precipitates were visible to the eye upon concentration. Large quantities of insoluble material could also be pelleted by centrifugation less than 24 hours after concentration. As the protein was less stable in DDM than SMA in this regard, freezing for storage was not attempted.

As EM and CD analysis of SMA-TRPM2 provided complementary results as to the state and folding of SMA-TRPM2 in each fraction from the purification, individual fractions from whole cell DDM-TRPM2 purifications were examined by CD (Figure 3.7E). Detergents, particularly DDM, are extensively used when examining CD of membrane proteins (Miles *et al.*, 2016). This removes the possibility of SMA contributing to the overall CD spectra and may give an indication as to the folded state

of protein in each fraction. Consistent with SMA purifications, fraction 1 contained no TRPM2 by SDS-PAGE and was not examined.

The CD spectra of DDM-TRPM2 fractions display a similar pattern to the SMA-TRPM2 preparations, but the loss in TRPM2 fold to a more disordered state in later fractions become strikingly clear (Figure 3.7E). E2 and E3 appear to have the characteristic spectra observed in SMA elution fractions, but DDM_TRPM2 starts to lose integrity from E4. From this data alone, E3 appears to contain the best quality protein. Interestingly, this data highlighted another pattern – that the FLAG peptide concentration might be contributing to the overall CD signal. This is evident as each elution pair (those fractions eluted with the same FLAG concentration), appear to display similar secondary structure properties in CD (see differences between E3-4, E5-6 and E7-8 in Figure 3.7C), and there is an apparent gradual increase in protein disorder with each spectra.

It was also clear that detergent purification of TRPM2 from whole cells came with a large degree of contamination and needed to be optimised further (Figure 3.7A and B). To increase the purity of DDM-TRPM2, a membrane isolation step was included prior to solubilisation. Isolation of cell membranes prior to purification is a long-standing procedure in the field of membrane protein structural biology, as it has many advantages over whole cell solubilisation; primarily the generation of a correctly folded product with increased purity (Eylar and Hagopian, 1971).

However, on more than one occasion no protein was visible in the elution fractions. To test the feasibility of an isolated membrane prep in producing enough protein for EM studies, a comparison solubilisation test was set up, with iterations of centrifugation and resuspension steps. Samples were taken from each stage of the

purification, normalised according to protein content (as measured BCA assay), and analysed by anti-FLAG western blotting against an SMA-solubilised control (Figure 3.7D). As expected, no TRPM2 was found in the soluble fractions prior to the addition of DDM (fractions labelled 3-5 in Figure 3.7D). It is likely that TRPM2 can be found in the soluble fraction after the 200,000 xg centrifugation step (denoted 4 in the schematic and blot, Figure 3.7D), but as the samples were normalised to the total protein content it is likely that the TRPM2 signal intensity was overshadowed. Back-calculation of the amount of TRPM2 solubilised from whole cells or membranes relative to the starting volume gave a loss of ~80 %. From this, it was discerned that membrane preparations were not a sustainable form of purification due to the sheer mass of cells required to make up for this sample loss, and for this reason, TRPM2 was only purified from whole cells for the purpose of these studies.

Previous data from SMA-TRPM2 purifications strongly suggest that fractions eluted later from the anti-FLAG column tend to be more aggregated, and it was interesting to see that this pattern followed through to DDM-purified samples.

3.2.4 TRPM2 purification in DDM with CHS

Detergent purification of TRPM2 with DDM alone was becoming fruitless. However, it was becoming more common in membrane protein cryo-EM to supplement DDM with cholesterol hemisuccinate (CHS). CHS is a natural cholesterol mimic which serves to stabilise the membrane protein of interest outside of its native lipid environment – particularly if the membrane protein in question sequesters to lipid rafts or more structurally rigid regions of the bilayer (Nicolson, 2014). For this reason, TRPM2 was solubilised with 1% DDM supplemented with 0.2% CHS and purified in

the same way as previously described for DDM-TRPM2. For washing and elution, the DDM:CHS concentration was dropped 0.1% DDM:0.02% CHS to remove excess micelles. SDS-PAGE analysis of the purification was successful, yielding high concentrations of TRPM2 (Figure 3.8A).

Based on previous results showing disparity of aggregation between fractions of SMA-TRPM2, fractions were treated and examined individually without pooling. Fractions E4-E6 were analysed by CD and showed that the protein in these fractions was folded (Figure 3.7C). These samples went on to be used in the CD thermal denaturation experiments described later in this thesis. Negative stain analysis revealed that fractions E5, E6 and 7 contained TRPM2 like particles, but were surrounded by excess detergent micelles (Figure 3.8D). Further purification attempts incorporated the use of centrifugal concentrators, which appeared to help reduce the number of background micelles, revealing TRPM2-sized particles in negative stain (Figure 3.8E).

LMNG:CHS purification of TRPM2 was also trialled and gave similar results, albeit the excess micelles from this preparation were more difficult to remove than the DDM:CHS micelles (data not shown).

Figure 3.8 (overleaf): DDM:CHS purification of TRPM2.

A) Wash and elution fractions of DDM:CHS_TRPM2 analysed by SDS-PAGE. The DDM concentration was decreased over this elution profile to 0.1%DDM:0.02%CHS in the elution fractions. B) Pooled eluent fractions 4, 5 and 6 from A were qualitatively quantified by comparison with varying nanogram (ng) concentrations of BSA alongside a molecular weight marker (M). C) The same elution fractions were analysed by circular dichroism. Negative stain micrographs were obtained of individual fractions E5, E6 and E7 (D), before concentrating these fractions together to give results in E.

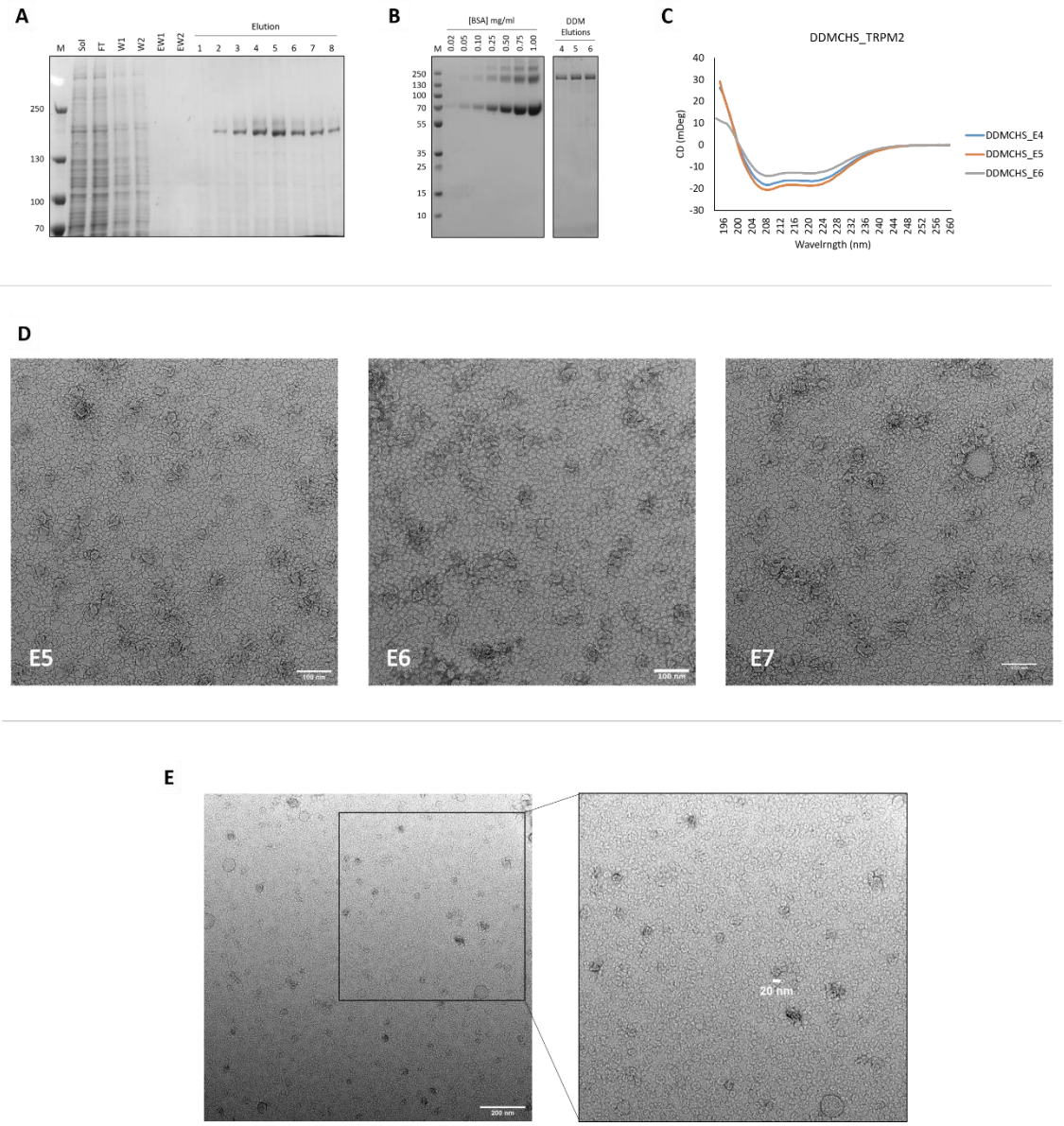

3.2.5 Lipid Analysis of SMA-Extracted TRPM2 by TLC

These experiments were conducted with the generous help of Arndt Rohwedder.

Thin layer chromatography can be used to separate lipid species in a given mixture by polarity. It had been demonstrated that the SMA polymer extracts and sequesters lipids within its transmembrane annulus (Postis *et al.*, 2015a), and this has also been reflected

in the excess mass that membrane proteins in SMA can carry (SEC-MALLs and by native-PAGE).

Fractions E3-5 were taken from a standard purification and kept separately for lipid analysis. Each fraction was subject to methanol:chloroform extraction by a modified Folch method (Yang and Han, 2016) - which includes the addition of hydrochloric acid - to remove the protein, SMA polymer and salts, leaving an organic phase containing lipid-only particles. Due to the hydrophobicity of membrane proteins, care was taken as to not include the precipitant layer at the interphase.

Samples were then spotted in a linear fashion onto a HPTLC plate and developed in two sequential runs - first with a less polar solvent to facilitate migration of neutral lipids and sterols, then a more polar solvent for phospholipids. The plates were then stained with copper sulphate and charred for visualisation (Figure 3.9; Churchward et al., 2008).

Each fraction was shown to contain a portion of phospholipids and cholesterol (CH), which were partially expected as TRPM8 (Morenilla-Palao *et al.*, 2009), and other TRP channels, particularly TRPV's (Taberner *et al.*, 2015), have been shown to sequester to lipid raft domains rich in cholesterol. Perhaps the most surprising result was the abundance of cerebrosides (CB) present in the sample. The concentration of cholesterol and cerebrosides extracted from the samples together almost oversaturated the detector, potentially masking the presence of other lipids in the sample, but these were still visible as bands of; phosphatidic acid (PA), phosphatidylethanolamine (PE), phosphatidylinositol (PI) and phosphatidylcholine (PC). No sphingomyelin was detected, which was surprising given its ~11 % contribution to HEK293 cell membranes (Dawaliby *et al.*, 2016). However, one study examining the effect and

activation of TRPM3 by sphingosines has previously pointed stated that TRPM2 did not significantly respond sphingosine when tested (Grimm *et al.*, 2005). The lipidome of HEK293 cells has not been fully explored, but it is known that they are somewhat more similar to neurons in their physiology than kidney cells (Shaw *et al.*, 2002), and it would not be surprising to find they contain this lipid enrichment in the bilayer.

Results from the TLC experiment not only confirm the presence of lipids in the SMA-extracted protein but demonstrate that a wide range of native lipids have been extracted alongside TRPM2 that may also have a physiological role in channel function.

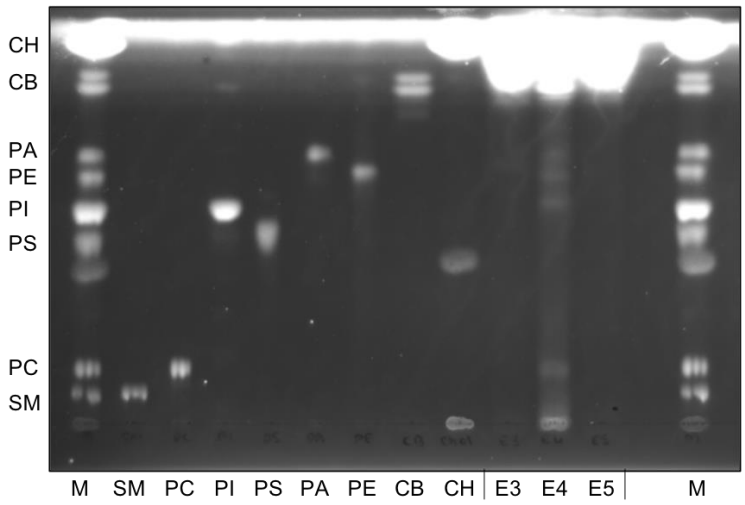

Figure 3.9: Thin-layer chromatography of lipids extracted from SMA purified TRPM2 samples.

M represents an overall lipid 'marker', which is a mixture of cholesterol (CH), cerebrosides (CB), phosphatidic acid (PA), phosphatidylethanolamine (PE), phosphatidylinositol (PI), phosphatidylserine (PS), phosphatidylcholine (PC) and sphingomyelin (SM) lipid standards. The standards were also run individually alongside samples E3, E4 and E5, which represent the lipid extracts from individual fractions of a standard SMA_TRPM2 purification.

3.3 Summary of TRPM2 Expression and Purification

The aim of this project is to characterise the TRPM2 channel *in vivo*, primarily using cryo-EM. To perform these experiments, TRPM2 must first be expressed and purified to sufficient quality – displaying homogeneity and monodispersity when examined by negative stain, and correct folding when analysed with CD – in high yields for structure determination. Homogeneity was achieved through introduction of a FLAG peptide elution gradient, which as shown in negative stain, significantly improved particle monodispersity and reduced aggregation (Section 3.2.2). Using large quantities (~5g) of cell pellet and reducing the elution volume of each fraction from the anti-FLAG resin also increased the yield.

Previous structures of TRP channels had been solved at concentrations of 5 μM (~0.47 mg/ml) and 0.5 mg/ml for TRPV1 (Liao *et al.*, 2013) and TRPA1 (Paulsen *et al.*, 2015), respectively, so these were the target concentrations. After initial optimisation of the anti-FLAG purification by the introduction of a gradient, results here demonstrate that SMA_TRPM2 eluted from the anti-FLAG resin in fraction E4 consistently at concentrations between ~0.2-0.3 mg/ml. This was below the target concentrations cited in the literature, but as TRPM2 was almost twice as large as TRPV1 and 1/3 larger than TRPA1, it was hoped that the size compensated in particle visibility when samples were examined in cryo-EM.

Another emerging concern was the use of the SMA polymer for downstream experiments, as divalent cations would be required for functional assays. Additionally, use of the SMA polymer seemed to be an emerging problem during cryo-grid preparation, as conventional blotting paper used during vitrification contains divalent

cations which can destabilise the complex (Drulyte *et al.*, 2018). To create an additional avenue for TRPM2 characterisation, detergent purifications were also trialled.

Initial purifications of TRPM2 in detergent were largely unsuccessful, consistent with previous reporting of TRP channel instability in detergent systems without additives (Paulsen *et al.*, 2015). As demonstrated in this chapter, it is clear that the inclusion of a cholesterol hemi-succinate (CHS) – a cholesterol mimic – was crucial to the successful purification of TRPM2 in a detergent system for downstream analysis. With CHS, the purified protein had an increased half-life, and appeared stable and folded when analysed with circular dichroism (Section 3.2.4). However, when DDM:CHS_TRPM2 was examined by electron microscopy, it was clear that DDM:CHS micelles were a significant contamination (Figure 3.8). Detergent contamination has been previously reported as a consistent issue in single particle electron microscopy, as it reduces the signal-to-noise ratio and micelle contamination can often overshadow the presence of protein on the grid (Gewering et al., 2018). Further attempts to remove excess micelles were made by size exclusion chromatography, but this led to complete loss of the sample in the chromatography system (data not shown). However, it was possible to continue with spectroscopic studies of TRPM2 using techniques such as circular dichroism.

The importance of CHS addition to the preparation of TRPM2 was later discovered upon lipidomic assessment of the native SMA_TRPM2. When lipids were extracted from the purified SMA_TRPM2 complex and analysed by thin-layer chromatography (TLC), it was surprising to discover not only that cholesterol and cerebrosides co-extracted, but that they were significantly abundant in the sample (Figure 3.9). This

was the first demonstration of cholesterol and cerebroside co-localisation with TRPM2, and has significant implications for channel function, regulation and potential sequestration to lipid microenvironments. This has been particularly eluded to for TRPM8 – the closest family member of TRPM2 (Fleig and Penner, 2004b). For TRPM8, segregation to lipid rafts and the role of glycosylation have been directly linked (Morenilla-Palao *et al.*, 2009). Additionally, identification of phosphoinositol (PI) in purified SMA_TRPM2 has exciting implications as to the functionality of the purified TRPM2 product, as PI lipids have been shown to facilitate regulatory roles in a number of TRP channels (Jirku *et al.*, 2015; Morales-Lázaro, Lemus and Rosenbaum, 2017), including TRPM2 (Tóth and Csanády, 2012; Z. Zhang *et al.*, 2018b).

These findings are discussed further in Chapter 7, and form the basis of further investigation into the differential characteristics of TRPM2 in detergents vs native membranes via a number of biochemical and biophysical techniques.

Chapter 4:

Bioinformatic Analysis of TRPM2

4.1 Introduction

TRPM2 contributes in a large number of cell physiological and pathophysiological processes through interactions with ROS, ADPR, Calcium and lipids (Sumoza-Toledo and Penner, 2011). However, in the absence of structural information, its precise mechanism remains unknown. Elucidating the structure-function relationship of TRPM2 was a primary goal of this project and is explored experimentally and bioinformatically in Chapter 4 and Chapter 5, respectively.

In this chapter, the architecture and conformation of TRPM2 was examined *in silico* with structure prediction servers Phyre2 (Kelley *et al.*, 2015), I-TASSER (Roy, Kucukural and Zhang, 2010), and SWISS-MODEL (Biasini *et al.*, 2014), using the primary protein sequence of *hs*TRPM2 (UniProt ID: O94759, isoform 1). All structure prediction servers start by assigning secondary structures to the primary sequence, according to the propensity of a given amino acid to form α-helices, β-strands, or irregular coiled domains, according to their backbone geometry (Kabsch and Sander, 1983).

Template-based structure prediction servers Phyre2, I-TASSER and SWISS-MODEL couple this experimentally-derived geometric data with comparative modelling – a method that performs multiple-sequence alignments to proteins of known structure – to predict the possible folding and topology of whole proteins and their sub-domains (Roy, Kucukural and Zhang, 2010; Biasini *et al.*, 2014; Kelley *et al.*, 2015). The prediction servers then generate 3D models; SWISS-MODEL applies the protein sequence directly to the highest scoring homologous structure (Biasini *et al.*, 2014), whereas I-TASSER and Phyre2, generate *ab initio* models by threading – the process

of threading parts of the protein sequence through the homologous structures to generate a model – and performing a final simulation to create an energetically favourable model (Roy, Kucukural and Zhang, 2010; Kelley *et al.*, 2015). Regions of interest identified as a result of homology modelling were then analysed with EV Complex (Hopf *et al.*, 2014) – which searches for potentially co-evolved residues within a protein sequence or between two given sequences – to discern possible PPIs between sub-domains in the full-length TRPM2 homotetramer.

However, structure predictions for large membrane protein sequences can be unreliable (Gniewek *et al.*, 2012), as they often contain several sub-domains which can be incorrectly aligned when grafting into one single polypeptide chain (Kelley *et al.*, 2015), and contain extensive hydrophobic regions which can collapse during simulations (Jefferys, Kelley and Sternberg, 2010; Deng, Jia and Zhang, 2018). For all three modelling programmes used here, potential transmembrane regions are identified but are discounted during modelling and subsequent simulations (Roy, Kucukural and Zhang, 2010; Biasini *et al.*, 2014; Kelley *et al.*, 2015).

At the time of analysis, high resolution structures were available only for TRPV1 (Liao *et al.*, 2013) and TRPA1 (Paulsen *et al.*, 2015), and the structure predictions presented here provided exciting insights into the TRPM family architecture, including TRPM2. However, during the course of this project, several high resolutions structures of TRPM family members (Huang *et al.*, 2020), including TRPM2, were solved from high (≤3.5 Å) to moderate (≤6.5 Å) resolution, in a combination of ligand-bound and ligand-free states (Table 1). As a result, comparisons between the structures predicted bioinformatically by Phyre2, I-TASSER and SWISS-MODEL, to the recently published structures of TRPM2 by Huang et al., 2019 have been made within the text.

4.2 Results and Discussion

4.2.1 Structural Bioinformatics

4.2.1.1 Identification of coiled-coil domains and putative calmodulin-binding domains.

Coiled-coils (CC) function in a wide variety of intra- and inter-molecular protein-protein interactions (PPI). For mammalian TRP channels, the C-terminal CC functions in channel assembly, trafficking to the membrane and through PPI can add another mechanism of regulation (Erler *et al.*, 2006; Mei *et al.*, 2006; Tsuruda, Julius and Minor, 2006). In *Drosophila*, oligomerisation of TRP is a result of an N-terminal CC domain (Xu *et al.*, 2000), and mammalian TRPC channels utilise both an N- and C-terminal CC domains to control oligomerisation (Myeong *et al.*, 2016). A high-resolution crystal structure of the TRPM7 C-terminal CC revealed a tightly packed, antiparallel, left-handed tetrameric assembly in isolation (Fujiwara and Minor, 2008). The same study suggests that only TRPM1/3/6/7 are predicted to form anti-parallel CCs (Fujiwara and Minor, 2008).

Later structures of TRPM2 and most other TRPM channels lack density in this region, but the structure of TRPM4 shows a parallel CC domain (Winkler *et al.*, 2017), consistent with the prediction by Fujiwara and Minor (2008). However, steric hinderance from the downstream CTD in other TRPM channels would suggest that an anti-parallel CC cannot form within an individual channel, and this may be more a mechanism of regulation by splice variants which can negatively affect channel trafficking and activity (Launay et al., 2004; Tsuruda et al., 2006; Erler et al., 2006).

Sequence alignments of TRPM channels have predicted the presence of an N-terminal CC domain, but due to the low probability of forming this domain (40%; Tsuruda et al., 2006), it was not reported further until 2009, when Mei and Jiang (2009) identified a region between residues 658-681 of TRPM2 with high (90%) CC-forming probability. However, in that time the structures of TRPV1 and TRPA1 were published and were not found to have an N-terminal CC (Liao *et al.*, 2013; Paulsen *et al.*, 2015), and more data on coiled-coil regions had become available for prediction algorithms. For this reason, the TRPM2 primary sequence was re-assessed.

To identify the coiled-coil regions of TRPM2, the protein primary sequence was analysed by PCOILS (Lupas, Van Dyke and Stock, 1991; Zimmermann *et al.*, 2018). PCOILS compares input sequence to known coiled-coil forming sequences taken from a common MTIDK matrix, derived from structural information from myosins, paramyosins, tropomyosins, intermediate filaments type I - V, desmosomal proteins and kinesin. The primary sequence is then scored according to coiled-coil forming propensity and heptad periodicity in sliding windows of 14, 21 and 28 residues – for TRPM2, sliding windows of 28 were used in the original publication from Tsuruda et al., 2006, and windows of 24 and 28 were used by (Mei and Jiang, 2009). Calculations can also be weighted or unweighted to account for unreliable scoring of highly charged sequences, which may at first seem like coiled-coil domains but do not follow conventional heptad periodicity.

Both weighed and unweighted results highlighted two regions of interest within the TRPM2 primary sequence with high probability; residues 658-680 in the N-terminal cytosolic domain, and residues 1172-1200 in the C-terminal cytosolic domain. These are consistent with the previously reported results by Mei and Jiang, 2009. The only

available structure for the C-terminal CC domain is of a high-resolution X-ray crystal structure of the TRPM7 C-terminal CC region, which revealed a tightly packed, antiparallel, left-handed tetrameric CC assembly (Fujiwara and Minor, 2008). However, in the context of an individual channel, an anti-parallel CC is unlikely, as steric hinderance from the CTD may prevent the channel folding back on itself. When both CCs identified here are mapped to the recent TRPM2 structure (Huang *et al.*, 2019), these residues are seen to flanks the transmembrane domain, and do not form a clear CC-like structures (Figure 4.1). Additionally, no density is available for the C-terminal CC domain in any of the available TRPM2 structures, so this remains to be discovered (Figure 4.1). Although it is interesting to speculate that anti-parallel CCs may play a role in inhibition by splice variants, there is no clear evidence for the orientation, or location of the C-terminal CC relative to the rest of the structure.

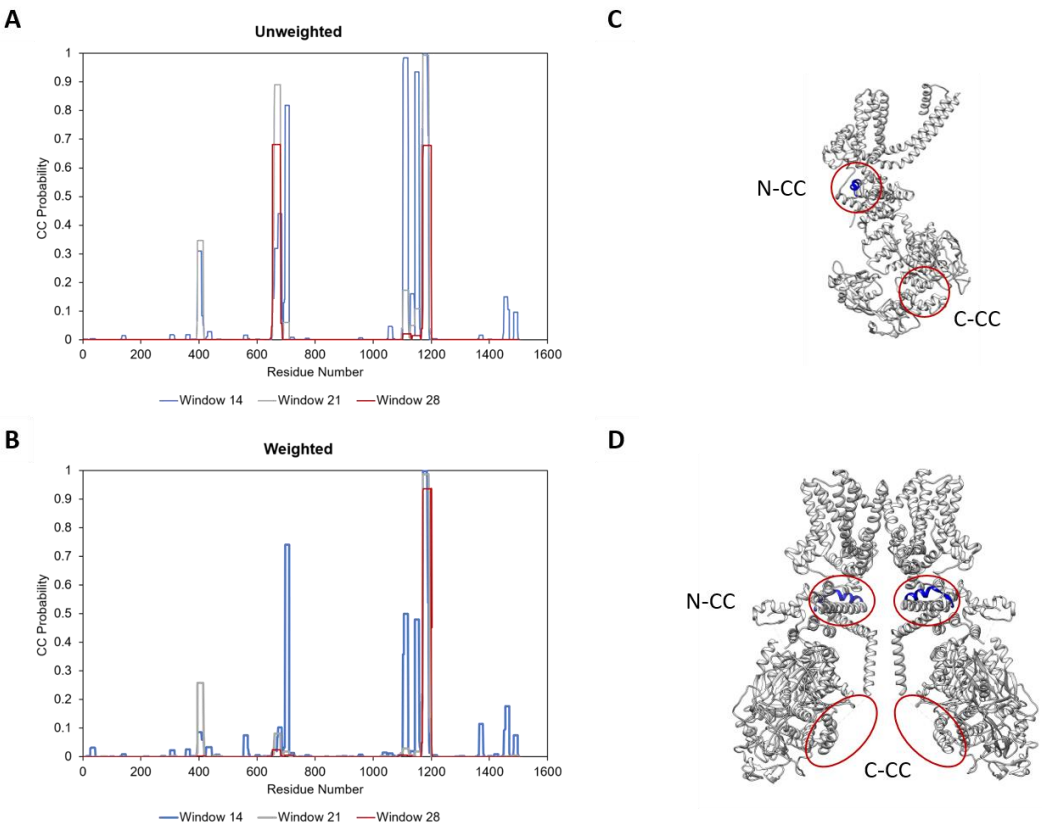

Figure 4.1: Probability of coiled-coil forming regions within the TRPM2 primary sequence. Unweighted (A) and weighted (B) PCOILs predictions of coiled-coil forming probability (0-1) for each residue in the TRPM2 primary sequence, according to sliding windows of 14, 21 and 28 residues. Predicted CC domains 658-680 and 1172-1200 were mapped to locations on a either one (C) or two (D) chains of the tetrameric TRPM2 structure, shown in orange and highlighted with blue circles (PDB: 6PUU).

4.2.1.2 Bioinformatic identification of calmodulin-binding domains.

While it is useful to analyse the TRPM2 primary sequence for inherent structural motifs, it would be beneficial to highlight any potential PPI motifs or domains so that they can be explored as stabilising factors for EM, as well as potential binding studies with purified protein. The calcium-binding modulatory protein Calmodulin (CaM), has been previously shown to influence TRPM2 function through direct binding to a canonical IQ motif in the intracellular N-terminal region (residues 404-416) (Tong *et al.*, 2006). The TRPM2 primary sequence was therefore screened by the calmodulin target database to search for further potential CaM-binding domains (results in figure 4.1E). The prediction server correctly identified the known IQ-motif corresponding to the calmodulin binding site in the N-terminal region of TRPM2 between residues 404-416, albeit with a maximum scoring of 5/9. According to the server, values <5/9 are of low confidence.

Two additional putative CaM binding sites between residues 768-780, and 950-968 were also indicated. Neither site had been reported previously, but the existence of a CaM binding domain between residues 1087-1101 has been eluded to (Lockhart, 2012). The site at 768-780 scored equally with the known CaM binding site (5/9), but when mapped to the published structure, is situated in or near the transmembrane domain, and is therefore an unlikely true CaM-binding candidate (Figure 4.1E). Interestingly, the highest scoring CaM-binding region was flagged between residues 943-980, located in the pore domain. The highest scoring residues (>7/9) in this region span aa. 950-968, which map precisely to the extracellular loops of the S5-pore helix domain (Figure 4.1F). While a role for extracellular CaM signalling has been

suggested in mammals, this field remains almost unexplored (O'Day, Huber and Suarez, 2012). This peptide sequence is also conserved within TRPM8 (Mei, Mao and Jiang, 2006). In *nv*TRPM2, Asp1017 functions as a glycosylation site in the pore domain (Iordanov *et al.*, 2019). Based on sequence alignments of *nv*TRPM2 and *hs*TRPM2, there likely is a putative glycosylation site in this region, and it is therefore an unlikely CaM binding site.

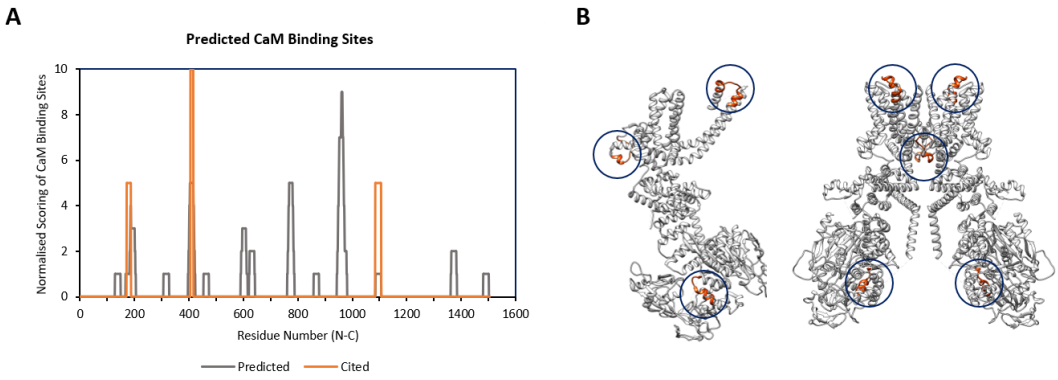

Figure 4.2: Predicted calmodulin-binding sites.

A) Results from the Calmodulin Target Database (grey; Predicted) mapped according to the database scoring system from 1-9 for each residue. Cited calmodulin binding sites according to the literature have been manually added with a score of 10 for confirmed and 5 for speculative (yellow). B) Predicted CaM domains 404-416, 768-780 and 950-968 were mapped to the structure of TRPM2 (orange) and highlighted for clarification with blue circles.

4.2.2 3D Structure Prediction

4.2.2.1 Phyre2

Phyre2 is a 3D modelling software which uses published structures from the Protein Data Bank (PDB) to predict a structural model for a given protein sequence (Kelley *et al.,* 2015). The transmembrane and C-terminal regions of TRPM2 are already well characterised in terms of their structural homology; but the 3D structure of the intracellular N-terminal TRPM homology region (MHR) remains elusive. The full protein sequence as well as isolated N-terminal residues 1-752 were input to the Phyre2 structure prediction server to shed light on the secondary and tertiary structure of this region.

The server was able to assign 83% of the full protein sequence into structured or disordered regions. The remaining 17% of the sequence was not assigned due to low confidence scores. Tertiary structures could be assigned to residues 168-390 and 432-744, accounting for 71.2% of the N-terminal domain. The transmembrane and NUDT9H domains were mapped to known TRPV (PDB ID: 3J5P) and mitochondrial NUDT9 structural homologues PDB ID: 1YDH), but their assembly within the context of TRPM2 as a whole channel could not be discerned.

4.2.2.1.1 Identification and implication of 'SLOG' domains in TRPM2

The top 10 structural homologues generated from analysis of the N-terminal MHR suggested that protein folds reminiscent of molybdenum *co*-factor carrier proteins (MCP/YspA-like proteins), lysine2 decarboxylase-like domains, and 'Lonely Guy'

(LOG) could be identified within the TRPM2 sequence. These primarily eluded to the presence of this domain between residues ~168-390, with a fold and alignment confidence of ≥97.8 % (Figure 4.3).

The 'Lonely Guy' or LOG protein is a cytokinin-activating enzyme initially identified from a mutant strain of rice (Kurakawa *et al.*, 2007). It was later identified in *Arabidopsis thaliana* (*A.t*) (Kuroha *et al.*, 2009). In both organisms, the LOG protein functions as a dimer to hydrolyse cytokinin nucleoside 5'-monophosphates into D-ribose 5-phosphate and the associated cytokinin product (Kuroha *et al.*, 2009). A homologue of this LOG protein was later identified in *Mycobacterium tuberculosis* (*M.tb*), where it is responsible for proteasome-mediated NO resistance, and facilitates *M.tb* persistence *in vitro* and *in vivo* (Samanovic *et al.*, 2015; Zhu and Javid, 2015).

These domains adopt a three-layer α/β sandwich Rossmannoid-fold, which facilitates nucleotide binding (Figure 4.1; Rao and Rossmann, 1973; Burroughs et al., 2015). At the time, the only other reference to a nucleotide binding pocket in the MHR was for TRPM4, where two intracellular N-terminal Walker-B motifs and an ABC-transporter signature-like motif had been described (Nilius *et al.*, 2005). This pocket was not reported in any study of TRPM2 when these results were generated. However, an exciting finding came from a comparative genomics study, which was the only evidence in the literature linking LOG domains to the TRPM family of ion channels (Burroughs *et al.*, 2015). The term 'SLOG' was coined in this genomics study, which stemmed from the sequence similarity of the TRP MHRs to another LOG family of nucleotide and molybdenum binding proteins known as SMF/Dpr-A (SLOG), and this nomenclature was adopted here.

The discovery of the SLOG domain has interesting and novel implications for the function of TRPM2. For example, mammals do not synthesise cytokinin's, so this could imply the TRPM2 and perhaps, TRPMs, could play a connecting role in plant cytokinin sensing in mammalian pathophysiology. Specifically, plant cytokinin's have been recently linked to calcium regulation of insulin release in diabetes (Bruzzone *et al.*, 2008), cell proliferation (Scarfì *et al.*, 2009), apoptosis (Voller *et al.*, 2010), and inflammation (Bruzzone *et al.*, 2007). TRPM2 has been found to play a role in all of the aforementioned physiological processes and would be interesting to speculate a role for TRPM2 in the sensing of plant signalling molecules. There is evidence of adenosine A_{2A} receptor activation as a result of raised cyclic-AMP levels from cytokinin activation of GPCRs (Lappas, 2015), but besides that, no direct cytokinin receptor has been identified to date.

4.2.2.1.2 Identification and Implication of ANK-like domains in TRPM2

Of the remaining hits, a large number eluded to the presence of highly helical components potentially associated with an ankyrin-repeat domain between residues 432-744, analogous to those found in TRPV1 (Figure 4.3). This region is mapped after the SLOG domain, between the CaM-binding IQ motif and transmembrane region. It was concluded early on that the TRPM channels contained no ANK domains, as insertions and deletions in the TRPM MHR cause it to bear little sequence homology to other ANK-rich TRP channel subfamilies (Harteneck, Plant and Schultz, 2000). No studies have mapped canonical ANK motifs to the MHR of any TRPM channel family member since, confirming its absence and divergence (Montell *et al.*, 2002b). However, the same genomic study that identified the presence of the SLOG domain in

the MHR, also linked this region to a divergent 3x ANK-motif, following a similar SLOG+ANK+Ion channel architecture to proteins found in choanoflagellates and algae (Schnitzler *et al.*, 2008; Burroughs *et al.*, 2015).

4.2.2.2 SWISS-MODEL and I-TASSER

To provide further evidence for the existence of the SLOG and ANK-like domains, the N-terminal sequence of TRPM2 was analysed by two other 3D structure prediction servers – I-TASSER (Roy, Kucukural and Zhang, 2010) and SWISS-MODEL (Biasini *et al.*, 2014).

As Phyre2 had indicated the presence of the SLOG and ANK-like domains in relatively close proximity, the search terms were narrowed to residues 1-554. This range of residues would hopefully encompass the SLOG domain, as well as one full ANK-like repeat unit, to form a continuous structure of this part of the N-terminal region. Once confirmed, these results together would provide a relatively high confidence 3D model of this region for use with cryo-EM reconstructions.

Figure 4.3: Results compiled from Phyre2 3D model predictions.

(Next Page): Topology and relative location of each of the TRPM2 SLOG domain, ankyrin-repeat domain (ARD), transmembrane region and NUDT9-H domains, as well as the coiled-coil (CC) and calmodulin-binding (CaM) domains mentioned in section 4.2.1.1. The output 3D structures from Phyre2 are shown in colour-coded in boxes. Within the structure, the SLOG domain is coloured according to secondary elements to highlight Rossmannoid fold, whereas the ARD, transmembrane and NUDT9 domains are coloured according to chainbows (rainbow chains).

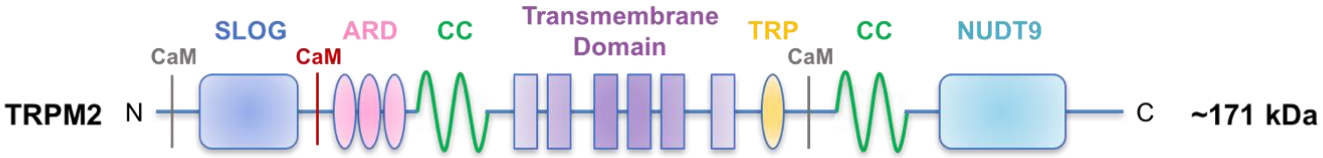

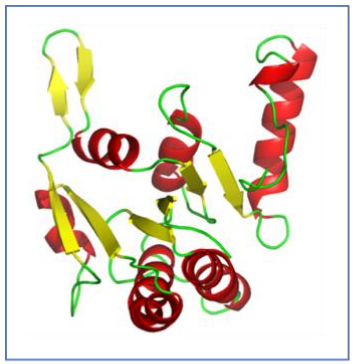

SLOG

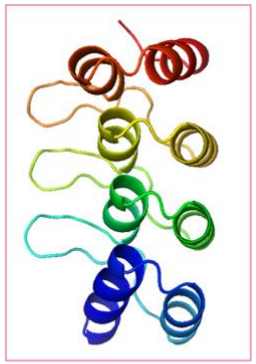

ARD

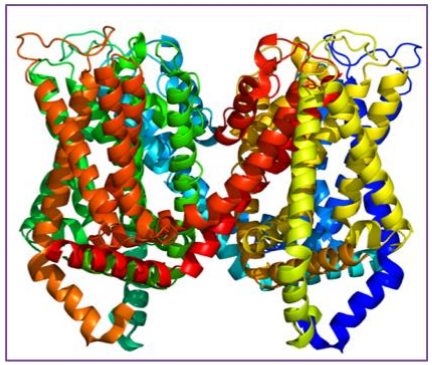

Transmembrane Domain

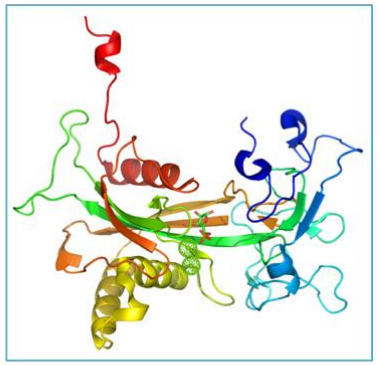

NUDT9

Both SWISS-MODEL and I-TASSER identified the presence of the N-terminal SLOG domain, and both mapped the structure of the *Claviceps purpurea* LOG protein to residues 164-366 as the top hit (Figures 4.3-E). The structure of the Rossmannoid-fold region of the *Streptococcus pneumoniae* dihydrodipicolinate synthase aligns to residues 288-438. I-TASSER also flagged the existence of this fold topology in caspases and a molybdenum/nucleotide binding feature (highlighted in cyan, Figure 4.3E), which has further implication for the SLOG domain as a genuine functional feature of TRPM2.

However, in the absence of a TRPM2 structure it would be difficult to predict how the tertiary elements described here come together to form the complete homomeric channel. EV Complex, another bioinformatic tool, was therefore employed to shed light on potential SLOG and NUDIX interactions.

4.2.2.3 EV Complex

Another interesting insight into TRPM2 channel function comes with the discovery that SLOG domains are often naturally found in conjunction to or associated with NUDIX domains in a variety of organisms (Burroughs *et al.*, 2015). Their natural synergy for detection of ROS and ADP-ribose (ADPR) may have exciting implications for the underlying mechanisms of TRPM2 activation, which may be individually or by association of these domains. To further explore this possibility, the full TRPM2 sequence was submitted to the EV Complex server, which examines two sequences for evolutionarily conserved interaction residues (Hopf *et al.*, 2014). Additionally, ANK domains can be mapped historically to other membrane proteins containing SLOG domains to form SLOG-ANK-TM regions (Burroughs *et al.*, 2015). This

supports the idea that the result found from 3D modelling is potentially not an artefact and may genuinely represent the architecture of the N-terminal domain. Not only this, but the interaction between SLOG and NUDIX domains identified in other families may also give insight into its location relative to and interactions with the C-terminal NUDIX domain. The full-length sequence of human TRPM2 was submitted for comparison with itself by EV Complex. EV Complex searches for evolutionary coupled pairs of residues, that have been evolved with each other over time.

EV complex was able to identify conserved residues between the SLOG and NUDT9H domain, which were able to give an approximate orientation and interaction of these two regions relative to each other in the full TRPM2 structure (Figure 4.3F). Loop residues 242-264 in the N-terminal SLOG domain were mapped to interact with residues clustered around looped regions 1375-1386 and 1470-1476 of the NUDT9H domain (Figure 1.8).

Figure 4.3: I-TASSER and SWISS-MODEL Structure Predictions of the SLOG domain, and EV complex interactions of the SLOG and NUDT9H domain.

(Next Page): SWISS-MODEL (A and B) and I-TASSER (C, D and E) 3D modelling results for N-terminal residues 1-554 of TRPM2. A) The homologous structures of PDB entries 5AJT and 3VFL mapped to the input sequence of TRPM2 (B). Colour coded according to location in sequence. C) I-TASSER complete 3D model output for the input TRPM2 N-terminal residues. The region highlighted in cyan was built in the structure of a SLOG domain, and has been expanded in D and E. E shows D rotated to best demonstrate the highlighted residues implicated in ligand/nucleotide binding. F) EV Complex predicted interactions of the SLOG domain (taken from the Phyre2 model, shown in green) and the NUDT9H domain (cyan). Notable residues were shown on Phyre2 output structures of the SLOG and NUDT9H domains, which have been oriented here to align the identified conserved residues.

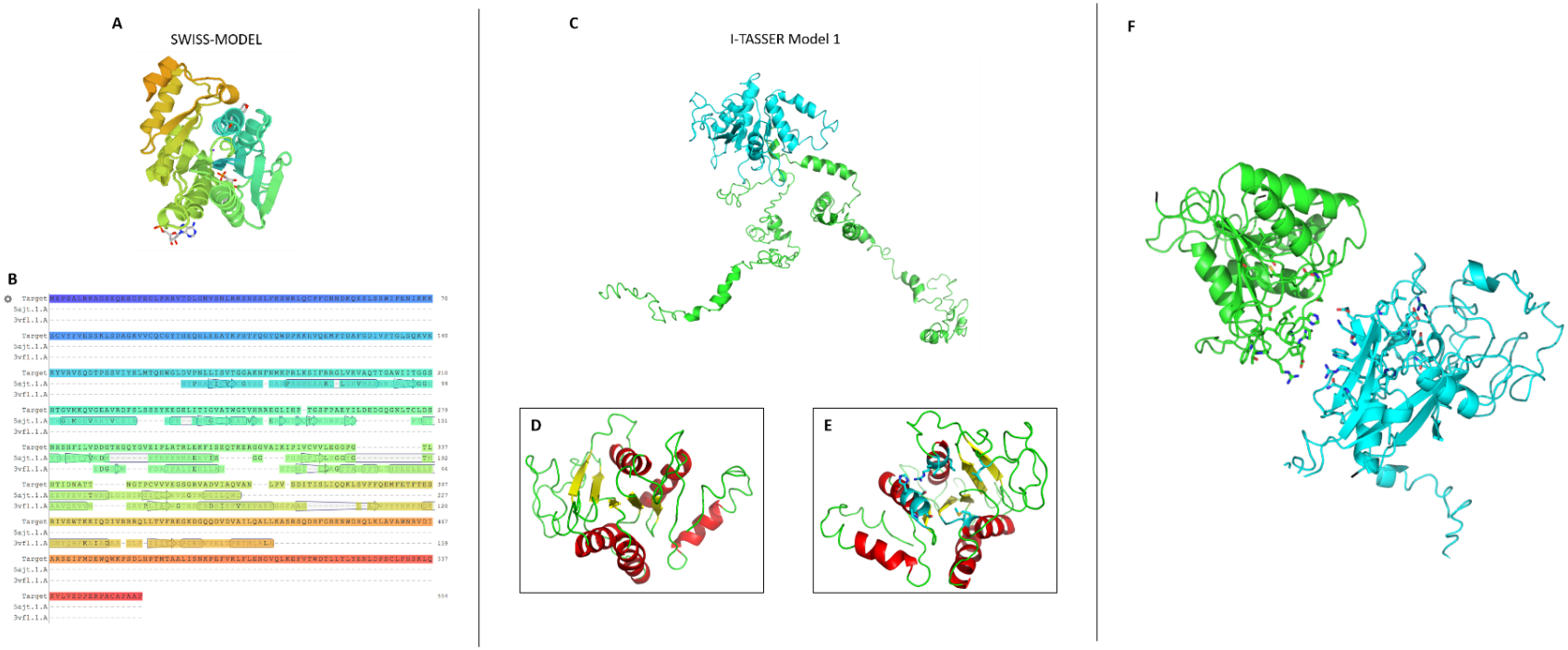
A
SWISS-MODEL
B
C
I-TASSER Model 1
D
E
F

4.3 Summary of Bioinformatic Analysis of TRPM2

In this chapter, bioinformatic tools were used to predict the presence of structural features from the TRPM2 primary sequence. Phyre2, I-Tasser and SWISS-MODEL were used to generate information on the 3D structure of TRPM2 and its subdomains, and PCOILS, the Calmodulin Target Database and EV Complex were used to predict potential inter- and intra-protein interactions.

PCOILS and the Calmodulin Target Database predictions did not give more insights than to what was already published. However, the most striking finding was the alignment of the N-terminal TRPM homology region (MHR) to a reactive nitrogen species (RNS) sensory protein from *Mycobacterium tuberculosis*, known as 'Lonely Guy', or LOG. The only other evidence in the literature supporting the presence of this domain was in the form of an independent genomic study, which had linked SMF/Dpr-A LOG (SLOG) domains to TRPM MHR purely by sequence analysis (Burroughs *et al.*, 2015). However, at this time, no further evidence had been presented at the experimental level. Further examination of the literature identified some tenuous but interesting connections between the role of SLOG domains and TRPM2 physiology and could have implications for the molecular mechanisms governing TRPM2 activation by ROS and ribonucleotides (discussed further in Chapter 7).

Ankyrin (ANK) repeat structures were also identified within the TRPM2 MHR, despite firm conclusion in the literature that TRPM channels do not contain ANK regions. However, proteins with similar SLOG+ANK+Ion channel architecture were identified in ancient species of choanoflagellates and algae (Burroughs *et al.*, 2015), and previous studies have suggested that TRPM2 lineage pre-dates other TRPM

channels and is linked to its NUDIX domain presence and function (Schnitzler *et al.*, 2008). This has interesting implications for the origin of the TRPM sub-family, which possess more unique characteristics between subfamily members than any other TRP channel subfamily (Harteneck, Plant and Schultz, 2000; Schnitzler *et al.*, 2008). This finding can also be linked back to the results from EV Complex, which identified conserved interaction patterns between the SLOG and NUDT9H domain or TRPM2 (Figure 4.2F). However, little was known or confirmed with regard to the structure of TRPM2 and it was difficult to conclude that the interactions predicted by EV complex were genuine.

In 2018 through to 2019, several high-resolution EM structures of TRPM2 were solved (Table 1). It was not only striking to discover that the SLOG domain was indeed identifiable in the published structures, but also that it forms extensive interactions with the NUDT9H domain to facilitate channel activation and gating (Figure 1.8; (Huang *et al.*, 2019). The resolution of the published structures are not high enough to discern residue-level interactions and binding, but they do suggest that the interactions described in EV complex are reminiscent of the TRPM2 activated state (Figure 1.8).

Chapter 5:

Structural and Functional Characterisation of TRPM2

5.1 Introduction

A primary goal of this project was to elucidate the molecular mechanisms underpinning TRPM2's response to environmental stimuli using cryo-electron microscopy (cryo-EM). Prior to the publication of the TRPM4 structure solved by cryo-EM in 2017 (Guo *et al.*, 2017; Winkler *et al.*, 2017), very little was known about the overall architecture of TRPM channels, particularly TRPM2 with its unique NUDT9-H domain. The MHR had no discernible fold and function (Huang *et al.*, 2020), and a low, 2.8 nm resolution negative stain reconstruction of the full-length TRPM2 homotetramer revealed only an overall 'bell-shaped' shell of the channel (Maruyama *et al.*, 2007). Predicted structures and homology models generated during this project (detailed in Chapter 4) provided some insights into potential structural elements in the MHR and indicated inter-subunit PPI between the MHR and NUDT9-H, but may not be representative of the true channel conformation.

This chapter explores the structure-function relationship of purified TRPM2 (purification described in Chapter 3), using experimentally derived data from biochemical and structural techniques, including; thermostability assays, circular dichroism (CD) and electron microscopy (EM). Each technique lends well towards building an overall picture of TRPM2 structure and function, and novel insights into channel dynamics may have been unveiled, particularly with regard to channel stability in different solubilisation scaffolds. As described previously in Chapter 1 and Chapter 4, several high resolution structures of TRPM2 were solved by cryo-EM during the course of this project (Table 1), and some retrospective comparisons have been made within the text to describe the validity of the results obtained herein.

5.2 Results and Discussion

5.2.1 Thermal Stability Assays

5.2.1.1 TRPM2 in SMA versus DDM

Thermal-shift assays are often used to test the stability of membrane proteins by following unfolding in different solution and ligand conditions. For purification and structural analysis of TRPM2, it would be beneficial to identify a stabilising agent or binding partner to reduce its conformational flexibility for cryo-EM. N-[4-(7-diethylamino-4-methyl-3-coumarinyl)phenyl] maleimide (CPM) is a thiol-specific fluorochrome that binds to solvent accessible cysteine residues the protein unfolds or destabilizes. Upon binding, the CPM fluoresces and the absorbance can be used as a measure of protein integrity. The CPM assay was specifically designed as a rapid throughput method for testing membrane protein stabilisation in specific conditions and by *co*-factors, as the CPM dye is influenced less by the presence of detergents, surfactants or highly hydrophobic patches (Alexandrov *et al.*, 2008; Majd *et al.*, 2018). The excitation and emission wavelengths for CPM are 387 nm and 463 nm, respectively, and unfolding assays can be performed on a simple qPCR machine with appropriate filters installed (Alexandrov *et al.*, 2008).

This assay has been specifically adapted to use low quantities of protein while still reporting on its overall stability in a given condition by determination of the protein's overall melting temperature (Tm). The Tm is defined as the point in which the percentage of unfolded protein vs folded protein reaches equilibrium and can be determined by calculation of the first derivative of each melting curve. This can

provide a quick and easy way of testing protein stability under a large number of conditions, with an array of binding partners (Alexandrov *et al.*, 2008; Senisterra, Chau and Vedadi, 2012; Crichton *et al.*, 2015; Majd *et al.*, 2018).

TRPM2 has 29 cysteine residues; 14 within the cytoplasmic N-terminal domain, 5 within the transmembrane helices, 5 within the cytoplasmic C-terminal domain, and the remaining 5 within loops. These cysteine residues are likely to become exposed when the protein unfolds, allowing CPM to bind and release a fluorescent signal. To first determine the appropriate protein concentration for the assay, a single, pure fraction was taken from DDM- and SMA-solubilised TRPM2, and serially diluted 6X from 0.1 mg/ml. The increase in fluorescence intensity was measured alongside a protein-free control to ensure the signal was not influenced by the buffer or dye. Each datapoint was measured in triplicate at the temperature end point.

Characteristic sigmoidal melting curves were observed in the raw data for both TRPM2-SMA (Figure 5.1) and TRPM2-DDM (Figure 5.2), which suggested that concentrations close to these values should be used for further CPM assays. There can be some confidence in the amenability of this technique to both DDM and SMA, as the starting fluorescence for SMA and DDM increase proportionally to the increasing protein concentration. For SMA and DDM, a concentration of 0.05 and 0.1 mg/ml, respectively gave the most signal without sacrificing too much sample, and these were used for further ligand binding experiments (Figure 5.3). The buffer-only control gave no distinguishable signal during the temperature ramp, but the buffer + CPM dye controls show a slight but gradual increase in fluorescence when temperatures exceed 60 °C. The data were examined with the CPM control subtracted from the signal and

independently, but subtraction made no difference to the primary Tm calculated for each melting curve and was not included in the final analysis.

The melting temperature was calculated by two methods for comparison. In the first method, data was initially smoothed by applying a moving average trendline. The data were then differentiated to generate a melting curve, where the maximum indicates the Tm (shown in Figures 5.1B and 5.2B). The calculated Tm's from the polynomial fitting were cross-referenced with sigmoidal fitting for validation as the second method.

Small characteristic melting curves were observed for both calculations, and generated an overall plateau at ~60-65 °C with an agreed approximate Tm of ~50 °C for TRPM2 in SMA and DDM (Figure 5.1B and 5.2B). These observed melting curves and estimated Tm's are characteristic of membrane proteins (Wang *et al.*, 2015).

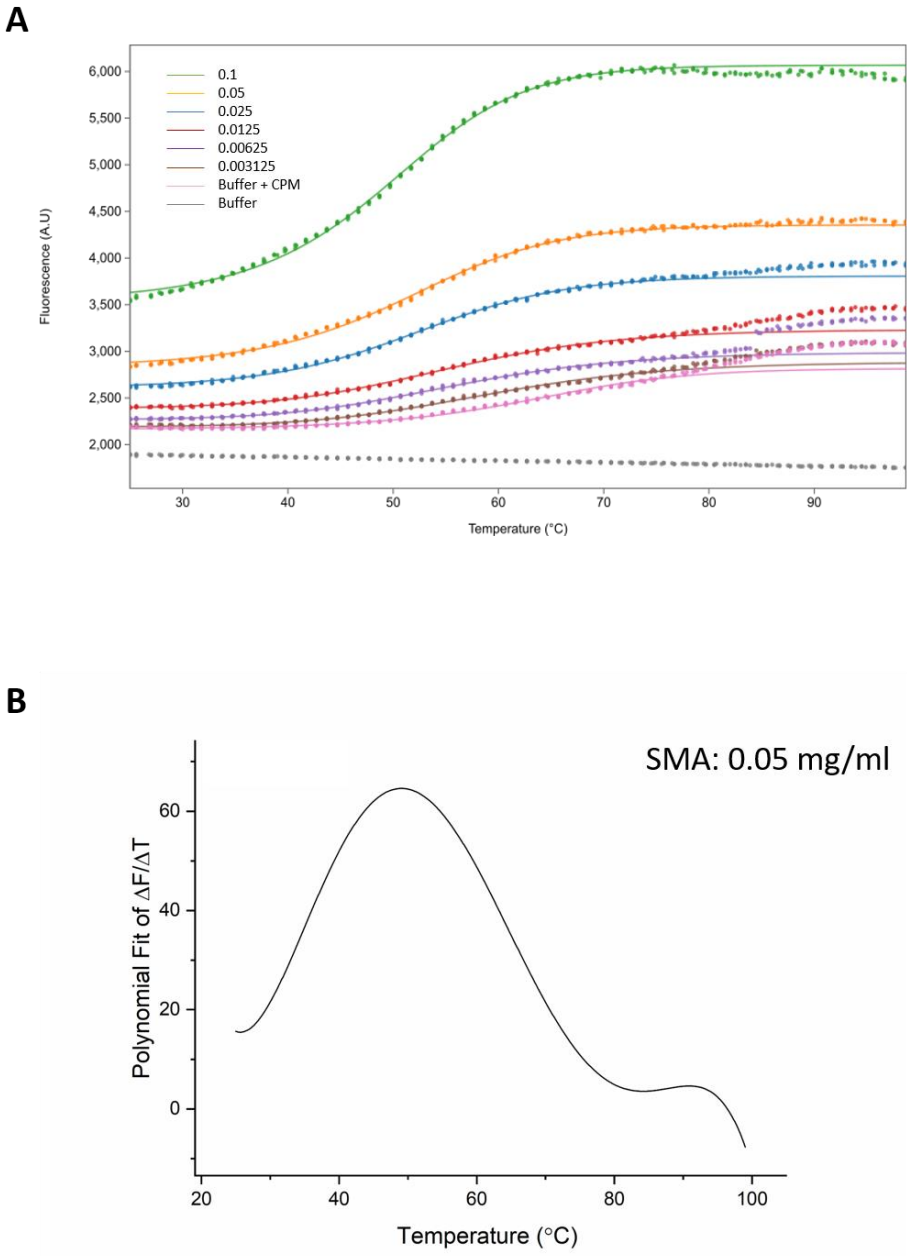

Figure 5.1: CPM assay results from thermal denaturation of TRPM2 in SMA.

A) Raw fluorescence data of 6X diluted TRPM2 samples, ranging from 0.1-0.003 mg/ml presented in arbitrary units (A.U.) vs temperature. Each datapoint is measured and visualised in triplicate. Sigma-5 curves have been fitted to a minimum Tm of 25 °C and a maximum Tm cut off of 80 °C. B) The differentiated curve of the 0.05 mg/ml sample shown in A (orange line), plotted as a fourth-order polynomial.

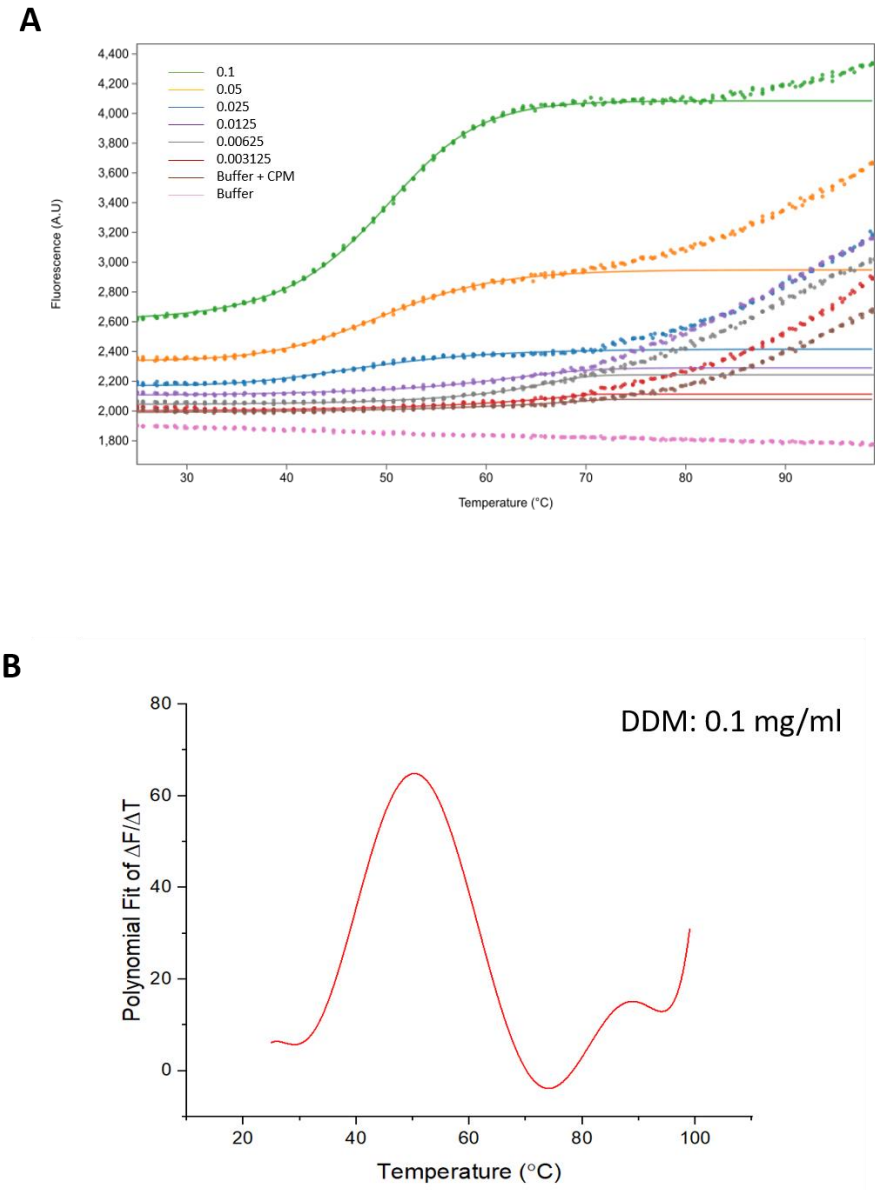

Figure 5.2: CPM assay results from thermal denaturation of TRPM2 in SMA.

A) Raw fluorescence data of 6X diluted TRPM2 samples, ranging from 0.1-0.003 mg/ml presented in arbitrary units (A.U.) vs temperature. Each datapoint is measured and visualised in triplicate. Sigma-5 curves have been fitted to a minimum Tm of 25 °C and a maximum Tm cut off of 70 °C. B) The differentiated curve of the 0.1 mg/ml sample shown in A (green line), plotted as a fifth-order polynomial.

5.2.1.2 CPM Assays to search for TRPM2 stabilising *co*-factors

After the initial experimental parameters had been determined, ligands and *co*-factors were mixed with purified TRPM2 samples to search for a stabilising agent. The aim is to decrease conformational flexibility and heterogeneity in the sample for EM, as well as providing insight into TRPM2 ligand-binding properties. Calcium ions, ADPR and Calmodulin are known TRPM2 binding partners with roles in channel activation and gating (Tong *et al.*, 2006; Starkus *et al.*, 2007; Csanády and Törocsik, 2009; Kühn *et al.*, 2015; Iordanov *et al.*, 2016b). Magnesium (Mg^{2+}) was also tested as conventional NUDIX domains require the presence of magnesium for ADPR hydrolysis (Bessman, Frick and O'Handley, 1996; Perraud *et al.*, 2003). Additionally, the potency of Mg^{2+} for the SMA polymer is lower than that of calcium (Fiori *et al.*, 2017), so if found to be stabilising, it may be able to be included in purification buffers. While these *co*-factors are known activators or regulators of channel activity *in vivo*, it is unknown whether they will have a stabilising or destabilising effect on the extracted protein.

Initially, $CaCl_2$, $MgCl_2$, CaM and ADPR were screened individually to examine binding and stabilisation of DDM_TRPM2 and SMA_TRPM2 (Figure 5.3D and E). They were then screened in combination, whereby CaM or ADPR were mixed with their naturally associated ions Ca^{2+} and Mg^{2+}, respectively. It was hoped that the presence of CaM would reduce conformational flexibility in the N-terminal region, and ADPR would lock the NUDT9H domain of the C-terminal region. It was also the hope that an increase in stability would provide a more suitable candidate for cryo-EM, and the binding partner would be visible in the structure.

TRPM2:CaM was used at a molar ration of 1:4, to account for the 4 IQ motifs in the tetramer (Tong *et al.*, 2006). However, samples with CaM added appeared to give a much larger secondary unfolding peak at ~ 70 °C in the SMA sample (Figure 5.3A), and closer to 75 °C in the DDM sample (Figure 5.3C). This is likely indicative of CaM unfolding or sample aggregation, rather than a TRPM2 unfolding event.

Addition of Ca^{2+} and Mg^{2+} gave conflicting results for SMA_TRPM2 vs DDM_TRPM2. No additives were able to stabilise DDM_TRPM2, according to the Tm's calculated from figure 5.3, shown in Tables 5.1 and 5.2. However, the presence of Ca^{2+} and Mg^{2+} seemed to increase the Tm of SMA_TRPM2 closer to 60 °C (Figure 5.3A, D and E). It was unclear whether the divalent cations were interacting with the SMA polymer directly, causing aggregation and falsely giving higher Tm's. However, it was clear that the combination of Mg^{2+} and Ca^{2+} ions was detrimental to SMA_TRPM2 stability, reducing the Tm to ~46 °C.

The data produced from ligand and co-factor derived melting curves produced complicated unfolding patterns, plateauing slightly at several points in the melting curve, indicating several potential unfolding events. In Figure 5.3, each potential transition temperature is indicated by dotted lines, and corresponding Tm values for each transition shown in Tables 5.1 and 5.2. This could be a result of differential ligand binding, creating different species within a sample that unfold at different temperatures (Senisterra, Chau and Vedadi, 2012). However, it is impossible to attribute specific unfolding events to a particular structure or domain within the solubilised TRPM2 complex by CPM assay, or the order in which they unfold. Overall, these results indicate that TRPM2 undergoes multiple unfolding events, particularly in detergent

samples, suggesting that the solubilisation vehicle can play a significant role in TRPM2 stability.

Table 5.1: Tm values calculated for SMA_TRPM2 from CPM assays in Figure 5.3. Top table indicates the transition temperatures calculated from 5.3A and B. Bottom table corresponds to data in 5.3E and F.

SMA Additive and Tm No.	*Tm*	*R2*	*Min T*	*Max T*
CaM Tm1	47.5	0.994	24.6	54.7
Tm2	52.8	0.997	25.6	61.7
Tm3	69.0	0.998	60.7	84.5
CaM + $CaCl_2$ Tm1	41.4	0.989	25.6	49.7
Tm2	52.3	0.991	25.6	62.7
Tm3	69.3	0.998	60.7	84.5
$CaCl_2$ Tm1	37.1	0.924	29.0	42.7
Tm2	51.9	0.996	29.0	60.7
Tm3	69.8	0.998	60.7	84.9
Overall	65.2	0.999	29.0	84.9
$MgCl_2$ Tm1	33.1	0.950	25.6	39.7
Tm2	45.0	0.991	35.8	51.7
Tm3	67.5	0.985	60.7	75.5
Tm4	76.9	0.982	71.7	86.7
Overall	63.8	0.999	25.6	94.7

SMA Additive and $Tm_{Average}$	*Tm*	*R2*	*Min T*	*Max T*
$MgCl_2$	63.2	0.999	30.0	86.5
$CaCl_2$	58.4	0.998	24.8	82.5
ADPR	49.8	0.999	24.8	79.5
$MgCl_2$ + $CaCl_2$	46.8	0.999	24.8	68.7
$CaCl_2$ + ADPR	47.9	0.998	24.8	70.7
$MgCl_2$ + ADPR	54.5	0.999	24.8	92.7

Table 5.2: Tm values calculated for DDM_TRPM2 from CPM assays in Figure 5.3.

DDM Additive and Tm No.	*Tm*	*R2*	*Min T*	*Max T*
CaM Tm1	45.6	0.996	27.0	64.5
Tm2	75.0	0.993	65.5	84.7
CaM + $CaCl_2$ Tm1	49.2	0.998	25.6	64.7
Tm2	73.4	0.998	65.7	84.7
$CaCl_2$	49.7	0.999	25.6	72.7
$MgCl_2$	48.0	0.999	24.8	69.7

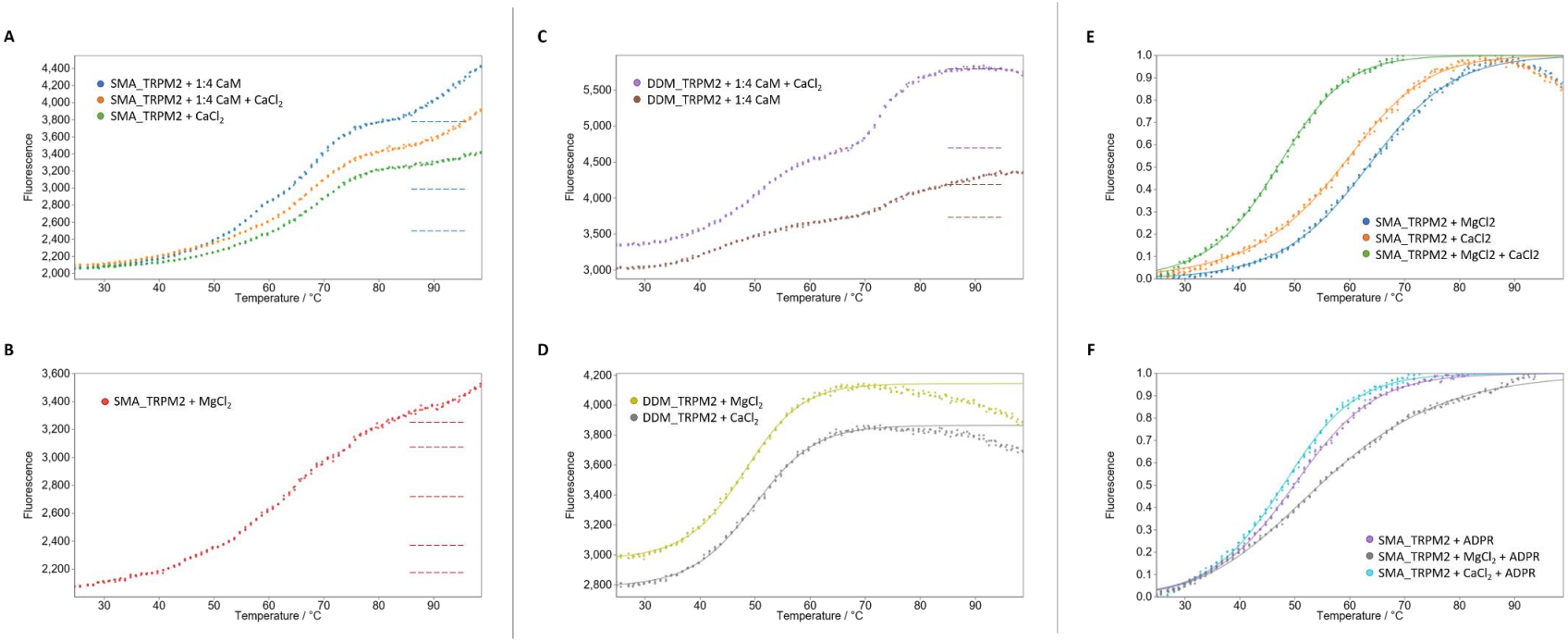

Figure 5.3: Melting curves for SMA_TRPM2 and DDM_TRPM2 in the presence of ligands.

CPM melting curves of 0.5 mg/ml SMA- (A, B, E and F) and 0.1 mg/ml DDM- (C and D) purified TRPM2 in the presence of agonists and inhibitors; Calmodulin (CaM), $CaCl_2$, $MgCl_2$ and ADP-ribose (ADPR). Figure legends are associated with each plot describing the condition of each curve. Dashed lines indicate the maximum temperature cut offs used to determine transition temperatures or each feature. E) and F) were normalised relative to all samples in the experiment.

5.2.2 Circular Dichroism to examine Tm and Unfolding of TRPM2.

CPM assays are commonly used to determine the stability of membrane proteins, but provide little insight into the type and order of unfolding events that occur during denaturation. Additionally, while CPM assays offer advantages in the form of accessibility and throughput, there is some scepticism as to the interpretability of their results (Wang *et al.*, 2015). Wang *et al.* (2015), noticed that membrane protein melting temperatures determined with CPM assays consistently fell within the same range – between 45-55 °C – and that exposure of cysteine residues was not an absolute requirement to obtain unfolding data with the CPM dye. While they concluded that this assay is useful and does indicate unfolding, it has been recommended that alternative techniques, such as circular dichroism, are used in compliment (Wang *et al.*, 2015). Circular dichroism (CD) is powerful technique for examining protein secondary and tertiary structure in solution, and could provide great insight into unfolding dynamics of TRPM2 (Greenfield, 2006a, 2006b; Siligardi *et al.*, 2014).

While CD has its advantages over CPM, in that a change in CD is directly interpreted as a change in a specific type of secondary structure, it also has its downfalls. It is conventionally a very low-throughput technique that requires large volumes of sample (~200 µl) to perform a single experiment with specialist equipment (Kelly, Jess and Price, 2005b). It also requires very controlled experimental conditions with low oxygen environments and specific buffer compositions for suitable data acquisition and analysis.

Synchrotron radiation CD (SRCD) has become an attractive option for use with membrane proteins (Miles *et al.*, 2016), offering high signal to noise spectra and

facilitating sample volumes as low as 70 µl to combat some of the issues with conventional CD (Miles and Wallace, 2006; Siligardi *et al.*, 2014). SRCD has recently implemented a high throughput capability, moving beyond small volume capillary cuvettes (Hussain *et al.*, 2016), and other high-throughput stability testing techniques involving intrinsic tryptophan fluorescence have been recently developed as in-house sources (Kotov *et al.*, 2019; Moore-Kelly *et al.*, 2019), but are not yet widely cited. However, these facilities are not so easily accessible as in-house sources, and as with most experiments, it is often the sample preparation and longevity that is a limiting factor.

Despite minor drawbacks associated with sample requirements and data acquisition, CD has so far proven itself to be a powerful technique for determining optimum samples from TRPM2 purifications (Chapter 3). As well as following protein unfolding, thermal melting curves taken using CD can also provide information on unfolding patterns and kinetics (Greenfield, 2006a, 2007). This makes it a very powerful tool for analysing a wide variety of proteins, particularly for exploring the thermo-sensitivity of TRP channels.

5.2.2.1 Thermal Denaturation of TRPM2 followed with Circular Dichroism

The first TRPM2 thermal denaturation experiment was performed using FLAG-affinity purified protein. The consistent purification procedure yielded 0.2 mg/ml of pure TRPM2 in fraction E3-E4, at a volume of ~250 µl, which was sufficient for CD analysis with the in-house Chirascan system and available cuvettes of 1 mm path length. The experiment was set up to record spectra from wavelengths of 190-260 nm at 20 °C, before ramping up to 90 °C. Whole spectra were recorded at 1 °C intervals,

to follow folding and unfolding of each domain, and a final reading was re-taken after the temperature ramp at 20 °C (Figure 5.7A).

At 90 °C, there was significant loss in almost all secondary structure elements, particularly any alpha-helical content, indicated by a decrease in 208 and 222 signal and shift towards a characteristic 'disordered' spectrum. Interestingly, some helical content appears to be regained after the temperature has decreased to take the final reading at 20 °C (Figure 5.7B).

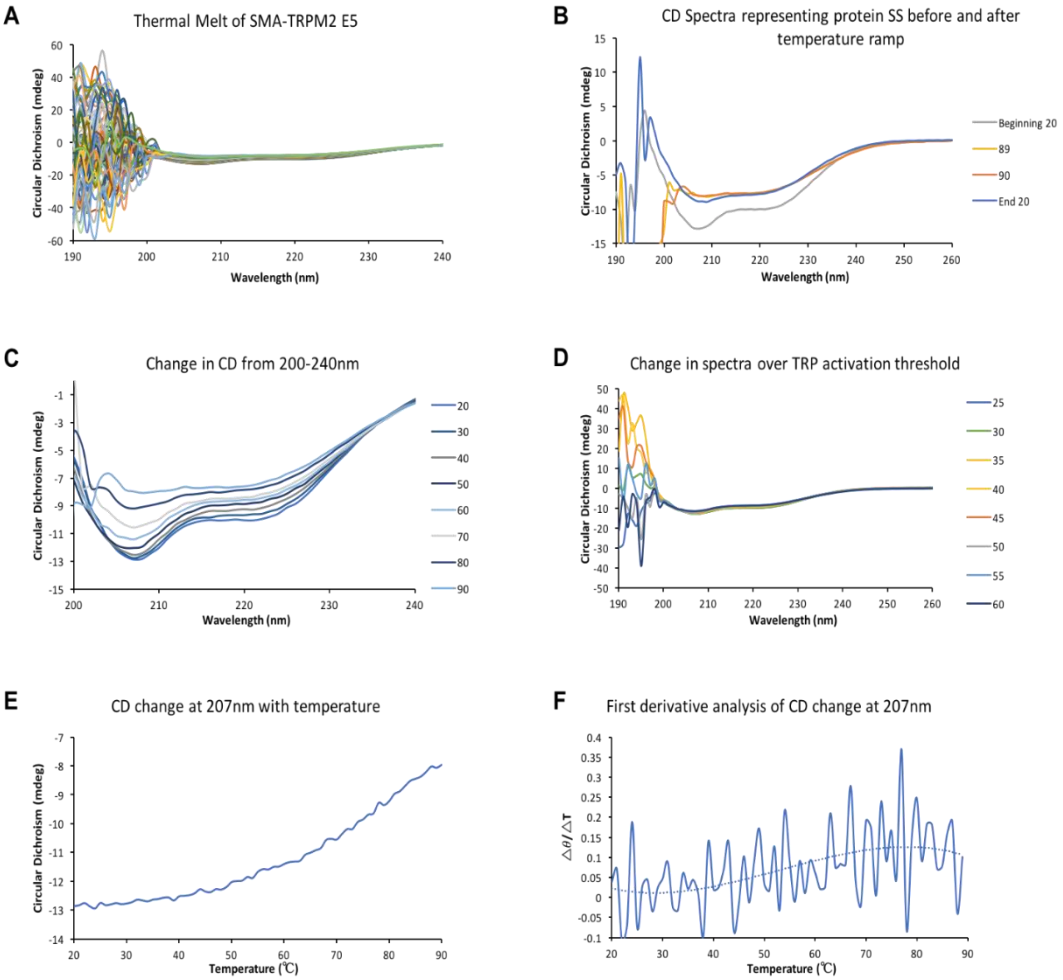

Figure 5.7: Circular dichroism (CD) spectral analysis of SMA-TRPM2 temperature ramp experiment, at a protein concentration of 0.2 mg/ml.

A) The raw data for each spectral recording between 190-260nm at each temperature, from 20-90 °C. B) Beginning and end spectra measured at 20 °C, as well as 89 °C and 90 °C spectra extracted and zoomed in between CD reading of -15 mDeg and +15 mDeg for clarity. C) Spectra at every 10 °C represented only between wavelengths 200-260nm. D) Spectra observed between TRPM2-specifc temperatures of interest. The Tm value was calculated using the change in signal at a wavelength of 207nm across the entire temperature range (E), by fitting a second order polynomial to the first derivative results (F).

Another potentially interesting feature was the dramatic change in signal between 190-205nm around TRPM2's activation temperature of ~37-40 °C (Figure 5.7D) (Togashi *et al.*, 2006; Song, Wang, Gretel B Kamm, *et al.*, 2016; Tan and McNaughton, 2018). While it is clear that the data obtained has very poor signal to noise in this region, one could speculate that this change is related to a significant disruption in the solution – whether that is protein or buffer related is not discernible – but re-assessing with NaF instead of NaCl could provide some interesting insights into the activation temperature of the channel. If different results were obtained for DDM_TRPM2, a more compelling argument could be made for increased retention of native lipids in the transmembrane annulus when extracting with SMA over detergent (observed initially in Chapter 3, Figure 3.9), affecting structural integrity.

An approximate melting temperature was also calculated using data points from a wavelength of 207nm, where the recording for this particular spectrum held its largest negative peak (Figures 5.7E). The first derivative of this curve was taken to give an approximate Tm of ~78 °C, but the spectrum was extremely noisy and curve fitting was difficult (Figure 5.7F). This is also considered extremely high for a membrane

protein and is not consistent with the results obtained in CPM assays. Initial thoughts as to an explanation looked to the SMA polymer, which is stable up to ~130 °C (~270 °F) (Moore, 1986), and has previously been shown by CD to stabilise membrane proteins beyond 80 °C (Knowles, Finka, Smith, Y. P. Lin, *et al.*, 2009)

The folding landscape of membrane proteins at high temperatures may not have been previously observed to this degree, as membrane proteins are often reconstituted in non-ionic detergents such as DDM, which can dissociate freely at higher temperatures (Gu and Sjöblom, 1992), and cause aggregation from exposure of hydrophobic regions. If, for example, the protein is purified in its native environment and forced to remain within the boundaries of the polymer, a significantly higher melting temperature may be recorded due to its inability to diffuse freely away from the polymer and potentially stabilising lipids. High melting temperatures for SMA-encapsulated proteins has been previously reported (Knowles, Finka, Smith, Y. P. Lin, *et al.*, 2009), but these experiments were not performed on predominantly alpha-helical proteins.

5.2.2.2 Modifications to CD Thermal Denaturation Parameters Reveals Multiple TRPM2 Unfolding Events

It was clear from these initial results that this experiment was not optimal, and after further research into the literature, a few essential modifications were implemented. Firstly, the use of NaCl in the buffer. Chloride ions (Cl^-) interfere with scattering of circularly polarised light between wavelengths of 190-200 nm (Miles *et al.*, 2016). Chloride ion interference manifests as extremely high background and contributes to solvent flattening, thereby counteracting any real absorbance by the molecule of

interest in this region. In future CD thermal-melt experiments, NaCl was avoided in favour of NaF. Additionally, exposure to UV light for extended periods of time can introduce free radicals into solution, which can bombard the protein and contribute to its denaturation (Hussain, Longo and Siligardi, 2018).

This UV radiation damage can influence the reliability of the unfolding data. Additionally, TRPM2 is a ROS-sensitive channel (Hara *et al.*, 2002), and the presence of ROS in solution may alter its fold and thus true unfolding pattern. To alleviate this, the frequency of spectral recording was occasionally decreased to 5 °C intervals to decrease the overall exposure, and only spectra at 208 nm were recorded for Tm calculations. However, this deviated according to the needs of the experiments as discussed later in this chapter. For temperature ramping, a complete spectrum was recorded at every 1 °C across a 20-90 °C. This became the standard procedure for thermal denaturation measurements of TRPM2, and unless otherwise stated, CD denaturation experiments were performed under these conditions.

With these modifications, the spectra quality improved significantly - the use of NaF instead of NaCl in the purification gave spectral readings with better signal-to-noise ratios up to 197 nm (Figure 5.8A). While there is signal beyond this into the far-UV range the signal-to-noise ratio is low, so the region beyond ~200 nm is not discussed in detail. Transition states and corresponding melting temperatures were calculated using Global3 analysis software, which automatically plots first derivative curves of ellipticity as a function of temperature and performs principle component analysis to approximate potential transition temperatures.

The unfolding landscapes of DDM_ TRPM2 appear overall slightly different due to the poor signal-to-noise measurement (Figure 4.8 ABC vs DEF), but again, it was observed that the protein does not become completely unfolded at 90 °C.

The most striking observation was the appearance of an interesting feature seen rising and falling in both DDM_TRPM2 and SMA_TRPM2 spectra at ~40 °C, indicating that alpha helical/beta sheet content is lost and regained briefly, before being lost entirely again as the temperature increases (highlighted with the black circle in Figure 5.8A and D). This feature is at approximately the activation temperature of the channel, ~37 °C, and differs slightly between TRPM2 in DDM (~35 °C) and SMA (~37 °C) (Song, Wang, Gretel B. Kamm, *et al.*, 2016; Kashio and Tominaga, 2017; Tan and McNaughton, 2018). Ellipticity of wavelengths 202 nm, 208 nm and 222 nm were isolated and plotted as a function of temperature to examine the feature further (Figures 5.8B and 5.8E). The spectra again revealed a complex unfolding pattern, so the raw data were smoothed, differentiated and plotted by polynomials to give approximate Tm's of each sample to represent this complexity (Figure 5.8C and 5.8F).

Figure 5.8: Modified thermal denaturation of TRPM2 solubilised in SMA and DDM.

A and D show the overall melting profile of TRPM2 in SMA (A) and DDM (D) as a function of ellipticity (mDegθ), time (min) and temperature (°C). The feature described in the text at ~40 °C is highlighted with a black circle in both A and D. B and E show the isolated wavelengths 202 nm, 208 nm and 222 nm from the data shown in A and D. C and F represent polynomial fits of the Savitsky-Goley smoothed data from figures B and E, corresponding to unfolding transition temperatures within the SMA_TRPM2 (top row, A) and DDM_TRPM2 (bottom row, B) samples.

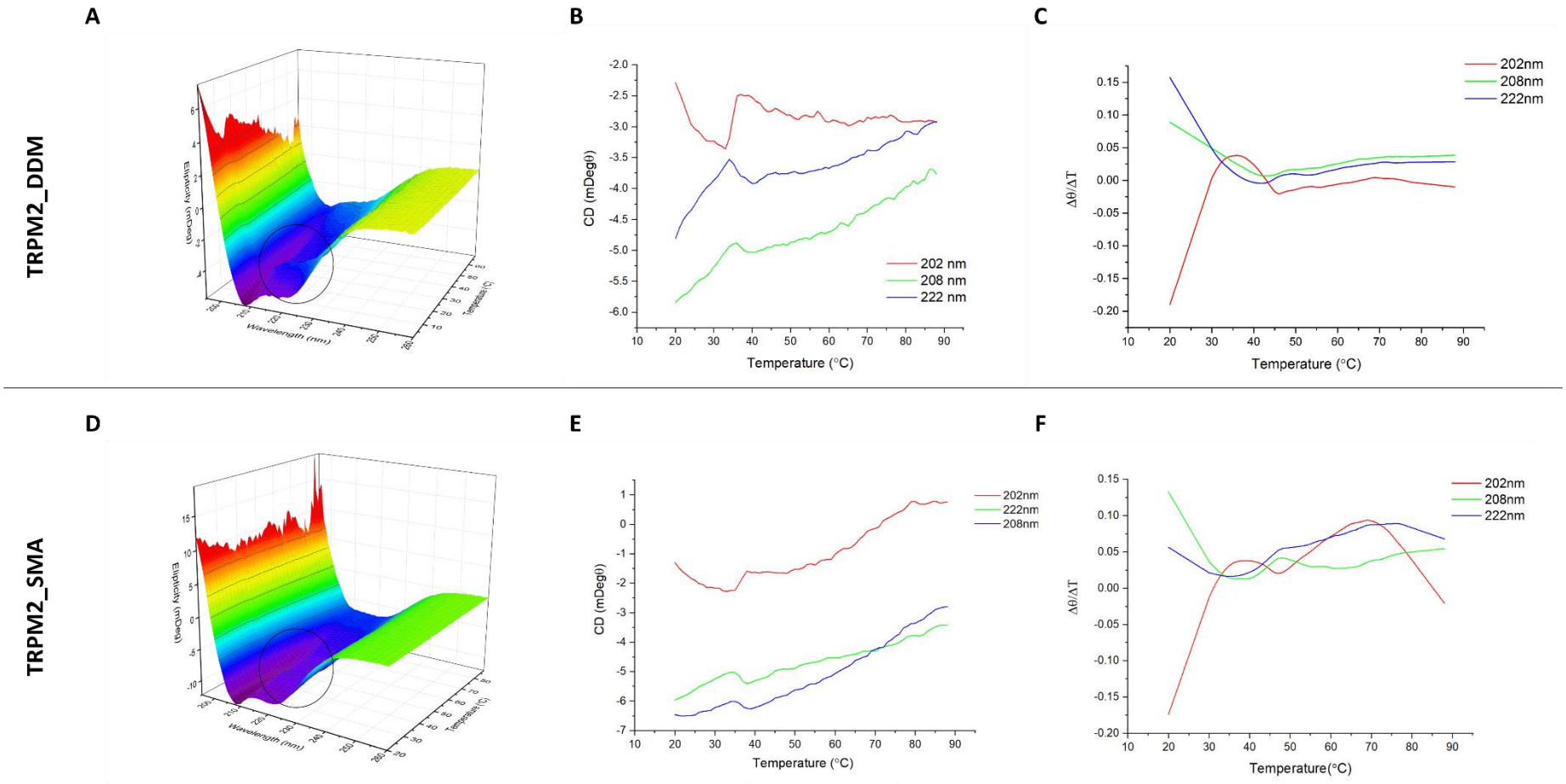
A
B
C
TRPM2_DDM
Ellipticity (mDeg)
Wavelength (nm)
Temperature (°C)
CD (mDegθ)
202 nm
208 nm
222 nm
Temperature (°C)
ΔθΔT
202nm
208nm
222nm
Temperature (°C)
D
E
F
TRPM2_SMA
Ellipticity (mDeg)
Wavelength (nm)
Temperature (°C)
CD (mDegθ)
202nm
222nm
208nm
Temperature (°C)
ΔθΔT
202nm
208nm
222nm
Temperature(°C)

These results reveal not just one, but several peaks and inflection points throughout the temperature ramp, indicative of multiple unfolding transitions (Figure 5.8C and 5.8F). For DDM_TRPM2, the change in CD is more dramatic at wavelengths 202 nm, 208 nm and 222 nm (Figure 5.8B), and there are only two apparent major transitions in the differentiated data (Figure 5.8C). For SMA_TRPM2, the change in CD is more subtle (Figure 5.8E), but the differential curves reveal three major inflection peaks in the CD unfolding data (Figure 5.8F). This agrees with the CPM results, which also demonstrated multiple unfolding events, and has significant implications for the effect of temperature on TRPM2. Global3 analysis software was used to determine the Tm of each transition event and suggested a total of 5 events for DDM and 6 events for SMA (Table 5.3). The calculations in this software are based on those published in Greenfield, 2006a, which defines the Tm as the midpoint of the unfolding transition. Temperatures above 60 °C have not been focused on, as CPM assays showed that the protein is unfolded beyond this temperature.

Table 5.3: Multiple transition temperatures from CD thermal denaturation as calculated by Global3. Approximate transition temperatures are given in °C.

	DDM	**SMA**
No. Transitions	5	6
Calculated Tm of each transition in ° C	25.0	31.4
	33.9	39.0
	41.4	57.8
	66.6	63.1
	77.5	68.1
		78.5

5.2.2.3 Examining the unfolding and refolding potential of TRPM2 at ~37 °C

Previously, whether temperature directly or indirectly affected TRPM2 was unknown. Reports suggest that this sensitivity comes from the lipids present in the membrane (Morales-Lázaro, Lemus and Rosenbaum, 2017), or secondary responses to increased H_2O_2 and ADPR concentrations as a result of cell stress (Hara *et al.*, 2002; Togashi *et al.*, 2006). However, in the absence of a cellular environment *in vitro*, it would be difficult to explore how temperature can directly affect channel dynamics and gating.

It was interesting to observe the differences between the two solubilisation systems – in this instance, the SMA versus DDM. It could be that the SMA polymer has retained more native lipids that may directly affect channel function and folding, or the polymer itself is influencing the protein structure by either restricting or enhancing motions within the transmembrane domain. However, no other CD thermal denaturation of other SMALP proteins have reported temperature features in this region, suggesting that it could indeed be the protein itself.

Whether this is a result of the retained lipids or the protein itself would be unknown, if not for the similar result observed for TRPM2 in DDM. In detergents, it is generally unknown to what degree a membrane protein will retain native lipids upon extraction and after purification until it can be analysed by an additional suitable technique. It would be interesting to see if the unfolding event was real, and if it was, if the observed unfolding/refolding event is reversible across the TRPM2 activation temperature range in both solubilisation systems.

To test the hypothesis that TRPM2 is directly affected by temperature and can elicit a reversible temperature change, another temperature ramp from 20-50 °C and back

again was set up with previous and further modifications. To enhance the signal to noise, more cell pellet was used for the purification, so a higher yield of protein could be obtained for each fraction from the purification. The samples were also purified in NaF instead of being equilibrated during purification. Fractions either side of the primary elution peak were also analysed with either the addition of calcium or magnesium ions – Ca^{2+} for the transmembrane binding sites, and Mg^{2+} for the NUDT9-H domain. As an additional stabilising factor, CHS was also included in the DDM_TRPM2 preparation, as it was observed that this increased protein yield and stability (Chapter 3).

The spectrum of each sample was recorded over an ascending ramp of 20-50, and a reverse descending ramp of 50-20, both at 1° intervals. Raw spectra for each condition trialled are shown in figure 5.9. For illustration purposes, only the spectra of isolated wavelengths 198 nm, 202 nm, 208 nm and 222 nm are shown and will be discussed here. In these samples, the protein concentration in SMA was lower than with DDM:CHS, as the SMA samples were generated from a larger cell pellet prep which was found to increase protein aggregation.

After sample optimisation for CD, for both SMA_TRPM2 and DDM:CHS_TRPM2, at 208 nm the feature at ~40 °C becomes strikingly clear. For the ascending ramp to 50 °C, both samples follow a similar overall unfolding/refolding pattern with multiple features, albeit with a 2 °C shift towards an increased recorded temperature for each feature in the DDM:CHS sample. Another difference is that the descending ramp SMA_TRPM2 fluctuates around -5.0 to -5.2 mDegθ, remaining at a more constant value after the initial unfolding in the ascending temperature ramp. In contrast, DDM:CHS_TRPM2 shows an overall decrease in ellipticity from -9.88 to -10.4

mDegθ in the descending ramp, indicating a regain of secondary structure. Therefore, the spectra are similar, but not precisely mirrored in both the ascending and descending temperature ramp. Spectra were not analysed further or deconvoluted as there was still noise in the far-UV region, which interfered too much with secondary structure percentage calculations. It is also noteworthy that these features are small and maybe a result of experimental error. However, the recorded HV and absorbance signals at 208 nm were within the appropriate limits of the equipment (400 units for HV, and <2.0 A.U. for absorbance). It is therefore likely that these features are a genuine function of the sample and demonstrate how polymer and detergent environments can differentially affect the secondary structure of TRPM2.

Figure 5.9: CD results of ascending and descending temperature ramps across the TRPM2 temperature threshold.

(Next Page): Overall CD from ascending and descending temperature ramps of SMA_TRPM2 (A) and DDM:CHS_TRPM2 (C) coloured according to ellipticity in mDegθ. CD measured at 208 nm was isolated and shown as a function of temperature for SMA_TRPM2 (B) and DDM:CHS_TRPM2 (D).

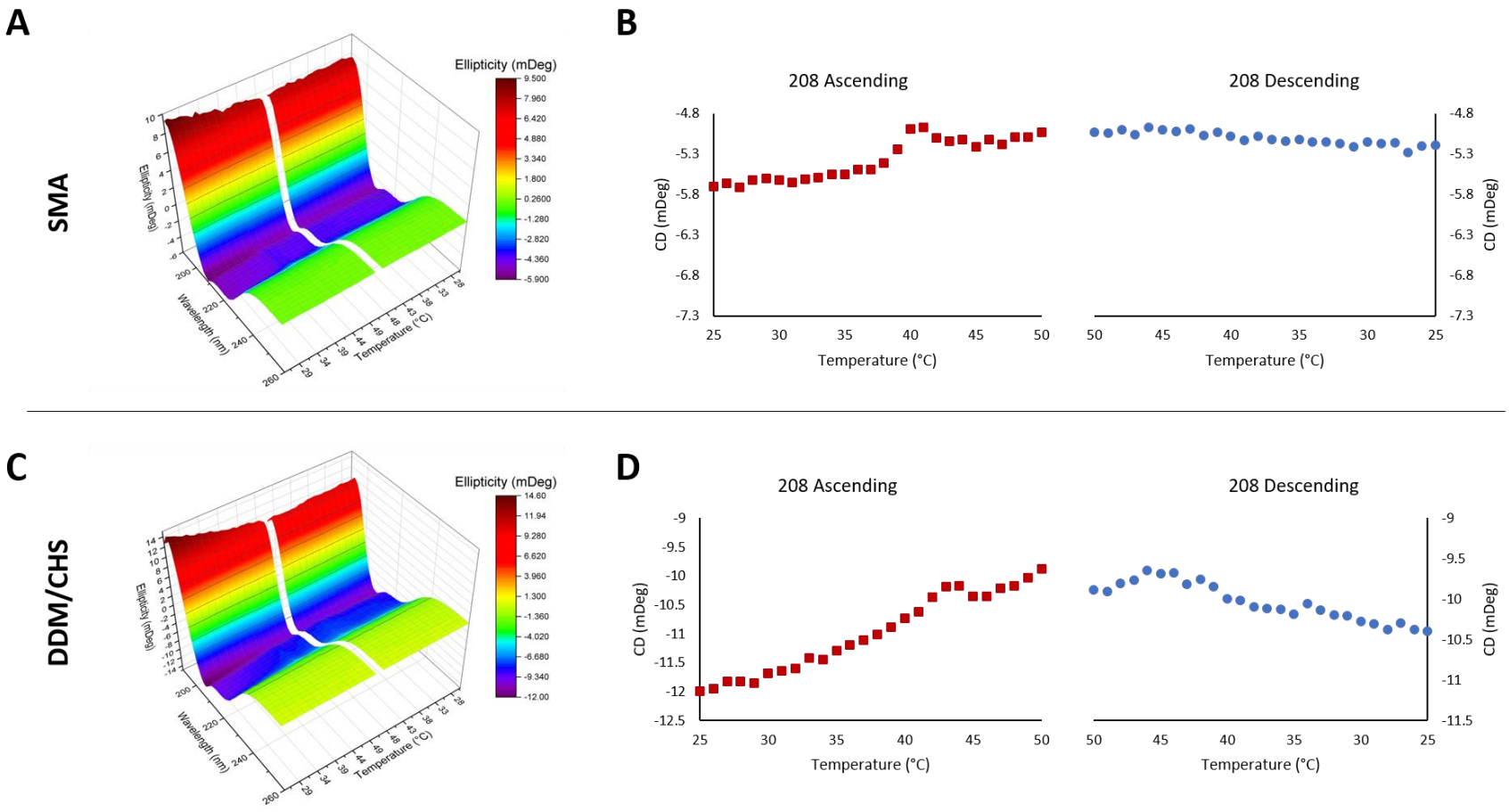
A
SMA
Ellipticity (mDeg)
9.500
7.960
6.420
4.880
3.340
1.800
0.2600
-1.280
-2.820
-4.360
-5.900
Ellipticity (mDeg)
Wavelength (nm)
Temperature (°C)
B
208 Ascending
208 Descending
CD (mDeg)
Temperature (°C)
C
DDM/CHS
Ellipticity (mDeg)
14.60
11.94
9.280
6.620
3.960
1.300
-1.360
-4.020
-6.680
-9.340
-12.00
Ellipticity (mDeg)
Wavelength (nm)
Temperature (°C)
D
208 Ascending
208 Descending
CD (mDeg)
Temperature (°C)

5.2.2.4 Examining the effect of *co*-factors on the transition temperatures of TRPM2

The analysis was extended further to examine the influence of *co*-factors on the fold and stability of TRPM2 during a thermal denaturation experiment, which has already proved fruitful in informing the TRPM2 structural perturbations in SMA and DDM alone. For TRPM2, lipid content is examined later in this chapter, but all that can be said for now is that there is a clear difference between these two systems that would need to be examined further.

CPM assays for TRPM2 in either DDM or SMA indicated a Tm of ~50 °C. Experiments with DDM_TRPM2 an SMA_TRPM2 in the presence of *co*-factors highlighted a number of potential unfolding events but gave conflicting results for each. Interestingly, SMA_TRPM2 consistently gave consistently higher Tm's for Ca^{2+} and Mg^{2+} despite its known propensity to aggregate in the presence of cations. There is evidence that TRPM2 activity is cooperatively enhanced by Ca^{2+} (McHugh *et al.*, 2003a), and that Ca^{2+} ions bind directly near the channel pore (Csanády and Törocsik, 2009), so stabilisation by low concentrations of Ca^{2+} is consistent.

To examine the effect of these cations on folding, additional CD thermal denaturation experiments were carried out using SMA_TRPM2 and DDM_TRPM2 purified in NaF, and recorded with or without the direct addition of 1 mM $MgCl_2$ or 1 mM $CaCl_2$. As adding cations to the SMA polymer was a concern, CD spectra were taken before and after the addition of 1mM $CaCl_2$ and 1 mM $MgCl_2$ for comparison (Figure 5.10A). The addition of Cl^- ions was accounted for, and the CD spectra for buffer blanks containing the same concentration of $MgCl_2$ and $CaCl_2$ were examined for interference in

isolation and later during buffer subtraction. Minor differences in the spectra between wavelengths 200-240 nm were observed after the addition of additives, particularly at 208nm and 222 nm where a positive shift is seen and could indicate a change in protein secondary structure. A control sample was also included, where the spectrum was taken immediately after the protein was take off ice, then again at 20 °C. Deconvolution of the spectra suggests an increase in alpha helical content in the sample containing Ca^{2+}, and a decrease in the Mg^{2+} sample relative to the native SMA_TRPM2 spectra (Figure 5.10B). However, to accurately interpret the helical and beta sheet content this is only recommended when results are of high quality down to at least 190 nm, so further optimisation is required for these results to be truly valid.

To examine whether the unfolding/refolding feature at ~37 °C was affected by the presence of Ca^{2+} or Mg^{2+}, preliminary denaturation experiments were performed with a full spectral recording (Figure 5.11A and B). For this experiment, TRPM2 was purified in DDM only, and due to sample limitations, could only be examined with Ca^{2+} as an additional cofactor (Figure 5.11C). Global3 analysis was also performed on this data to given preliminary Tm's and have been shown alongside previous results for SMA and DDM alone for comparison (Table 5.4).

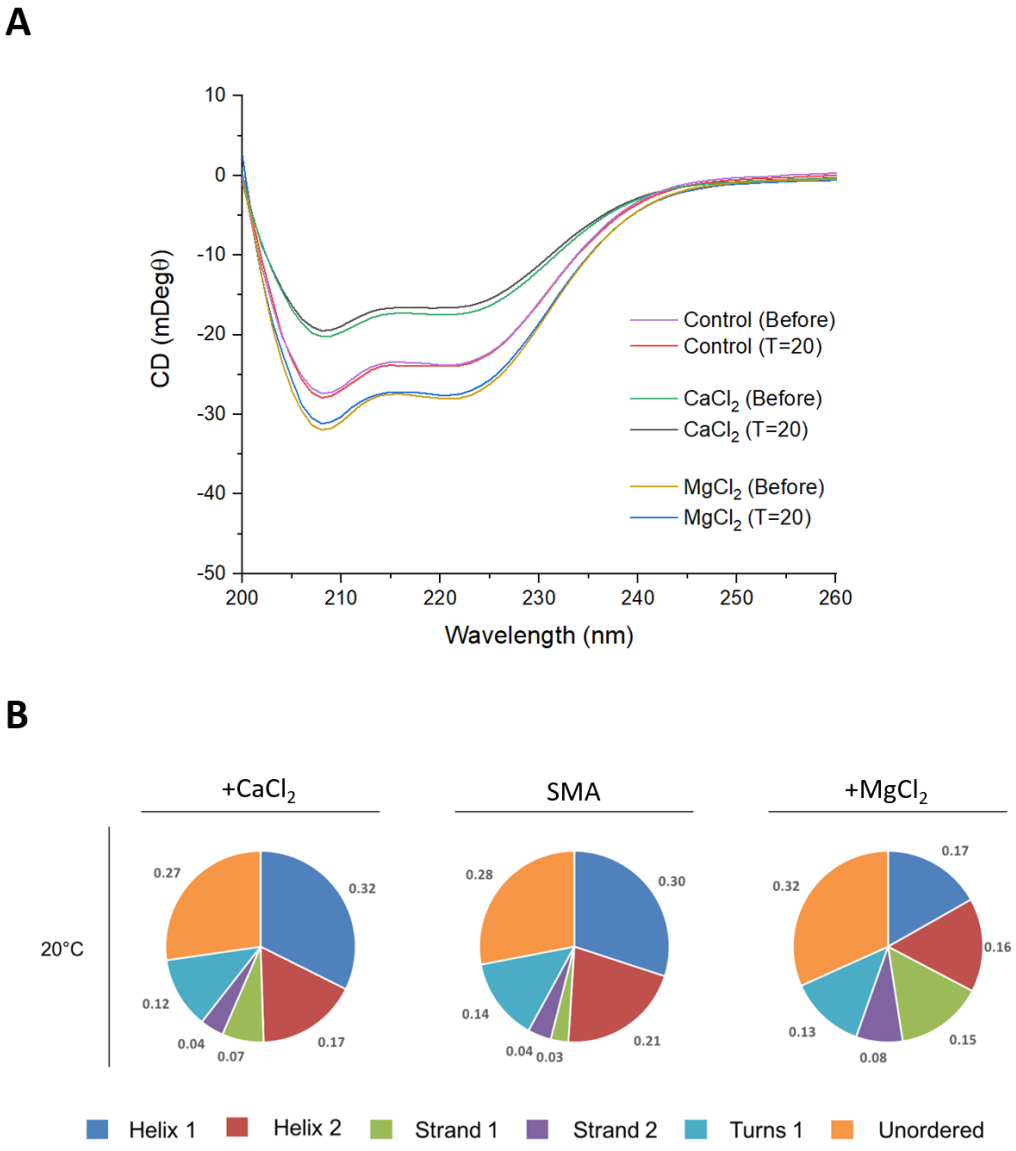

Figure 5.10: CD spectra and secondary structure of TRPM2 in SMA before and after the addition of divalent cations.

A) CD spectra of purified SMA_TRPM2 taken before '(Before)' and after '(T=20)' the addition of $CaCl_2$ or $MgCl_2$. B) Percentage of secondary structure elements in the deconvoluted spectra after the addition of divalent cations.

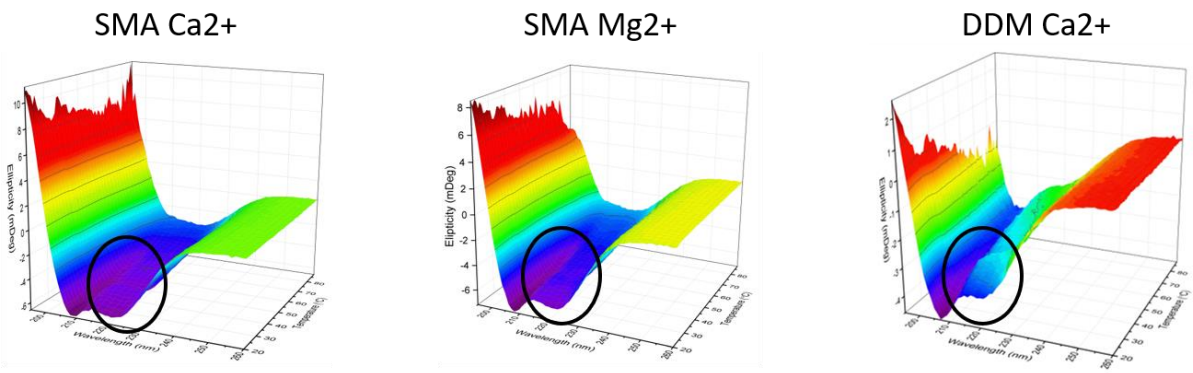

Figure 5.11: Unfolding/refolding feature of TRPM2 at ~37 °C.

The unfolding/refolding feature can be visualised in thermal melt experiments of SMA_TRPM2 with Ca^{2+} and Mg^{2+}, and DDM_TRPM2 with Ca^{2+} at ~37 °C.

Table 5.4: Calculated Tm's of each unfolding event for SMA_TRPM2 and DDM_TRPM2 with and without divalent cations according to Global3 analysis.

Melting temperatures are displayed in °C. Only temperatures below 70 °C are shown.

	DDM	**DDM Ca^{2+}**	**SMA Ca^{2+}**	**SMA**	**SMA Mg^{2+}**
# Transitions	5	2	4	6	7
Calculated Tm of each transition in °C (Global 3)	25.0	29.3	29.4	31.4	21.3
	33.9	36.5	36.1	39.0	33.8
	41.4		63.4	57.8	38.9
	66.6			63.1	50.4
				68.1	62.2

5.2.2.5 A closer look at the unfolding event of TRPM2 at ~37 °C

To examine whether the characteristic TRPM2 feature at 37 °C remained or altered in the presence of divalent cations Ca^{2+} and Mg^{2+}, a thermal denaturation experiment was

performed using the same parameters as in previous experiments - with a 20-50 ° C ramp up, before a 50-20 ° C ramp down. Strikingly, a number of potential folding and unfolding features are seen both for the ascending and descending ramps (Figure 5.12 and 5.13); what is more, the influence of DDM:CHS and SMA have on TRPM2 refolding during the descending ramp is surprising.

Despite the poor signal-to-noise from this particularly low concentration SMA_TRPM2 sample, there is a clear downward trend in the descending curve for DDM:CHS_TRPM2, vs SMA_TRPM2. The gradient of the ascending and descending curves were determined for each sample (listed as 'm' in Figure 5.12 and 5.13), and showed that SMA_TRPM2 unfolds up to 50 °C, and does not regain any secondary structure during the descending ramp (Figure 5.12). In contrast, DDM:CHS_TRPM2 shows a clear downward, refolding trend after reaching 50 °C and during the descending ramp (Figure 5.13). In fact, the DDM:CHS ascending and descending ramps are almost mirrored in native DDM:CHS_TRPM2, $+Ca^{2+}$ and $+Mg^{2+}$.

Unfortunately, despite insights into unfolding/refolding events, deconvolution of these spectra cannot be performed without better signal in the far-UV region. This could also be performed at a SRCD beamline to reduce sample volumes, background interference and provide absolute vacuum conditions, but was unfortunately beyond the scope of this thesis. Further insight into the unfolding and refolding dynamics of TRPM2, and TRP channels in general using this method could provide a wealth of knowledge on TRP channel dynamics and kinetics. In conjunction with the difference observed between the SMA polymer and DDM:CCHS prepared samples, this could also provide further insight into the effect detergents and polymers can have on a proteins fold, function and binding capacity for ligands and *co*-factors.

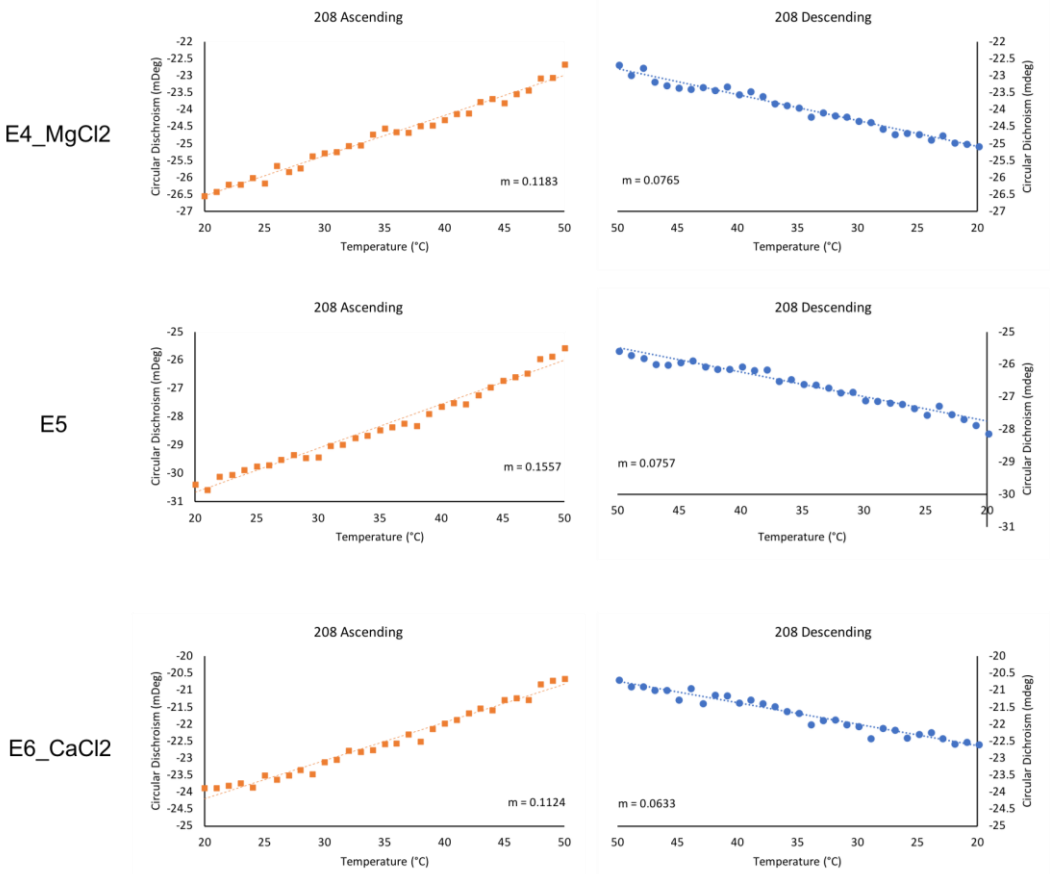

Figure 5.12: CD spectra at 208nm of ascending and descending ramps of DDM:CHS_TRPM2 from 20-50 °C.

The CD spectra recorded at 208nm plotted as a function of ascending (orange, left) and descending (blue, right) temperature ramps for DDM:CHS_TRPM2 samples in the presence of $MgCl_2$ (E4_$MgCl_2$; top row), in 'apo' form (E5, middle row), and with $CaCl_2$ (E6_$CaCl_2$, bottom row). Linear trendlines have been plotted to demonstrate the gradient of the unfolding and refolding events, displayed as 'm' for each graph.

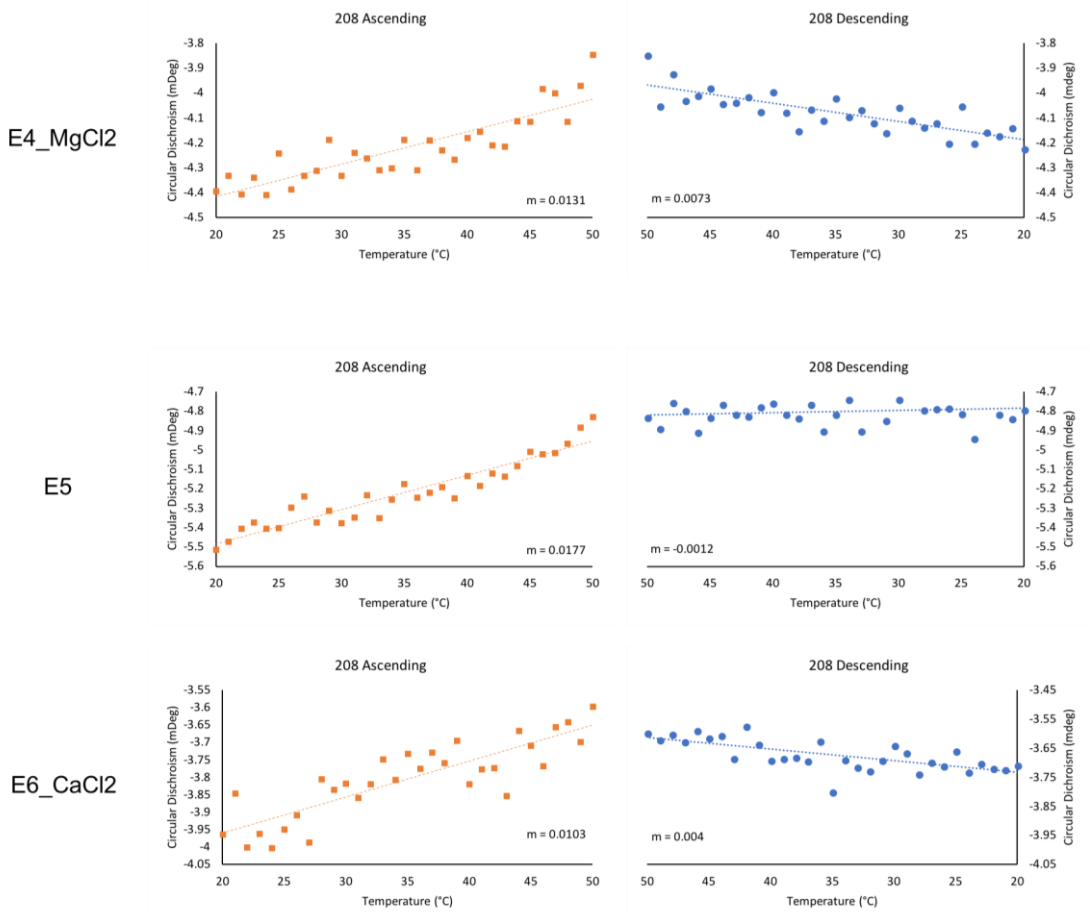

Figure 5.13: CD spectra at 208nm of ascending and descending ramps of SMA_TRPM2 from 20-50 °C .

The CD spectra recorded at 208nm plotted as a function of ascending (orange, left) and descending (blue, right) temperature ramps for SMA_TRPM2 samples in the presence of $MgCl_2$ (E4_$MgCl_2$; top), in 'apo' form (E5, middle), and with $CaCl_2$ (E6_$CaCl_2$). Linear trendlines have been plotted to demonstrate the gradient of the unfolding and refolding events, displayed as 'm' for each graph.

5.2.3 Electron Microscopy of TRPM2

A major goal of this project was to examine the structure-function relationship of TRPM2 by solving the structure of TRPM2 by cryo-electron microscopy (cryo-EM) in near-physiological conditions. Up until this point, a protein production and purification pipeline has been established in the previous chapter, and this chapter will focus on analysis – primarily in the different solubilisation scaffolds.

5.2.3.1 Initial results reveal TRPM2 particles in cryo-EM

Preliminary insights into the structure and integrity of TRPM2 in both SMA and DDM have been described in the previous chapter, and this section will build on that information with more in-depth structural analysis. As there is no set pipeline for structural analysis of membrane proteins by cryo-electron microscopy, this is described primarily through iterative development.

As described in chapter 3, TRPM2 could be successfully purified to sufficient quality for use with EM. While the sample appeared promising by simply visualising with negative stain microscopy, it was necessary to generate a small negative stain dataset and thus 2D-class reconstruction to provide compelling evidence that the protein was suitable for single-particle analysis by cryo-electron microscopy. Generating 2D classes from negative stain allows the user to assess the heterogeneity, conformational flexibility and quality of the sample, and provides an advantage over cryo-EM in that datasets can be obtained promptly with relative ease (Thompson *et al.*, 2016).

Negative stain grids of SMA-TRPM2 were very reproducible in terms of the sample quality, homogeneity and monodispersity, and a small dataset was collected from a sample represented in Figure 5.14B.

The 2D classes in this dataset appeared heterogeneous and amorphous, but a select few classes Maruyama et al., 2007, whom reported a negative stain reconstruction of TRPM2 with dimensions of 25 nm in height by ~17 nm in width. (Figure 5.14A and B). TRPM2 particles are consistently observed between ~25-30 nm, making them 1.5-2.0X the size of the available TRPV and TRPA1 structures at the time (Liao *et al.*, 2013; Paulsen *et al.*, 2015).

The remaining classes showed particles ranging from ~15-30 nm in diameter. At this point the purification process had not been fully optimised, so further clean-up was required to reduce this heterogeneity. The smaller ~15 nm particles were later attributed to the presence of leached anti-FLAG antibody, as occasionally a band of ~150 kDa was observed by SDS-PAGE. However, the visibility of TRPM2 within 2D classes of the negative stain dataset was promising.

After sample optimisation during the purification stages (Chapter 3), cryo-EM of TRPM2 was re-visited. In cryo-EM, particles of ~20 nm in diameter were observed within the foil holes of the grid, and a small dataset was collected and processed to the stage of 2D classification (representative particles shown in Figure 5.14D).

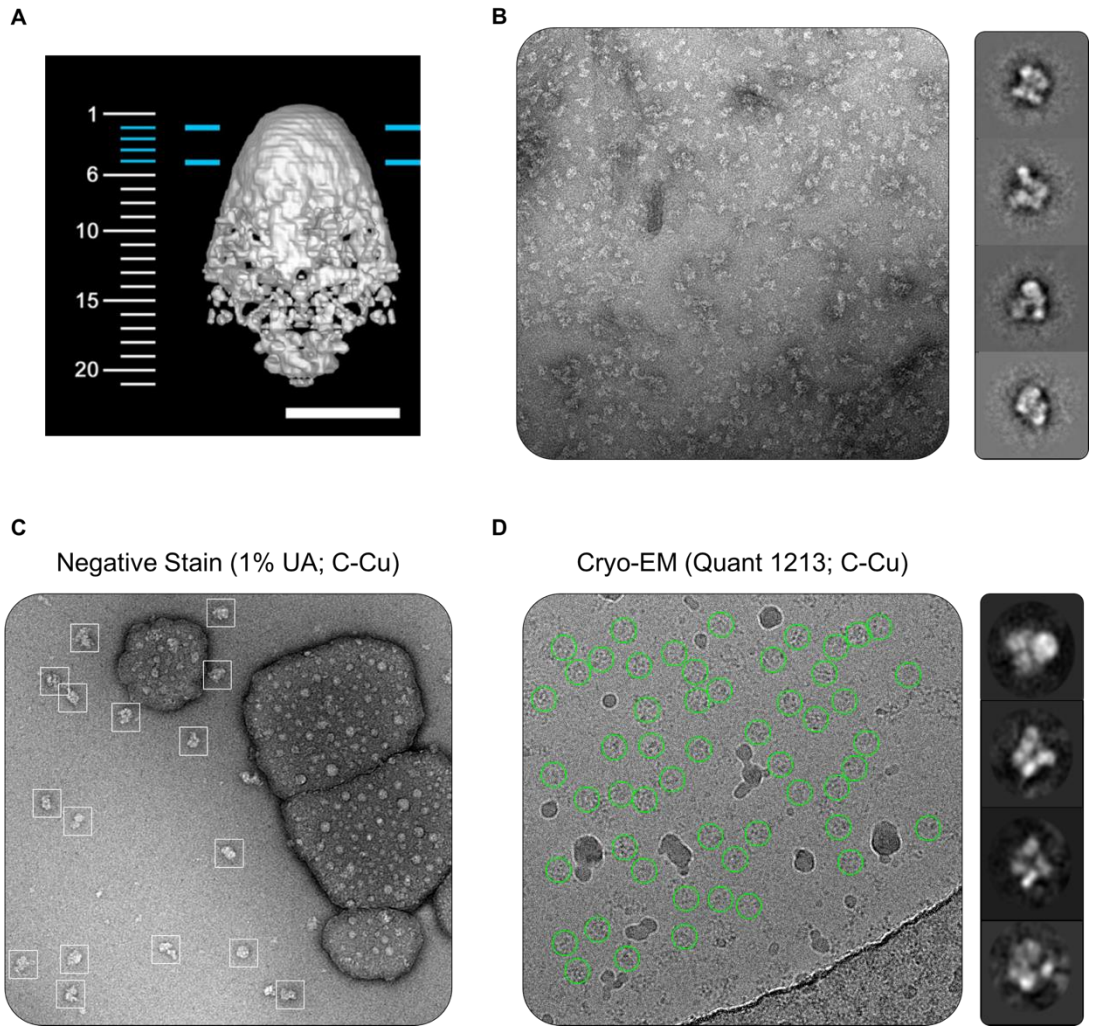

Figure 5.14: Negative stain and cryo-electron microscopy of TRPM2 reveals particles of the correct shape and size in data.

(Previous Page): A) The published negative stain 3D reconstruction of TRPM2 from Maruyama et al., 2007, showing the particle to be bell-shaped with approximate dimensions of ~20 nm x ~17 nm. B) Initial 2D classes generated from a negative stain dataset of the TRPM2 sample shown in the micrograph, where particles are more disperse on the grid. C) and D) represent the same sample of purified TRPM2 in negative stain (C) and cryo-electron microscopy. The grid conditions are shown above the example micrographs. D) shows the initial 2D classes generated from the small cryo-EM dataset that resemble those shown in B). Images are illustrative only and are not provided with scale bars.

At this point, the compatibility of the SMA polymer with cryo-EM had been brought into question as it may be particularly sensitive to the grid-making process. Standard vitrification procedures use blotting paper containing divalent cations (Arnold *et al.*, 2017), and the charge of the grid or polymer itself may also cause adherence to the air-water interface or carbon instead of settling within the foil-holes. Protein absorption and denaturation at the air-water interface is a widely reported phenomenon, particularly applicable to membrane proteins, as they contain a higher proportion of hydrophobic regions (Yano *et al.*, 2009). Although, it was also recently reported that 90 % of all proteins adhere to the air-water interface making this a universal problem with cryo-EM as a technique (Noble *et al.*, 2018).

Nonetheless, the 2D classes generated from this dataset were incredibly exciting and novel, but the selected 2D classes in Figure 5.14D were of very low occupancy and optimisations were needed. An extended dataset of SMA_TRPM2, analogous to that shown in Figure 5.14D, was collected on Quantafoils to increase particle number, but showed no significant improvement ('SMA: 48h Data Collection' in Figure 5.16). Due to low particle numbers per micrograph and high degrees of aggregation, the grid type, protein concentration and vitrification parameters required further optimisation.

5.2.3.2 Optimising grid conditions for cryo-EM

To address some of the issues associated with vitrification of membrane proteins in SMA, ash-less filter paper (Whatman 50) was used in further cryo-EM sample preparations, due to its decreased divalent cation content. Different grid materials and formations were also trialled to facilitate the use of lower protein concentration, and detergents were added to encourage particle distribution away from the carbon and into foil-holes (Figure 5.15). An on-grid cross-linking procedure was also performed in an attempt to reduce particle degradation as a result of the vitrification process.

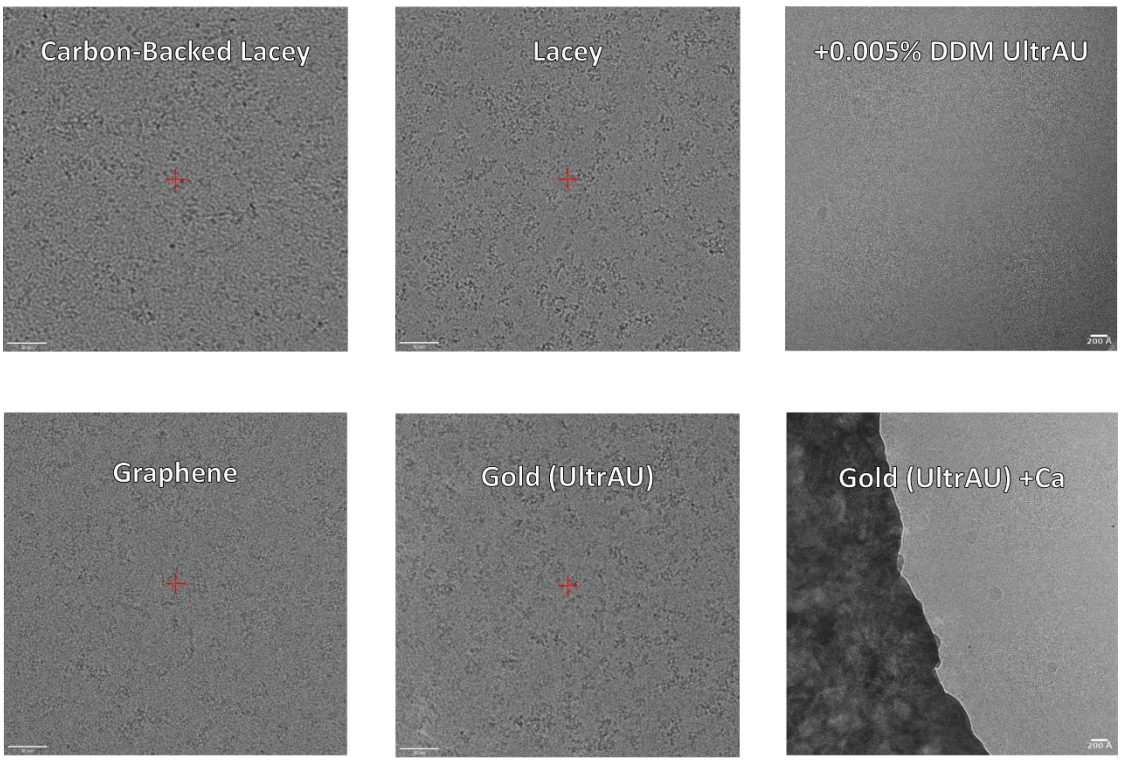

Figure 5.15: Different cryo-EM grids and their effect on TRPM2 particle distribution and degradation.

Sample micrographs of TRPM2 distribution and aggregation/degradation levels on different grid types. Particles can be seen in all micrographs. Scale bars represent 50 nm.

The protein concentration for each tested grid type shown in Figure 5.15 was ~0.3 mg/ml. Of the grid types tested, gold UltrAufoils appeared to give the least amount of contamination and clearer individual particles (bottom row, middle and right panels in Figure 5.15). From these results, grids were further iteratively optimised gold UltrAufoil grids were used to collect 24-hour datasets on SMA_TRPM2 and DDM:CHS_TRPM2. Microscope aberrations interfered with data collection and significantly reduced the number of total micrographs at the time, but some data could be processed to generate 2D classes shown in Figure 5.16.

For DDM:CHS_TRPM2, the dominant feature in the 2D classes were empty micelles (Figure 5.16, middle panel 'DDM:CHS_TRPM2: 24h Data Collection'). Some larger particles were observed in the data that could correspond to TRPM2, but the detergent background was too much to take this data further or draw any significant conclusions as to TRPM2 conformation. On the other hand, very promising classes were obtained from SMA_TRPM2 samples on UltrAUfoil grids. The 2D-classes were reminiscent of TRP channels and showed some tetrameric, 'bell-shaped' structures, similar to those observed in negative stain (Figure 5.14) and previously published by Maruyama et al., 2007. The channel is visible in one particular class as a tetramer potentially bound by four anti-flag antibodies (highlighted in red, adjacent to the selected 2D classes for TRPM2_SMA in the top row of figure 5.16). Maruyama et al., 2007 observed the same anti-FLAG antibody binding to the tetramer in their negative stain 2D classes, so it became an increasing concern that the leached anti-FLAG antibody was introducing heterogeneity and flexibility, inhibiting further processing of this dataset. Unfortunately, this issue was not resolved before the structures of TRPM2 were published (Table 1).

Figure 5.16: Cryo-EM 2D Classes of TRPM2 in SMA or DDM:CHS.

Selected 2D classes from cryo-EM preparations of TRPM2 samples in SMA (top and bottom) and DDM:CHS (middle). SMA datasets were collected on UltrAufoil grids (top) and Quantafoil grids (bottom) for 24 hours and 48 hours, respectively. The 2D class representing TRPM2 potentially bound by four anti-FLAG antibodies is highlighted in a red box adjacent to the other UltrAufoil 2D classes.

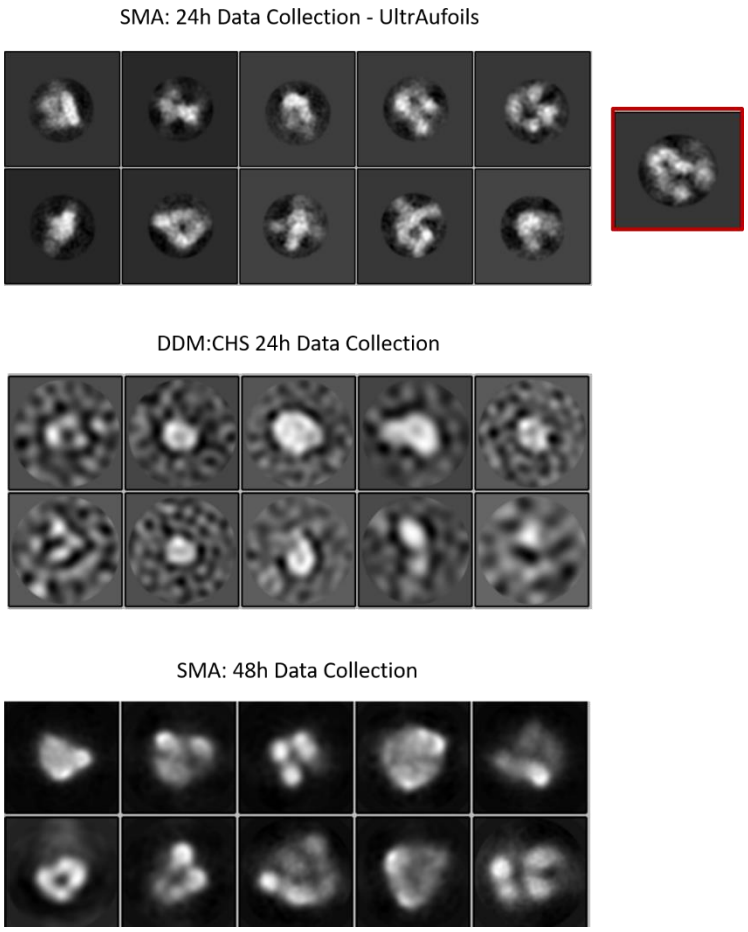

5.2.3.3 Cross-linking TRPM2 for cryo-EM and Negative Stain 3D Reconstruction

Despite efforts, obtaining a structure by cryo-EM appeared fruitless. In an attempt to reduce the conformational flexibility and reduce the heterogeneity and degradation of the sample, and on-grid cross-linking method was trialled. As previous attempts to generate a 3D model from negative stain 2D classes were unsuccessful, a small negative stain dataset was collected alongside a small cryo-EM dataset (Figure 5.17).

The particle distribution of TRPM2 in negative stain was homogeneous and showed no sign of aggregation – the cross-linking method appeared to not influence the integrity of the sample in the negative staining process, and TRP-like 2D classes were once again observed in the small dataset (Figure 5.17A). The same could not be said for the EM samples, which broadly demonstrated the presence of TRP channel-like 2D classes, but it was a concern that the cross-linking created too much noise in the data and this was not taken further. However, a 3D reconstruction was generated from the cross-linked negative stain dataset at 31 Å resolution - the highest resolution TRPM2 structure available at the time (Figure 5.17C). This structure was of 305 Å x 250 Å. Unfortunately, the dimensions could not be accurately calculated due to issues with microscope calibration and stability, but the overall shape of the structure is similar to that of Maruyama et al., 2007 (Figure 5.14A).

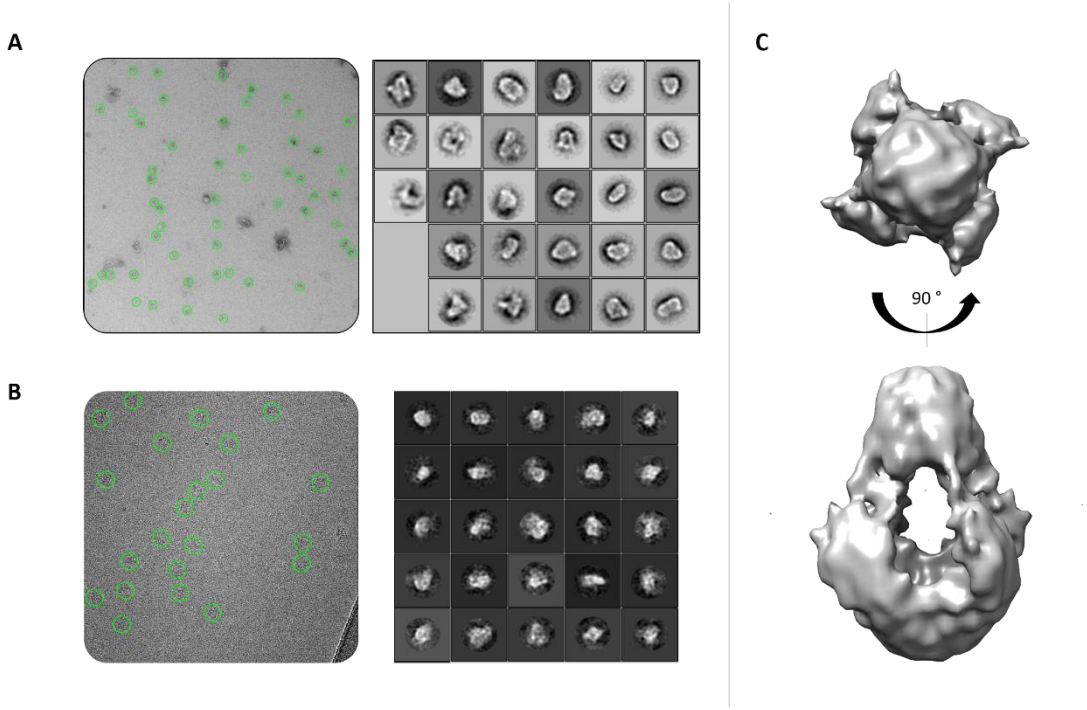

Figure 5.17: On-grid cross-linking results of SMA_TRPM2 in negative stain and cryo-EM with 3D reconstruction.

A) Negative stain micrograph of cross-linked TRPM2 and corresponding 2D classes. B) Cryo-EM micrograph of cross-linked TRPM2 and corresponding 2D classes. C) C4 symmetrised negative stain reconstruction using the 2D classes from A. Scale bars are not shown in these illustrative micrographs of picked particles.

5.3 Summary of Biochemical and Structural Characterisation of TRPM2.

In this chapter, steps were taken toward the structural characterisation of the TRPM2 cation channel using protein samples optimised as described in Chapter 3. Thermal stability assays and circular dichroism (CD) were key techniques for determining

thermodynamic and folding properties of TRPM2 in detergent and SMA, and electron microscopy (EM) gave insights into the overall architecture of TRPM2 in SMA.

CPM assays determined the melting temperature of SMA_TRPM2 and DDM_TRPM2 to be ~50 °C (Figures 5.1 and 5.2). To explore stabilising partners for use with EM, calcium (Ca^{2+}) and magnesium (Mg^{2+}) ions were sampled as additives. Ca^{2+} has an essential role in TRPM2 channel gating and activation, and four calcium-binding sites in the transmembrane domain of TRPM2 had already been defined at the time (Tong et al., 2006; Starkus et al., 2007; Csanády and Törocsik, 2009; Kühn et al., 2015; Iordanov et al., 2016b). A direct role for Mg^{2+} ions in TRPM2 physiology has not been reported, but canonical NUDIX domains require its presence for catalysis (Bessman et al., 1996; Perraud et al., 2003). Ca^{2+} and Mg^{2+} destabilise the SMA polymer at millimolar concentrations (Fiori et al., 2017), so both were examined here at low micromolar concentrations.

From CPM thermostability assays, the effect that Ca^{2+} and Mg^{2+} were having on both DDM_TRPM2 and SMA_TRPM2 stability was unclear, but the combination of the two appeared to be detrimental (Figure 5.3). Denaturation curves appeared to show that overall, the Tm of SMA_TRPM2 was increased in the presence of Ca^{2+} (Figure 5.3). However, it was difficult to attribute the results to an aggregation effect on the polymer, or the protein itself. Other co-factors gave similar results, and no co-factor or binding partner seemed to substantially increase the Tm, at least by this method. The unfolding curves also appeared to contain multiple transition temperatures, which could be broken down into smaller unfolding events, but due to limitations of the technique, it was unclear as to whether these transitions were genuine.

Circular dichroism (CD) was implemented to shed more light on these potential unfolding events by monitoring secondary structure changes during thermal denaturation and revealed some potentially novel insights into TRPM2 function.

When initial unfolding experiments were performed with CD, multiple unfolding events were observed in the spectra as changes in overall α-helix and β-sheet content, which made it difficult to assign only one overall melting temperature. However, other features were observed in the spectra which could have interesting implications for the mechanism of TRPM2 in different environments.

The first of these events was notices in initial thermal melt assays, whereby during the ramp down from 90 °C to the final 20 °C, TRPM2 appeared to regain some secondary structure, predominantly in the alpha helical part of the spectrum at ~208 nm (Figure 5.7B). The reason for this was unknown, but pointed to a potential inherent property of the protein and its behaviour at different temperatures. Further investigation into the overall unfolding/refolding events led to a focus on a temperature range between 20-50 °C - spanning the known TRPM2 activation temperature (Song, Wang, Gretel B. Kamm, et al., 2016; Kashio and Tominaga, 2017; Tan and McNaughton, 2018). Multiple transition events were tentatively observed in the spectra, but most striking of all was the observation of a significant unfolding/refolding feature consistently observed at ~40 °C in both DDM:CHS_TRPM2 and SMA_TRPM2 samples.

Interestingly, this unfolding/refolding feature appeared at a higher temperature in DDM:CHS_TRPM2 (~43 °C) relative to SMA_TRPM2 (~40 °C) (Figure 5.9). When the refolding events were examined more closely in a downward temperature ramp, it was also observed that TRPM2_SMA does not regain secondary structure lost in this temperature range, but DDM:CHS_TRPM2 does (Figures 5.12 and 5.13). The reason

for this is still unknown, but perhaps could be attributed to the flexibility granted by the detergent micelle over the SMA *co*-polymer. The occurrence of this phenomena in different detergent and polymer systems has exciting implications for the structure-function relationship of TRPM2 in the context of the lipid bilayer, but also for the protein as an inherent temperature sensor itself (discussed further in Chapter 7).

While CD was able to provide potentially exciting insights into the mechanism of TRPM2 and its' activation at ~37 °C, this cannot be attributed to any specific region of TRPM2 without further structural and functional data. Electron microscopy has the potential to provide great insight into the mechanisms of TRPM2 in different lipidic environments – in this case, encapsulated either within the SMA polymer or a detergent system. For detergents, unfortunately the plague of micelles could not be circumvented within this time frame to generate any meaningful structural data. Even in negative stain, there were issues with background detergent contamination in DDM:CHS_TRPM2 samples (Figure 3.8), which translated further when examined by cryo-EM (Figure 5.16). Future work on removing excess detergent micelles would improve the quality of this sample. However, significant ground was made with SMA_TRPM2.

In SMA, TRPM2 was stable and homogeneous enough to generate convincing 2D classes in both negative stain and cryo-EM (Figure 5.14). With some persistence and optimisation, cross-linking experiments were later able to yield a negative stain SMA_TRPM2 reconstruction which was processed to 31 Å (Figure 5.17). This was comparable to the previously published negative stain reconstruction by Maruyama et al., 2007, showing a similar dome-shaped architecture. This was the first example of a TRP channel in a SMALP system, and the highest resolution TRPM2 channel structure

at the time. However, unfortunately this success in negative stain was not translate to cryo-EM. While significant steps towards a cryo-EM structure were made, iterative optimisation of grid conditions, including protein concentration, vitrification parameters and grid type, unfortunately did not yield a final cryo-EM structure in this time frame. Additionally, during the course of this PhD, several high-resolution TRPM2 structures were solved (Table 1).

Of these, the highest resolution *hs*TRPM2 structures came from Huang et al., 2019. These structures were solved in detergent systems, but amazingly, the 2D classes used to generate these reconstructions showed some similarity to the TRPM2 2D classes generated here. The large cavity observed in the negative stain reconstruction generated here is also observed in these high resolution structures, as well as a splayed-open and narrow-closed conformations (Figure 1.7 and 1.8) which could also be interpreted from the 2D classes presented in this thesis (Figures 5.14 and 5.16). However, the SMA_TRPM2 system described here still offers some novelty, as it would be the first TRP channel structure with a truly native-like lipid environment. In future, now that initial parameters have been optimised, it would be very exciting to pursue the structure of SMA_TRPM2 for comparison.

In summary, steps were made towards the structural characterisation of TRPM2 using biophysical techniques, particularly CD and EM. Differences were observed between the behaviour of TRPM2 in detergent and SMA, which has interesting implications on temperature-sensing mechanisms, and regulation by the lipid bilayer – discussed further in Chapter 7.

Chapter 6:

Membrane Protein

Scaffold Exchange

6.1 Introduction

Traditional *in vitro* membrane protein characterisation methods edict that the protein is extracted in detergent, which strips away the native membrane and encapsulates the hydrophobic transmembrane region within a micelle to keep it suspended in solution, often delipidating the membrane protein complex in the process. The detergent then remains present throughout all stages of the purification but can be later exchanged for a different detergent or a more suitable detergent system/solubilisation platform for downstream experimentation. However, this process is not trivial, and often much time, money and resources are committed to optimisation of solubilisation and purification conditions.

A number of alternative reconstitution platforms have been developed to combat detergent-associated issues, such as membrane scaffold protein nanodiscs (Civjan *et al.*, 2003; Ritchie *et al.*, 2009), amphipols (Tribet, Audebert and Popot, 1996; Zoonens and Popot, 2014), peptidiscs (Carlson *et al.*, 2018), bicelles (Dürr, Gildenberg and Ramamoorthy, 2012) and liposomes (Rigaud, Pitard and Levy, 1995). However, all of these methods require an initial detergent solubilisation step, often resulting in reduced membrane protein activity and/or detrimental structural perturbations (Seddon, Curnow and Booth, 2004; Dörr *et al.*, 2014; Jamshad, Charlton, *et al.*, 2015; Reading, Walton, *et al.*, 2015; Gupta *et al.*, 2017).

In an attempt to overcome these issues entirely, styrene-maleic acid (SMA) lipid particles (SMALPs) were developed as a platform for membrane protein solubilisation (Knowles, Finka, Smith, Y.-P. Lin, *et al.*, 2009; Orwick-Rydmark *et al.*, 2012a; Jamshad, Grimard, *et al.*, 2015; Lee *et al.*, 2016).

While there have been many publications assessing the functional activity (Dörr *et al.*, 2014; Jamshad, Charlton, *et al.*, 2015) and lipidome (Oluwole *et al.*, 2017; Teo *et al.*, 2019), of SMALP:membrane protein complexes, only a few high resolution (<4 Å) cryo-EM structures have been published to date – namely Alternative Complex III (Sun *et al.*, 2018), and two multi-drug efflux pumps (Qiu *et al.*, 2018; Su *et al.*, 2019). The underlying reason for this difference between the number of proteins solubilised efficiently in SMA vs the number of structures solved by cryo-EM is not entirely known. There are several speculations in the literature and throughout the SMALP community as to why some potential incompatibilities may exist, such as: polymer heterogeneity as a direct result of SMA synthesis (Craig *et al.*, 2016); the inherent polymer properties, including charge and sensitivity to divalent cations (Dörr *et al.*, 2016); the quality of the starting material and hydrolysis of the SMA anhydride (Kopf *et al.*, 2019); and the as-of-yet undefined nature of the surrounding lipid annulus, which varies from protein-protein.

Despite these challenges in EM, one significant advantage of adopting a SMALP method is that it can extract and isolate the protein of interest in the presence of its native lipid annulus (Knowles, Finka, Smith, Y.-P. Lin, *et al.*, 2009; Jamshad, Grimard, *et al.*, 2015; Scheidelaar, Martijn C Koorengevel, *et al.*, 2015; Lee *et al.*, 2016). MS has recently emerged as a powerful complementary tool for exploring membrane protein:lipid complexes, both in native-MS to determine lipid stoichiometry (Gupta *et al.*, 2017, 2018; Pyle *et al.*, 2018), and denaturing-MS to examine their lipid profile (Pollock *et al.*, 2019; Teo *et al.*, 2019). However, while SMALPs have the potential to deliver this wealth of knowledge with MS, the heterogeneity of the SMA polymer and its inability to dissociate easily in the gas phase has rendered it

problematic for conventional mass spectrometers without the use of specialised systems (Hellwig *et al.*, 2018). Exchanging the bound SMA with a detergent or amphipol may overcome SMA-related issues, as both amphipols (Hopper *et al.*, 2013; Michael T Marty, Hoi and Robinson, 2016) and detergents (Reading, Liko, *et al.*, 2015a; Gupta *et al.*, 2018), have been extensively characterised in both EM and MS (Leney *et al.*, 2012; Watkinson *et al.*, 2017). This should be theoretically possible, as displacement of polymers for detergents or other surfactants has been previously described (Zoonens *et al.*, 2007a).

Thus far, analysis of SMA_TRPM2 in cryo-EM has been unsuccessful due to the heterogeneity, degradation and aggregation upon vitrification. This is believed to be caused by the SMA *co*-polymer and additional factors relating to grid-making procedures and reproducibility. This chapter therefore explores a more combinatorial approach to *in vitro* membrane protein characterisation, whereby the membrane protein of interest is first extracted in SMALPs, and subsequently exchanged into a more appropriate solubilisation system – either amphipol or detergent – to capitalise on the strengths of each system and increase sample compatibility with downstream applications, such as cryo-EM and MS (Figure 6.1).

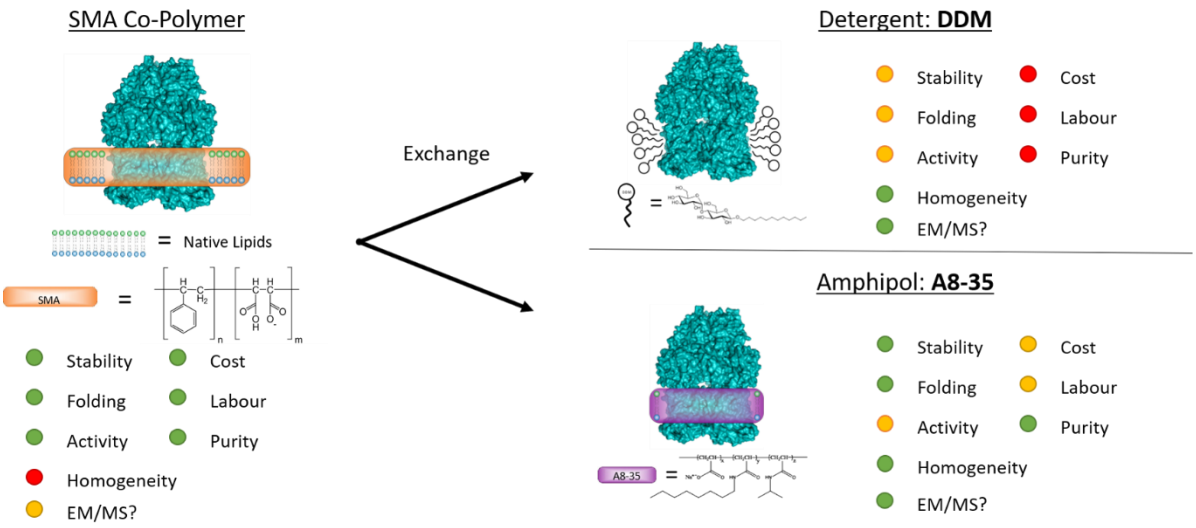

Figure 6.1: Traffic light schematic highlighting the strengths and weaknesses of SMA, amphipol (A8-35) and detergent (DDM).

Each system is accompanied by a list with representative published strengths (green), and weaknesses (red). Where there is literary evidence of both success and failure with regard to one aspect, these are assigned yellow dots. The schematic also includes information about the nature of the transmembrane annulus in each system, whether is polymer-bound and contains lipids, or whether it is in detergent and potentially delipidated.

The exchange between systems can also be used in synergy to obtain a better understanding of how lipids can directly affect membrane protein structure and function. In this context, SMALPs would act as a powerful tool for initial solubilisation and purification of membrane proteins, offering a significantly cheaper, stable alternative to conventional detergent purification methods, while retaining lipids from the membrane proteins' native environment. To test the feasibility of exchanging SMA for another solubilisation system, initial precipitation and exchange experiments were carried out on TRPM2, before moving onto AcrB in order to develop the method further.

6.2 Results and Discussion

6.2.1 SMA Chelation and Detergent Exchange of TRPM2

An initial attempt at exchanging SMA-TRPM2 for DDM-TRPM2 involved direct addition of 2mM $CaCl_2$ – a known SMA chelator at concentrations >5 mM (Stephen C L Hall *et al.*, 2018) – to a FLAG purified fraction of SMA-TRPM2. This was unsuccessful and saw the protein and polymer precipitate almost instantaneously out of solution. As this sensitivity has been linked to the polymer structure and not the protein within (Gulamhussein *et al.*, 2019), this was supposedly not related to TRPM2. However, there is evidence that TRPM2 binds $CaCl_2$ in a co-operative manner (Csanady and Torocsik, 2009; Du, Xie and Yue, 2009), so the addition of a direct TRPM2 activator could induce conformational changes that destabilise the polymer-protein complex, also potentially leading to precipitation. To soften the addition of 2 mM $CaCl_2$ and destabilise the polymer without precipitation, a single fraction equivalent to E3 from a standard FLAG affinity purification was dialysed against Elution Buffer (EB; 300 mM NaCl, 20 mM Tris.HCl, pH 7.5) and supplemented with 0.1 % DDM, and varying concentrations of $CaCl_2$.

Prior to dialysis, the CD spectra of SMA-TRPM2 in this fraction were recorded as a reference at a measured concentration of ~0.16 mg/ml (Figure 6.2B). The same sample was then added to a mini GeBAflex dialysis tube (8 kDa MWCO) and dialysed for two hours at 4 °C with 0.5 mM $CaCl_2$. After two hours, the sample was removed, centrifuged at 100,000 xg, then placed in the next dialysis buffer supplemented with 1 mM $CaCl_2$. This process was repeated in 0.5 mM increments up to a final concentration

of 2 mM $CaCl_2$, and 10 µl samples from the soluble fraction were collected between each increment. Any pellets generated as a result of centrifugation were resuspended in 10 µl SDS and analysed by western blot alongside their soluble counterparts to reveal whether the precipitant material contained TRPM2 protein, or the polymer alone (Figure 6.2A). Results show that TRPM2 remains in the soluble fraction for the majority of the experiment, with only a small amount of protein detected in the insoluble fraction for condition 2 mM $CaCl_2$ (Figure 6.2A). The final concentration was measured to compare any sample loss, and a CD spectrum was recorded for comparison to the starting material (Figure 6.2B).

Interestingly, the concentration of protein measured after the 'exchange' attempt increased to 0.21 mg/ml, according to the A_{280} recording by the same spectrophotometer with a complimentary buffer blank. When the CD spectrum of the final 'DDM exchanged' sample was processed and adjusted for a new concentration of 0.21 mg/ml instead, it was found to overlap almost exactly with SMA-TRPM2 spectra taken of another fraction from the same purification (E4), measured originally at half of the concentration of E3 (Figure 6.2B, yellow and dark blue). This was unexpected, and although the concentration of protein was now unclear, it did imply that the protein from the exchange had not undergone dramatic secondary structure changes relative to SMA-purified samples. Negative stain images were taken to further assess the protein integrity of the exchanged material, where TRPM2 particle outlines could be seen on a background of detergent noise (Figure 6.2C).

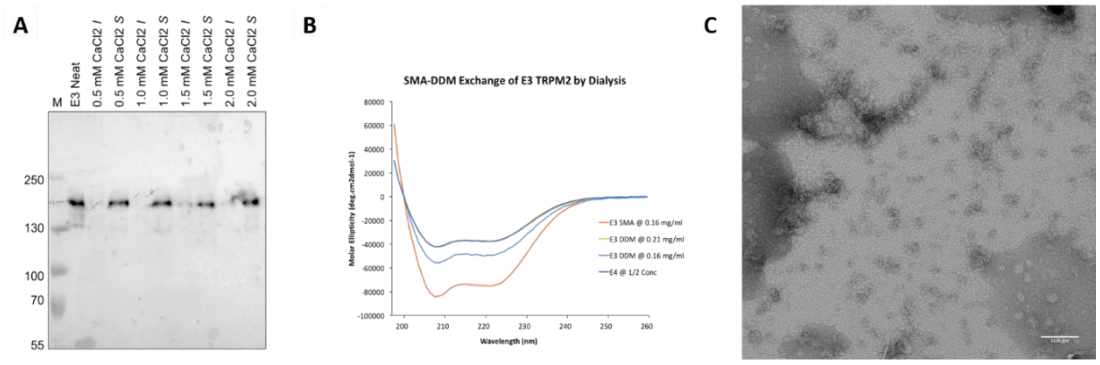

Figure 6.2: Exchanging SMA-TRPM2 to DDM-TRPM2 through dialysis.

A) Western blot following the presences of TRPM2 either in the insoluble (I) or soluble (S) fractions throughout the exchange, compared to the original starting material (E3 Neat) alongside a MW marker (M). B) CD spectra of the starting material (E3 SMA @ 0.16 mg/ml), end material corrected for the original protein concentration (E3 DDM @ 0.16 mg/ml), end material corrected for new protein concentration (E3 DDM @ 0.21 mg/ml), compared to another fraction from the same purification (E4 @ ½ concentration). C) Negative stain micrograph of final DDM-TRPM2 exchanged product. Scale bar = 100 nm.

At this point it was unclear whether the protein had undergone complete exchange into DDM, or if the detergent/SMA mix had integrated and formed a hybrid. Additionally, the advantage of the SMA polymer is that it eliminates the need for detergent, so it could be seen as counter-intuitive to add detergent-related issues back into the equation. However, to keep detergent-related issues out of the equation, a well-established polymer could be used for the exchange instead.

6.2.2 SMA-Amphipol Exchange of TRPM2

Amphipols have previously been used for structure determination of membrane proteins by cryo-EM, including infamous TRP family members such as TRPV (Liao et al., 2013) and TRPA (Paulsen *et al.*, 2015). At the time of conceptualisation, PMAL-C8 and A8-35 were the most prevalent in the literature and have been used successfully for publication of several high resolution cryo-EM structures (Liao *et al.*, 2013; Paulsen *et al.*, 2015; Jin *et al.*, 2017; Y. Zhang *et al.*, 2018). Their success in EM as well as mass spectrometry is largely due to their stabilising effect on the membrane protein of interest and ability to reduce heterogeneity by binding to the transmembrane region with high affinity (Tribet, Audebert and Popot, 1997; Zoonens *et al.*, 2007b; Liao *et al.*, 2013). For these reasons, they were good candidates for establishing and developing this exchange method. Other membrane protein scaffolds – nanodiscs, for example – were considered and have also been used successfully with cryo-EM, and while it would have been interesting to explore an SMA-nanodisc, it was beyond the scope of this project. Additionally, SMA-liposome exchange was established while these experiments were underway, which held some hope for success for the exchange (Smirnova, Ädelroth and Brzezinski, 2018).

6.2.2.1 SMA Chelation and Amphipol Selection

Conventionally, amphipols are mixed with detergent-purified samples at a w/w ratio determined through initial mixing experiments. The most commonly quoted ratio is 1:3 w/w protein:amphipol, and ratios of 1:3 w/w A8-35 and 1:5 w/w PMAL-C8 have been successfully used for structure determination of TRPV1 (Liao *et al.*, 2013) and TRPA1 (Paulsen *et al.*, 2015), respectively, by cryo-EM. Additionally, A8-35 has been

successful within the field of mass spectrometry (Calabrese *et al.*, 2015; Watkinson *et al.*, 2015). Due to their prevalence in the literature and prior verification with EM and MS, these were chosen as the amphipols to be explored for exchange experiments.

An additional consideration was the choice of SMA chelator to encourage precipitation. The use of $CaCl_2$ was suitable for detergent exchange as it has no adverse effects on DDM. However, amphipols are also sensitive to divalent cations, particularly Ca^{2+} (Picard *et al.*, 2006). Both PMAL-C8 and A8-35 are not reported to be as sensitive to $MgCl_2$, and can be stable up to concentrations of 10 mM $MgCl_2$ – greater than SMA's limit of 5 mM – so were still trialled here (Gorzelle *et al.*, 2002; Picard *et al.*, 2006).

For initial experiments, two fractions equivalent to Elution 3 (E3) and E4 were taken from the same purification (Figure 6.3A) and tested initially for a small-scale, 25 µl exchange, and a larger-scale, 200 µl exchange, respectively. Some additional contaminants from this prep were visible in SDS-PAGE, so E4 was examined by negative stain to test for suitability for this experiment. TRPM2 was clearly seen as monodisperse and relatively homogeneous particles with low background and no obvious other high molecular weight contaminants (Figure 6.3B), consistent with previous results. The protein content of E4 was measured at ~0.17 mg/ml (~1 µM TRPM2), and this fraction was split into eight 25 µl aliquots for miniature exchange trials to test the effect of $MgCl_2$ instead of $CaCl_2$. Four samples were mixed with A8-35, and the remaining four with PMAL-C8, both at an amphipol:protein w/w ratio of 1:3; before $MgCl_2$ was added at final concentrations ranging between 0.5-2 mM. Samples were then incubated with inversion overnight at 4 °C and harvested for

ultracentrifugation at 100k xg before being analysed by dot blot and negative-stain microscopy. While the dot blot demonstrated the presence of FLAG-tagged TRPM2 in every sample (Figure 6.3C), there were some issues with sample adsorption into the membrane which makes the results unclear. However, negative stain was able to show that not only was TRPM2 still present to some degree in every condition of the experiment (visible as ~20 nm particles), these particles appeared to retain their overall integrity (Figure 6.4).

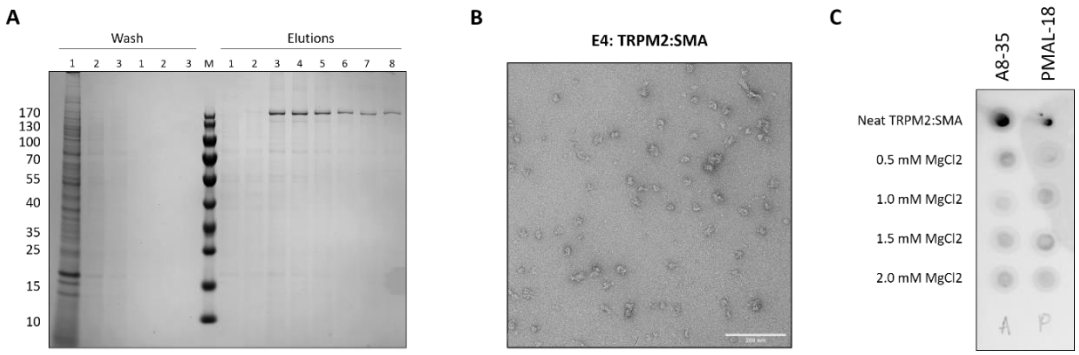

Figure 6.3: TRPM2 preparation for amphipol-exchange and initial results.

A) TRPM2 purification performed as standard, described in Chapter 3. B) Negative stain micrograph of elution fraction 4 (E4) from the purification shown in 'A'. C) Dot blot following soluble fractions of TRPM2 mixed with either A8-35 or PMAL-C8 in the presence of 0.5-2.0 mM $MgCl_2$. Samples were analysed alongside a 'neat' undiluted and untampered control.

The most striking observation from negative stain was the difference between the two amphipols. For PMAL-C8, very few particles were observed in all conditions. Conversely, A8-35-incubated particles appeared to be very similar to the original results obtained for SMA-TRPM2. However, it was noted that PMAL-C8 was quite

viscous and difficult to work with during sample preparation, so was easily wicked from the grid leaving few protein particles behind.

The reason for this disparity could be related to sample handling errors, but it was still a factor to consider when selecting an amphipol type for moving forward with the method. Additionally, PMAL-C8 gave significantly high background in the form of smaller, ~5 nm particles, compared to A8-35 which did not exhibit this behaviour. Although for A8-35, it was interesting to see that a concentration of 1 mM $MgCl_2$ appeared to negatively affect the sample and showed potential aggregation and degradation of the protein. However, for the A8-35 samples incubated with 1.5-2.0 mM $MgCl_2$, little aggregation was seen. The surviving particles from the A8-35 exchange at higher $MgCl_2$ concentrations seemed to be of similar size and behaviour to the original SMA-TRPM2 sample, potentially indicating some preservation of sample integrity.

These surviving particles were thought to have succeeded in forming a stable complex of polymer:protein, at $MgCl_2$ concentrations high enough to precipitate the SMA polymer, but low enough to maintain amphipol integrity; whereas too low, and only light disruption may occur causing aggregation. However, at this point it was unclear as to whether a SMA-A8-35 hybrid system had formed around the transmembrane region, and further investigation was required. Running this experiment on a larger scale would not only allow for the addition of another small purification step with the potential to perform downstream experiments, and if successful, would represent a novel initial protocol towards SMA-amphipol exchange. Another ideal experiment would be to optimise the amphipol:protein ratio further, but due to limitations in sample volume, concentration and cost, this was not be feasible with TRPM2.

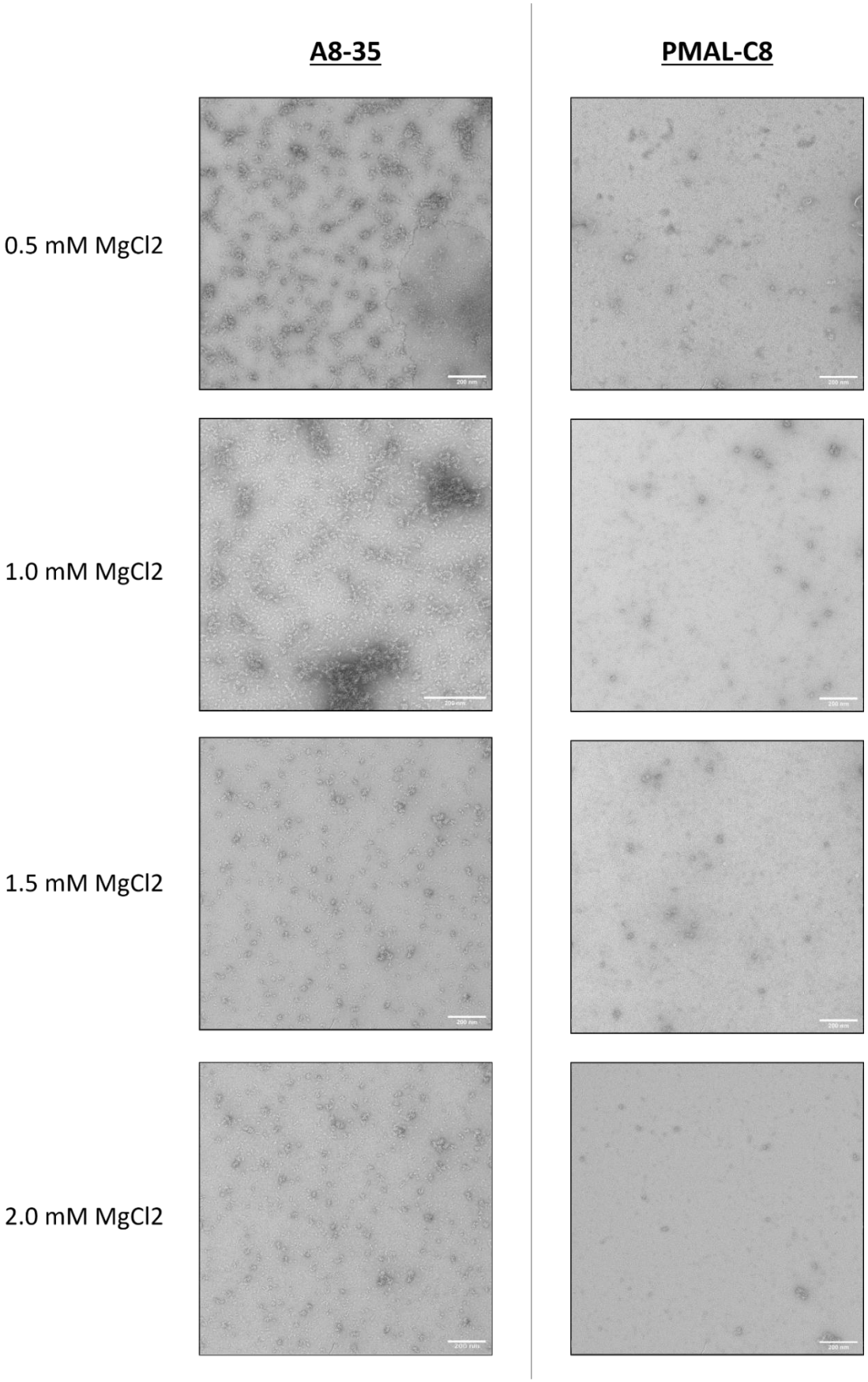
A8-35
PMAL-C8
0.5 mM MgCl2
1.0 mM MgCl2
1.5 mM MgCl2
2.0 mM MgCl2

Figure 6.4: Negative stain analysis of TRPM2 samples after incubation with either A8-35 or PMAL-C8 in the presence of MgCl2.

(Previous Page): TRPM2 was incubated with A8-35 or PMAL-C8 at concentrations of 0.5, 1.0, 1.5 and 2.0 mM MgCl2. Scale bars represent 200 nm.

6.2.2.3 Large-Scale Exchange Trial from SMA to A8-35

Based on the results of the small-scale study, 2mM $MgCl_2$ was incubated with TRPM2:SMA in the presence of A8-35 overnight at 4 °C. This is analogous to the experiment described in section 5.2.1 where $CaCl_2$ was directly added to the sample. After incubation, samples were examined by negative stain before and after centrifugation at 100,000 xg (Figures 6.5A and 6.5B). Results show that background aggregation and particle heterogeneity was reduced after ultracentrifugation, demonstrating the requirement of this final ultracentrifugation step on sample clean-up prior to further experimentation. As intended from this scale-up experiment, a larger volume of sample was available after the exchange, which allowed for testing of a small desalting or 'mini-SEC' step to further clean-up the sample.

Thirty-six fractions of 50 µl volume were eluted from 1 ml of rehydrated Superdex G-50 resin and analysed for the presence of TRPM2 by dot blot (Figure 6.5C). From the dot blot, fraction 4 contained the most protein, and was analysed as an undiluted solution by negative stain (Figure 6.5D). Unfortunately the 'mini-SEC' step did not seem to improve the sample quality; in fact, it appeared to increase background relative to the data obtained in Figure 6.5B and by nature of SEC fractionation, diluted the sample. However, upon closer inspection, particles resembling amphipol:TRP channel 2D classifications previously seen in the literature were visible through the background

noise (Figure 6.6) This was perhaps some indication that the method was working to reduce the size and heterogeneity of the transmembrane annulus surrounding TRPM2 – which was one of the goals of this method.

Another aim was to analyse the exchanged sample by mass spectrometry. Until now, protein concentration had been an issue for TRPM2 with this technique, as SMA-TRPM2 had the propensity to stick to filter membranes and was difficult to concentrate further by other means. However, it was the hope that exchanging SMA for A8-35 would facilitate concentration in this way. Additionally, excess polymer material from either A8-35 and SMA needed to be removed, so an online FPLC-SEC step was later tested.

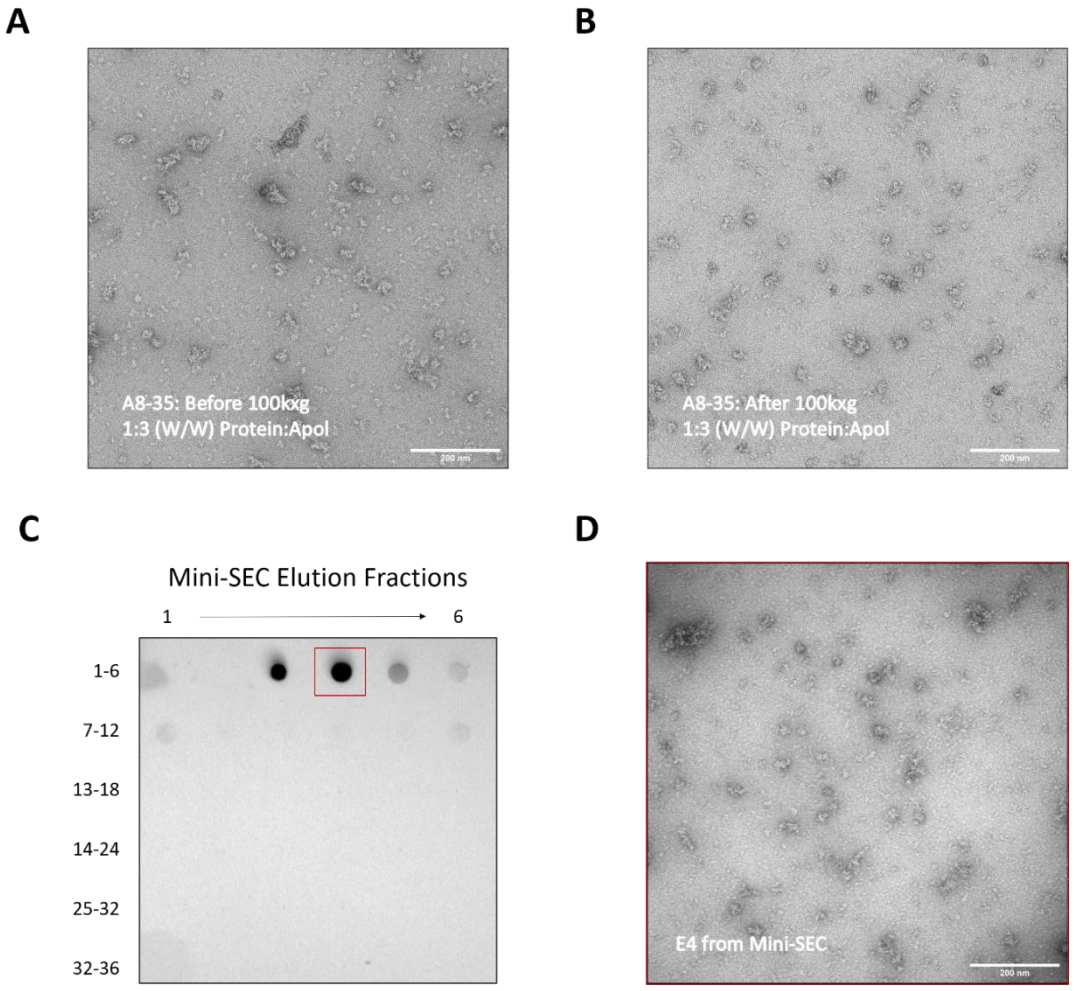

Figure 6.5: Results demonstrating the effect of ultracentrifugation and 'mini-SEC' on the final exchanged sample.

A) Negative stain micrograph of samples after incubation with A8-35 and $MgCl_2$, at the end of the exchange procedure. B) Negative stain micrograph of the same sample as in 'A)' after ultracentrifugation at 100,000 xg. C) Dot blot showing location of FLAG-TRPM2 in each fraction from the mini-SEC column. Fraction 4 is boxed in red. D) Negative stain of fraction 4 from 'C'.

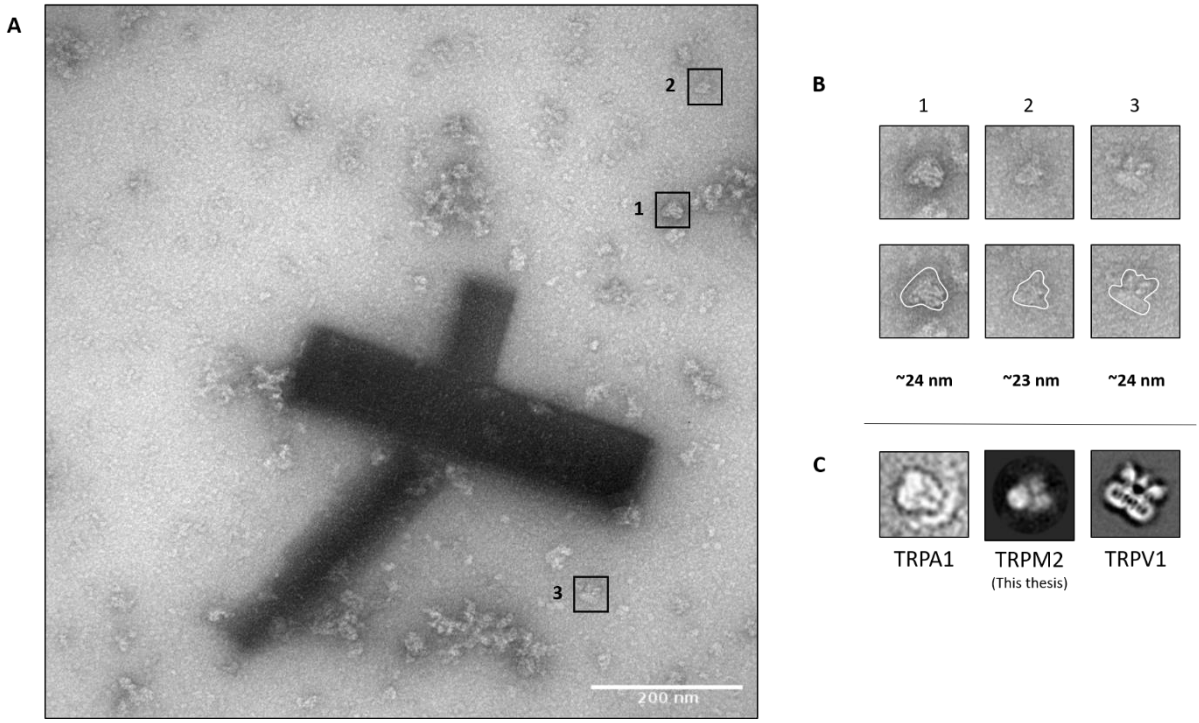

Figure 6.6: Further analysis of results from Figure 5.5.

A) Negative stain micrograph of TRPM2 as in Figure 5.5D, but at a different grid location. Particles of interest are highlighted in boxes labelled 1-3. B) Magnified and emphasised particles highlighted in '(A)' with measured diameters in nm at the longest point for each particle. C) Selected examples of 2D classes from TRPA1 (Paulsen *et al.*, 2015)and TRPV1 (Cao *et al.*, 2013) in amphipol A8-35 and amphipol PMAL-C8, respectively, and a 2D class of TRPM2 in SMA generated from the cryo-EM data described in Chapter 4 of this thesis.

6.2.2.4 Exploration of an online SEC Clean-Up Step

Another exchange attempt was performed on fractions taken from a purification using ~10 g of cell pellet with the aim of increasing final protein yield. Fraction E7 was the most concentrated (~0.5 mg/ml) and homogeneous sample according to SDS-PAGE and negative stain microscopy. A portion of fraction E7 (170 µl) was taken forward for the next exchange attempt, with two modifications: the amphipol concentration was increased to a w/w ratio of 1:5 (~87 µg TRPM2:450 µg A8-35) and the starting concentration of $MgCl_2$ was increased to 1 mM. Previous results suggest that SMA-TRPM2 can tolerate 1 mM concentrations of $MgCl_2$ without compromising the final result (Figure 6.4). It was hoped that this increase would remove an incubation and centrifugation step, shortening the exchange protocol by ¼ of the time. The amphipol ratio was also increased to see if this would benefit the exchange by increasing collision probability in solution. An additional centrifugation step at 13,000 xg was performed prior to centrifugation at 100,000 xg to test the feasibility of using a benchtop centrifuge to make the protocol more accessible.

A small pellet was visible in the tube after centrifugation at 13k xg, and the soluble fraction gave a final concentration of ~0.26 mg/ml (~55 µg of protein). After centrifugation at 100k xg, the protein concentration in the soluble fraction was observed to be ~0.25 mg/ml (~53 µg of protein). Under half of the total protein had been lost throughout the experiment. After the exchange, samples were analysed by negative stain to examine protein integrity after centrifugation at these two different speeds. Results were consistent with those described in the large-scale experiment and

showed that TRPM2 particles were visible in both micrographs, but background aggregates were also visible (Figure 6.7).

After the exchange, fast protein liquid chromatography (FPLC) using a Superose 6, 10/300 size exclusion column and the same buffer composition as the FLAG elution buffer (300 mM NaCl, 20 mM Tris, pH 7.5). Unfortunately, while a trace was visible during the purification (Figure 6.8A), no sample could be detected in the fractions by either coomassie (Figure 6.8A) or western blot (Figure 6.8B). There could be several reasons for this sample loss, but it is likely that they are related to the hardware of the FPLC, initial protein concentration and the protein itself, as amphipol:membrane protein complexes have been characterised extensively by SEC (Gohon *et al.*, 2006). Perhaps in future, re-application to the anti-flag resin and assessment with CD could provide a reasonable alternative to SEC and EM, as well as lowering the salt concentration to allow amphipol association to take place.

Despite initial positive results from the exchange – classified here as the incubation with A8-35 in the presence of increasing concentrations of $MgCl_2$ – the final exchanged samples consistently failed to yield a protein trace when trialled in native mass spectrometry. As it was expensive to express, purify and develop this method with TRPM2 – both in time and money – it was no longer viable to use as a test system for developing the method. In light of this, the *E. coli* multidrug efflux pump acridine resistance protein B (AcrB), was chosen as a model system to test the exchange, as it is easy and cheap to generate in-house. AcrB has also been characterised with a variety of biochemical and biophysical techniques in detergents(Murakami *et al.*, 2002; Du *et al.*, 2014), amphipols(Wang *et al.*, 2017) and SMALPs(Postis *et al.*, 2015c; Parmar *et*

al., 2018), so results generated from the exchange can be validated against those already available in the literature.

Figure 6.8: Size exclusion chromatography (SEC) of TRPM2 after exchange into A8-35. A) SEC profile of the TRPM2-exchange product showing 3 defined peaks in the UV A280 spectra (blue, labelled 1-3). Conductance measures (grey) and fractionation conditions (red) are also shown. SDS-PAGE gels correspond to peak fractions highlighted in SEC trace

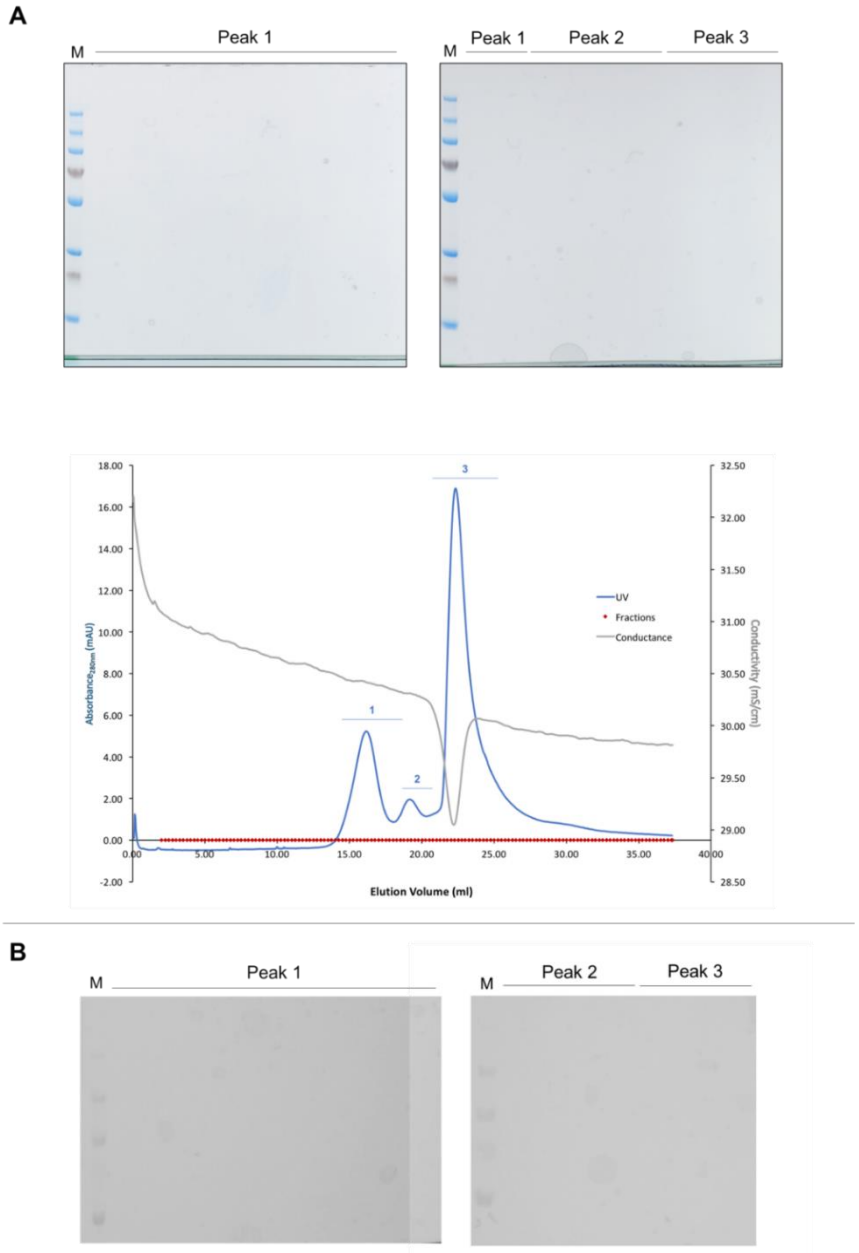

alongside molecular weight marker (M). B) Western blot analysis of the same fractions analysed in A.

6.2.3 Optimisation of Exchange Procedure using AcrB as a Model System

With AcrB as a model system in place, four requirements for the method were established as follows:

1. Membrane proteins (MPs) solubilised in SMA can be successfully exchanged into an amphipol, A8-35, for increased stability and compatibility with downstream biochemical/biophysical assays – particularly mass spectrometry.
2. The exchange can be performed entirely in the absence of detergent.
3. This method can be performed with minimal sample volume and protein concentration for compatibility with difficult expression systems, such as TRPM2 (50-200 µl; as low as 0.1 mg/ml).
4. Native lipids can be retained from solubilisation through to the final A8-35:AcrB complex.

A predominant drive for establishing the exchange process was to create a protocol that took the advantages of SMA extraction – such as lipid retention and increased solubilisation efficiency without detergents – and enhanced its applicability to a wider variety of downstream applications. Initially, attempts to analyse AcrB in SMA by native mass spectrometry were unsuccessful, and either no spray was formed, or no protein spectrum was visible above background noise (data not shown). The reason for this may be due to the charge, the polydispersity of the polymer, the polymer:protein

complex's inability to dissociate in the gas phase, or the stability of the protein itself (Hellwig *et al.*, 2018).

6.2.3.1 Purification of AcrB in SMA and DDM

For preliminary experiments, SMA-AcrB was kindly donated by Maya Patel and Vincent Postis as frozen stocks in 500 mM NaCl, 50 mM Tris.HCl, pH 8.0 and 10 % glycerol. As standard, samples were first dialysed into 300 mM NaCl, 50 mM Tris.HCl, pH 8.0 to remove the storage glycerol. However, it later became necessary to purify the protein in-house to generate further stocks.

AcrB was expressed and purified as previously published for SMA (Lee *et al.*, 2016), and this protocol was adapted for purification with DDM. Cell membranes were harvested, and 45 mg protein worth of membranes were solubilised with 2.0 % SMA and 1 % DDM, before purification with immobilised metal ion affinity chromatography (IMAC). Elution fractions were analysed by SDS-PAGE and demonstrated clear differences in the level of contamination when extracting with SMA vs DDM (Figure 6.9). These gels were representative of standard AcrB purifications. Fractions corresponding to E1 and E2 from AcrB purifications were routinely concentrated to a ~2 mg/ml, and snap-frozen in liquid nitrogen for later analysis. Concentration to higher than ~3 mg/ml would result in visible precipitation for SMA, so both were kept close to this value for comparison.

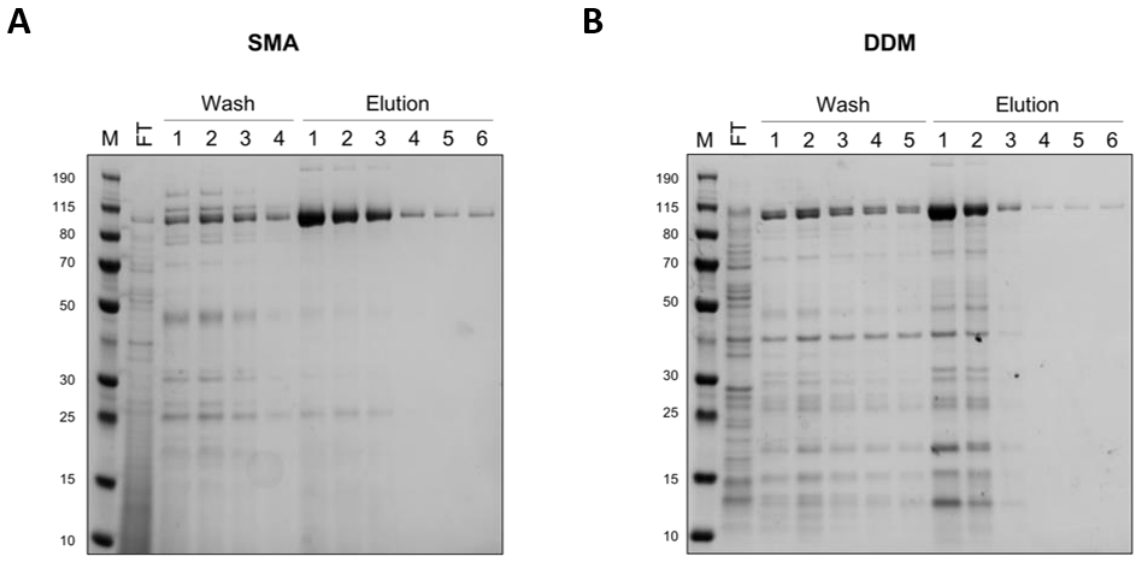

Figure 6.9: IMAC purification of AcrB in SMA and DDM.

A) Flow through (FT), wash and elution fractions from SMA-AcrB purification, alongside molecular weight marker (M). B) Flow through (FT), wash and elution fractions from DDM-AcrB purification, alongside molecular weight marker (M).

6.2.3.2 SMA-Amphipol Exchange Optimisation

6.2.3.2.1 Amphipol Selection and Ratio Optimisation

A8-35 and PMAL-C8 have been used at 1:3 w/w and 1:5 w/w ratios in the literature and gave interesting results with TRPM2, and these served as starting points for this experiment. Two additional conditions were trialled for the exchange based on the available knowledge that A8-35 and amphipols in general are more stable at lower salt concentrations (Tribet, Audebert and Popot, 1997; Zoonens *et al.*, 2007a). In the first, the protein was diluted 1:2 in ddH2O to give a final buffer composition of 150 mM

NaCl, 25 mM Tris.HCl, pH 8.0 prior to exchange, to reflect A8-35's preference for lower salt concentrations. This sample was also incubated with an amphipol:protein ratio of 1:5 w/w to increase the chance of collisions in the diluted solution. Another condition of 0.2 % v/v of A8-35 was set up to mimic the conventional approach of SMA purifications and mixing amphipols with detergent-solubilised proteins (Althoff *et al.*, 2011). An amphipol-free control was also included to see the effect of the process on the protein in the absence of such a 'rescue agent'.

The method is as previously described for TRPM2. Briefly, reactions were set up in 200 µl volumes and amphipols were incubated with the SMA-protein complex for 30 minutes, before adding $MgCl_2$ to a final concentration of 0.5 mM. The sample was then left to incubate with inversion for 1.5-2 hours, before a 1-hour centrifugation at 100,000 xg to remove insoluble components. These steps are iteratively repeated with increasing $MgCl_2$ concentrations, up to 2 mM – at this threshold, the SMA should be almost completely precipitated. The samples were diluted to ~20 µg/ml and visualised by negative stain after the final centrifugation (Figure 6.10A).

No particles were visible in micrographs of the amphipol-free control, indicating that the protein and polymer had precipitated from solution by the end of the incubation (Figure 6.10A). For the PMAL-C8 samples, results were consistent to that observed for TRPM2 - there were proteinaceous AcrB particles visible by negative stain, but they were difficult to discern due to the high level of background contamination (Figure 6.10C). This background was seen in the TRPM2 exchange but is more visible as particles of ~5-7 nm at the higher magnifications required for AcrB. PMAL-C8 was also consistently difficult to work with.

On the other hand, again similar to TRPM2, A8-35 gave the most promising results as protein resembling the AcrB trimer were visible in almost every condition (Figure 6.10C-E), except for the sample with 0.2 % A8-35, where individual particles were difficult to discern (Figure 6.10H). The sample containing a 1:5 protein:amphipol ratio at first glance gave the most aggregation, however it did appear that AcrB was still intact, but almost overshadowed by the amount of background noise from the excess amphipols (Figure 6.10D). Results here indicate that a 1:3 w/w protein: amphipol ratio is the most suitable for further experiments, as this sample was effective in generating monodisperse, homogeneous AcrB trimers, gave the minimum background and kept material costs low. Western blot also showed that the protein from the 1:3 w/w sample had not degraded during the exchange (Figure 6.10B).

While the particles appear to be stabilised in the presence of A8-35 and 2 mM $MgCl_2$, the effect these conditions have on the nature of the protein and surrounding annulus is unknown. Further experiments in this thesis have attempted to address this question using SEC and mass spectrometry.

Figure 6.10: Negative stain analysis of AcrB following amphipol exchange with varying concentrations of PMAL-C8 and A8-35.

A) Micrograph of amphipol exchange control sample containing only $MgCl_2$ and no amphipol. B) Western blot of AcrB sample before and after the exchange procedure had been performed with a 1:3 w/w ratio of A8-35. C-H) Final negative stain results of the exchange from all conditions containing amphipol. Amphipol:protein ratios for each sample are described in white text for each condition. Scale bar = 100 nm in all micrographs.

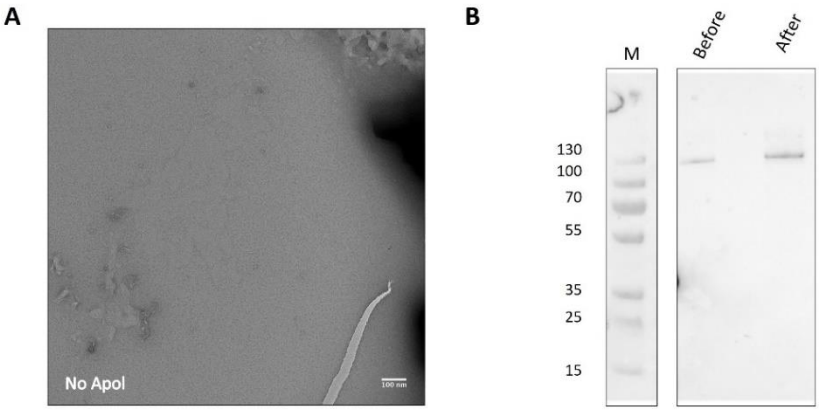

Condition after final incubation with Amphipol + 2.0 mM $MgCl_2$

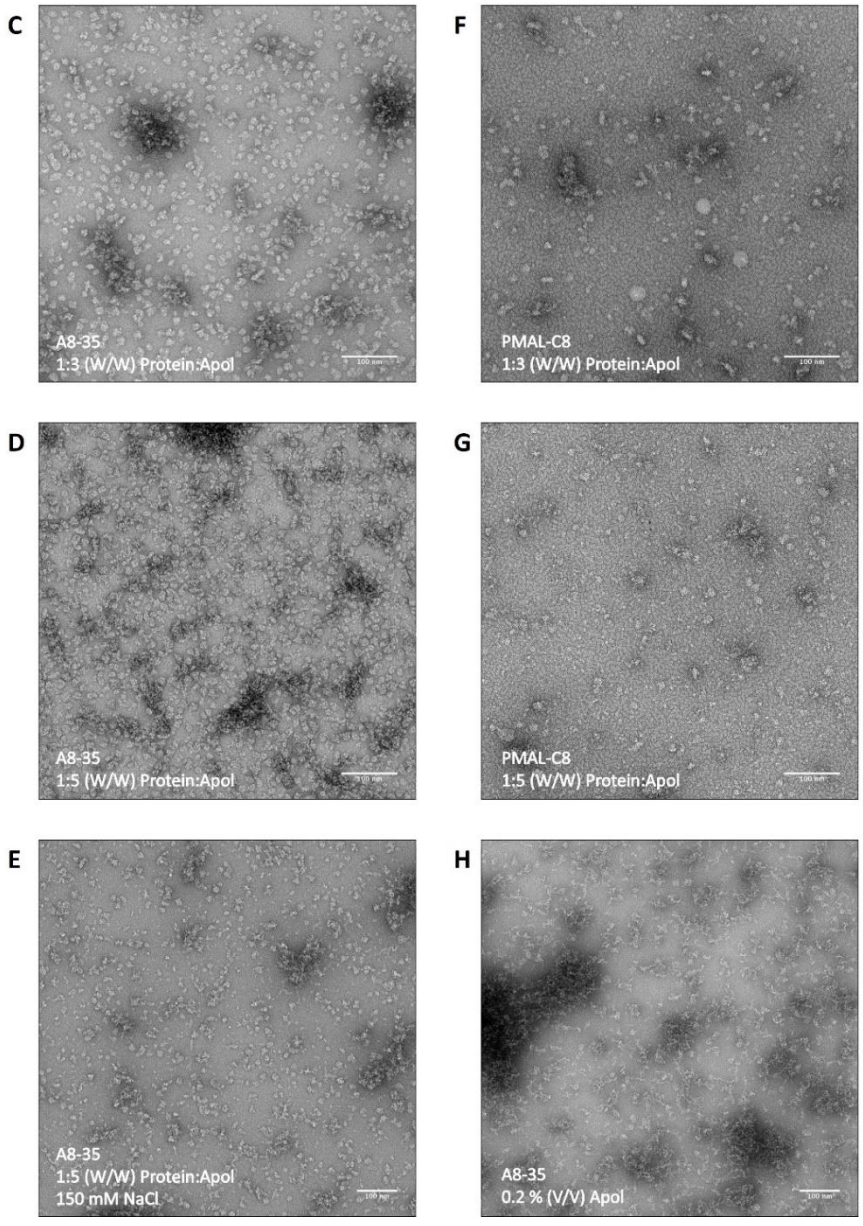

6.2.3.3 Detergent-SMA Exchange Optimisation

6.2.3.3.1 Conventional Exchange for Determination of Amphipol:AcrB Ratio

Amphipols are conventionally used to stabilise detergent-solubilised membrane proteins. To allow optimal solubilisation and stabilisation, the amphipol:protein ratio needs to be empirically determined. Previous experiments with SMA-AcrB and amphipol A8-35 have been performed with 1:3 ratios of AcrB:A8-35, based on published literary examples and prior SMA-exchange pilot experiments. To test this empirically with detergent solubilised AcrB, 1.3 mg/ml DDM-AcrB was mixed with A8-35 at the following w/w ratios: 1:2, 1:3, 1:4 and 1:5. Samples were incubated with A8-35 for 30 minutes on ice, before ultracentrifugation at 200k xg for 30 minutes to replicate original detergent-amphipol exchange experiments (Tribet, Audebert and Popot, 1997). Samples were taken from the supernatant and insoluble fraction for dot blot (Figure 5.11A), A_{280} measurement (Table 6.1) and CD (Figure 6.11B). Together, these results show that the samples remained soluble at each amphipol concentration except for the ratio of 1:2, which appeared to be detrimental, although no complete removal of amphipol was attempted. These experiments further highlighted the requirement of using AcrB as a test system to develop this method, as this would not have been possible with TRPM2.

Table 6.1: Concentration of DDM-amphipol exchanged samples at varying A8-35:AcrB w/w ratios.

Sample Ratio (AcrB:A8-35)	*[After Exchange] (mg/ml)*	*Difference (mg/ml)*
Control	1.147	-0.153
1:2	1.052	-0.248
1:3	1.327	+0.027
1:4	1.239	-0.061
1:5	1.459	+0.159

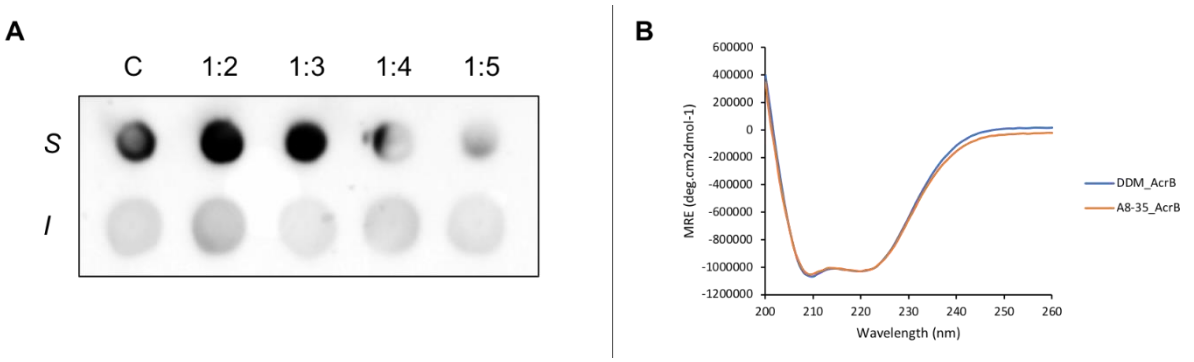

Figure 6.11 (Overleaf): Dot blot and CD results from conventional amphipol exchange.

A) α-His dot blot of soluble (S) and insoluble (I) DDM-AcrB after mixing with amphipol A8-35 at w/w concentrations of 1:2, 1:3, 1:4 and 1:5 DDM-AcrB:A8-35. (B) Concentration-corrected circular dichroism spectra showing folding of DDM-AcrB before exchange (blue line) and after exchange (orange line).

6.2.3.3.2 SMA-Detergent Exchange

Similar to TRPM2, an SMA-DDM exchange was explored using AcrB as a model system. Results compiled from the literature and insofar demonstrated that an amphipol:protein ratio of 1:3 was suitable for retaining AcrB solubility and structure. A detergent exchange experiment was set up in a similar way to those described in previous chapters, albeit with 1 % DDM added instead of A8-35. The soluble and insoluble fractions were followed via dot-blot (Figure 6.12A), which showed that almost no protein precipitated during the exchange. This can be similar to results from TRPM2, where the detergent was able to rescue the sample from complete precipitation upon $CaCl_2$ addition. In this example, the donated starting material exhibited major contamination – potentially with excess SMA polymer – which can result from inadequate washing of IMAC columns before elution (Figure 6.12B). However, this exemplified the exchange procedure's ability to clean up the sample, as the resulting particles were homogeneous, monodisperse and accurate representations of AcrB in DDM (Figure 6.12C). This was often the case with detergent exchange, which seemed to maintain protein concentration during the exchange for both TRPM2 and AcrB.

Figure 6.12: SMA-DDM Exchange of AcrB.

(Next Page): A) Dot blot following soluble (S) and insoluble (I) protein over the course of the exchange experiment. B) SMA-AcrB sample before exchange. C) DDM-AcrB after the exchange.

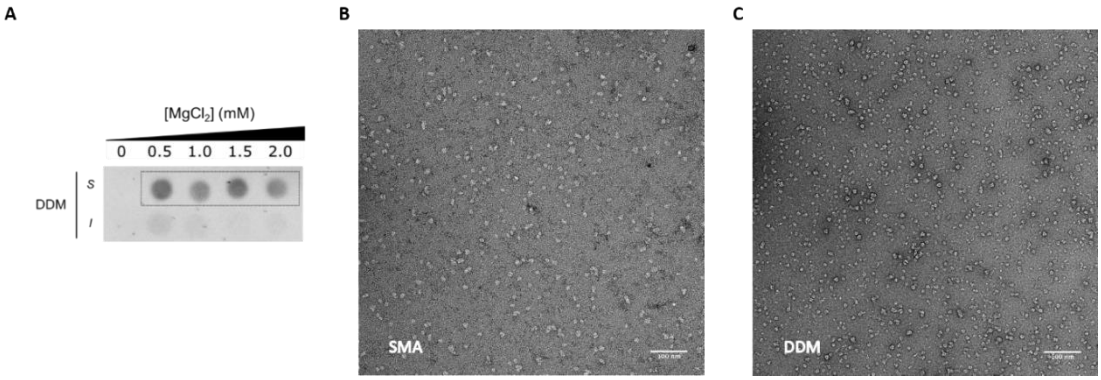

6.2.3.4 Reproducibility Testing and Further Modifications

Experiments thus far have established that incubation of SMA-solubilised protein can be stabilised by a 'rescue agent' – either detergent or other amphipathic polymer – in the presence of divalent cations. This allows the protein, either TRPM2 or AcrB, to remain in solution and withstand $MgCl_2$ concentrations up to 2 mM. However, a few small but critical observations and changes to the overall exchange method required attention, and experiments required repeating to demonstrate consistency.

For exchange from SMA-A8-35, an additional control of A8-35 without $MgCl_2$ was included (+A8-35). This was to examine the effect the polymer alone on the SMA-protein complex. When the initial vs final concentrations of repeat experiments were evaluated, it became clear that the +A8-35 samples performed similarly to the exchange sample with the $MgCl_2$ precipitant. This was demonstrated by dot blot and A_{280} measurement, which showed a similar quantity of sample had been lost from both. However, this appeared to be concentration dependent, where the +A8-35 was detrimental to more concentrated samples (Table 6.2), in this instance, control 2 was

set up at a much lower volume than control 4. Although this was not always reflected by dot- or western-blot, which consistently demonstrated that +A8-35 alone suffered from some sample loss (Figure 6.13A and C).

Table 6.2: Repeat measurements of the initial and final concentration of samples in the exchange experiment.

Sample Name	$MgCl_2$	A8-35	Protein Before (µg)	A8-35 Added (µg)	Protein Conc. After (mg/ml)	Protein After (µg)	Fold Reduction
Control 1	+	-	72.0	-	0.229	2.9	24.83
Control 2	-	+	72.0	216.0	0.765	10.4	6.92
Control 3	+	-	116.8	-	0.141	17.6	6.63
Control 4	-	+	116.8	350.4	0.335	41.8	2.79
Sample 1	+	+	116.8	350.4	0.340	42.5	2.75
Sample 2	+	+	116.8	350.4	0.327	40.8	2.86
Sample 3	+	+	196.0	588.0	0.789	73.6	2.66

Conditions of each sample at the start of the experiment are shown in the leftmost columns in green, where control 1 is AcrB with $MgCl_2$ alone, control 2 is AcrB with A8-35 alone, and samples 1, 2 and 3 are repeats of the exchange experiment containing AcrB with both $MgCl_2$ and A8-35. The final sample parameters measured after the exchange are shown in the rightmost columns in blue.

Another small but crucial modification was the addition of SDS and DTT to the samples prior to dot blot. During previous experiments, the samples containing excess amphipols formed a waxy residue on the membrane surface and did not penetrate well.

The best example of this can be seen in Figure 5.3C. To overcome this, samples were mixed with 0.2 % SDS supplemented with 0.25 mM DTT, which allowed the protein to penetrate the membrane more easily instead of sitting on top (Figure 6.13A +SDS vs -SDS). From this, direct dot blots began reflecting the results also shown by western blot, which consistently highlighted the difference in concentration between starting and end protein content from each condition (Figure 6.13C). For DDM-exchanged AcrB, this was never an issue as detergent was already present and gave consistent results (Figure 6.13B).

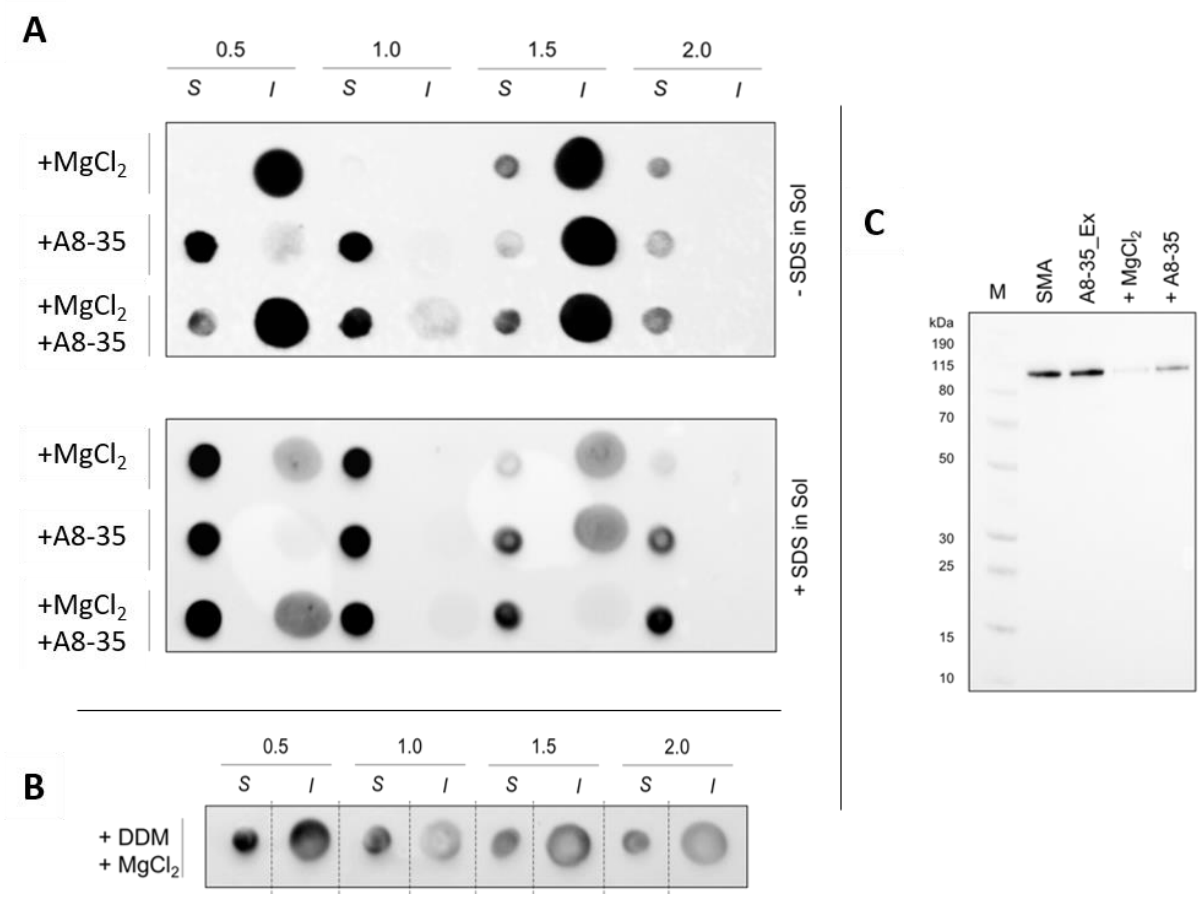

Figure 6.13: Optimisation of dot- and western-blots to demonstrate effect of exchange on protein concentration and results interpretation.

A) Dot blot following a standard exchange procedure of the same samples, but without (top) and with (bottom) the extra addition of SDS. Soluble (S) and insoluble (I) samples were run in order of increasing MgCl2 concentration, except for the +A8-35 only sample, which contained no $MgCl_2$. B) Repeat dot blot experiment of DDM samples in the same format as 'A'. C) Western blot analysis of soluble fractions from SMA-amphipol exchange of AcrB procedure alongside molecular weight marker (M). Before exchange = SMA, after exchange = A8-35_Ex.

6.2.3.5 Assessing Heterogeneity of Exchanged Samples by SEC-MALLS

SMA *co*-polymers have an average polydispersity index of ~2.6 (*SMA Technical Documentation*, 2016; Grethen *et al.*, 2017). This polymer heterogeneity makes the membrane protein-SMA particle characterisation difficult, particularly when used in conjunction with techniques that prioritise sample homogeneity. There have been attempts to decrease the heterogeneity of the polymer by altering the synthesis procedure and polymer length, but it has been suggested that the SMA *co*-polymer's solubilisation efficiency is owed to this heterogeneity (Craig *et al.*, 2016). This protocol was therefore designed to reduce sample heterogeneity without interfering with the original polymer synthesis procedure.

6.2.3.5.1 Inherent Polymer Heterogeneity and Lipid Controls

To examine the effect that SMA and A8-35 can have on the polydispersity of a sample, protein-free SMA lipid particles (SMA_LP) and A8-35 lipid particles (A8-35_LP)

were examined by size exclusion chromatography with multi-angle laser light scattering (SEC-MALLS), and their absorbance was monitored across multiple wavelengths (Figure 6.14A and 6.14B). SMA_LP significantly absorbed in the UV spectrum from ~200-270 nm, with a gradual drop in absorbance before 280 nm. When the absorbance at 220 nm for SMA_LP, A8-35_LP and another control of DDM_A8-35 (simply DDM and A8-35 mixed), the true broadness of the SMA_LP peak was highlighted (Figure 6.14C). This showed that the SMA_LP eluted slowly as a smear from the SEC column, visualised as a broad primary elution peak spanning >5 minutes of the total 20-minute run. The A8-35_LP did not display similar characteristics, and instead eluted in a sharper peak spanning ~2.5 minutes of retention time. The absorbance spectra from 190-300 nm of SMA_LP, A8-35_LP, DDM-A8-35, and the individual components alone were measured in triplicate to validate these absorbance readings (Figure 6.14D).This highlights the advantages of using amphipols as a homogeneous tool instead of SMA for techniques such as EM and MS.

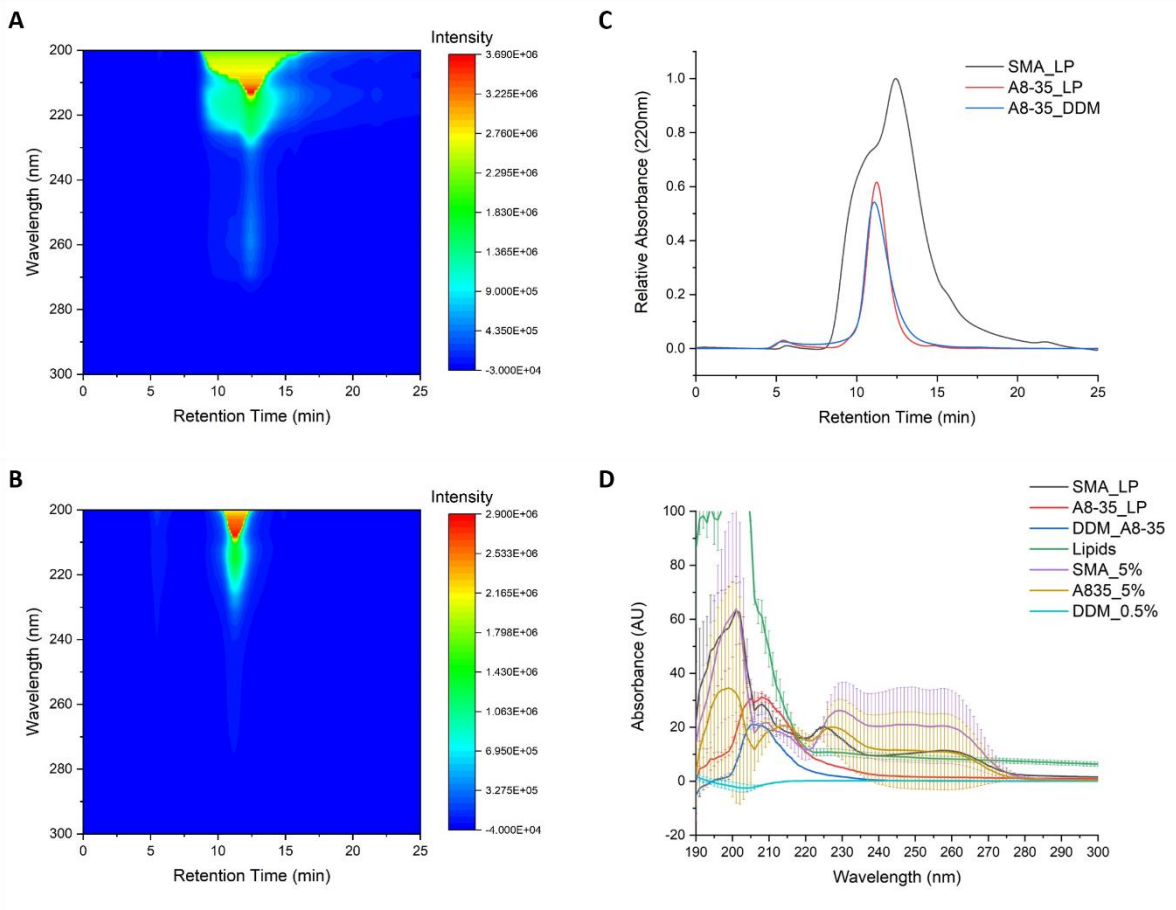

Figure 6.14: SEC-MALLS and UV-VIS analysis of SMA, A8-35 and DDM with and without lipids.

A)) Multi-wavelength SEC profile of protein-free SMA lipid particle (SMA_LP) in heat map representation. Relative absorbance at each wavelength is shown as intensity, ranging from highest absorbance (red) to the lowest (blue), and plotted according to retention time in minutes. B) As A, but with amphipol A8-35 lipid particles (A8-35_LP). C) Isolated absorbance 220 nm profile of SMA and A8-35 lipid particles, alongside DDM-A8-35 particle by SEC-MALLS. D) UV absorbance of DDM alongside SMA_LP and A8-35_LP from A and B. A8-35 was also mixed with DDM (DDM_A8-35) to clarify the polymer and lipid contributions to absorbance across a range of wavelengths. Error bars represent triplicate results.

6.2.3.5.2 Amphipol-Exchanged AcrB

Exchanged AcrB samples were also analysed by SEC-MALLS to determine whether sample homogeneity had improved. Comparison of the SEC-MALLS chromatograms of SMA:AcrB and the A8-35 exchanged (A8-35_Ex) sample showed a reduction in heterogeneity between the starting material and final exchanged product, indicated by a leading trail before the primary elution peak for SMA:AcrB (Figure 6.15, blue line), and a sharp elution peak for A8-35_Ex at ~10 minutes (Figure 6.15, red line); and is further demonstrated by a more consistent molar mass distribution of A8-35_Ex across this peak (Figure 6.15). Aggregates of high laser light scattering (LLS) and low UV absorbance were also observed in the void volume for the SMA:AcrB sample, potentially indicating the presence of polymer-only aggregates. No such aggregation was observed in the void volume for A8-35_Ex, but a large LLS peak corresponding to the size of empty A8-35 lipid particle was consistently observed after the exchange at an elution time of ~11.35 min (Gohon *et al.*, 2006) (Figure 6.15).

Accurate molar masses could not be determined for SMA:AcrB due to discrepancy in the literature describing the refractive index increment (dn/dc) for SMA *co*-polymers (Jamshad, Grimard, *et al.*, 2015; Morrison *et al.*, 2016; Domínguez Pardo *et al.*, 2018), but a dn/dc polymer modifier of 0.15 (Gohon *et al.*, 2006) could be applied to the A8-35 sample to give an estimated molar mass of ~450 kDa at the highest peak (Figure 6.15). Analytical ultracentrifugation has previously determined the molecular mass of AcrB in SMA to be >400 kDa42, although it has been observed at variable molecular weights ranging from its native ~340 kDa up to and exceeding 800 kDa (Postis *et al.*, 2015d; Pollock *et al.*, 2019). These results suggest that the inherent heterogeneity of the SMA *co*-polymer contributes to overall SMA:protein heterogeneity. From the data,

it could be suggested that the broad elution peak is reminiscent of an initial higher molecular weight SMA-AcrB complex which contains more lipid and polymer, and later elutes to a less-bulky SMA-AcrB complex with reduced lipid and polymer content (depicted in 6.15).

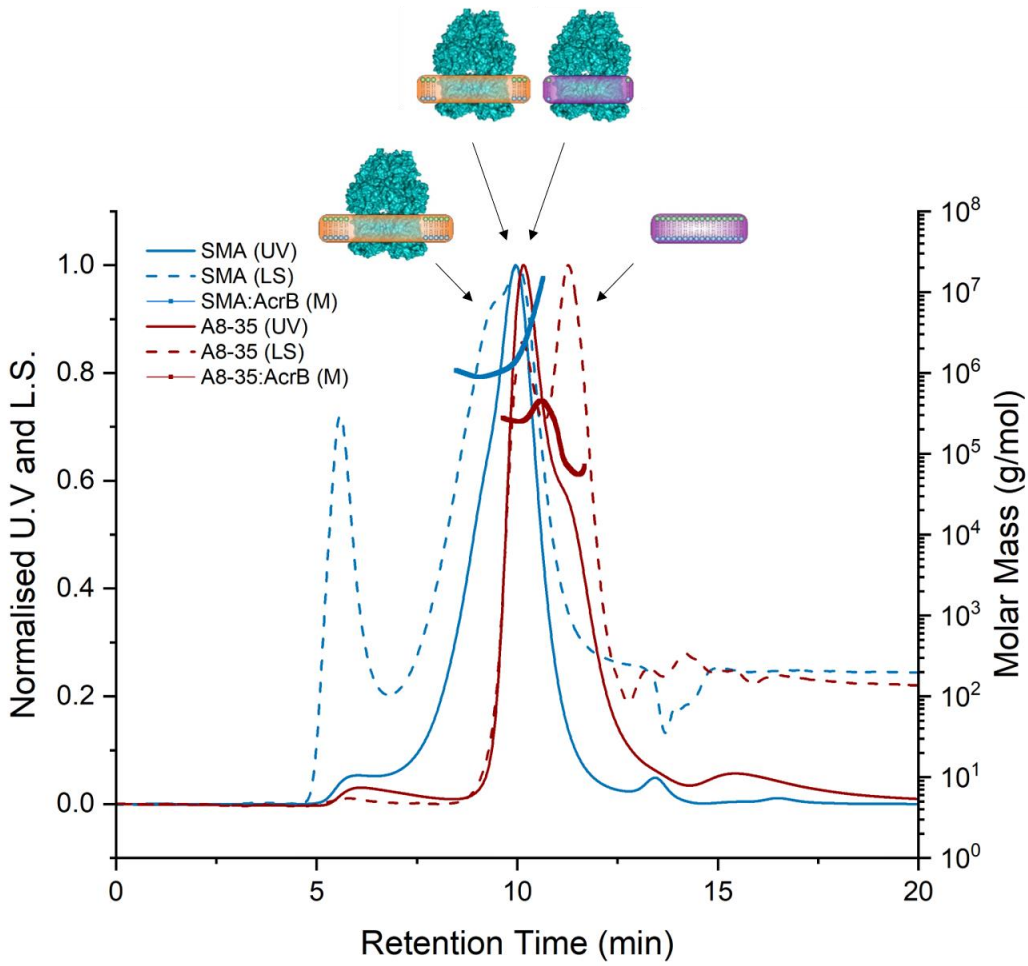

Figure 6.15: SEC-MALLS analysis of SMA:AcrB (blue) and A8-35_Ex (red).

Solid lines represent UV absorbance at 280 nm and dashed lines represent light scattering signal. Traces were normalized relative to the highest peak (Normalized U.V.) and plotted as

a function of retention time in minutes. A refractive index increment (dn/dc) value of 0.16 mL/g from (Stephen C. L. Hall *et al.*, 2018) was applied for SMA molar mass calculations, but there are clear issues with the calculations and this is included purely for illustrative purposes. Schematics above each peak indicate the predicted appearance of each complex throughout sample elution, with SMA-AcrB in orange and A8-35-AcrB in purple. Lipid content of each sample is shown proportionally as blue/ green lipid schematics. The purple band with lipids represents free A8-35 particles. Experiment performed by David Klebl.

6.2.3.5.3 Detergent-Exchanged AcrB

AcrB was also exchanged into DDM (DDM_Ex) and analysed alongside a control sample that had been solubilised and purified in DDM (Figure 6.9B). No significant aggregation was observed in the SEC-MALLS elution profile of either sample (6.16). The DDM_Ex elution peak also has a slight decrease in retention time (~ 10.2 min) compared to the DDM purified sample (~10.4 min) (6.16). Despite this peak shift, the primary elution peak for DDM_Ex at 10 minutes is still less broad. However, a modifier dn/dc value of 0.143, corresponding to the DDM micelle RI, was applied to both samples, and gave a similar molar mass distribution (~400 kDa) to the A8-35_Ex sample. The molar mass distribution shows a homogeneous mixture at this point, and the reason for this is unclear, but could again be due to the unclear nature of the lipid annulus.

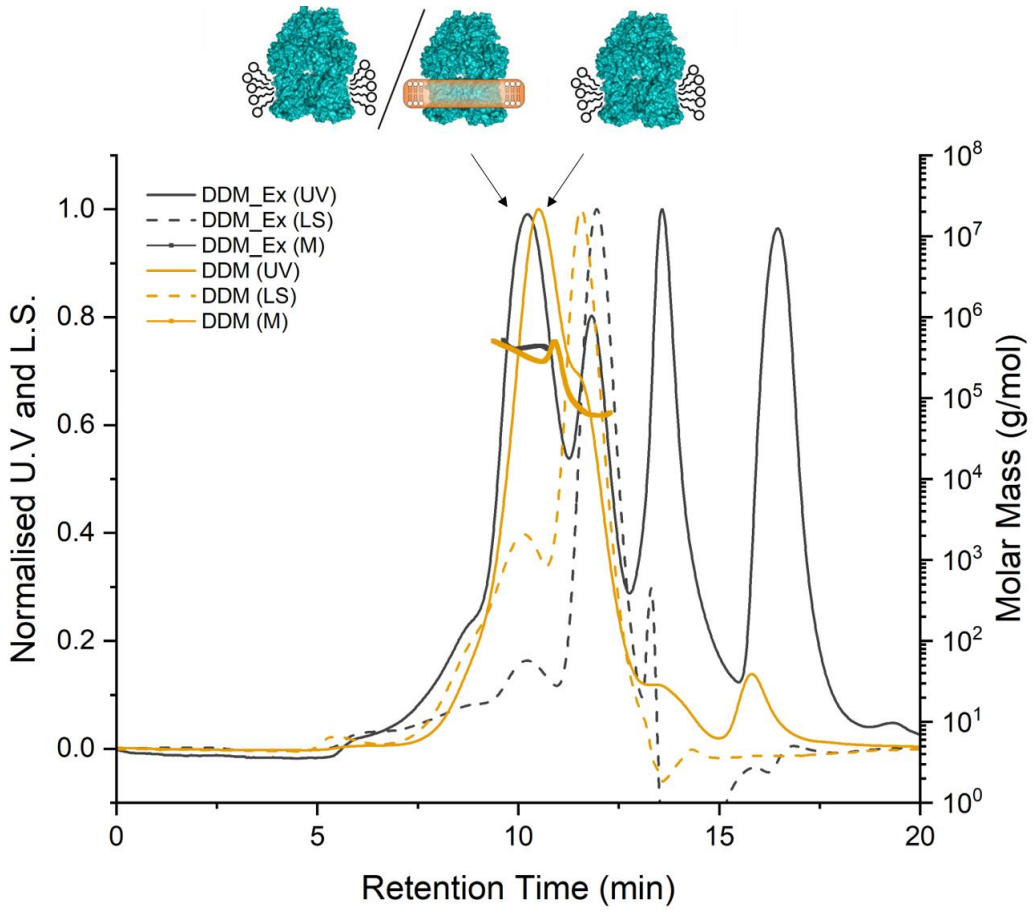

Figure 6.16: SEC-MALLS analysis of DDM:AcrB (gold) and DDM_Ex (grey).

Solid lines represent UV absorbance at 280 nm and dashed lines represent light scattering signal. Traces were normalized relative to the highest peak (Normalized U.V.) and plotted as a function of retention time in minutes. Calculated molar mass distributions are shown across the entire peak for both samples. Schematics above each peak indicate the predicted appearance of each complex throughout sample elution, depicting for the exchanged sample either DDM-AcrB with detergent molecules, or an SMA-DDM-AcrB hybrid. DDM-AcrB from DDM-purified sources is depicted as AcrB with a detergent schematic belt.

6.2.3.6 Testing Exchanged Samples in Mass Spectrometry

6.2.3.6.1 Buffer Compatibility

Following these results, a large-scale experiment was set up using freshly purified SMA-AcrB (Figure 6.9A), with the aim of having enough final product could be examined by native MS.

The experiment followed the same conditions as those previously described, albeit for the inclusion of an overnight incubation with 2 mM $MgCl_2$ to fully facilitate exchange and have enough sample remaining for analysis with CD, which is a previously proven cheaper alternative to EM. As with TRPM2, samples were taken after each ultracentrifugation step to be examined by dot blot, which showed consistent results with those previously described within this chapter (Figure 6.17A). The final samples were examined by CD before the exchange, after the exchange, and then once again after buffer exchange into ammonium acetate for compatibility with mass spectrometry (Figure 6.17B). An amphipol-free control was also analysed alongside the exchange and was examined by CD after incubation with 0.5 mM $MgCl_2$, and again after the final overnight incubation with 2 mM $MgCl_2$.

The CD spectra were normalised according to protein concentration as much as possible, but as excess amphipols in solution likely introduce inaccuracies, these concentrations may not be truly representative. CD results of AcrB in SMA gave a clear spectrum, displaying peaks at 208 and 222 nm – expected of alpha-helical proteins (Figure 6.17B, yellow line). Similar spectra were obtained for the A8-35 exchanged samples after an overnight incubation with 2 mM MgCl2 (Figure 6.17B,

grey lines. The control sample contains some helical characteristics after a 2-hour incubation with 0.5 mM $MgCl_2$, but the signal almost disappears due to high background the end of the experiment (Figure 6.17B, blue lines). The final A8-35 sample was then buffer-exchanged into ammonium acetate (AmAc) for mass spectrometry and analysed by CD (Figure 6.17B, orange line). However, acetate ions absorb highly in the far UV (>0.5 AU) and interfere with CD signals beyond ~210 nm (Miles *et al.*, 2016). Therefore, the fold of proteins in ammonium acetate solution cannot be accurately assessed with CD and was not used in future validation.

While the CD results could not inform on the fold of the 'exchanged' AcrB, there was still sufficient sample for analysis with negative stain microscopy (Figure 6.17C) and native mass spectrometry. However, negative stain microscopy revealed that the buffer was affecting the protein, and clearly showed significant sample background, degradation and loss after being exchanged into ammonium acetate (Figure 6.17C). Additionally, it was unclear from negative stain and CD alone whether a complete scaffold exchange from SMA to A8-35 had both occurred and increased the sample homogeneity. It was hoped that mass spectrometry could give some answers to this question.

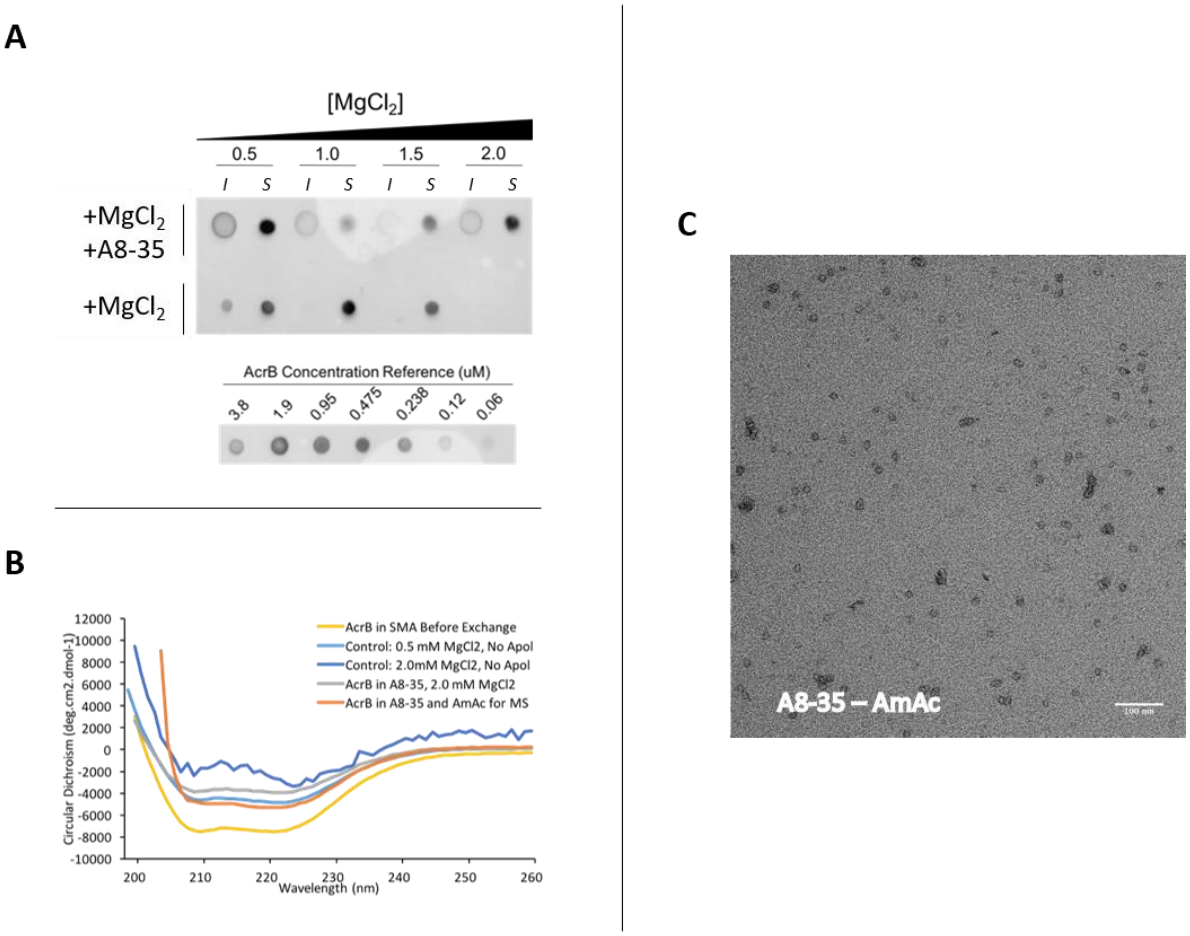

Figure 6.17: SMA-Amphipol Exchange into Ammonium Acetate.

A) Dot blot showing soluble (S) and insoluble (I) proportions of AcrB for an SMA-amphipol exchange procedure and amphipol-free control over increasing MgCl2 concentrations. AcrB concentrations were provided as a reference. B) Circular dichroism of AcrB throughout the exchange into A8-35 (before = yellow and after = grey), and after exchange into ammonium acetate (AmAc) for mass spectrometry (MS). Control samples from the A8-35-free condition at 0.5 mM (light blue) and 2.0 mM $MgCl_2$ (dark blue). C) Negative stain micrograph of the SMA-amphipol exchanged sample, after it had been subject to buffer exchange into ammonium acetate. Scale bar = 100 nm.

6.2.3.6.2 SMA-Exchanged AcrB in Mass Spectrometry

These results were generated with the help of David Klebl and Jeroen Van Dyke.

Initial experiments with AcrB in native mass spectrometry were unsuccessful and did not yield any comparable protein trace in the spectrum. It was thought that the concentration of the protein may be too low, that AmAc could be destabilising the protein during ESI, or that the excess A8-35 in solution may be blocking the capillary spray. However, it was later shown by negative stain microscopy that the sample was unstable in ammonium acetate (Figure 6.17C). After personal communication with experts in the field (Albert Konijnenberg), it was discovered that AcrB was not a suitable system for mass spectrometry, and had a reputation for not spraying, not being visible in the spectrum, or degrading in the gas phase. Nonetheless, prior to the time that this was discovered, it was found that the key to success in generating a spectra for AcrB in native- MS was rapid buffer exchange and immediate injection – before the protein had time to precipitate and degrade in ammonium acetate. With this, native mass spectra of both amphipol-exchanged and detergent-exchanged AcrB were obtained (Figure 6.18A and B).

Native-MS showed that the exchange of the protein from SMA to both A8-35 and DDM was achieved to some degree. Firstly, spectra had been observed where this was not previously possible for samples in SMA. Secondly, the observed spectra are similar to that of the published detergent:AcrB spectrum, which was repeated here as described in the original publication: specifically, DDM-purified AcrB was buffer exchanged into a more delipidating detergent, C_8E_4, and revealed a peak at an m/z of ~12,000 (Reading, Liko, *et al.*, 2015b) (Figure 6.18A). These traces were of low

resolution, even at high collision energies, which could be a result of the sample degradation with this technique or may suggest that a small amount of SMA *co*-polymer remains. However, overall demonstrate that a more homogeneous, tractable sample had been generated for application to native-MS, and native AcrB spectra could be observed where it could not before.

To take this one step further, based on previous evidence of lipid retention in SMA (Oluwole *et al.*, 2017; Teo *et al.*, 2019), I also hypothesised that native lipids were carried through during the transfer from SMA:AcrB to A8-35_Ex, as the protein was not initially extracted in delipidating conditions. DDM is known to delipidate membrane proteins in mass spectrometry, but this information is not available for amphipols (Gupta *et al.*, 2018). After the exchange, lipids of the non-detergent exposed A8-35_Ex sample were extracted, and the crude extract was directly subjected to MS analysis. The resulting spectra show a large number of putative lipid peaks.

The most intense peak at m/z = 719.5 was taken forward to tandem MS and assigned to phosphatidylglycerol (16:0/16:1) according to previously published data (Bechara *et al.*, 2015). This was further validated using LIPID MAPS glycerophospholipid MS/MS prediction (Fahy *et al.*, 2009) (Figure 6.18B). Albeit a very preliminary result, this shows that lipids can be retained through this entirely detergent free purification and exchange procedure and provides a base for future investigation into how the relationship between solubilising agent (polymer/detergent) can define the nature of the lipid annulus, and thus how membrane proteins interact with their native bilayer.

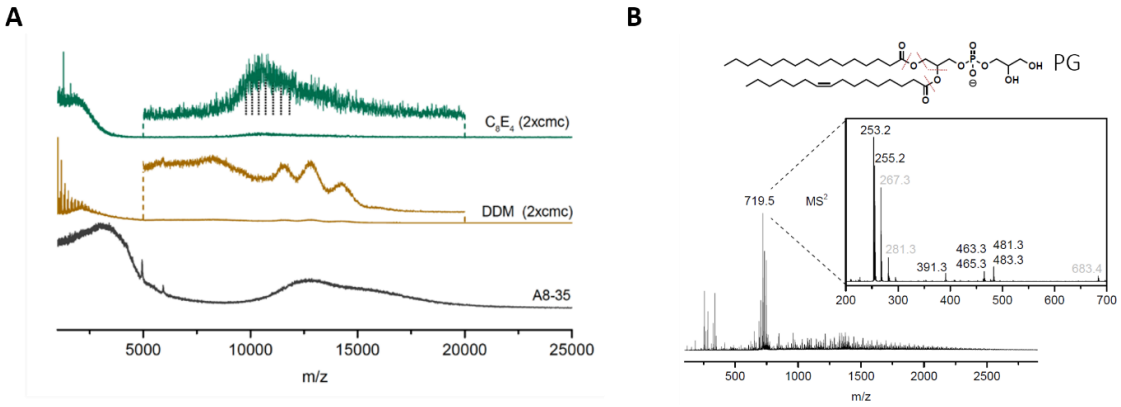

Figure 6.18C: Native and denaturing-MS of A8-35- and DDM-exchanged samples.

A) Native-MS spectrum of A8-35-exchanged AcrB (black), DDM-exchanged AcrB (gold) and a control C_8E_4-exchanged AcrB; according to mass/charge (m/z) ratio. Results for DDM-exchanged AcrB were magnified between 5000-20,000 m/z. **B)** Tandem mass spectra (MS/MS) of lipids extracted from A8-35_Ex, demonstrating that at least one lipid can be identified as phosphatidylglycerol (PG). The preferential fragmentation positions of PG (16:0/16:1) are indicated by red dotted lines. MS/MS-peaks which could not be explained were labelled in grey. Experiment performed by David Klebl.

Chapter 7:

Conclusion, General Discussion and Future Directions

7.1 Overall discussion

Overall, there were two key factors relating to success of this project, the use of the styrene-maleic acid (SMA) *co*-polymer for TRPM2 solubilisation, and the optimisation of purification conditions for use with CD and EM. The stability induced either as a result of the polymer's activity on the hydrophobic transmembrane domain region of TRPM2, or its retention of native lipids in the surrounding annulus proved essential to channel stability outside of the native bilayer. This was additionally demonstrated by the lack of stability in the DDM-purified TRPM2 (DDM_TRPM2) channel. The inclusion of a FLAG peptide gradient is trivial but was essential in the reproducible separation of homogeneous TRPM2 samples from aggregates in a one-step purification. While not reported here, numerous other attempts were made to clean up the DDM:CHS and SMA samples by size exclusion chromatography using a variety of resins and systems. From which, the sample was either too dilute or lost. Other detergent and polymer systems were also trialled, but none were as fruitful as DDM:CHS and SMA described here. This discussion will reiterate some of the key findings from the project, as well as describe them in the context of novel avenues for future directions.

7.1.1 TRPM2 Highlights and Key Findings

7.1.1.1 Structural insights into the mechanism of TRPM2 from Bioinformatics and Electron Microscopy

In addition to mechanistic insights arising from CD, structural insights were gained from bioinformatic and EM characterisation of TRPM2 in this thesis.

Bioinformatic analysis identified the presence of a conserved 'SLOG' domain in the N-terminal TRPM homology region (Section 4.2). This domain topology typically functions in nucleotide, cytokine or molybdenum binding, and in *Mycobacterium tuberculosis* conveys protection against host ROS/RNS species (Burroughs *et al.*, 2015; Zhu and Javid, 2015). Previous studies had also identified this domain as the primary active site for activation by H_2O_2 (Hara *et al.*, 2002; Kashio *et al.*, 2012), and is perhaps indicative of an extra TRPM2 binding modality. Perhaps tangentially, abscisic acid – a cytokine – has also been reported to elicit a similar cADPR induced calcium response in pancreatic islets, and has been linked to immune signalling in human granulocytes and can be inhibited by 8-BR-cADPR (Bruzzone et al., 2007; Bruzzone et al., 2008).

Additionally, a 31 Å resolution 3D structure of TRPM2 determined by negative stain microscopy was presented here, shown to adopt a similar bell structure to the negative stain reconstruction published by Maruyama et al., 2007 (Section 5.2.3). The 2D classes generated from TRPM2 datasets presented here still require sample and processing optimisation, but there is great potential for a future SMA_TRPM2 structure by cryo-EM. However, during the course of this project, several high-resolution structures of TRPM2 were solved, providing unprecedented details into the TRPM2 structure-function relationship beyond what has been determined here.

These high-resolution structures of TRPM family members, including *hs*TRPM2, confirmed the presence of the 'SLOG' domain identified here, defining it as MHR1/2. In the TRPM2 structures published by Huang et al., 2019, this domain was solved with a U-shape ADPR molecule bound in the MHR1/2 cleft. This was also discovered to be the binding site of 8-Br-cADPR, and was suggested to be the primary gating site for

ADPR activation and priming of TRPM2 (Huang *et al.*, 2019). Future mutational analysis could help find the answer. However, considering the disparity in the literature with regard to true TRPM2 ligands, it could perhaps now be deduced that TRPM2 is able to bind multiple cyclic or U-shape molecules in this binding pocket, including abscisic acid (Bruzzone *et al.*, 2007) and arachidonic acid (Hara *et al.*, 2002; Lindström, Pierce and Latz, 2017). It would be interesting to determine whether abscisic acid and arachidonic acid are true activators of *hs*TRPM2, as well as develop the cryo-EM results further to generate a high resolution SMA_TRPM2 structure containing native lipids.

7.1.1.2 TRPM2 re-structuring as a function of temperature.

The primary goal of this project was to develop the TRPM2 purification pipeline to maximise sample quality, yield and stability for characterisation by cryo-EM. This was achieved by iterative optimisation of purification conditions until a robust protocol had been established – yielding pure, homogeneous TRPM2 samples for downstream characterisation (Chapter 3). The use of SMA for TRPM2 purification was a vital for the success of this project, and direct comparison with detergent (DDM or DDM:CHS) purified TRPM2 complexes revealed mechanistic insights into temperature-induced structural rearrangements of the channel at ~37 °C (Section 5.2.2).

The activation temperature of TRPM2 *in vivo* is reported as ~37 °C (Song, Wang, Gretel B. Kamm, *et al.*, 2016; Tan and McNaughton, 2016). Prior to these experiments, it was unknown whether temperature activation was a property of the channel itself, the lipid environment (Morales-Lázaro, Lemus and Rosenbaum, 2017), or as a result of increased intracellular ADPR and H_2O_2 (Hara *et al.*, 2002; Togashi *et al.*, 2006).

Thermal denaturation experiments performed here eluded to numerous transition unfolding/folding events within TRPM2, both by circular dichroism (Section 5.2.2), and also – albeit less so – CPM thermostability assays (Section 5.2.1). While the CD spectra generated from the TRPM2 thermal melt experiments are not of sufficient quality for deconvolution to discern the relative proportions of secondary structure elements, the large domain motions observed in the published cryo-EM TRPM2 structures from Huang *et al.* 2019 (depicted in Figures 1.7 and 1.8) are in support of multiple transition/unfolding events.

In future, it would be beneficial to obtain higher quality CD spectra at specific transition temperatures so that the domain motions in the static EM structures could be related to sequential unfolding transitions in solution by CD. This could be achieved with larger scale purification preparations, SRCD, and enhanced buffer systems. Additionally, if cryo-EM grids could be prepared at 37 °C, it may reveal conformations complimentary to the dynamic information provided by CD to provide novel insights into its inherent mechanisms as a ThermoTRP.

7.1.1.3 The role of lipids in TRPM2 activation and regulation

Circular dichroism thermal melt assays indicated a difference between DDM:CHS_TRPM2 and SMA_TRPM2 in channel unfolding/refolding (Section 5.2.2). After an increased temperature ramp to 50 °C, past the published TRPM2 activation temperature of ~37 °C (Tan and McNaughton, 2016), DDM:CHS_TRPM2 was observed to regain secondary structure in a similar manner to the ascending ramp (Figure 5.12). This was not the case for TRPM2 in SMA, which showed no similar features during the descending temperature ramp from 50-20 °C (Figure 5.13). It could

be speculated that lipids within the SMA structure could be stabilising or holding the channel in a specific conformation, or that the temperature increase has removed an essential lipid that cannot rebind due to the presence of the polymer. Phosphatidylinositol 4,5-bisphosphate (PIP_2) binds TRPM2 with high affinity, and its presence is a requirement for channel activation (Toth and Csanady, 2012). Once bound, the channel remains active for extended period of time (Tóth and Csanády, 2012). In the DDM:CHS purified sample, it is possible that lipids may have been removed entirely, so that restructuring by PIP_2 cannot occur. However, the dynamic nature of the detergent micelle may allow rebinding at lower temperatures, and thus lead to this refolding.

Attention was turned to the lipids that could be co-extracted with SMA_TRPM2. Thin layer chromatography revealed that SMA_TRPM2 not only retained PA, PC, PI and PC, but co-purified with an abundance of cholesterol and cerebrosides (Figure 3.9). This is the first demonstration of its kind for mammalian membrane proteins in SMA, and has exciting, novel implications as to the role of TRPM2 regulation by sequestration to membrane microdomains or lipid rafts (Morenilla-Palao *et al.*, 2009; Ogiso, Taniguchi and Okazaki, 2015). Additionally, TRPM2 is highly expressed in the nervous system where cerebrosides and ceramides are abundant (Cermenati *et al.*, 2015; Belrose and Jackson, 2018), and their co-purification here may elude to the importance of extracellular sugar moieties in TRPM2 channel structure, stability and function. Interaction with cerebrosides and sphingomyelins has not been eluded to for any other TRP channel to date, but has been shown for the Kv1.11 (ERG-1) channel, which is reported to sequester to cholesterol and sphingomyelin-rich domains which directly affect its function (Balijepalli *et al.*, 2007).

Channel sequestration to cholesterol-rich domains could act as a fundamental regulator of TRPM2 channel activity, and likely explains its structural instability and minimal longevity when purified in DDM alone. This could particularly be the case if TRPM2 is reliant on membrane tension or packing within the membrane, which has not been described for *hs*TRPM2 channels. Mechanosensation of other TRP channel family members has been reported, but it has recently been demonstrated that this is not the case (Nikolaev *et al.*, 2019). To further examine channel properties in the context of the membrane, different scaffolds were explored and ultimately lead to the development of a new SMA-exchange method.

7.1.2 Motivation towards developing an SMA-exchange method

The overarching theme of this thesis is the importance of native lipids in membrane protein stability and function. During the course of this project, further hurdles were encountered with regard to TRPM2 stability perhaps not as a result of the protein, but as a result of the SMA *co*-polymer. There were two major drivers behind the development of this method – the first is that TRPM2 is a cation channel, and in the SMA-bound form, cannot be subject to any functional assays in the presence of Ca^{2+}. In the absence of a functional assay, many of the results here can be scrutinised. Secondly, experiments involving native mass spectrometry (MS) of membrane proteins and their associated lipid interactions were gaining traction in the literature (Reading, Liko, *et al.*, 2015a; Michael T. Marty, Hoi and Robinson, 2016; Gupta *et al.*, 2017). It was hoped that native MS could be used to analyse the lipids co-purified with SMA_TRPM2, but preliminary experiments did not yield any results. Additionally, the SMA polymer is extremely heterogeneous, and this does not bode

well for either MS or EM. For these reasons, an exchange method was developed in an attempt to overcome some of the bottlenecks associated with SMA_TRPM2 characterisation.

7.1.3 SMA-Exchange Method Conclusions

It was the aim of this method to combine the advantages of multiple membrane protein solubilisation vehicles, and create a new dogma of membrane protein characterisation, by which the protein is first extracted in SMA, and exchanged for a solubilisation vehicle more suited to a specific analytical technique. The method capitalises on the ability of $MgCl_2$ to precipitate the SMA co-polymer (Fiori *et al.*, 2017), in the presence of an alternative solubilisation platform such as detergents or amphipols. Experiments started on TRPM2, but this was found to be too costly to continue optimisation. AcrB was then chosen as a model system to test the exchange, as it has already been characterised by a number of biochemical and biophysical techniques in numerous reconstitution platforms (Murakami *et al.*, 2002; Du *et al.*, 2014; Postis *et al.*, 2015a; Wang *et al.*, 2017).

There would be several advantages to the success of this exchange. Firstly, it would allow native lipids to be carried through the initial protein solubilisation/purification steps, which enhances the stability of the membrane protein the MPs in solution giving them a prolonged half-life. Secondly, as detergents and amphipols are not required in the membrane protein preparation until the final exchange step, it can significantly reduce labour and costs associated with standard detergent purifications. To this end, AcrB was successfully purified with the SMA co-polymer and exchanged the polymer for an alternative platform – namely, amphipol, A8-35 and detergent, DDM (Section

6.2.3). The final exchange product was more homogeneous, could withstand millimolar concentrations of $MgCl_2$ and was suitable to give observable spectra in native-MS analysis, which were my initial objectives (Chapter 6).

The exchange process can also be performed on a small scale with minimal sample loss, which is beneficial to more difficult systems where low protein concentrations are obtained. Mass spectrometry was also able to suggest that lipids are carried over from the transfer of SMA into A8-35 (Section 6.2.3.6), which opens up the possibility of analysing the first native-MS spectrum of a membrane protein:lipid complex that has been extracted and purified in the complete absence of detergent, alongside a complimentary lipid profiles. Overall, this method has the potential to provide further insights into native membrane protein:lipid interactions by adding to the ever-expanding SMA toolbox for membrane protein characterisation (Figure 7.1).

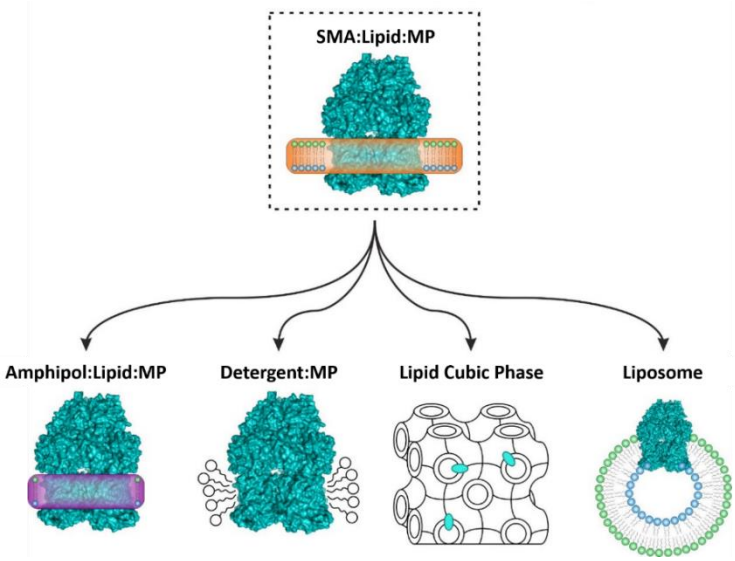

Figure 7.1: SMALPs as a vehicle for transfer into downstream membrane protein solubilisation platforms.

The alternative dogma for membrane protein characterisation, where membrane proteins are first solubilised in SMA, before exchanging into a more suitable solubilisation system for downstream analysis.

List of References

Alberts, B. *et al.* (2002) 'Principles of Membrane Transport'. Garland Science. Available at: https://www.ncbi.nlm.nih.gov/books/NBK26815/ (Accessed: 13 September 2020).

Alexandrov, A. I. *et al.* (2008) *Microscale Fluorescent Thermal Stability Assay for Membrane Proteins, Structure*. doi: 10.1016/j.str.2008.02.004.

Althoff, T. *et al.* (2011) 'Arrangement of electron transport chain components in bovine mitochondrial supercomplex $I_1 III_2 IV_1$', *The EMBO Journal*. John Wiley & Sons, Ltd, 30(22), pp. 4652–4664. doi: 10.1038/emboj.2011.324.

Andréll, J. and Tate, C. G. (2013) 'Overexpression of membrane proteins in mammalian cells for structural studies', *Molecular Membrane Biology*. Taylor & Francis, 30(1), pp. 52–63. doi: 10.3109/09687688.2012.703703.

Arnold, S. A. *et al.* (2017) 'Blotting-free and lossless cryo-electron microscopy grid preparation from nanoliter-sized protein samples and single-cell extracts', *Journal of Structural Biology*. Academic Press Inc., 197(3), pp. 220–226. doi: 10.1016/j.jsb.2016.11.002.

Balazs, D. A. and Godbey, W. T. (2011) 'Liposomes for Use in Gene Delivery', *Journal of Drug Delivery*. Hindawi Publishing Corporation, 2011, p. 12. doi: 10.1155/2011/326497.

Balijepalli, R. C. *et al.* (2007) 'Kv11.1 (ERG1) K+ channels localize in cholesterol

and sphingolipid enriched membranes and are modulated by membrane cholesterol', *Channels*. Taylor and Francis Inc., 1(4), pp. 263–272. doi: 10.4161/chan.4946.

Bavec, A. *et al.* (1999) 'Peptitergent PD1 affects the GTPase activity of rat brain cortical membranes', *Peptides*. Elsevier Inc., 20(2), pp. 177–184. doi: 10.1016/S0196-9781(98)00162-4.

Bechara, C. *et al.* (2015) 'A subset of annular lipids is linked to the flippase activity of an ABC transporter', *Nature Chemistry*, 7(3), pp. 255–262. doi: 10.1038/nchem.2172.

Belrose, J. C. and Jackson, M. F. (2018) 'TRPM2: A candidate therapeutic target for treating neurological diseases', *Acta Pharmacologica Sinica*. 2018/04/20, 39(5), pp. 722–732. doi: 10.1038/aps.2018.31.

Bessman, M. J., Frick, D. N. and O'Handley, S. F. (1996) 'The MutT proteins or "Nudix" hydrolases, a family of versatile, widely distributed, "housecleaning" enzymes', *Journal of Biological Chemistry*. American Society for Biochemistry and Molecular Biology, pp. 25059–25062. doi: 10.1074/jbc.271.41.25059.

Biasini, M. *et al.* (2014) 'SWISS-MODEL: modelling protein tertiary and quaternary structure using evolutionary information.', *Nucleic acids research*. Oxford University Press, 42(Web Server issue), pp. W252-8. doi: 10.1093/nar/gku340.

Le Bon, C. *et al.* (2018) 'Folding and stabilizing membrane proteins in amphipol A8-35', *Methods*. Elsevier, 147(December 2017), pp. 95–105. doi: 10.1016/j.ymeth.2018.04.012.

Borch, J. and Hamann, T. (2009) 'The nanodisc: A novel tool for membrane protein studies', *Biological Chemistry*. Biol Chem, pp. 805–814. doi: 10.1515/BC.2009.091.

Bowie, J. U. (2001) ‘Stabilizing membrane proteins’, *Current Opinion in Structural Biology*. Elsevier Ltd, pp. 397–402. doi: 10.1016/S0959-440X(00)00223-2.

Brady, N. G., Qian, S. and Bruce, B. D. (2019) ‘Analysis of styrene maleic acid alternating copolymer supramolecular assemblies in solution by small angle X-ray scattering’, *European Polymer Journal*. Elsevier Ltd, 111, pp. 178–184. doi: 10.1016/j.eurpolymj.2018.11.034.

Broecker, J., Eger, B. T. and Ernst, O. P. (2017) ‘Crystallogenesis of Membrane Proteins Mediated by Polymer-Bounded Lipid Nanodiscs’, *Structure*, 25(2), pp. 384–392. doi: 10.1016/j.str.2016.12.004.

Bruzzone, S. *et al.* (2007) ‘Abscisic acid is an endogenous cytokine in human granulocytes with cyclic ADP-ribose as second messenger.’, *Proceedings of the National Academy of Sciences of the United States of America*. National Academy of Sciences, 104(14), pp. 5759–64. doi: 10.1073/pnas.0609379104.

Bruzzone, S. *et al.* (2008) ‘Abscisic acid is an endogenous stimulator of insulin release from human pancreatic islets with cyclic ADP ribose as second messenger.’, *The Journal of biological chemistry*. American Society for Biochemistry and Molecular Biology, 283(47), pp. 32188–97. doi: 10.1074/jbc.M802603200.

Buelow, B., Song, Y. and Scharenberg, A. M. (2008) ‘The Poly(ADP-ribose) Polymerase PARP-1 Is Required for Oxidative Stress-induced TRPM2 Activation in Lymphocytes’, *Journal of Biological Chemistry*. American Society for Biochemistry and Molecular Biology, 283(36), pp. 24571–24583. doi: 10.1074/jbc.M802673200.

Burroughs, A. M. *et al.* (2015) ‘Comparative genomic analyses reveal a vast, novel network of nucleotide-centric systems in biological conflicts, immunity and

signaling.', *Nucleic acids research*. Oxford University Press, 43(22), pp. 10633–54. doi: 10.1093/nar/gkv1267.

Calabrese, A. N. *et al.* (2015) 'Amphipols outperform dodecylmaltoside micelles in stabilizing membrane protein structure in the gas phase.', *Analytical chemistry*. American Chemical Society, 87(2), pp. 1118–26. doi: 10.1021/ac5037022.

Cao, E. *et al.* (2013) 'TRPV1 structures in distinct conformations reveal activation mechanisms.', *Nature*. NIH Public Access, 504(7478), pp. 113–8. doi: 10.1038/nature12823.

Carlson, M. L. *et al.* (2018) 'The Peptidisc, a simple method for stabilizing membrane proteins in detergent-free solution', *eLife*, 7. doi: 10.7554/eLife.34085.

Carpenter, E. P. *et al.* (2008) 'Overcoming the challenges of membrane protein crystallography', *Current Opinion in Structural Biology*. Elsevier, pp. 581–586. doi: 10.1016/j.sbi.2008.07.001.

Caterina, M. J. *et al.* (1997) 'The capsaicin receptor: A heat-activated ion channel in the pain pathway', *Nature*. Nature Publishing Group, 389(6653), pp. 816–824. doi: 10.1038/39807.

Cermenati, G. *et al.* (2015) 'Lipids in the nervous system: From biochemistry and molecular biology to patho-physiology', *Biochimica et Biophysica Acta - Molecular and Cell Biology of Lipids*. Elsevier B.V., 1851(1), pp. 51–60. doi: 10.1016/j.bbalip.2014.08.011.

Chae, P. S. *et al.* (2010) 'Maltose-neopentyl glycol (MNG) amphiphiles for solubilization, stabilization and crystallization of membrane proteins', *Nature Methods*. NIH Public Access, 7(12), pp. 1003–1008. doi: 10.1038/nmeth.1526.

Cheng, Y. (2018) ‘Single-particle cryo-EM-How did it get here and where will it go’, *Science*. American Association for the Advancement of Science, pp. 876–880. doi: 10.1126/science.aat4346.

Cherezov, V. (2009) ‘Crystallizing membrane proteins using lipidic mesophases’, *Nature Protocols*. NIH Public Access, 4(5), pp. 706–731. doi: 10.1038/nprot.2009.31.

Cheung, J. Y. and Miller, B. A. (2017) ‘Transient Receptor Potential-Melastatin Channel Family Member 2: Friend or Foe’, *Transactions of the American Clinical and Climatological Association*, pp. 308–329.

Churchward, M. A. *et al.* (2008) ‘Copper (II) sulfate charring for high sensitivity on-plate fluorescent detection of lipids and sterols: quantitative analyses of the composition of functional secretory vesicles’, *Journal of Chemical Biology*. doi: 10.1007/s12154-008-0007-1.

Civjan, N. R. *et al.* (2003) ‘Direct solubilization of heterologously expressed membrane proteins by incorporation into nanoscale lipid bilayers’, *BioTechniques*, 35(3), pp. 556–563. doi: 10.2144/03353rr02.

Craig, A. F. *et al.* (2016) ‘Tuning the size of styrene-maleic acid copolymer-lipid nanoparticles (SMALPs) using RAFT polymerization for biophysical studies’, *Biochimica et Biophysica Acta (BBA) - Biomembranes*. Elsevier, 1858(11), pp. 2931–2939. doi: 10.1016/J.BBAMEM.2016.08.004.

Crichton, P. G. *et al.* (2015) ‘Trends in thermostability provide information on the nature of substrate, inhibitor, and lipid interactions with mitochondrial carriers’, *Journal of Biological Chemistry*. American Society for Biochemistry and Molecular

Biology Inc., 290(13), pp. 8206–8217. doi: 10.1074/jbc.M114.616607.

Csanady, L. and Torocsik, B. (2009) 'Four Ca2+ ions activate TRPM2 channels by binding in deep crevices near the pore but intracellularly of the gate', *J Gen Physiol*. 2009/01/28, 133(2), pp. 189–203. doi: 10.1085/jgp.200810109.

Csanády, L. and Törocsik, B. (2009) 'Four Ca2+ ions activate TRPM2 channels by binding in deep crevices near the pore but intracellularly of the gate.', *The Journal of general physiology*. The Rockefeller University Press, 133(2), pp. 189–203. doi: 10.1085/jgp.200810109.

Cuevas Arenas, R. *et al.* (2016) 'Influence of lipid bilayer properties on nanodisc formation mediated by styrene/maleic acid copolymers', *Nanoscale*. The Royal Society of Chemistry, 8(32), pp. 15016–15026. doi: 10.1039/C6NR02089E.

Dawaliby, R. *et al.* (2016) 'Phosphatidylethanolamine is a key regulator of membrane fluidity in eukaryotic cells', *Journal of Biological Chemistry*. American Society for Biochemistry and Molecular Biology Inc., 291(7), pp. 3658–3667. doi: 10.1074/jbc.M115.706523.

Deng, H., Jia, Y. and Zhang, Y. (2018) 'Protein structure prediction', *International Journal of Modern Physics B*. World Scientific Publishing Co. Pte Ltd, 32(18). doi: 10.1142/S021797921840009X.

Denisov, I. G. and Sligar, S. G. (2017) 'Nanodiscs in Membrane Biochemistry and Biophysics', *Chemical Reviews*. American Chemical Society, pp. 4669–4713. doi: 10.1021/acs.chemrev.6b00690.

Domínguez Pardo, J. J. *et al.* (2018) 'Membrane Solubilization by Styrene-Maleic Acid Copolymers: Delineating the Role of Polymer Length', *Biophysical Journal*,

115(1), pp. 129–138. doi: 10.1016/j.bpj.2018.05.032.

Dörr, J. M. *et al.* (2014) 'Detergent-free isolation, characterization, and functional reconstitution of a tetrameric K + channel: The power of native nanodiscs', *Proceedings of the National Academy of Sciences*, 111(52), pp. 18607–18612. doi: 10.1073/pnas.1416205112.

Dörr, J. M. *et al.* (2016) 'The styrene–maleic acid copolymer: a versatile tool in membrane research', *European Biophysics Journal*, 45(1), pp. 3–21. doi: 10.1007/s00249-015-1093-y.

Drulyte, I. *et al.* (2018) 'Approaches to altering particle distributions in cryo-electron microscopy sample preparation', *Acta Crystallographica Section D: Structural Biology*. Wiley-Blackwell, 74(6), pp. 560–571. doi: 10.1107/S2059798318006496.

Du, D. *et al.* (2014) 'Structure of the AcrAB–TolC multidrug efflux pump', *Nature*, 509(7501), pp. 512–515. doi: 10.1038/nature13205.

Du, J., Xie, J. and Yue, L. (2009) 'Intracellular calcium activates TRPM2 and its alternative spliced isoforms.', *Proceedings of the National Academy of Sciences of the United States of America*. National Academy of Sciences, 106(17), pp. 7239–44. doi: 10.1073/pnas.0811725106.

Dürr, U. H. N., Gildenberg, M. and Ramamoorthy, A. (2012) 'The Magic of Bicelles Lights Up Membrane Protein Structure', *Chemical Reviews*, 112(11), pp. 6054–6074. doi: 10.1021/cr300061w.

Erler, I. *et al.* (2006) 'Trafficking and assembly of the cold-sensitive TRPM8 channel', *Journal of Biological Chemistry*. American Society for Biochemistry and Molecular Biology, 281(50), pp. 38396–38404. doi: 10.1074/jbc.M607756200.

Eylar, E. H. and Hagopian, A. (1971) '[15] Isolation of plasma membranes from mammalian cells', *Methods in Enzymology*. Academic Press, 22, pp. 123–130. doi: 10.1016/0076-6879(71)22017-6.

Fahy, E. *et al.* (2009) 'Update of the LIPID MAPS comprehensive classification system for lipids.', *Journal of lipid research*. American Society for Biochemistry and Molecular Biology, 50 Suppl(Suppl), pp. S9-14. doi: 10.1194/jlr.R800095-JLR200.

Finkel, T. and Holbrook, N. J. (2000) 'Oxidants, oxidative stress and the biology of ageing', *Nature*. Nature, pp. 239–247. doi: 10.1038/35041687.

Fiori, M. C. *et al.* (2017) 'Polymer-encased nanodiscs with improved buffer compatibility', *Scientific Reports*. Nature Publishing Group, 7(1), p. 7432. doi: 10.1038/s41598-017-07110-1.

Fleig, A. and Penner, R. (2004a) 'The TRPM ion channel subfamily: Molecular, biophysical and functional features', *Trends in Pharmacological Sciences*. Elsevier Current Trends, pp. 633–639. doi: 10.1016/j.tips.2004.10.004.

Fleig, A. and Penner, R. (2004b) 'The TRPM ion channel subfamily: Molecular, biophysical and functional features', *Trends in Pharmacological Sciences*, pp. 633–639. doi: 10.1016/j.tips.2004.10.004.

FOLCH, J., LEES, M. and SLOANE STANLEY, G. H. (1957) 'A simple method for the isolation and purification of total lipides from animal tissues.', *The Journal of biological chemistry*.

Fujiwara, Y. and Minor, D. L. (2008) 'X-ray Crystal Structure of a TRPM Assembly Domain Reveals an Antiparallel Four-stranded Coiled-coil', *Journal of Molecular Biology*. Academic Press, 383(4), pp. 854–870. doi: 10.1016/j.jmb.2008.08.059.

Gewering, T. *et al.* (2018) 'Know your detergents: A case study on detergent background in negative stain electron microscopy', *Journal of Structural Biology*. Academic Press Inc., 203(3), pp. 242–246. doi: 10.1016/j.jsb.2018.05.008.

Gniewek, P. *et al.* (2012) 'How noise in force fields can affect the structural refinement of protein models?', *Proteins: Structure, Function and Bioinformatics*. NIH Public Access, 80(2), pp. 335–341. doi: 10.1002/prot.23240.

Goehring, A. *et al.* (2014) 'Screening and large-scale expression of membrane proteins in mammalian cells for structural studies', *Nature Protocols*. Nature Publishing Group, 9(11), pp. 2574–2585. doi: 10.1038/nprot.2014.173.

Gohon, Y. *et al.* (2006) 'Well-defined nanoparticles formed by hydrophobic assembly of a short and polydisperse random terpolymer, amphipol A8-35', *Langmuir*. doi: 10.1021/la052243g.

Gohon, Y. and Popot, J.-L. (2003) 'Membrane protein-surfactant complexes', *Current Opinion in Colloid and Interface Science*, 8, pp. 15–22. doi: 10.1016/S1359-0294(03)00013-X.

Gorzelle, B. M. *et al.* (2002) 'Amphipols can support the activity of a membrane enzyme', *Journal of the American Chemical Society*, 124(39), pp. 11594–11595. doi: 10.1021/ja027051b.

Greenfield, N. J. (2006a) 'Using circular dichroism collected as a function of temperature to determine the thermodynamics of protein unfolding and binding interactions.', *Nature protocols*. NIH Public Access, 1(6), pp. 2527–35. doi: 10.1038/nprot.2006.204.

Greenfield, N. J. (2006b) 'Using circular dichroism spectra to estimate protein

secondary structure.', *Nature protocols*. NIH Public Access, 1(6), pp. 2876–90. doi: 10.1038/nprot.2006.202.

Greenfield, N. J. (2007) 'Analysis of the kinetics of folding of proteins and peptides using circular dichroism', *Nature Protocols*. NIH Public Access, 1(6), pp. 2891–2899. doi: 10.1038/nprot.2006.244.

Grethen, A. *et al.* (2017) 'Thermodynamics of nanodisc formation mediated by styrene/maleic acid (2:1) copolymer', *Scientific Reports*. Nature Publishing Group, 7(1), p. 11517. doi: 10.1038/s41598-017-11616-z.

Grimm, C. *et al.* (2005) 'Activation of the melastatin-related cation channel TRMP3 by D-erytho-sphingosine', *Molecular Pharmacology*. American Society for Pharmacology and Experimental Therapeutics, 67(3), pp. 798–805. doi: 10.1124/mol.104.006734.

Gu, T. and Sjöblom, J. (1992) 'Surfactant structure and its relation to the Krafft point, cloud point and micellization: Some empirical relationships', *Colloids and Surfaces*. Elsevier, 64(1), pp. 39–46. doi: 10.1016/0166-6622(92)80160-4.

Gulamhussein, A. A. *et al.* (2019) 'Examining the stability of membrane proteins within SMALPs', *European Polymer Journal*. Pergamon, 112, pp. 120–125. doi: 10.1016/J.EURPOLYMJ.2018.12.008.

Guo, J. *et al.* (2017) 'Structures of the calcium-activated, non-selective cation channel TRPM4', *Nature*. Nature Publishing Group, 552(7684), pp. 205–209. doi: 10.1038/nature24997.

Guo, Y. R. and MacKinnon, R. (2017) 'Structure-based membrane dome mechanism for piezo mechanosensitivity', *eLife*. eLife Sciences Publications Ltd, 6. doi:

10.7554/eLife.33660.

Gupta, K. *et al.* (2017) 'The role of interfacial lipids in stabilizing membrane protein oligomers', *Nature*. Nature Publishing Group, 541(7637), pp. 421–424. doi: 10.1038/nature20820.

Gupta, K. *et al.* (2018) 'Identifying key membrane protein lipid interactions using mass spectrometry', *Nature Protocols*, 13(5), pp. 1106–1120. doi: 10.1038/nprot.2018.014.

Hall, Stephen C L *et al.* (2018) 'An acid-compatible co-polymer for the solubilization of membranes and proteins into lipid bilayer-containing nanoparticles.', *Nanoscale*. Royal Society of Chemistry, 10(22), pp. 10609–10619. doi: 10.1039/c8nr01322e.

Hall, Stephen C. L. *et al.* (2018) 'Influence of Poly(styrene- *co* -maleic acid) Copolymer Structure on the Properties and Self-Assembly of SMALP Nanodiscs', *Biomacromolecules*. American Chemical Society, 19(3), pp. 761–772. doi: 10.1021/acs.biomac.7b01539.

Hantute-Ghesquier, A. *et al.* (2018) 'TRPM family channels in cancer', *Pharmaceuticals*. 2018/06/08, 11(2). doi: 10.3390/ph11020058.

Hara, Y. *et al.* (2002) 'LTRPC2 Ca2+-Permeable Channel Activated by Changes in Redox Status Confers Susceptibility to Cell Death', *Molecular Cell*, 9(1), pp. 163–173. doi: 10.1016/S1097-2765(01)00438-5.

Hardy, D. *et al.* (2016) 'Overcoming bottlenecks in the membrane protein structural biology pipeline', *Biochemical Society Transactions*. 2016/06/11, 44(3), pp. 838–844. doi: 10.1042/BST20160049.

Harteneck, C., Plant, T. D. and Schultz, G. (2000) 'From worm to man: three subfamilies of TRP channels', *Trends in Neurosciences*, 23(4), pp. 159–166. doi: 10.1016/S0166-2236(99)01532-5.

Hattori, M., Hibbs, R. E. and Gouaux, E. (2012) 'A fluorescence-detection size-exclusion chromatography-based thermostability assay for membrane protein precrystallization screening.', *Structure (London, England : 1993)*. NIH Public Access, 20(8), pp. 1293–9. doi: 10.1016/j.str.2012.06.009.

Heiner, I. *et al.* (2006) 'Endogenous ADP-ribose enables calcium-regulated cation currents through TRPM2 channels in neutrophil granulocytes', *Biochemical Journal*. Portland Press Ltd, 398(2), pp. 225–232. doi: 10.1042/BJ20060183.

Hellwig, N. *et al.* (2018) 'Native mass spectrometry goes more native: Investigation of membrane protein complexes directly from SMALPs', *Chemical Communications*. Royal Society of Chemistry, 54(97), pp. 13702–13705. doi: 10.1039/c8cc06284f.

Hopf, T. A. *et al.* (2014) 'Sequence co-evolution gives 3D contacts and structures of protein complexes', *eLife*, 3. doi: 10.7554/eLife.03430.

Hopper, J. T. S. *et al.* (2013) 'Detergent-free mass spectrometry of membrane protein complexes', *Nature Methods*. Nature Publishing Group, 10(12), pp. 1206–1208. doi: 10.1038/nmeth.2691.

Huang, Y. *et al.* (2018) 'Architecture of the TRPM2 channel and its activation mechanism by ADP-ribose and calcium', *Nature*. Nature Publishing Group, 562(7725), pp. 145–163. doi: 10.1038/s41586-018-0558-4.

Huang, Y. *et al.* (2019) 'Ligand recognition and gating mechanism through three

Ligand-binding sites of human TRPM2 channel', *eLife*. eLife Sciences Publications Ltd, 8. doi: 10.7554/eLife.50175.

Huang, Y. *et al.* (2020) 'A structural overview of the ion channels of the TRPM family', *Cell Calcium*. Elsevier Ltd, p. 102111. doi: 10.1016/j.ceca.2019.102111.

Hunter, J. J. *et al.* (1998) 'Chromosomal localization and genomic characterization of the mouse melastatin gene (Mlsn1)', *Genomics*. Academic Press Inc., 54(1), pp. 116–123. doi: 10.1006/geno.1998.5549.

Hussain, R. *et al.* (2016) 'High-throughput SRCD using multi-well plates and its applications', *Scientific Reports*. Nature Publishing Group, 6. doi: 10.1038/srep38028.

Hussain, R., Longo, E. and Siligardi, G. (2018) 'UV-Denaturation assay to assess protein photostability and ligand-binding interactions using the high photon flux of diamond B23 beamline for SRCD', *Molecules*. MDPI AG. doi: 10.3390/molecules23081906.

Huynh, K. W. *et al.* (2016) 'Structure of the full-length TRPV2 channel by cryo-EM.', *Nature communications*. Nature Publishing Group, 7, p. 11130. doi: 10.1038/ncomms11130.

Huynh, K. W., Cohen, M. R. and Moiseenkova-Bell, V. Y. (2014) 'Application of amphipols for structure-functional analysis of TRP channels.', *The Journal of membrane biology*. NIH Public Access, 247(9–10), pp. 843–51. doi: 10.1007/s00232-014-9684-6.

Iordanov, I. *et al.* (2016a) 'The proposed channel-enzyme transient receptor potential melastatin 2 does not possess ADP ribose hydrolase activity.', *eLife*. eLife Sciences

Publications, Ltd, 5. doi: 10.7554/eLife.17600.

Iordanov, I. *et al.* (2016b) 'The proposed channel-enzyme transient receptor potential melastatin 2 does not possess ADP ribose hydrolase activity', *eLife*. 2016/07/08, 5(JULY). doi: 10.7554/eLife.17600.

Iordanov, I. *et al.* (2019) 'Enzyme activity and selectivity filter stability of ancient trpm2 channels were simultaneously lost in early vertebrates', *eLife*. eLife Sciences Publications Ltd, 8. doi: 10.7554/eLife.44556.

Jacob, F. and Monod, J. (1961) 'Genetic regulatory mechanisms in the synthesis of proteins', *Journal of Molecular Biology*, pp. 318–356. doi: 10.1016/S0022-2836(61)80072-7.

Jamshad, M., Charlton, J., *et al.* (2015) 'G-protein coupled receptor solubilization and purification for biophysical analysis and functional studies, in the total absence of detergent', *Bioscience Reports*, 35(2), pp. 1–10. doi: 10.1042/BSR20140171.

Jamshad, M., Grimard, V., *et al.* (2015) 'Structural analysis of a nanoparticle containing a lipid bilayer used for detergent-free extraction of membrane proteins', *Nano Research*, 8(3), pp. 774–789. doi: 10.1007/s12274-014-0560-6.

Jefferys, B. R., Kelley, L. A. and Sternberg, M. J. E. (2010) 'Protein folding requires crowd control in a simulated cell', *Journal of Molecular Biology*. Academic Press, 397(5), pp. 1329–1338. doi: 10.1016/j.jmb.2010.01.074.

Jiang, L. H., Gamper, N. and Beech, D. J. (2011) 'Properties and therapeutic potential of transient receptor potential channels with putative roles in adversity: focus on TRPC5, TRPM2 and TRPA1.', *Current drug targets*. Bentham Science Publishers, 12(5), pp. 724–36. Available at:

http://www.ncbi.nlm.nih.gov/pubmed/21291387 (Accessed: 16 November 2016).

Jin, P. *et al.* (2017) 'Electron cryo-microscopy structure of the mechanotransduction channel NOMPC', *Nature*. Nature Publishing Group, 547(7661), pp. 118–122. doi: 10.1038/nature22981.

Jirku, M. *et al.* (2015) 'Characterization of the part of N-terminal PIP2 binding site of the TRPM1 channel', *Biophysical Chemistry*. Elsevier, 207, pp. 135–142. doi: 10.1016/J.BPC.2015.10.005.

Jones, J. *et al.* (2005) 'Optimization of tetracycline-responsive recombinant protein production and effect on cell growth and ER stress in mammalian cells', *Biotechnology and Bioengineering*, 91(6), pp. 722–732. doi: 10.1002/bit.20566.

Kabsch, W. and Sander, C. (1983) 'Dictionary of protein secondary structure: Pattern recognition of hydrogen-bonded and geometrical features', *Biopolymers*. John Wiley & Sons, Ltd, 22(12), pp. 2577–2637. doi: 10.1002/bip.360221211.

Kashio, M. *et al.* (2012) 'Redox signal-mediated sensitization of transient receptor potential melastatin 2 (TRPM2) to temperature affects macrophage functions', *Proceedings of the National Academy of Sciences of the United States of America*. National Academy of Sciences, 109(17), pp. 6745–6750. doi: 10.1073/pnas.1114193109.

Kashio, M. and Tominaga, M. (2017) 'The TRPM2 channel: A thermo-sensitive metabolic sensor', *Channels*. Taylor and Francis Inc., pp. 426–433. doi: 10.1080/19336950.2017.1344801.

Kelley, L. A. *et al.* (2015) 'The Phyre2 web portal for protein modeling, prediction and analysis', *Nature Protocols*, 10(6), pp. 845–858. doi: 10.1038/nprot.2015.053.

Kelly, S. M., Jess, T. J. and Price, N. C. (2005a) 'How to study proteins by circular dichroism', *Biochimica et Biophysica Acta - Proteins and Proteomics*. Elsevier, pp. 119–139. doi: 10.1016/j.bbapap.2005.06.005.

Kelly, S. M., Jess, T. J. and Price, N. C. (2005b) *How to study proteins by circular dichroism, Biochimica et Biophysica Acta - Proteins and Proteomics*. doi: 10.1016/j.bbapap.2005.06.005.

Knowles, T. J., Finka, R., Smith, C., Lin, Y. P., *et al.* (2009) 'Membrane proteins solubilized intact in lipid containing nanoparticles bounded by styrene maleic acid copolymer', *Journal of the American Chemical Society*. American Chemical Society, 131(22), pp. 7484–7485. doi: 10.1021/ja810046q.

Knowles, T. J., Finka, R., Smith, C., Lin, Y.-P., *et al.* (2009) 'Membrane Proteins Solubilized Intact in Lipid Containing Nanoparticles Bounded by Styrene Maleic Acid Copolymer', *Journal of the American Chemical Society*, 131(22), pp. 7484–7485. doi: 10.1021/ja810046q.

Kolisek, M. *et al.* (2005) 'Cyclic ADP-Ribose and Hydrogen Peroxide Synergize with ADP-Ribose in the Activation of TRPM2 Channels', *Molecular Cell*, 18(1), pp. 61–69. doi: 10.1016/j.molcel.2005.02.033.

Kopf, A. H. *et al.* (2019) 'A simple and convenient method for the hydrolysis of styrene-maleic anhydride copolymers to styrene-maleic acid copolymers', *Chemistry and Physics of Lipids*. Elsevier Ireland Ltd, 218, pp. 85–90. doi: 10.1016/j.chemphyslip.2018.11.011.

Kotov, V. *et al.* (2019) 'High-throughput stability screening for detergent-solubilized membrane proteins', *Scientific Reports*. Nature Publishing Group, 9(1), p. 10379.

doi: 10.1038/s41598-019-46686-8.

Kudoh, J. *et al.* (1997) 'Localization of 16 exons to a 450-kb region involved in the autoimmune polyglandular disease type I (APECED) on human chromosome 21q22.3.', *DNA research : an international journal for rapid publication of reports on genes and genomes*, 4(1), pp. 45–52. doi: 10.1093/dnares/4.1.45.

Kühn, F. J. P. *et al.* (2010) 'Contribution of the S5-pore-S6 domain to the gating characteristics of the cation channels TRPM2 and TRPM8', *Journal of Biological Chemistry*. American Society for Biochemistry and Molecular Biology, 285(35), pp. 26806–26814. doi: 10.1074/jbc.M110.109975.

Kühn, F. J. P. *et al.* (2015) 'Functional Characterisation of a TRPM2 orthologue from the sea anemone Nematostella vectensis in human cells', *Scientific Reports*. Nature Publishing Group, 5(1), p. 8032. doi: 10.1038/srep08032.

Kühn, F., Kühn, C. and Lückhoff, A. (2017) 'Different Principles of ADP-Ribose-Mediated Activation and Opposite Roles of the NUDT9 Homology Domain in the TRPM2 Orthologs of Man and Sea Anemone', *Frontiers in Physiology*. Frontiers Media S.A., 8(OCT), p. 879. doi: 10.3389/fphys.2017.00879.

Kurakawa, T. *et al.* (2007) 'Direct control of shoot meristem activity by a cytokinin-activating enzyme', *Nature*. Nature Publishing Group, 445(7128), pp. 652–655. doi: 10.1038/nature05504.

Kuroha, T. *et al.* (2009) 'Functional analyses of LONELY GUY cytokinin-activating enzymes reveal the importance of the direct activation pathway in Arabidopsis', *Plant Cell*. American Society of Plant Biologists, 21(10), pp. 3152–3169. doi: 10.1105/tpc.109.068676.

Lappas, C. M. (2015) ‘The plant hormone zeatin riboside inhibits T lymphocyte activity via adenosine A2A receptor activation’, *Cellular and Molecular Immunology*. Chinese Soc Immunology, 12(1), pp. 107–112. doi: 10.1038/cmi.2014.33.

Launay, P. *et al.* (2004) ‘TRPM4 regulates calcium oscillations after T cell activation’, *Science*. American Association for the Advancement of Science, 306(5700), pp. 1374–1377. doi: 10.1126/science.1098845.

Lee, S. C. *et al.* (2016) ‘A method for detergent-free isolation of membrane proteins in their local lipid environment’, *Nature Protocols*. 2016/06/03, 11(7), pp. 1149–1162. doi: 10.1038/nprot.2016.070.

Leney, A. C. *et al.* (2012) ‘Amphipathic polymers enable the study of functional membrane proteins in the gas phase.’, *Analytical chemistry*. American Chemical Society, 84(22), pp. 9841–7. doi: 10.1021/ac302223s.

Levy, L. S. *et al.* (1982) ‘The selection, expression, and organization of a set of head-specific genes in Drosophila’, *Developmental Biology*, 94(2), pp. 451–464. doi: 10.1016/0012-1606(82)90362-1.

Li, J. *et al.* (2017) ‘TRPM2: a potential drug target to retard oxidative stress.’, *Frontiers in bioscience (Landmark edition)*, 22, pp. 1427–1438. Available at: http://www.ncbi.nlm.nih.gov/pubmed/28199210 (Accessed: 16 February 2017).

Liao, M. *et al.* (2013) ‘Structure of the TRPV1 ion channel determined by electron cryo-microscopy’, *Nature*, 504(7478), pp. 107–112. doi: 10.1038/nature12822.

Lindström, J. B., Pierce, N. T. and Latz, M. I. (2017) ‘Role of TRP channels in dinoflagellate mechanotransduction’, *Biological Bulletin*. University of Chicago

Press, 233(2), pp. 151–167. doi: 10.1086/695421.

Lockhart, B. (2012) ‘Calclium-calmodulin regulation of TRPM2 currents’, *Electronic Thesis and Dissertation Repository*. Available at: https://ir.lib.uwo.ca/etd/663 (Accessed: 19 May 2020).

Lupas, A., Van Dyke, M. and Stock, J. (1991) ‘Predicting coiled coils from protein sequences’, *Science*, 252(5009), pp. 1162–1164. doi: 10.1126/science.252.5009.1162.

Lyons, J. A. *et al.* (2016) ‘Expression strategies for structural studies of eukaryotic membrane proteins’, *Current Opinion in Structural Biology*. Elsevier Ltd, pp. 137–144. doi: 10.1016/j.sbi.2016.06.011.

Le Maire, M., Champeil, P. and Møller, J. V. (2000) ‘Interaction of membrane proteins and lipids with solubilizing detergents’, *Biochimica et Biophysica Acta - Biomembranes*. Elsevier, pp. 86–111. doi: 10.1016/S0304-4157(00)00010-1.

Majd, H. *et al.* (2018) ‘Screening of candidate substrates and coupling ions of transporters by thermostability shift assays’, *eLife*. eLife Sciences Publications Ltd, 7. doi: 10.7554/eLife.38821.

Markossian, K. A. and Kurganov, B. I. (2004) ‘Protein Folding, Misfolding, and Aggregation. Formation of Inclusion Bodies and Aggresomes’, *Biochemistry (Moscow)*, 69(9), pp. 971–984. doi: 10.1023/B:BIRY.0000043539.07961.4c.

Marty, Michael T., Hoi, K. K. and Robinson, C. V. (2016) ‘Interfacing Membrane Mimetics with Mass Spectrometry’, *Accounts of Chemical Research*, 49(11), pp. 2459–2467. doi: 10.1021/acs.accounts.6b00379.

Marty, Michael T, Hoi, K. K. and Robinson, C. V (2016) 'Interfacing Membrane Mimetics with Mass Spectrometry.', *Accounts of chemical research*. Europe PMC Funders, 49(11), pp. 2459–2467. doi: 10.1021/acs.accounts.6b00379.

Maruyama, Y. *et al.* (2007) 'Three-dimensional reconstruction using transmission electron microscopy reveals a swollen, bell-shaped structure of transient receptor potential melastatin type 2 cation channel.', *The Journal of biological chemistry*. American Society for Biochemistry and Molecular Biology, 282(51), pp. 36961–70. doi: 10.1074/jbc.M705694200.

Massullo, P. *et al.* (2006) 'TRPM channels, calcium and redox sensors during innate immune responses', *Seminars in Cell & Developmental Biology*, 17(6), pp. 654–666. doi: 10.1016/j.semcdb.2006.11.006.

McHugh, D. *et al.* (2003a) 'Critical intracellular Ca2+ dependence of transient receptor potential melastatin 2 (TRPM2) cation channel activation', *Journal of Biological Chemistry*. J Biol Chem, 278(13), pp. 11002–11006. doi: 10.1074/jbc.M210810200.

McHugh, D. *et al.* (2003b) 'Critical intracellular Ca2+ dependence of transient receptor potential melastatin 2 (TRPM2) cation channel activation', *Journal of Biological Chemistry*. American Society for Biochemistry and Molecular Biology, 278(13), pp. 11002–11006. doi: 10.1074/jbc.M210810200.

Mei, Z.-Z. and Jiang, L.-H. (2009) 'Requirement for the N-terminal coiled-coil domain for expression and function, but not subunit interaction of, the ADPR-activated TRPM2 channel.', *The Journal of membrane biology*. Springer, 230(2), pp. 93–9. doi: 10.1007/s00232-009-9190-4.

Mei, Z. Z. *et al.* (2006) 'Intracellular coiled-coil domain engaged in subunit interaction and assembly of melastatin-related transient receptor potential channel 2', *Journal of Biological Chemistry*. Europe PMC Funders, 281(50), pp. 38748–38756. doi: 10.1074/jbc.M607591200.

Mei, Z. Z., Mao, H. J. and Jiang, L. H. (2006) 'Conserved cysteine residues in the pore region are obligatory for human TRPM2 channel function', *American Journal of Physiology - Cell Physiology*. Europe PMC Funders, 291(5), p. C1022. doi: 10.1152/ajpcell.00606.2005.

Miles, A. J. *et al.* (2016) 'Circular dichroism spectroscopy of membrane proteins', *Chem. Soc. Rev.* The Royal Society of Chemistry, 45(18), pp. 4859–4872. doi: 10.1039/C5CS00084J.

Miles, A. J. and Wallace, B. A. (2006) 'Synchrotron radiation circular dichroism spectroscopy of proteins and applications in structural and functional genomics', *Chemical Society Reviews*, pp. 39–51. doi: 10.1039/b316168b.

Minke, B. (2006) 'TRP channels and Ca2+ signaling', *Cell Calcium*. Elsevier Ltd, pp. 261–275. doi: 10.1016/j.ceca.2006.05.002.

Minke, B. and Cook, B. (2002) 'TRP channel proteins and signal transduction', *Physiological Reviews*. American Physiological Society, pp. 429–472. doi: 10.1152/physrev.00001.2002.

Montell, C. *et al.* (1985) 'Rescue of the Drosophila phototransduction mutation trp by germline transformation', *Science*. doi: 10.1126/science.3933112.

Montell, C. (2001) 'Physiology, phylogeny, and functions of the TRP superfamily of cation channels.', *Science's STKE : signal transduction knowledge environment*.

American Association for the Advancement of Science, 2001(90), p. re1. doi: 10.1126/stke.2001.90.re1.

Montell, C. *et al.* (2002a) 'A Unified Nomenclature for the Superfamily of TRP Cation Channels', *Molecular Cell*, pp. 229–231. doi: 10.1016/S1097-2765(02)00448-3.

Montell, C. *et al.* (2002b) 'A Unified Nomenclature for the Superfamily of TRP Cation Channels', *Molecular Cell*. Cell Press, 9(2), pp. 229–231. doi: 10.1016/S1097-2765(02)00448-3.

Montell, C. (2005) 'The TRP superfamily of cation channels.', *Science's STKE : signal transduction knowledge environment*. American Association for the Advancement of Science, pp. re3–re3. doi: 10.1126/stke.2722005re3.

Montell, C. and Rubin, G. M. (1989) 'Molecular characterization of the drosophila trp locus: A putative integral membrane protein required for phototransduction', *Neuron*. doi: 10.1016/0896-6273(89)90069-X.

Moore-Kelly, C. *et al.* (2019) 'Automated High-Throughput Capillary Circular Dichroism and Intrinsic Fluorescence Spectroscopy for Rapid Determination of Protein Structure', *Analytical Chemistry*. American Chemical Society, 91(21), pp. 13794–13802. doi: 10.1021/acs.analchem.9b03259.

Moore, E. R. (1986) 'Properties of Styrene-Maleic Anhydride Copolymers', *Industrial and Engineering Chemistry Product Research and Development*. American Chemical Society, 25(2), pp. 315–321. doi: 10.1021/i300022a033.

Morales-Lázaro, S. L., Lemus, L. and Rosenbaum, T. (2017) 'Regulation of thermoTRPs by lipids', *Temperature*. Routledge, pp. 24–40. doi:

10.1080/23328940.2016.1254136.

Morenilla-Palao, C. *et al.* (2009) 'Lipid raft segregation modulates TRPM8 channel activity', *Journal of Biological Chemistry*, 284(14), pp. 9215–9224. doi: 10.1074/jbc.M807228200.

Morrison, K. A. *et al.* (2016) 'Membrane protein extraction and purification using styrene-maleic acid (SMA) copolymer: effect of variations in polymer structure', *Biochemical Journal*, 473(23), pp. 4349–4360. doi: 10.1042/BCJ20160723.

Murakami, S. *et al.* (2002) 'Crystal structure of bacterial multidrug efflux transporter AcrB', *Nature*. Nature Publishing Group, 419(6907), pp. 587–593. doi: 10.1038/nature01050.

Myeong, J. *et al.* (2016) 'The interaction domains of transient receptor potential canonical (TRPC)1/4 and TRPC1/5 heteromultimeric channels', *Biochemical and Biophysical Research Communications*. Elsevier B.V., 474(3), pp. 476–481. doi: 10.1016/j.bbrc.2016.04.138.

Nagamine, K. *et al.* (1997) 'Positional cloning of the APECED gene', *Nature Genetics*. Nature Publishing Group, 17(4), pp. 393–398. doi: 10.1038/ng1297-393.

Nagamine, K. *et al.* (1998) 'Molecular Cloning of a Novel Putative Ca2+Channel Protein (TRPC7) Highly Expressed in Brain', *Genomics*, 54(1), pp. 124–131. doi: 10.1006/geno.1998.5551.

Nath, A., Atkins, W. M. and Sligar, S. G. (2007) 'Applications of phospholipid bilayer nanodiscs in the study of membranes and membrane proteins', *Biochemistry*. Biochemistry, pp. 2059–2069. doi: 10.1021/bi602371n.

Nicolson, G. L. (2014) ‘The Fluid - Mosaic Model of Membrane Structure: Still relevant to understanding the structure, function and dynamics of biological membranes after more than 40 years’, *Biochimica et Biophysica Acta - Biomembranes*. Elsevier, pp. 1451–1466. doi: 10.1016/j.bbamem.2013.10.019.

Nikolaev, Y. A. *et al.* (2019) ‘Mammalian TRP ion channels are insensitive to membrane stretch’, *Journal of Cell Science*. Company of Biologists Ltd, 132(23). doi: 10.1242/jcs.238360.

Nilius, B. *et al.* (2005) ‘Regulation of the Ca2+ sensitivity of the nonselective cation channel TRPM4’, *Journal of Biological Chemistry*. American Society for Biochemistry and Molecular Biology, 280(8), pp. 6423–6433. doi: 10.1074/jbc.M411089200.

Nilius, B. and Owsianik, G. (2011) ‘The transient receptor potential family of ion channels.’, *Genome biology*. BioMed Central, 12(3), p. 218. doi: 10.1186/gb-2011-12-3-218.

Nilius, B. and Szallasi, A. (2014) ‘Transient Receptor Potential Channels as Drug Targets: From the Science of Basic Research to the Art of Medicine’, *Pharmacological Reviews*. American Society for Pharmacology and Experimental Therapeutics, 66(3), pp. 676–814. doi: 10.1124/PR.113.008268.

Noble, A. J. *et al.* (2018) ‘Routine single particle CryoEM sample and grid characterization by tomography’, *eLife*. eLife Sciences Publications Ltd, 7. doi: 10.7554/eLife.34257.

O’Day, D. H., Huber, R. J. and Suarez, A. (2012) ‘Extracellular calmodulin regulates growth and cAMP-mediated chemotaxis in Dictyostelium discoideum’, *Biochemical*

and Biophysical Research Communications. Academic Press, 425(4), pp. 750–754. doi: 10.1016/j.bbrc.2012.07.147.

O'Malley, M. A. *et al.* (2011) 'Toward rational design of protein detergent complexes: Determinants of mixed micelles that are critical for the in vitro stabilization of a g-protein coupled receptor', *Biophysical Journal*. The Biophysical Society, 101(8), pp. 1938–1948. doi: 10.1016/j.bpj.2011.09.018.

Ogiso, H., Taniguchi, M. and Okazaki, T. (2015) 'Analysis of lipid-composition changes in plasma membrane microdomains.', *Journal of lipid research*. American Society for Biochemistry and Molecular Biology, 56(8), pp. 1594–605. doi: 10.1194/jlr.M059972.

Oluwole, A. O. *et al.* (2017) 'Solubilization of Membrane Proteins into Functional Lipid-Bilayer Nanodiscs Using a Diisobutylene/Maleic Acid Copolymer', *Angewandte Chemie International Edition*, 56(7), pp. 1919–1924. doi: 10.1002/anie.201610778.

Orwick-Rydmark, M. *et al.* (2012a) 'Detergent-free incorporation of a seven-transmembrane receptor protein into nanosized bilayer lipodisq particles for functional and biophysical studies', *Nano Letters*, 12(9), pp. 4687–4692. doi: 10.1021/nl3020395.

Orwick-Rydmark, M. *et al.* (2012b) 'Detergent-Free Incorporation of a Seven-Transmembrane Receptor Protein into Nanosized Bilayer Lipodisq Particles for Functional and Biophysical Studies', *Nano Letters*, 12(9), pp. 4687–4692. doi: 10.1021/nl3020395.

Orwick, M. C. *et al.* (2012) 'Detergent-free formation and physicochemical

characterization of nanosized lipid-polymer complexes: Lipodisq', *Angewandte Chemie - International Edition*. John Wiley & Sons, Ltd, 51(19), pp. 4653–4657. doi: 10.1002/anie.201201355.

Overduin, M. and Esmaili, M. (2019) 'Native Nanodiscs and the Convergence of Lipidomics, Metabolomics, Interactomics and Proteomics', *Applied Sciences*. MDPI AG, 9(6), p. 1230. doi: 10.3390/app9061230.

Owsianik, G. *et al.* (2006) 'PERMEATION AND SELECTIVITY OF TRP CHANNELS', *Annual Review of Physiology*. Annual Reviews, 68(1), pp. 685–717. doi: 10.1146/annurev.physiol.68.040204.101406.

Parmar, M. *et al.* (2018) 'Using a SMALP platform to determine a sub-nm single particle cryo-EM membrane protein structure', *Biochimica et Biophysica Acta - Biomembranes*. 2017/10/11, 1860(2), pp. 378–383. doi: 10.1016/j.bbamem.2017.10.005.

Paulsen, C. E. *et al.* (2015) 'Structure of the TRPA1 ion channel suggests regulatory mechanisms', *Nature*. Nature Publishing Group, 520(7548), pp. 511–517. doi: 10.1038/nature14367.

Perraud, A. L. *et al.* (2001) 'ADP-ribose gating of the calcium-permeable LTRPC2 channel revealed by Nudix motif homology', *Nature*. Nature Publishing Group, 411(6837), pp. 595–599. doi: 10.1038/35079100.

Perraud, A. L. *et al.* (2003) 'NUDT9, a member of the Nudix hydrolase family, is an evolutionarily conserved mitochondrial ADP-ribose pyrophosphatase', *Journal of Biological Chemistry*, 278(3), pp. 1794–1801. doi: 10.1074/jbc.M205601200.

Perraud, A. L. *et al.* (2005) 'Accumulation of free ADP-ribose from mitochondria

mediates oxidative stress-induced gating of TRPM2 cation channels', *Journal of Biological Chemistry*. American Society for Biochemistry and Molecular Biology, 280(7), pp. 6138–6148. doi: 10.1074/jbc.M411446200.

Phillips, A. M., Bull, A. and Kelly, L. E. (1992) 'Identification of a Drosophila gene encoding a calmodulin-binding protein with homology to the trp phototransduction gene', *Neuron*. doi: 10.1016/0896-6273(92)90085-R.

Picard, M. *et al.* (2006) 'Protective and inhibitory effects of various types of amphipols on the Ca 2+-ATPase from sarcoplasmic reticulum: A comparative study', *Biochemistry*. American Chemical Society , 45(6), pp. 1861–1869. doi: 10.1021/bi051954a.

Pollock, N. L. *et al.* (2019) 'SMA-PAGE: A new method to examine complexes of membrane proteins using SMALP nano-encapsulation and native gel electrophoresis', *Biochimica et Biophysica Acta (BBA) - Biomembranes*. Elsevier, 1861(8), pp. 1437–1445. doi: 10.1016/J.BBAMEM.2019.05.011.

Popot, J.-L. *et al.* (2011) 'Amphipols From A to Z*', *Annual Review of Biophysics*, 40(1), pp. 379–408. doi: 10.1146/annurev-biophys-042910-155219.

Portolano, N. *et al.* (2014) 'Recombinant protein expression for structural biology in HEK 293F suspension cells: A novel and accessible approach', *Journal of Visualized Experiments*. Journal of Visualized Experiments, (92). doi: 10.3791/51897.

Postis, V. *et al.* (2015a) 'The use of SMALPs as a novel membrane protein scaffold for structure study by negative stain electron microscopy', *Biochimica et Biophysica Acta - Biomembranes*. Elsevier B.V., 1848(2), pp. 496–501. doi: 10.1016/j.bbamem.2014.10.018.

Postis, V. *et al.* (2015b) 'The use of SMALPs as a novel membrane protein scaffold for structure study by negative stain electron microscopy', *Biochimica et Biophysica Acta - Biomembranes*. Elsevier Pub. Co, 1848(2), pp. 496–501. doi: 10.1016/j.bbamem.2014.10.018.

Postis, V. *et al.* (2015c) 'The use of SMALPs as a novel membrane protein scaffold for structure study by negative stain electron microscopy', *Biochimica et Biophysica Acta - Biomembranes*. 2014/12/03, 1848(2), pp. 496–501. doi: 10.1016/j.bbamem.2014.10.018.

Postis, V. *et al.* (2015d) 'The use of SMALPs as a novel membrane protein scaffold for structure study by negative stain electron microscopy', *Biochimica et Biophysica Acta (BBA) - Biomembranes*. Elsevier, 1848(2), pp. 496–501. doi: 10.1016/J.BBAMEM.2014.10.018.

Privé, G. G. (2007) 'Detergents for the stabilization and crystallization of membrane proteins', *Methods*. Academic Press, 41(4), pp. 388–397. doi: 10.1016/j.ymeth.2007.01.007.

Pyle, E. *et al.* (2018) 'Structural Lipids Enable the Formation of Functional Oligomers of the Eukaryotic Purine Symporter UapA.', *Cell chemical biology*. Elsevier, 25(7), pp. 840-848.e4. doi: 10.1016/j.chembiol.2018.03.011.

Qiu, W. *et al.* (2018) 'Structure and activity of lipid bilayer within a membrane-protein transporter', *Proceedings of the National Academy of Sciences of the United States of America*. National Academy of Sciences, 115(51), pp. 12985–12990. doi: 10.1073/pnas.1812526115.

Rao, S. T. and Rossmann, M. G. (1973) 'Comparison of super-secondary structures

in proteins', *Journal of Molecular Biology*. Academic Press, 76(2), pp. 241–256. doi: 10.1016/0022-2836(73)90388-4.

Reading, E., Walton, T. A., *et al.* (2015) 'The Effect of Detergent, Temperature, and Lipid on the Oligomeric State of MscL Constructs: Insights from Mass Spectrometry', *Chemistry & Biology*. Cell Press, 22(5), pp. 593–603. doi: 10.1016/J.CHEMBIOL.2015.04.016.

Reading, E., Liko, I., *et al.* (2015a) 'The Role of the Detergent Micelle in Preserving the Structure of Membrane Proteins in the Gas Phase', *Angewandte Chemie International Edition*. John Wiley & Sons, Ltd, 54(15), pp. 4577–4581. doi: 10.1002/anie.201411622.

Reading, E., Liko, I., *et al.* (2015b) 'The Role of the Detergent Micelle in Preserving the Structure of Membrane Proteins in the Gas Phase', *Angewandte Chemie International Edition*, 54(15), pp. 4577–4581. doi: 10.1002/anie.201411622.

Rigaud, J.-L., Pitard, B. and Levy, D. (1995) 'Reconstitution of membrane proteins into liposomes: application to energy-transducing membrane proteins', *Biochimica et Biophysica Acta (BBA) - Bioenergetics*. Elsevier, 1231(3), pp. 223–246. doi: 10.1016/0005-2728(95)00091-V.

Ritchie, T. K. *et al.* (2009) 'Chapter 11 - Reconstitution of membrane proteins in phospholipid bilayer nanodiscs.', *Methods in enzymology*. NIH Public Access, 464, pp. 211–31. doi: 10.1016/S0076-6879(09)64011-8.

Rosano, G. L. and Ceccarelli, E. A. (2014) 'Recombinant protein expression in Escherichia coli: Advances and challenges', *Frontiers in Microbiology*. Frontiers Research Foundation. doi: 10.3389/fmicb.2014.00172.

Rosevear, P. *et al.* (1980) 'Alkyl Glycoside Detergents: A Simpler Synthesis and their Effects on Kinetic and Physical Properties of Cytochrome C Oxidase', *Biochemistry*. American Chemical Society, 19(17), pp. 4108–4115. doi: 10.1021/bi00558a032.

Roy, A., Kucukural, A. and Zhang, Y. (2010) 'I-TASSER: a unified platform for automated protein structure and function prediction', *Nature Protocols*. Nature Publishing Group, 5(4), pp. 725–738. doi: 10.1038/nprot.2010.5.

Salim, M. *et al.* (2014) 'Amphiphilic designer nano-carriers for controlled release: From drug delivery to diagnostics', *MedChemComm*. Royal Society of Chemistry, pp. 1602–1618. doi: 10.1039/c4md00085d.

Samanovic, M. I. *et al.* (2015) 'Proteasomal Control of Cytokinin Synthesis Protects Mycobacterium tuberculosis against Nitric Oxide', *Molecular Cell*. Cell Press, 57(6), pp. 984–994. doi: 10.1016/j.molcel.2015.01.024.

Scarfì, S. *et al.* (2009) 'The plant hormone abscisic acid stimulates the proliferation of human hemopoietic progenitors through the second messenger cyclic ADP-ribose', *Stem Cells*, 27(10), pp. 2469–2477. doi: 10.1002/stem.173.

Schafmeister, C. E., Miercke, L. J. W. and Stroud, R. M. (1993) 'Structure at 2.5 Å of a designed peptide that maintains solubility of membrane proteins', *Science*. American Association for the Advancement of Science, 262(5134), pp. 734–738. doi: 10.1126/science.8235592.

Scheidelaar, S., Koorengevel, Martijn C, *et al.* (2015) 'Molecular model for the solubilization of membranes into nanodisks by styrene maleic Acid copolymers.', *Biophysical journal*. The Biophysical Society, 108(2), pp. 279–90. doi:

10.1016/j.bpj.2014.11.3464.

Scheidelaar, S., Koorengevel, Martijn C., *et al.* (2015) 'Molecular Model for the Solubilization of Membranes into Nanodisks by Styrene Maleic Acid Copolymers', *Biophysical Journal*, 108(2), pp. 279–290. doi: 10.1016/j.bpj.2014.11.3464.

Scheres, S. H. W. (2012) 'RELION: Implementation of a Bayesian approach to cryo-EM structure determination', *Journal of Structural Biology*, 180(3), pp. 519–530. doi: 10.1016/j.jsb.2012.09.006.

Schnitzler, M. M. y *et al.* (2008) 'Evolutionary determinants of divergent calcium selectivity of TRPM channels', *The FASEB Journal*. Wiley, 22(5), pp. 1540–1551. doi: 10.1096/fj.07-9694com.

Schuck, S. *et al.* (2003) 'Resistance of cell membranes to different detergents', *Proceedings of the National Academy of Sciences of the United States of America*. National Academy of Sciences, 100(10), pp. 5795–5800. doi: 10.1073/pnas.0631579100.

Seddon, A. M., Curnow, P. and Booth, P. J. (2004) 'Membrane proteins, lipids and detergents: Not just a soap opera', *Biochimica et Biophysica Acta - Biomembranes*, pp. 105–117. doi: 10.1016/j.bbamem.2004.04.011.

Seki, K. and Tirrell, D. A. (1984) 'pH-Dependent Complexation of Poly(Acrylic Acid) Derivatives with Phospholipid Vesicle Membranes', *Macromolecules*. American Chemical Society, 17(9), pp. 1692–1698. doi: 10.1021/ma00139a009.

Senisterra, G., Chau, I. and Vedadi, M. (2012) 'Thermal denaturation assays in chemical biology', *Assay and Drug Development Technologies*. Mary Ann Liebert, Inc. 140 Huguenot Street, 3rd Floor New Rochelle, NY 10801 USA , pp. 128–136.

doi: 10.1089/adt.2011.0390.

Shaw, G. *et al.* (2002) 'Preferential transformation of human neuronal cells by human adenoviruses and the origin of HEK 293 cells.', *The FASEB journal : official publication of the Federation of American Societies for Experimental Biology*. FASEB J, 16(8), pp. 869–871. doi: 10.1096/fj.01-0995fje.

Shen, B. W. *et al.* (2003) 'The Crystal Structure and Mutational Analysis of Human NUDT9', *Journal of Molecular Biology*. Academic Press, 332(2), pp. 385–398. doi: 10.1016/S0022-2836(03)00954-9.

Siligardi, G. *et al.* (2014) 'Ligand- and drug-binding studies of membrane proteins revealed through circular dichroism spectroscopy', *Biochimica et Biophysica Acta - Biomembranes*. Elsevier, pp. 34–42. doi: 10.1016/j.bbamem.2013.06.019.

SMA Technical Documentation (2016). Available at: http://www.crayvalley.com/docs/technical-paper/sma-multi-functional-resins-(europe).pdf.

Smirnova, I. A., Ädelroth, P. and Brzezinski, P. (2018) 'Extraction and liposome reconstitution of membrane proteins with their native lipids without the use of detergents', *Scientific Reports*. Nature Publishing Group, 8(1), p. 14950. doi: 10.1038/s41598-018-33208-1.

Smith, A. J. *et al.* (2019) 'Styrene maleic acid recovers proteins from mammalian cells and tissues while avoiding significant cell death', *Scientific Reports*. Nature Research, 9(1), pp. 1–10. doi: 10.1038/s41598-019-51896-1.

Song, K., Wang, H., Kamm, Gretel B, *et al.* (2016) 'The TRPM2 channel is a hypothalamic heat sensor that limits fever and can drive hypothermia.', *Science (New*

York, N.Y.). American Association for the Advancement of Science, 353(6306), pp. 1393–1398. doi: 10.1126/science.aaf7537.

Song, K., Wang, H., Kamm, Gretel B., *et al.* (2016) 'The TRPM2 channel is a hypothalamic heat sensor that limits fever and can drive hypothermia', *Science*. American Association for the Advancement of Science, 353(6306), pp. 1393–1398. doi: 10.1126/science.aaf7537.

Starkus, J. *et al.* (2007) 'Regulation of TRPM2 by extra- and intracellular calcium.', *The Journal of general physiology*. The Rockefeller University Press, 130(4), pp. 427–40. doi: 10.1085/jgp.200709836.

Stuart, M. C. A. and Boekema, E. J. (2007) 'Two distinct mechanisms of vesicle-to-micelle and micelle-to-vesicle transition are mediated by the packing parameter of phospholipid-detergent systems', *Biochimica et Biophysica Acta - Biomembranes*. Elsevier, 1768(11), pp. 2681–2689. doi: 10.1016/j.bbamem.2007.06.024.

Su, C. C. *et al.* (2019) 'Cryo-electron microscopy structure of an acinetobacter baumannii multidrug efflux pump', *mBio*. American Society for Microbiology, 10(4). doi: 10.1128/mBio.01295-19.

Sumoza-Toledo, A. and Penner, R. (2011) 'TRPM2: a multifunctional ion channel for calcium signalling.', *The Journal of physiology*. Wiley-Blackwell, 589(Pt 7), pp. 1515–25. doi: 10.1113/jphysiol.2010.201855.

Sun, C. *et al.* (2018) 'Structure of the alternative complex III in a supercomplex with cytochrome oxidase', *Nature*. Nature Publishing Group, 557(7703), pp. 123–126. doi: 10.1038/s41586-018-0061-y.

Swainsbury, D. J. K. *et al.* (2017) 'The effectiveness of styrene-maleic acid (SMA)

copolymers for solubilisation of integral membrane proteins from SMA-accessible and SMA-resistant membranes', *Biochimica et Biophysica Acta - Biomembranes*. Elsevier B.V., 1859(10), pp. 2133–2143. doi: 10.1016/j.bbamem.2017.07.011.

Taberner, F. J. *et al.* (2015) 'TRP channels interaction with lipids and its implications in disease', *Biochimica et Biophysica Acta (BBA) - Biomembranes*. Elsevier, 1848(9), pp. 1818–1827. doi: 10.1016/J.BBAMEM.2015.03.022.

Tan, C. H. and McNaughton, P. A. (2016) 'The TRPM2 ion channel is required for sensitivity to warmth', *Nature*. Nature Publishing Group, 536(7617), pp. 460–463. doi: 10.1038/nature19074.

Tan, C. H. and McNaughton, P. A. (2018) 'TRPM2 and warmth sensation', *Pflugers Archiv European Journal of Physiology*. 2018/03/20, 470(5), pp. 787–798. doi: 10.1007/s00424-018-2139-7.

Tate, C. G. (2001) 'Overexpression of mammalian integral membrane proteins for structural studies', in *FEBS Letters*. John Wiley & Sons, Ltd, pp. 94–98. doi: 10.1016/S0014-5793(01)02711-9.

Teo, A. C. K. *et al.* (2019) 'Analysis of SMALP co-extracted phospholipids shows distinct membrane environments for three classes of bacterial membrane protein', *Scientific Reports*. Nature Publishing Group, 9(1), p. 1813. doi: 10.1038/s41598-018-37962-0.

Thompson, R. F. *et al.* (2016) 'An introduction to sample preparation and imaging by cryo-electron microscopy for structural biology', *Methods*, 100, pp. 3–15. doi: 10.1016/j.ymeth.2016.02.017.

Togashi, K. *et al.* (2006) 'TRPM2 activation by cyclic ADP-ribose at body

temperature is involved in insulin secretion', *EMBO Journal*. EMBO J, 25(9), pp. 1804–1815. doi: 10.1038/sj.emboj.7601083.

Tong, Q. *et al.* (2006) 'Regulation of the transient receptor potential channel TRPM2 by the Ca 2+ sensor calmodulin', *Journal of Biological Chemistry*. American Society for Biochemistry and Molecular Biology, 281(14), pp. 9076–9085. doi: 10.1074/jbc.M510422200.

Tonge, S. (2006) 'Compositions Comprising a Lipid and Copolymer of Styrene and Maleic Acid. US Patent 8623414. Jan 7th 2014, to Malvern Cosmeceutics Ltd.'

Tonge, S. R. and Tighe, B. J. (2001) 'Responsive hydrophobically associating polymers: A review of structure and properties', *Advanced Drug Delivery Reviews*. Adv Drug Deliv Rev, pp. 109–122. doi: 10.1016/S0169-409X(01)00223-X.

Toth, B. and Csanady, L. (2012) 'Pore collapse underlies irreversible inactivation of TRPM2 cation channel currents', *Proc Natl Acad Sci U S A*. 2012/08/01, 109(33), pp. 13440–13445. doi: 10.1073/pnas.1204702109.

Tóth, B. and Csanády, L. (2012) 'Pore collapse underlies irreversible inactivation of TRPM2 cation channel currents.', *Proceedings of the National Academy of Sciences of the United States of America*. National Academy of Sciences, 109(33), pp. 13440–5. doi: 10.1073/pnas.1204702109.

Tribet, C., Audebert, R. and Popot, J.-L. (1996) 'Amphipols: Polymers that keep membrane proteins soluble in aqueous solutions', *Proceedings of the National Academy of Sciences*. National Academy of Sciences, 93(26), pp. 15047–15050. doi: 10.1073/PNAS.93.26.15047.

Tribet, C., Audebert, R. and Popot, J. L. (1997) 'Stabilization of hydrophobic

colloidal dispersions in water with amphiphilic polymers: Application to integral membrane proteins', *Langmuir*. American Chemical Society , 13(21), pp. 5570–5576. doi: 10.1021/la970136j.

Tsuruda, P. R. *et al.* (2006) 'Coiled coils direct assembly of a cold-activated TRP channel.', *Neuron*. NIH Public Access, 51(2), pp. 201–12. doi: 10.1016/j.neuron.2006.06.023.

Tsuruda, P. R., Julius, D. and Minor, D. L. (2006) 'Coiled Coils Direct Assembly of a Cold-Activated TRP Channel', *Neuron*. NIH Public Access, 51(2), pp. 201–212. doi: 10.1016/j.neuron.2006.06.023.

Uhlén, M. *et al.* (2015) 'Tissue-based map of the human proteome', *Science*. American Association for the Advancement of Science, 347(6220), pp. 1260419–1260419. doi: 10.1126/science.1260419.

Venkatachalam, K. and Montell, C. (2007) 'TRP Channels TRP: Transient Receptor Potential', *Annu Rev Biochem*. NIH Public Access, 76, pp. 387–417. doi: 10.1146/annurev.biochem.75.103004.142819.

Voets, T. (2016) 'Warm feelings for TRPM2', *Cell Research*. Nature Publishing Group, pp. 1174–1175. doi: 10.1038/cr.2016.121.

Voller, J. *et al.* (2010) 'Anticancer activity of natural cytokinins: A structure-activity relationship study', *Phytochemistry*. Elsevier Ltd, 71(11–12), pp. 1350–1359. doi: 10.1016/j.phytochem.2010.04.018.

Wallin, E., Gunnar, A. and Heijne, V. (1998) 'Genome-wide analysis of integral membrane proteins from eubacterial, archaean, and eukaryotic organisms', *Protein Science*.

Wang, L. *et al.* (2018) 'Structures and gating mechanism of human TRPM2', *Science*. American Association for the Advancement of Science, 362(6421). doi: 10.1126/science.aav4809.

Wang, L. and Sigworth, F. J. (2009) 'Structure of the BK potassium channel in a lipid membrane from electron cryomicroscopy', *Nature*. Nature, 461(7261), pp. 292–295. doi: 10.1038/nature08291.

Wang, Z. *et al.* (2015) 'Cysteine residue is not essential for CPM protein thermal-stability assay', *Analytical and Bioanalytical Chemistry*. Springer Berlin Heidelberg, 407(13), pp. 3683–3691. doi: 10.1007/s00216-015-8587-4.

Wang, Z. *et al.* (2017) 'An allosteric transport mechanism for the AcrAB-TolC multidrug efflux pump', *eLife*, 6. doi: 10.7554/eLife.24905.

Watkinson, T. G. *et al.* (2015) 'Systematic analysis of the use of amphipathic polymers for studies of outer membrane proteins using mass spectrometry.', *International journal of mass spectrometry*. Elsevier, 391, pp. 54–61. doi: 10.1016/j.ijms.2015.06.017.

Watkinson, T. G. *et al.* (2017) 'FPOP-LC-MS/MS Suggests Differences in Interaction Sites of Amphipols and Detergents with Outer Membrane Proteins', *Journal of The American Society for Mass Spectrometry*. Springer US, 28(1), pp. 50–55. doi: 10.1007/s13361-016-1421-1.

Wehage, E. *et al.* (2002) 'Activation of the cation channel long transient receptor potential channel 2 (LTRPC2) by hydrogen peroxide. A splice variant reveals a mode of activation independent of ADP-ribose.', *The Journal of biological chemistry*. American Society for Biochemistry and Molecular Biology, 277(26), pp. 23150–6.

doi: 10.1074/jbc.M112096200.

Wes, P. D. *et al.* (1995) 'TRPC1, a human homolog of a Drosophila store-operated channel', *Proceedings of the National Academy of Sciences of the United States of America*. National Academy of Sciences, 92(21), pp. 9652–9656. doi: 10.1073/pnas.92.21.9652.

Winkler, P. A. *et al.* (2017) 'Electron cryo-microscopy structure of a human TRPM4 channel', *Nature*. Nature Publishing Group, 552(7684), pp. 200–205. doi: 10.1038/nature24674.

Xu, X. Z. S. *et al.* (2000) 'TRPγ, a Drosophila TRP-related subunit, forms a regulated cation channel with TRPL', *Neuron*. Cell Press, 26(3), pp. 647–657. doi: 10.1016/S0896-6273(00)81201-5.

Yang, K. and Han, X. (2016) 'Lipidomics: Techniques, Applications, and Outcomes Related to Biomedical Sciences.', *Trends in biochemical sciences*. Elsevier, 41(11), pp. 954–969. doi: 10.1016/j.tibs.2016.08.010.

Yano, Y. F. *et al.* (2009) 'Driving force behind adsorption-induced protein unfolding: A time-resolved x-ray reflectivity study on lysozyme adsorbed at an air/water interface', *Langmuir*. American Chemical Society, 25(1), pp. 32–35. doi: 10.1021/la803235x.

Yao, F. *et al.* (1998) 'Tetracycline repressor, tetR, rather than the tetR-mammalian cell transcription factor fusion derivatives, regulates inducible gene expression in mammalian cells', *Human Gene Therapy*. Mary Ann Liebert Inc., 9(13), pp. 1939–1950. doi: 10.1089/hum.1998.9.13-1939.

Yin, Y., Le, S. C., *et al.* (2019) 'Structural basis of cooling agent and lipid sensing by

the cold-activated TRPM8 channel', *Science*. American Association for the Advancement of Science, 363(6430). doi: 10.1126/science.aav9334.

Yin, Y., Wu, M., *et al.* (2019) 'Visualizing structural transitions of ligand-dependent gating of the TRPM2 channel', *Nature Communications*. Nature Publishing Group, 10(1), pp. 1–14. doi: 10.1038/s41467-019-11733-5.

Yu, P. *et al.* (2019) 'Direct Gating of the TRPM2 Channel by cADPR via Specific Interactions with the ADPR Binding Pocket', *Cell Reports*. Elsevier B.V., 27(12), pp. 3684-3695.e4. doi: 10.1016/j.celrep.2019.05.067.

Zhang, Y. *et al.* (2018) 'Structural Basis for Cholesterol Transport-like Activity of the Hedgehog Receptor Patched', *Cell*. Cell Press, 175(5), pp. 1352-1364.e14. doi: 10.1016/j.cell.2018.10.026.

Zhang, Z. *et al.* (2018a) 'Structure of a TRPM2 channel in complex with Ca2+explains unique gating regulation', *eLife*. 2018/05/11, 7. doi: 10.7554/eLife.36409.001.

Zhang, Z. *et al.* (2018b) 'Structure of a TRPM2 channel in complex with Ca2+explains unique gating regulation', *eLife*, 7, pp. 1–22. doi: 10.7554/eLife.36409.001.

Zhu, J.-H. and Javid, B. (2015) 'Tuberculosis: Hey There, Lonely Guy!', *Molecular Cell*, 57(6), pp. 951–952. doi: 10.1016/j.molcel.2015.03.004.

Zimmermann, L. *et al.* (2018) 'A Completely Reimplemented MPI Bioinformatics Toolkit with a New HHpred Server at its Core', *Journal of Molecular Biology*. Academic Press, 430(15), pp. 2237–2243. doi: 10.1016/j.jmb.2017.12.007.

Zoonens, M. *et al.* (2007a) 'Dynamics of membrane protein/amphipol association studied by Förster resonance energy transfer: Implications for in vitro studies of amphipol-stabilized membrane proteins', *Biochemistry*. American Chemical Society , 46(36), pp. 10392–10404. doi: 10.1021/bi7007596.

Zoonens, M. *et al.* (2007b) 'Dynamics of membrane protein/amphipol association studied by Förster resonance energy transfer: Implications for in vitro studies of amphipol-stabilized membrane proteins', *Biochemistry*, 46(36), pp. 10392–10404. doi: 10.1021/bi7007596.

Zoonens, M. and Popot, J. L. (2014) 'Amphipols for Each Season', *Journal of Membrane Biology*, 247(9–10), pp. 759–796. doi: 10.1007/s00232-014-9666-8.

Zorman, S. *et al.* (2015) 'Advances and challenges of membrane-protein complex production', *Current Opinion in Structural Biology*. Elsevier Ltd, 32, pp. 123–130. doi: 10.1016/j.sbi.2015.03.010.